MECHANICAL AND PHYSICAL CHARACTERIZATION OF RECYCLED PET BALES FOR USE AS LIGHTWEIGHT FILL MATERIAL

by

Jacob Joseph Garbini

A dissertation submitted to the faculty of
The University of North Carolina at Charlotte
in partial fulfillment of the requirements
for the degree of Doctor of Philosophy in
Infrastructure and Environmental Systems

Charlotte

2016

Approved by:

_____

Dr. Kimberly Warren

_____

Dr. Miguel Pando

_____

Dr. James Bowen

_____

Dr. Vincent Ogunro

_____

Dr. Susan Sell

ABSTRACT

JACOB JOSEPH GARBINI. Mechanical and physical characterization of recycled PET bales for use as lightweight fill material. (Under the direction of DR. KIMBERLY WARREN (Co-Advisor) and DR. MIGUEL PANDO (Co-Advisor))

Waste generation rates are increasing so there is a need to determine alternative methods of dealing with waste to accommodate a sustainable future. Polyethylene Terephthalate (PET) plastic represents a large portion of the domestic waste generated. This research focuses on characterizing the mechanical and physical properties of recycled PET bales and their constituents after being processed at a material recovery facility. The intent of this study was to assess the technical feasibility of using recycled PET bales as lightweight fill in embankments and engineered slopes. The tensile strength and short-term, one-dimensional deformation characteristics of recycled PET bale constituents were evaluated using full-bottle and chopped PET plastic test specimens. The long-term deformation (creep) of a full-scale PET bale was tested during a large scale unconfined compression test. Additionally, the shear strength of the PET bale constituents were evaluated using a modified direct shear apparatus and triaxial compression tests. A detailed description of the materials tested, the testing protocol developed for each test, and the results and analysis for each evaluation will be presented in this dissertation. The results from all tests conducted herein were subsequently utilized in limit equilibrium analyses to assess the feasibility of using recycled PET bales as lightweight fill in slope stability applications. The analyses systematically evaluated multiple lightweight fill configurations within two slope inclinations and two different soil conditions. The recycled PET bales were compared to EPS Geofoam and tire bales.

ACKNOWLEDGEMENTS

TABLE OF CONTENTS

LIST OF FIGURES

LIST OF TABLES

LIST OF SYMBOLS AND ABBREVIATIONS

ε = Axial strain (%)

ΔL = Change in specimen length (cm)

L_o = Initial specimen length (cm)

σ_t = Nominal tensile stress (kPa)

T = Tensile force from load cell (kPa)

A_{AVG} = Average specimen area using average initial width and thickness (cm)

ΔH = Change in specimen height (cm)

H_o = Initial specimen height (cm)

σ_c = Compressive stress (MPa)

F = Compressive force (kN)

A = Contact area (m^2)

M_s = Constrained secant modulus increment from σ_o to σ_n (kPa)

$\Delta\sigma$ = Change in compressive stress (kPa)

$\Delta\varepsilon$ = Change in axial strain from stress increment from σ_o to σ_n

σ_o = Seating load normal stress (kPa) [constant for all tests equal to 10 kPa]

σ_n = Applied vertical normal stress (kPa) [constant for all tests equal to 120 kPa]

τ = Nominal shear stress (kPa)

F_s = Shear force (kN)

Δu = change in the specimen pore pressure that occurs as a result of a change in the chamber pressure when the specimen drainage valves are closed (kPa)

$\Delta\sigma_3$ = isotropic change in the chamber pressure (kPa)

$P(\varepsilon)$ = measured applied deviator load at strain ε (kPa)

A_{corr} (ε) = corrected cross-sectional area at strain ε (cm^2)

V_c = volume after compress (dry specimen) or after consolidation (saturated specimen) (cm^3)

ΔV_{ε} = change in volume form beginning of shear to any strain (cm^3)

ΔH_{ε} = change in height from beginning of shear to any strain (cm)

$\Delta(\sigma_1 - \sigma_3)$ = correction to be subtracted from the measured principal stress difference (deviator stress) (kPa)

$D_c = (4A_c/\pi)^{0.5}$ = diameter of specimen after consolidation (mm)

E_m = Young's modulus for the membrane material (kPa)

t_m = thickness of the membrane (mm)

E_t = Initial tangent modulus (kPa)

E_2 = Second tangent modulus (kPa)

PET = Polyethylene Terephthalate

MRF = Materials Recovery Facility

1D = One-dimensional

EPS = Expanded Polystyrene

MSW = Municipal Solid Waste

EPA = Environmental Protection Agency

TDA = Tired Derived Aggregate

HDPE = High Density Polyethylene

LDPE = Low Density Polyethylene

LVDT = Linear Variable Differential Transformer

M1 = Method 1 Loading Scheme

M2 = Method 2 Loading Scheme

CHAPTER 1: INTRODUCTION

1.1 Problem Statement

The world is a complex, closed, and dynamic system. In order to sustain human existence on this planet for generations to come, innovative infrastructure must be expedited through progressive design and philosophies. The research conducted herein investigates the technical feasibility of using polyethylene terephthalate (PET) plastic as a lightweight fill in embankments. In general, earthen embankments can be constructed using several conventional methods. Typically soils and aggregates are excavated, transported to the site (if necessary), and utilized to construct embankments for roads, highways, and other infrastructure demands. The methods necessary to evaluate soil properties and compact the soil on-site are well established. Typical design considerations for embankments include: i) displacements of the embankment should below allowable values; ii) slope stability and iii) bearing capacity. Therefore the material used for the construction of the embankment must have the required engineering properties to meet the design criteria. Typically the most important properties are deformation properties, such as the elastic Young's modulus and the constrained modulus, and shear strength properties, such as the effective friction angle. Slopes of embankments, if the slope is very steep or the embankment material shear strength is not high enough, can also be constructed using steel or geosynthetic reinforcing inclusions to either increase the performance of a slope design without them

or increase the slope inclination due to real estate limitations on-site. When the foundation soils supporting an embankment are weak and compressible it is common to use light weight fill materials to decrease the induced pressures by the embankment and thus decrease embankment settlements and deformations. Expanded Polystyrene blocks, commonly known as EPS Geofoam, is commonly used as lightweight fill in embankments and bridge approaches. EPS Geofoam is an advantageous construction material due to the documented reduction in construction time, predictable behavior of the material, and the inert property of the material. However, EPS Geofoam is a manufactured material, not a recycled waste product.

The author of this study is passionate about sustainability. It is important to note that waste generation rates are increasing with decreasing finite spatial resources to accommodate the waste so there is a need to determine alternative methods of dealing with waste to accommodate a sustainable future. The growing population is proportional to the infrastructure demand. This point, combined with the challenges associated with the maintenance of existing infrastructure creates a demand for innovation and infrastructure designed to accommodate a sustainable future. Additionally, natural resource availability is decreasing due to the increasing anthropogenic impacts, which require the demand for alternative infrastructure components. As part of this research project, recycled PET plastic bales are investigated as a potential lightweight fill for embankment applications. As mentioned above, to determine the technical feasibility of using recycled PET plastic bales in this type of engineering application, it is important to evaluate the engineering properties of the material with an emphasis on compressibility and shear strength.

1.2 Research Objectives

This research focuses on characterizing the mechanical and physical properties of recycled PET bales and their constituents after being processed at a material recovery facility (MRF). The main intent of this study was to assess the technical feasibility of using recycled PET bales for use as lightweight fill in embankments and engineered slopes. The tensile strength and short-term, one-dimensional (1D) deformation characteristics of recycled PET bale constituents were evaluated using full-bottle and chopped PET plastic test specimens. The long-term deformation (creep) of a full-scale PET bale was tested during a large scale unconfined compression test. Additionally, the shear strength of the PET bale constituents were evaluated through interface shear tests using a modified direct shear apparatus and shear strength triaxial compression tests. A detailed description of the materials tested, the testing protocol developed for each test, and the results and analysis for each evaluation are presented in subsequent chapters. The results from all tests were subsequently utilized in a limit equilibrium analysis to assess the feasibility of using recycled PET bales as lightweight fill in slope stability applications. The analysis systematically evaluated multiple lightweight fill configurations within two slope inclinations and two different subsurface soil conditions. The use of recycled PET bales for lightweight fill was compared to alternative materials including EPS Geofoam and shredded tire bales. Table 1.1 provides a summary of all tests conducted during this evaluation.

Table 1.1: Summary of key components of experimental research apart of this study

Test Report Sections (No. Tests)	Test Specimen Description	Test Configuration	Test Variables
Tensile Strength Sections 3.3-3.4 (200)	• Individual Recycled PET Constituents (Groups 1/2/3)	• UTS Tensile Machine • Curtis Hydraulic grips	• Displacement Rate = 1.27 mm/min, 12.7 mm/min
1D Confined Compression Section 4.2 (42)	• Full-Bottle Constituents • Chopped Constituents (Group 1 Only)	• Displacement Rate = 3.81 cm/min • 127 cm String Potentiometer (1) • 445 kN Load Cell • Hydraulic Piston • Steel Cylinders	• Loading Scheme = M1, M2 • γ_{PET} = 2.36 kN/m³, 3.93 kN/m³ • Test Specimen Diameter = 22.86 cm, 45.72 cm
Interface Direct Shear Section 4.3 (9)	• Select Recycled PET plastic (Group 1 Only)	• Geotac Direct Shear Apparatus • Displacement Rate = 0.01 cm/min • Normal Stress = 50 kPa, 100 kPa, and 200 kPa	• Texture: Flat, Ribbed-Orthogonal, and Ribbed-Aligned
Triaxial Compression Section 4.4 (24)	• Chopped Constituents (Group 1 Only)	• ELE Load Frame • 4.45 kN Load Cell • Axial Strain Transducer • 15.24 cm Diameter Triaxial Cell • Confining Pressure (17.24 kPa, 34.47 kPa, 51.71 kPa, 68.95 kPa)	• Disp. Rate: 0.02 - 10 mm/min • γ_{PET} = 0.79 kN/m³ -2.36 kN/m³ • Saturation: Dry and Saturated
Unconfined Compression Sections 5.2-5.4 (1)	• Full-Scale Recycled PET Bale (Groups 1/2/3)	• 127 cm String Potentiometers (4) • Short Term (1.5 hours) Applied Stress = 42.4 kPa • Long Term (15,330 hours) Creep Stress = 23.5 kPa	
Limit Equilibrium Analysis Sections 6.1-6.6 (80)	• Simulated Lightweight Zones within the Subsurface	• SLIDE (Version 6.035 – Rocscience) • Fixed Circular Failure Surface (Center Located 30 m Above Toe) • γ_{PET} = 2.36 kN/m³, 3.93 kN/m³ $\gamma_{Geofoam}$ = 0.20 kN/m³ $\gamma_{Tire\ bale}$ = 5.50 kN/m³ γ_{Clay} = 19 kN/m³ γ_{Sand} = 18 kN/m³	• Material Type: SW Soil, CL Soil, EPS Geofoam, and Tire Bales • Bale Configuration • PET Friction Angle: 5°, 10°, 15° • Slope Inclination: 3H:1V, 2H:1V

The specific objectives for this research are:

- Characterize the recycled PET plastic bale in comparison to competing engineering materials such as EPS Geofoam and recycled tire bales.

- Examine the tensile strength of recycled PET plastic bale full-scale constituents to identify the possible stress-strain behaviors if utilized in the construction of embankments reinforced with plastic waste.

- Examine the 1D confined compressibility of recycled PET plastic bale full-scale and chopped constituents to identify the possible deformation and stress-strain characteristics while assessing the effects of varying load applications, specimen sizes, particle sizes, and unit weights.

- Examine the interface direct shear strength of recycled PET plastic bale modified constituents under direct shear boundary conditions using varying normal loads.

- Examine the triaxial compressive shear strength of recycled PET plastic bale chopped constituents under various load conditions using geotechnical testing techniques.

- Quantify the effects of unconfined short-term loading experienced by a recycled PET plastic bale under a sustained load for 90 minutes.

- Quantify the effects of unconfined creep experienced by a recycled PET plastic bale under a sustained load for 21 consecutive months.

- Conduct a parametric evaluation within a limit equilibrium analysis to assess the feasibility of recycled PET plastic bale configurations using the triaxial compression data collected from this study, which served as a conservative estimate of shear strength.

1.3 Research Scope

This dissertation has been organized into the following chapters. A brief description of each chapter has been included:

- Chapter 2 outlines the results obtained during the literature review conducted as part of this research project.

- Chapter 3 describes the PET material and summarizes the data acquisition equipment, sensors, installation procedures, and the results of the tensile strength tests conducted on the recycled PET bale constituents.

- Chapter 4 describes the data acquisition equipment, sensors, installation procedures, and the results acquired during the short-term 1D compression, interface direct shear, and triaxial compression tests that were conducted on recycled PET bale constituents as part of this study.

- Chapter 5 summarizes the data acquisition equipment, sensors, installation procedures, and the short-term and long-term results collected during the large-scale, unconfined compression test performed using a full-scale recycled PET plastic bale.

- Chapter 6 summarizes the experimental data acquired during this research and describes the limit equilibrium analysis conducted to determine the effects of integrating recycled PET bales into embankments, dependent on material properties, slope inclinations, and the reinforcing zone configurations with a comparison between EPS Geofoam and recycled tire bales.

- Chapter 7 outlines the summary and conclusions from the research with recommendations for future work.

CHAPTER 2: LITERATURE REVIEW

2.1 Introduction

The purpose of this research project is to examine the engineering behavior and properties of a recycled compressed plastic, polyethylene terephthalate (PET) material (bale and constituents), for use as a lightweight fill material in geotechnical applications. The recycled material will be examined using geotechnical testing techniques combined with limit equilibrium slope stability analysis methods. This literature review will describe the proposed application, identify and describe select comparable technologies for civil engineering applications, and summarize the research initiatives and case studies that have been conducted in civil engineering applications using other similar recycled materials including EPS Geofoam and tire bales.

Municipal solid waste (MSW) generation rates have been examined as far back as 1960 (EPA, 2012). These rates indicate a continual increase in rates from 88.1 million metric tons to 249.9 million metric tons over a 50-year period. The solid line in Figure 2.1 displays the total tons of MSW generated per year (axis on left side of the figure), while the dotted line represents the generation per capita in pounds/person/day from 1960 to 2010 in the United States of America (axis on the right side of the figure). Figure 2.1 indicates a sharp increase in total MSW generation, which correlates with the economic expansion experienced by the United States in the late 1980's through 2000.

There is a slight decline in the MSW generation rates beginning after 2001 likely due to

the economic downfall.
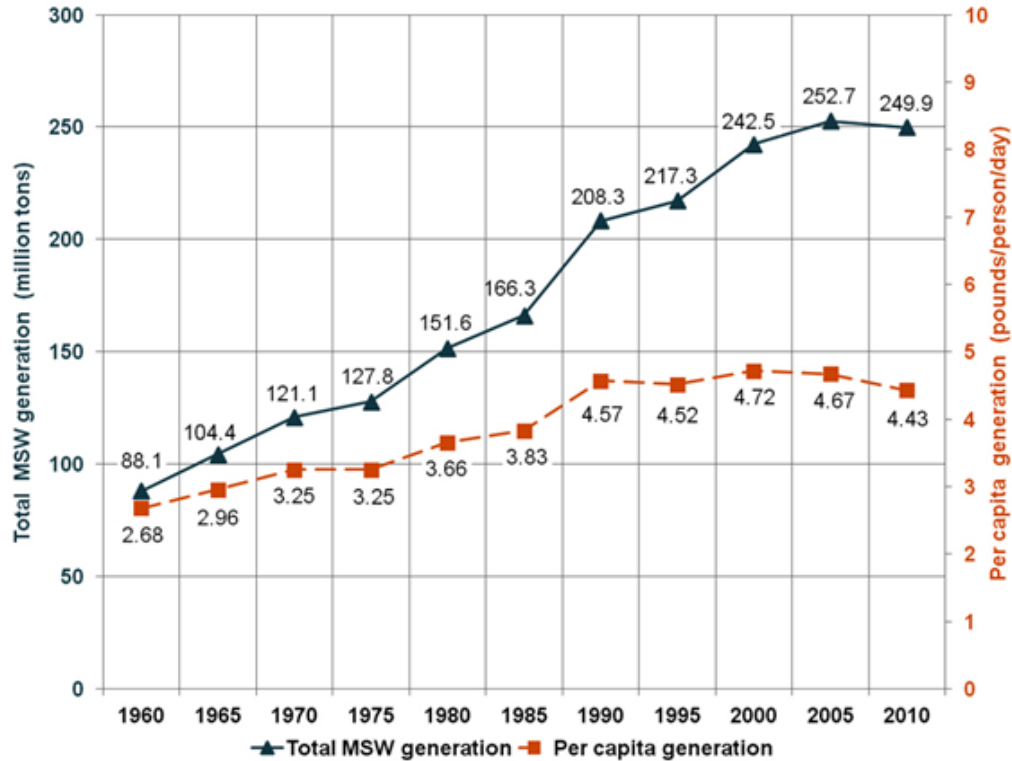
Figure 2.1: Municipal solid waste generation rates in the United States of America from 1960-2010 (EPA, 2012)

Figure 2.2 depicts MSW recycling rates. The solid line in Figure 2.2 indicates tons

of MSW recycled while the dashed line shows the percentage recycled. In 1960, the U.S.

generated 88.1 million tons of waste, equivalent to 2.68 pounds/person/day (Figure 2.1),

but only 5.6 million tons (6.4%) were recycled (Figure 2.2). In 2010, the U.S. generated

249.9 million tons of waste, equivalent to 4.43 pounds/person/day (Figure 2.1), but only

85.1 million tons (34.1%) were recycled (Figure 2.2).
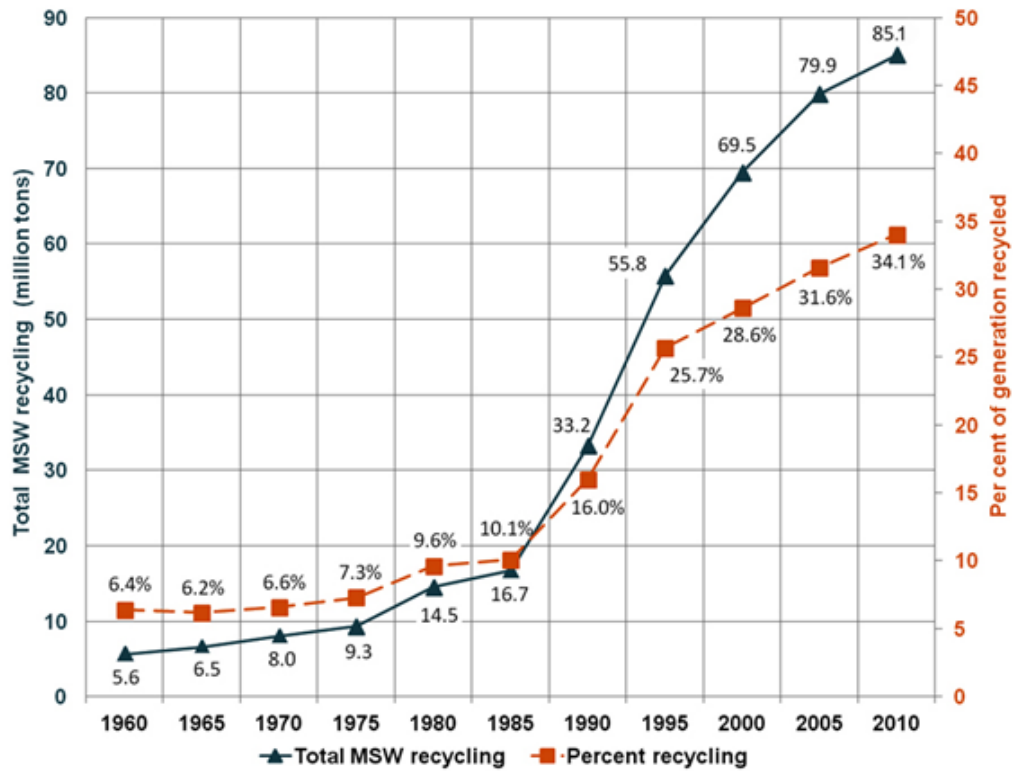
Figure 2.2: Municipal solid waste recycling rates from in the United States of America 1960-2010 (EPA, 2012)

The constituents of the 250 million tons of MSW generated in the U.S. in 2010 are displayed by category in Figure 2.3. Plastic is the fourth-largest constituent on the list with 31 million tons (12.4%). The EPA study revealed that approximately 50% of the plastic was polyethylene terephthalate (PET). Roughly 15.5 million tons of PET waste was generate in 2010 (EPA, 2012).
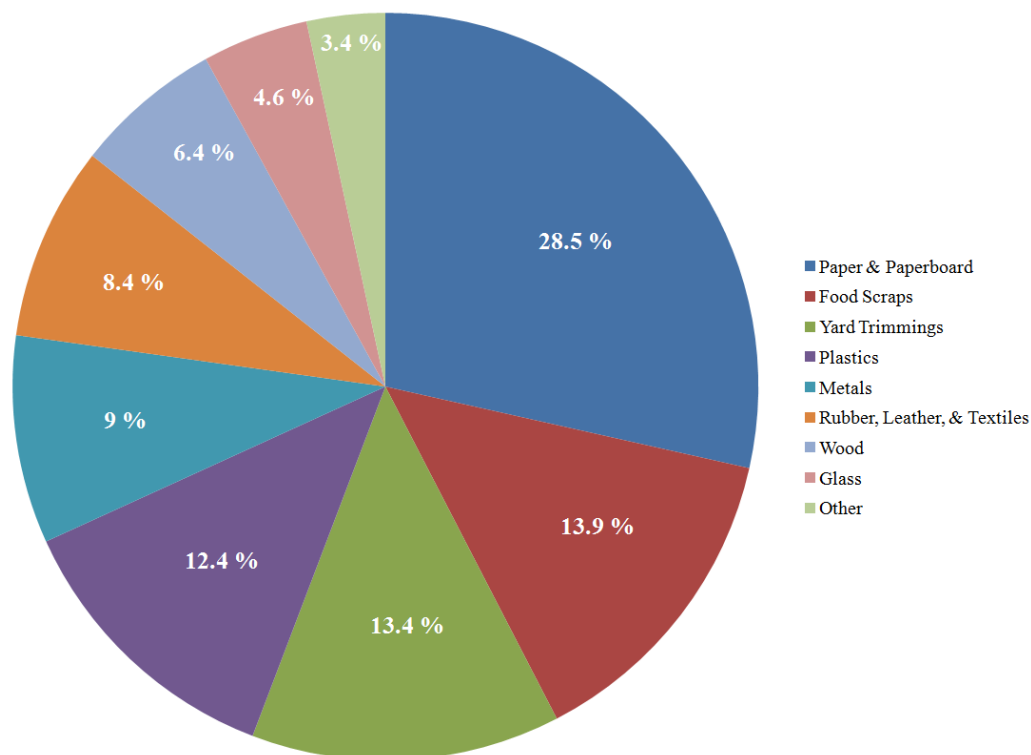
Figure 2.3: Municipal solid waste constituents for 2010 in the United States of America (EPA, 2012)

Figure 2.4 displays the recycling rates for select recycled MSW constituents in 2010, as reported by the EPA (2012). According to the figure, only 29.2% of PET bottles, containers, and jars were recycled. In comparison, approximately 96.2% of the auto batteries generated as waste were recycled. Only 4.52 million tons of the 15.5 million tons of plastic PET were recycled. The larger portion was distributed into landfills or other forms of waste-management. The recycled PET material often gets sold back to manufacturers of post-consumer plastic products.
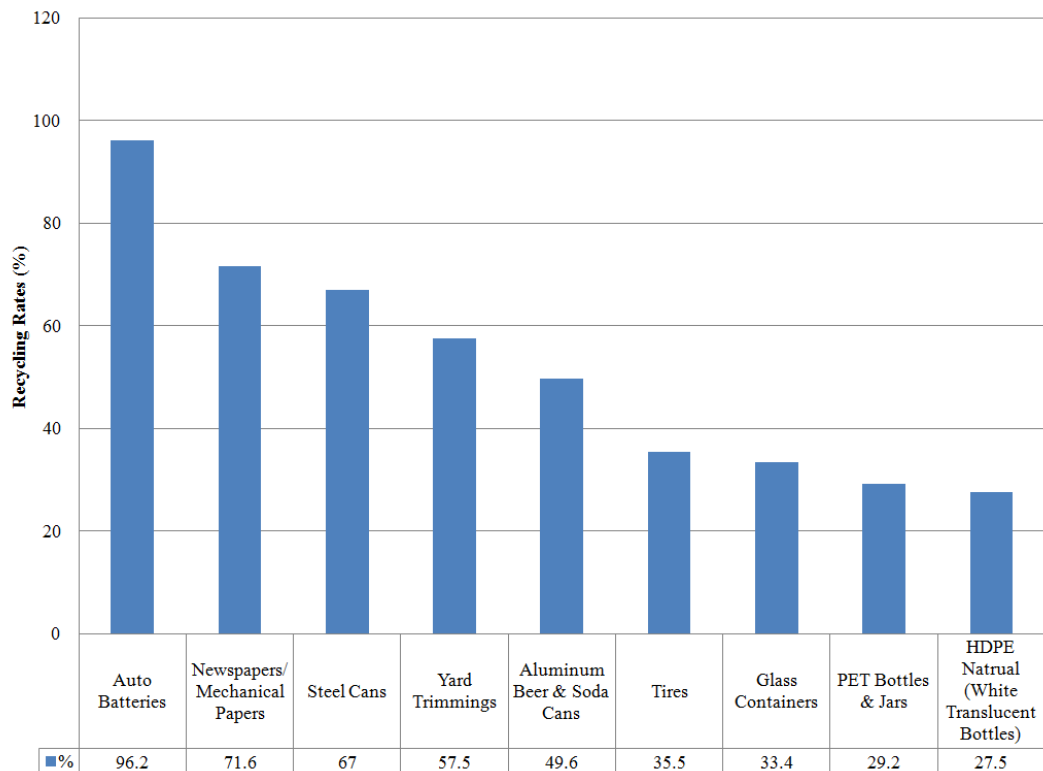
Figure 2.4: Recycling rate of select MSW constituents in 2010 (EPA, 2012)

There are benefits to incorporating recycled materials into nonconventional applications. For example, some school playgrounds are utilizing tire shreds from recycled tires as fill around playground equipment to provide a softer impact material for children (CalRecycle, 2015). The current study proposes the use of polyethylene terephthalate (PET) plastic bales as a recycled, lightweight, geotechnical fill for embankment applications. To date, the use of recycled plastic material bales for this type of geotechnical applications has not been explored.

This literature review will describe the proposed application in detail and then provide literature references including studies that used recycled plastic material in other applications or as a comparable lightweight fill material. EPS Geofoam blocks and tire

bales serve as comparable lightweight materials. Sections 2.2, 2.3, and 2.4 cover studies associated with reinforcing 'zones', recycled materials used as reinforcing 'inclusions', and recycled 'particulate materials', respectively. These three comparable groups (i.e., reinforcing zones, reinforcing inclusions, and recycled particulate materials) are presented as individual schematics in Figure 2.5. To understand the behavior and provide an adequate design of each embankment, the engineering properties of each material should be evaluated. The lightweight bale/zone group displayed in Figure 2.5(a) can be represented using EPS Geofoam (Expanded Polystyrene or EPS), recycled plastic material bales, or tire bales. The second reinforcing element group displayed in Figure 2.5(b), can be represented by any of the recycled reinforcing elements presented in Section 2.4. The particulate material group displayed in Figure 2.5(c), can be represented by any of the recycled particulate materials presented in Section 2.5. Table 2.1 summarizes the references associated with each group of materials reviewed in this chapter.
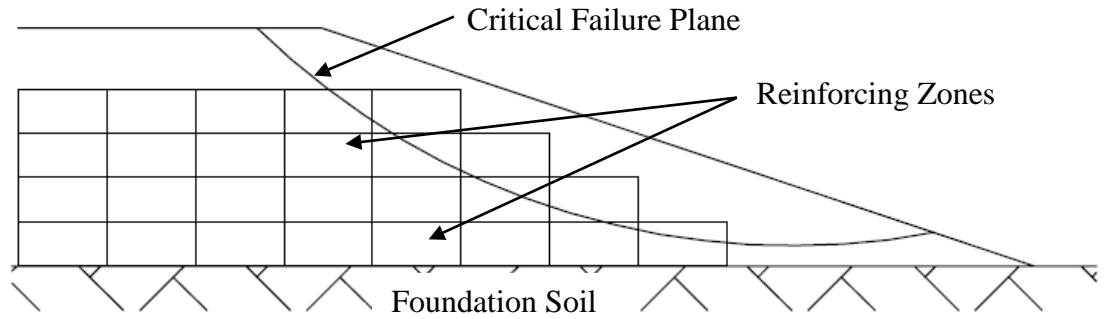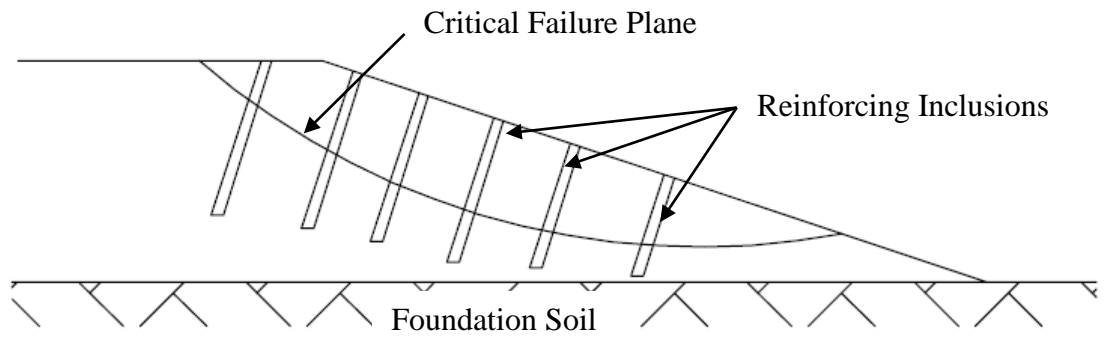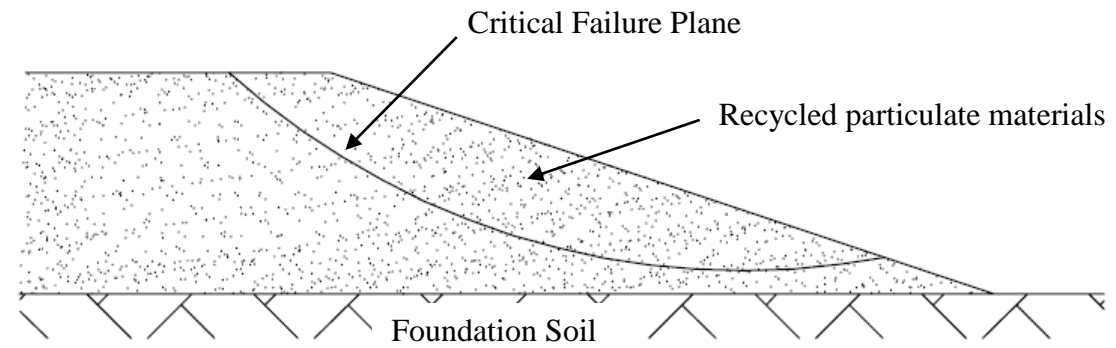
Figure 2.5: Schematics of three defined group categories: (a) Group 1 - reinforcing zones; (b) Group 2 – recycled reinforcing inclusions; and (c) Group 3 –particulate materials

Table 2.1: Material categories described in Literature Review

Group Category	Engineering Material	Selected Reference(s)
Group 1 - Reinforcing Zones	Expanded Polystyrene (EPS Geofoam)	Frydenlund & Aaboe (1988); Negussey & Jahanandish (1993); Horvath (1994); Jutkofsky et al. (2000); Elragi et al. (2000); GRC (2000); Mann & Stark (2007); Negussey (2007); Arellano & Stark (2009); Arellano et al. (2010); Newman et al. (2010); Horvath (2010); AFM Technologies (2015)
	Recycled Tire Bales	La Rocque et al. (2005); Winter et al. (2009); Zornberg et al. (2004)
Group 2 – Reinforcing Inclusions	Recycled Plastic Fibers	Hoare (1979); Gray & Ohashi (1983); Gray &Al-Refeai (1986); Maher & Gray (1990); Lawton et al. (1993); Benson & Khire (1994); Consoli et al. (2002); Zornberg (2002); Sobhan & Mashnad (2003); Viratjandr (2006); Dutta & Rao(2007); Babu & Chouksey (2011); Okoro et al. (2011)
	Recycled Plastic Pins	Loehr et al. (2000 and 2004); Bowders et al. (2003); Parra et al. (2003)
Group 3 - Particulate Materials	Recycled Glass	Reddy (1999); Wartman et al. (2004); Grubb et al. (2006 and 2007); Ooi et al. (2008)
	Recycled Styrofoam Beads	Oh et al. (2002)
	Recycled Tire Derived Aggregate	Dodds et al. (1983); Bernal et al. (1996); Humphrey (2003); Amoozegar & Robarge (2006); Scardaci et al. (2012); Finney et al. (2013)

2.2 Review of Comparable Group 1 Materials - Reinforcing Zones

This study evaluates the feasibility of using recycled PET plastic bales for use as a lightweight reinforcing zones in embankments to assess engineering behaviors of the material (Figure 2.5(a)). The bales are lightweight, which can reduce driving forces and minimize foundation settlements. The engineering properties required to assess the technical feasibility of the proposed application will evaluate deformation properties and shear strength for embankment slope stability using limit equilibrium analysis. The engineering properties will be utilized within the limit equilibrium analysis to establish the optimal design configuration of the bales/reinforced zones within an embankment. It is important to note there is a cost associated with purchasing the recycled bales from the Materials Recovery Facility (MRF) that processes and compacts the bales.

EPS Geofoam is an established solution for lightweight fill in a variety of civil engineering applications, but it is not a recycled material so it must be manufactured and purchased. The limitations and engineering behaviors of recycled tire bales are also currently under investigation as a viable alternative. Figure 2.6 displays the schematics of two possible reinforcing zone configurations within an embankment. Figure 2.6(a) displays the bales installed in rows at two different elevations. Figure 2.6(b) assumes the bales are stacked on top of each other, representing the majority of the embankment mass.

In comparison to typical soil fill, lightweight reinforcing zones will have a substantially lower unit weight and thus drastically decrease the driving force of the critical sliding mass. However, the potential for a decrease in the resisting force due to the lower shear strength is in question. The research conducted herein will evaluate the shear strength of PET bale material to determine the impact of this material to the overall

stability of the embankment. Additionally, this study will evaluate the impact of using PET bale materials in the short-term and long-term time periods.

The settlements associated to the foundation are outside the scope of the proposed study. A suite of bale configurations, including those displayed in Figure 2.6, will be evaluated as part of a limit-equilibrium analysis to determine the optimum design configuration using the properties measured for the PET bales during this study. The limit equilibrium analysis will be supplemented with a similar evaluation assuming the bales that are manufactured with EPS Geofoam and the bales that are constructed using recycled tires for comparison.
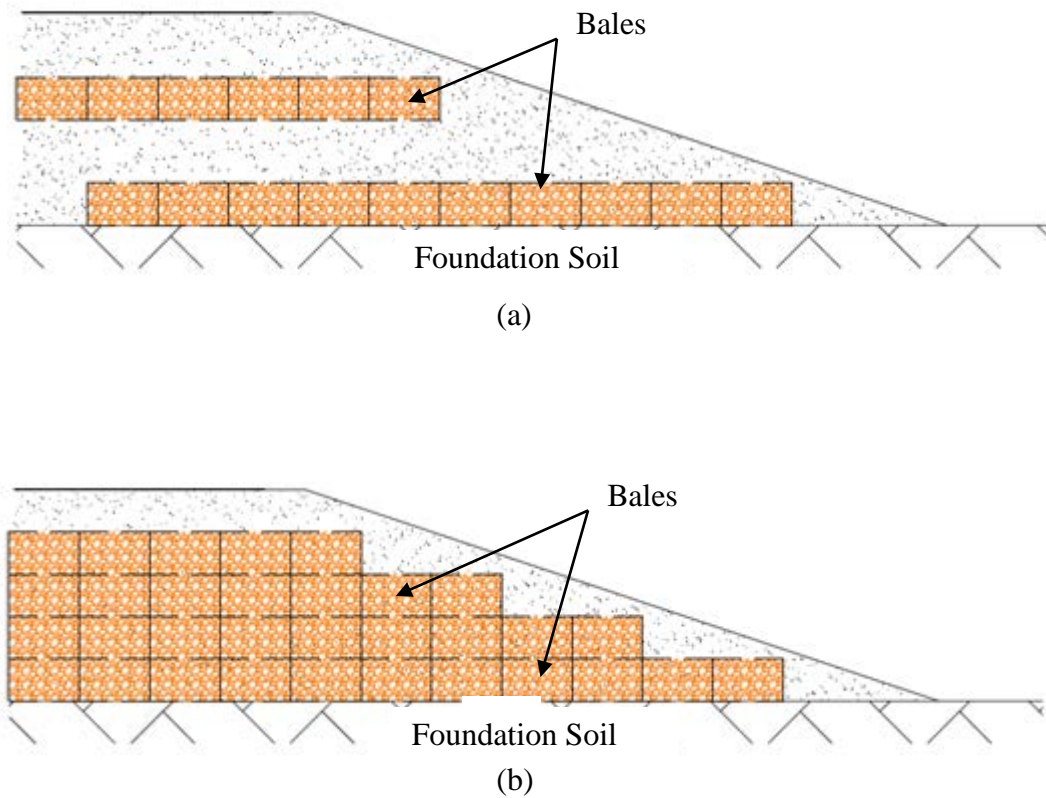
Figure 2.6: Proposed bale/zone configurations: (a) rows; and (b) stacked

This section summarizes the literature that reported use of lightweight zones within a slope or embankment. The review is presented in subsections corresponding to the main types of lightweight zones, namely: i) EPS Geofoam and ii) recycled tire bales. Each of these materials are reviewed in details in this section because they can utilized as lightweight fill zones in embankments to the proposed solution.

2.2.1 Expanded Polystyrene (Geofoam)

EPS Geofoam has been used as a geotechnical material since the 1960's (Horvath, 1994). EPS Geofoam blocks are large lightweight units manufactured from a proprietary petrochemical, most commonly 2 m by 0.75 m by 0.75 m in dimension. EPS blocks have a typical unit weight of 0.21 kN/m^3 which corresponds to approximately 1% of typical soil unit weight (AFM Technologies, 2015). Therefore EPS Geofoam zones alleviates soil stresses by providing a lighter substitute to the conventional soil fill. EPS Geofoam has been used as subgrade material in roads, foundation fill, retaining wall backfill, bridge abutment backfill, and as fill for embankments. (AFM Technologies, 2015).

Figure 2.7 illustrates the use of EPS Geofoam as a lightweight fill in an embankment application while Figure 2.8 illustrates typical EPS block Geofoam applications involving side hill fills.
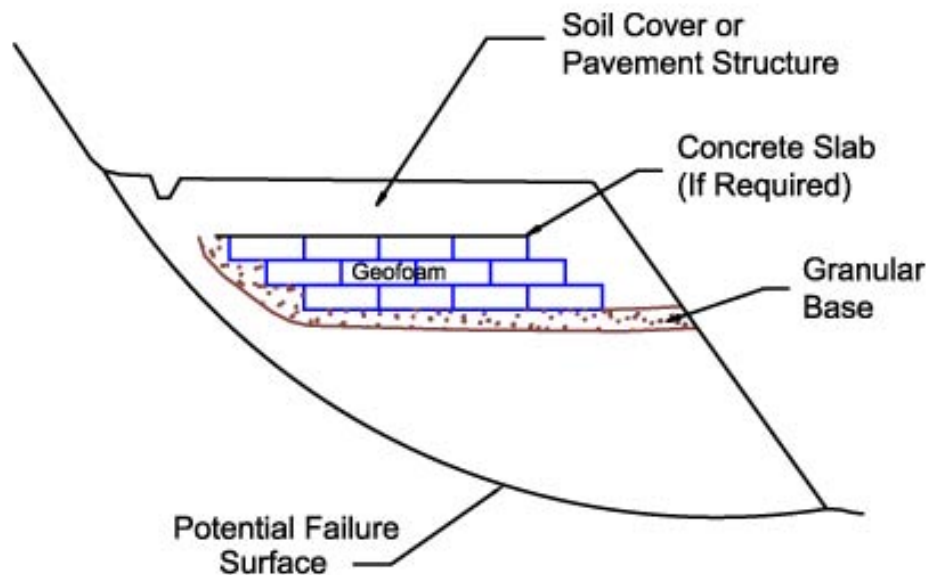
Figure 2.7: Schematic showing use of EPS Geofoam blocks as a lightweight fill in an embankment application (Geofoam Research Center, 2000)

(a)

(b)
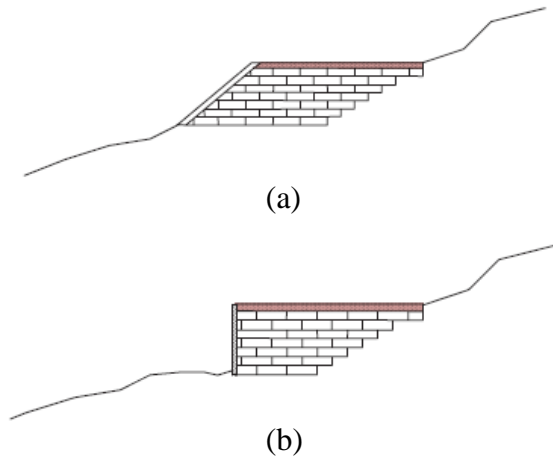
Figure 2.8: Typical EPS block EPS Geofoam applications involving side hill fills: (a) slopes; (b) walls (Geofoam Research Center, 2000)

While EPS Geofoam is currently used as lightweight fill in civil engineering applications, and it comes readily available in customizable sizes and densities, it is important to note that EPS Geofoam is not a recycled material, which propagates a cradle-to-grave life cycle. Table 2.2 summarizes the minimum values of key physical properties of EPS Geofoam properties in accordance with ASTM D6817 (2015). Note that the properties of the EPS Geofoam are dependent upon the unit weight of the block. For example, the compressive resistance of an EPS Geofoam with a unit weight of 0.11 kN/m^3 ranges from 15-40 kPa, depending on the strain rate, while an EPS Geofoam with a unit weight of 0.45 kN/m^3 has a compressive resistance ranging from 128-345 kPa. Thus, most project specifications using EPS Geofoam indicate the required unit weight. Additionally, the friction angle for EPS Geofoam was documented by AFM Technologies (2015) at 35°. This minimum unit weight is dependent on the type of application and the design considerations required. The following paragraphs review select case studies involving the use of EPS Geofoam in geotechnical engineering applications.

Table 2.2: Summary of minimum mechanical properties of EPS Geofoam as a function of unit weight adopted from AFM Technologies (2015)

Categories	Minimum Unit Weight (kN/m^3)						
	0.11	0.14	0.18	0.21	0.28	0.38	0.45
Minimum Compressive Resistance (kPa @ 1% strain)	15	25	40	50	75	103	128
Minimum Compressive Resistance (kPa @ 5% strain)	35	55	90	115	170	241	300
Minimum Compressive Resistance (kPa @ 10% strain)	40	70	110	135	200	276	345
Minimum Elastic Modulus (kPa)	1500	2500	4000	5000	7500	10300	12800
Minimum Flexural Strength (kPa)	69	172	207	240	345	414	517
Minimum Oxygen Index (Volume %)	24	24	24	24	24	24	24

Frydenlund and Aaboe (1988) studied EPS Geofoam as a lightweight fill with the goal of defining EPS Geofoam characteristics for slope-stability and fill-material applications. Their research illustrated that EPS Geofoam could be successfully used as a lightweight fill for roadways constructed on soft and sensitive clays. This study also reported EPS Geofoam as a feasible backfill material for bridge abutments and for construction as vertical EPS Geofoam walls. The computations suggested there was potential to reduce or prevent the transfer of lateral pressures on retaining walls or bridge abutments. The EPS Geofoam blocks could be used as structural elements and/or for rapid construction of pedestrian underpasses (Frydenlund and Aaboe, 1988). The EPS Geofoam blocks were selected because of their low unit weight (0.20 kN/m^3). In addition, the low unit weight makes EPS Geofoam blocks easy to handle on site, reducing the requirements for the use of construction equipment to handle this material.

Negussey and Jahanandish (1993) compared the engineering properties of EPS blocks with those of silica sand and soft inorganic clay measured from one-dimensional compression and unconfined compression tests, respectively. The stress-strain curves obtained from the EPS materials mirrored the curves obtained using typical soils. It was determined that unit weight was a good index for selecting design parameters and the classification of the EPS Geofoam because the strength and modulus of EPS. This material is directly proportional with unit weight. Field observations indicated that seating and gap-closure movements occurred during construction while post-construction and differential settlements of EPS Geofoam fills have generally remained tolerable compared to typical soil fills (Negussey and Jahanandish, 1993). The research concluded that EPS could contain portions of recycled content for subsurface construction, and EPS can be successfully be used as a lightweight material in geotechnical applications (Negussey and Jahanandish, 1993).

Horvath (1994) performed short-term and long-term unconfined compression laboratory tests on multiple 50 mm cube specimens of EPS Geofoam. The strain rate varied from 1% to 20% per minute, but most tests were varied out at 10% per minute at a laboratory temperature and relative humidity level of 23°C and 50%, respectively. A typical stress-strain curve from a 10% per-minute strain rate test on a specimen with a unit weight equal to 0.21 kN/m^3 is shown in Figure 2.9. This study indicated that the linear elastic behavior occurred between 1% and 2% strain, yield occurred over a range of axial strains rather than a single point, and the post-yield showed a strain hardening behavior (Horvath, 1994). The Young's modulus for the unconfined EPS Geofoam specimen was larger under 1% to 3% strain and continued to decrease until the

compressive strain values reached more than 80%. The Young's modulus under 1% was 8750 kPa. Strain hardening was observed after an axial strain of approximately 20%. The strain-hardening rate increases gradually until an axial strain of about 70%. At that point, where a marked increase of strain hardening rate was observed.
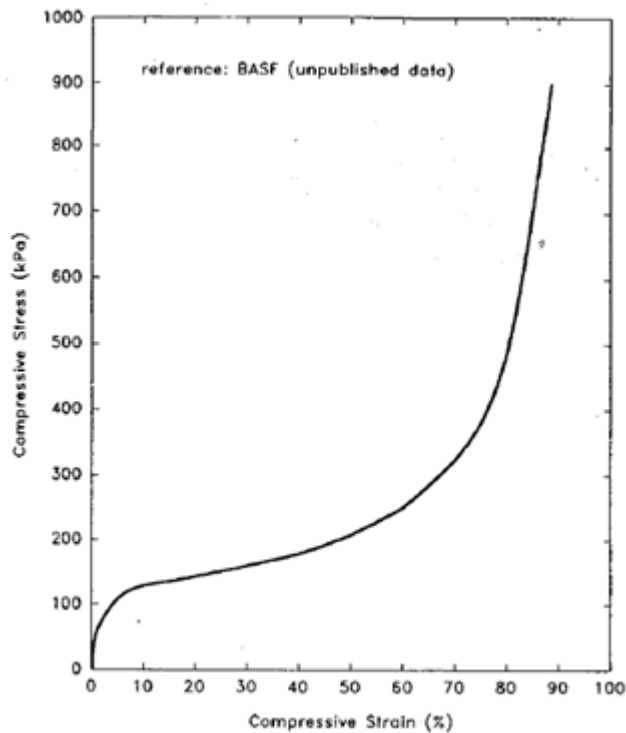
Figure 2.9: Typical unconfined compression stress-strain curve of a 50 mm cube EPS Geofoam specimen (0.21 kN/m^3 unit weight) (Horvath, 1994)

Horvath (1994) also examined the long-term behavior of EPS Geofoam under unconfined compression for load durations up to 10,000 hours. Results from these long-term tests are displayed in Figure 2.10. The stress-strain curves shown in this figure were built using a creep test displaying the compressive strain at different duration levels carried out using EPS Geofoam specimen of a unit weight equal to 0.23 kN/ m^3 up to 10,000 hours (Horvath, 1994).

The long-term load-deformation data revealed three key findings. Test specimens that were initially strained up to 0.5% strain exhibited relatively little additional deformation with time. Specimens strained initially to 1% strain exhibited modest deformation (approximately 0.5% additional strain) after 10,000 hours. There was also a rapid transition to a condition of significant additional deformation with time for specimens strained initially to between 1.5 and 2% strain (Horvath, 1994).
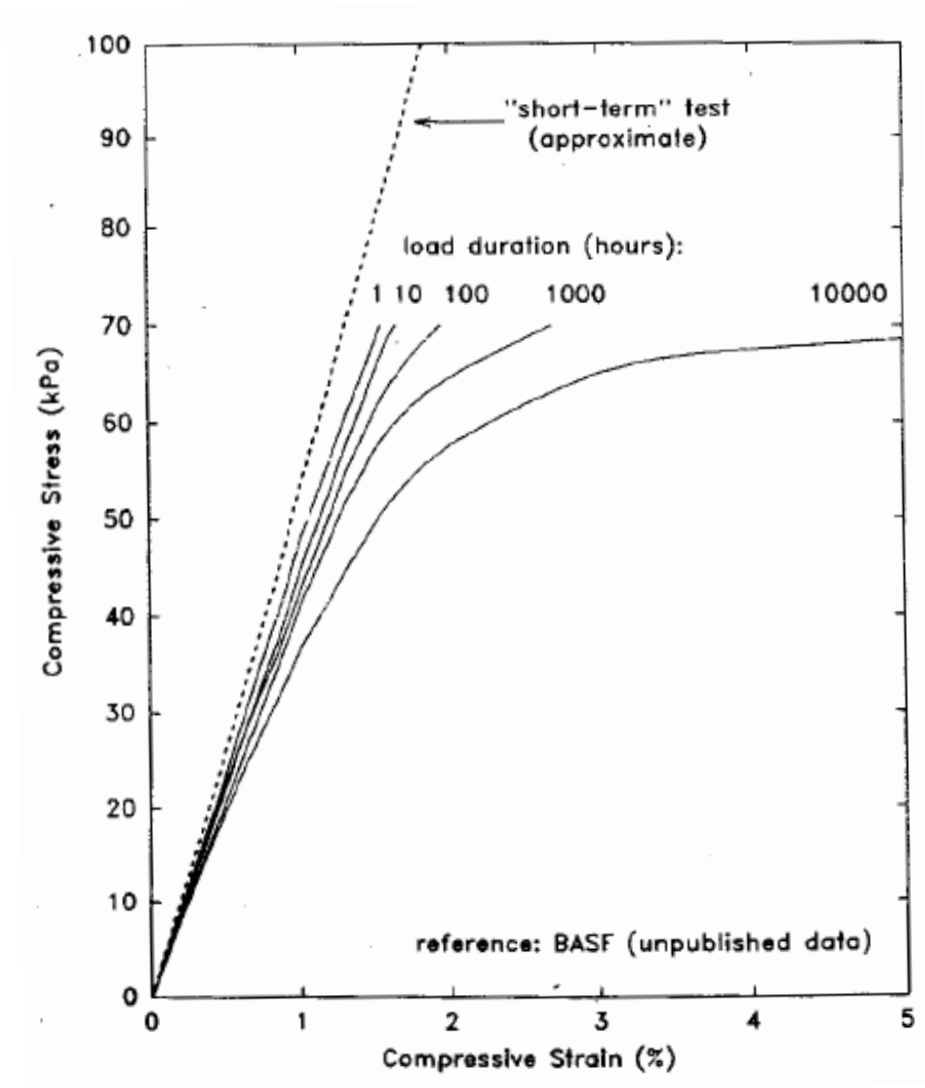
Figure 2.10: Time-dependent stress-strain behavior of 0.23 kN/m³ EPS Geofoam in unconfined axial compression (based on creep-test data) (Horvath, 1994).

Jutkofsky et al. (2000) examined the use of EPS Geofoam for use in slope-stability applications. An embankment was constructed with EPS Geofoam to analyze the effects of slope stabilization using instrumented extensometers. The slope was analyzed using the simplified Bishop method with a minimum factor of safety of 1.0. The EPS Geofoam was modeled as a surcharge with a moisture-absorbed unit weight equal to 0.94 kN/m^3 and without contribution of shear strength to the overall slope stability (Jutkofsky et al., 2000). Figure 2.11 displays a typical section of the embankment slope. Four extensometers were installed between EPS Geofoam layers to detect and measure possible sliding between blocks or sliding at the interface between the EPS Geofoam mass and the crushed stone drainage blanket. The EPS Geofoam dimensions were 0.6 m by 1.2 m by 2.4 m. To promote interlock within each layer and avoid continuous vertical joints, the EPS Geofoam blocks were placed in a staggered pattern. After four years of post-construction monitoring of the embankment, the EPS Geofoam blocks showed no indication of movement or settlement (Jutkofsky et al., 2000). Interface shear testing of EPS Geofoam to EPS Geofoam (unit weight of 0.20 kN/m^3) was conducted under two different normal loads of 23.9 and 32.1 kPa. Results are displayed in Figure 2.12. Note that both tests show a similar behavior with peak values varied at small displacements (2 mm to 3 mm) and a gradual drop towards a residual value. The approximate friction angles calculated from Figure 2.12's peak values (21 kPa and 27 kPa) and residuals values (17 kPa and 22 kPa) were 40.51° and 34.78°, respectively.
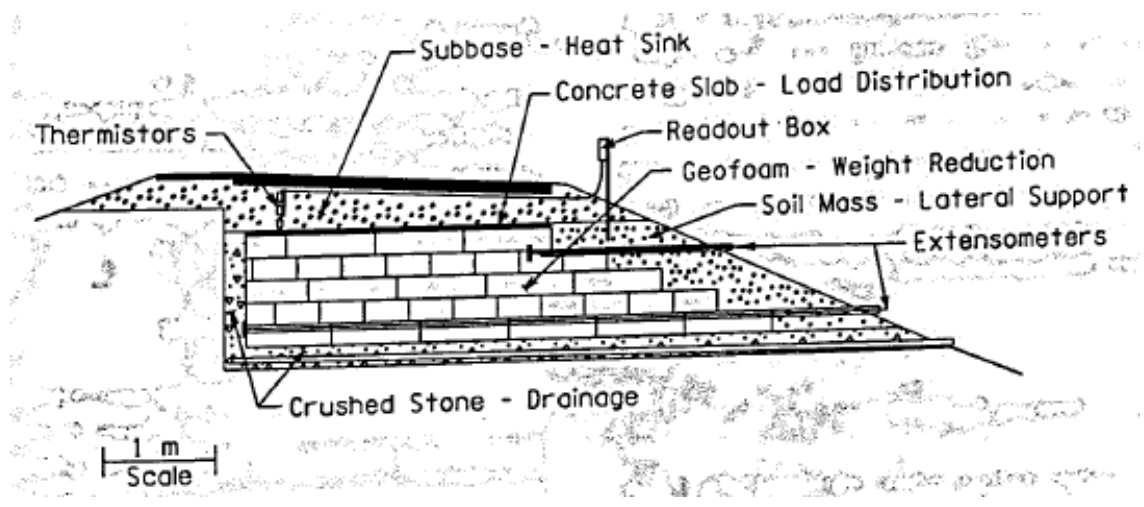
Figure 2.11: Typical section of treatment embankment (Jutkofsky et al., 2000)
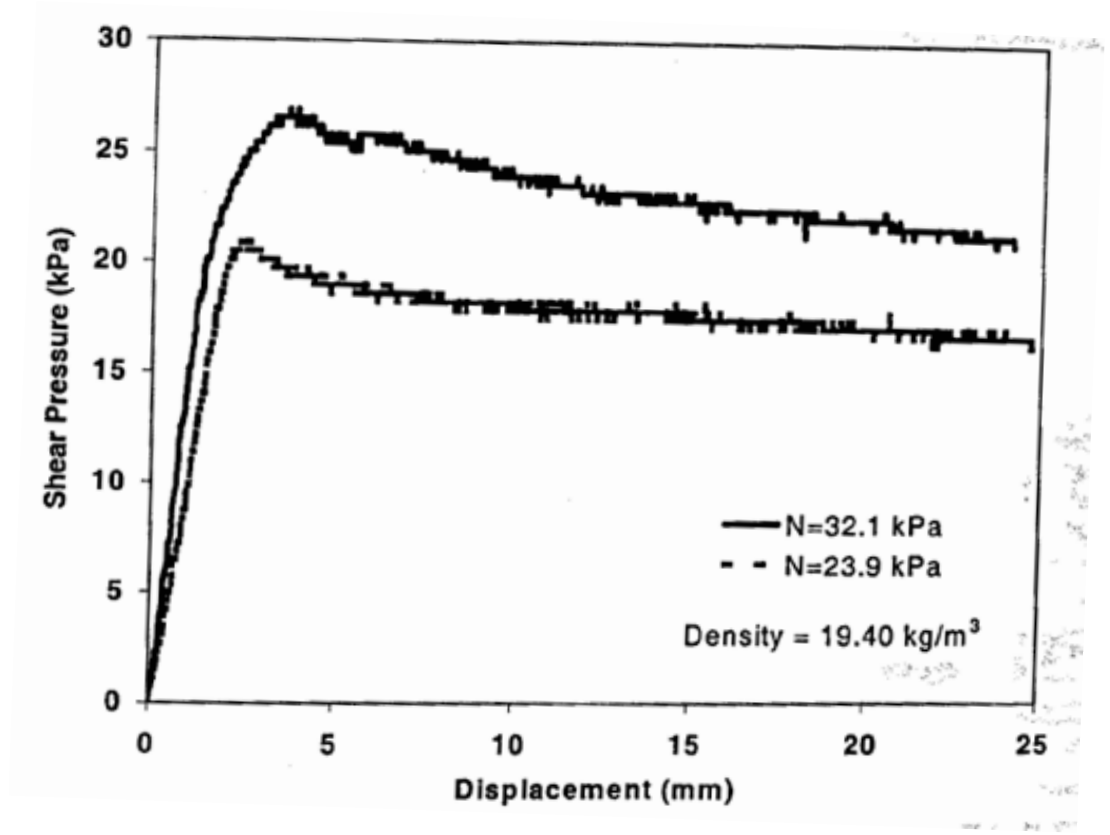
Figure 2.12: Interface shear resistance for EPS Geofoam-to-EPS Geofoam surfaces at two stress levels (Jutkofsky et al., 2000)

Elragi et al. (2000) examined the sample size and shape effects of EPS Geofoam. Unconfined compression strength testing was conducted on cubic and cylindrical test specimens with varying material densities. The cubic specimens (0.37m and 0.84 m) and the cylindrical specimens (0.08 meter in diameter with varying heights) were tested. The densities varied between 15 kg/m^3 (unit weight of 0.15 kN/m^3) and 0.29 kg/m^3 (unit weight of 0.29 kN/m^3) for all samples. The initial Young's modulus values were formed to increase as density increased as shown in Figure 2.13. Additionally, this figure also shows the cube sample size had a strong influence on the initial modulus values. Figure 2.13 shows 0.84 m cube samples had initial Young modulus values approximately twice the values obtained from the 0.37 m cubes. Figure 2.14 displays the measured Poisson's ratio values from a 0.84 m cubic specimen as a function of vertical strain (0% to 2%). The upper curve evaluates vertical strain for the middle-third segment of the sample while the lower curve evaluates vertical strain computed using the entire sample height.

Initial Young's modulus and Poisson's ratio values were needed to simulate the behavior of EPS Geofoam as an elastic material (Elragi et al., 2000). The measurements of strain using the middle third and the full specimen height revealed that the distribution of vertical strains over the height of a EPS Geofoam sample was not uniform and therefore results from conventional 0.37 m cubic samples (0.05 m^3 in volume) significantly underestimates Young's modulus values for EPS Geofoam (Elragi et al., 2000). The research suggests that commonly assumed Poisson ratio values were lower than what was measured using large samples while monitoring localized deformations. The main cause for the under-estimation of both Young's moduli and Poisson's ratio was attributed to crushing and damage near the EPS Geofoam and rigid platen-loading

interfaces (Elragi et al., 2000). It was concluded that the specimen size affected the behavior of EPS Geofoam.
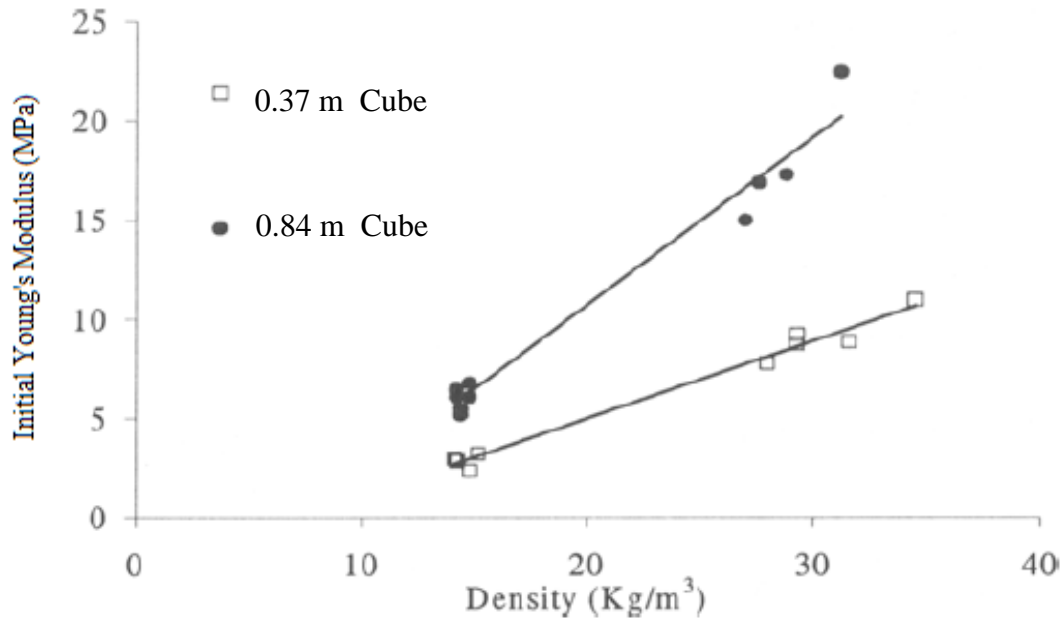
Figure 2.13: Initial Young's moduli as a function of density and specimen size for EPS geofoam (Elragi et al., 2000)
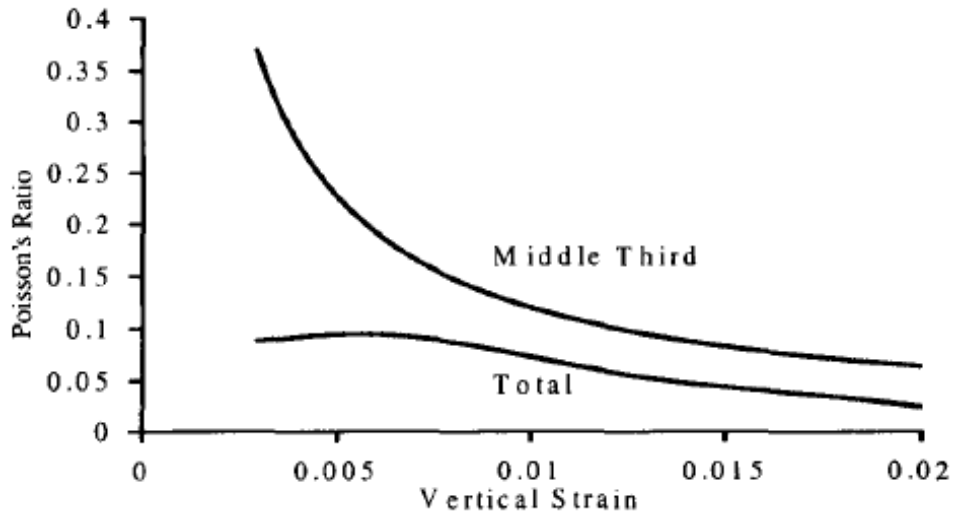
Figure 2.14: Poisson's ratio for different vertical strain levels using EPS Geofoam (Elragi et al., 2000)

Mann and Stark (2007) conducted a full-scale slope stabilization project using EPS Geofoam rather than a more conventional heavily-anchored soldier pile and timber-lagging wall. The project involved a slope repair project on a house located at the edge of a slope shown in Figure 2.15. The compressive strength of the EPS Geofoam was 310 kPa at less than 2% axial strain with a unit weight of 0.35 kN/m^3. The dimensions of the EPS Geofoam blocks used on this project were 8 feet long, 4 feet wide and 4 feet thick. The 4-foot thickness proved difficult to handle, especially in moderate to high wind conditions. To facilitate handling, the contractor cut the blocks in half with a hot wire cutter. This size reduction allowed a single workman to lift, carry, and place the individual blocks with ease.

Figure 2.15 illustrates the cross-section, geometry, and materials evaluated in the stability analyses conducted by Mann and Stark (2007). The slope stability analysis used Spencer, (1967) and Bishop, (1955) stability methods as coded in Slope/W (GEO-SLOPE, 2007). Based on the cross-section in Figure 2.15, the minimum static factor of safety is 2.1. The critical static failure surfaces obtained using Bishop's (lower solid line) and Spencer's (upper solid line) stability methods are also shown in Figure 2.15. These critical surfaces occur on the down slope of the existing wall, which was in good agreement with field observations. The dashed failure surface in Figure 2.15 was also analyzed to investigate the global stability of the repair. The pseudo-static (dynamic) analysis was conducted using a horizontal seismic acceleration of 0.2g and the critical static failure surfaces. The minimum computed pseudo-static factor of safety was 1.197.

In summary, the stability analyses indicated that both the anchored and vertical pile supported the concrete wall, and the new anchored soldier pile and timber-lagging

wall should be stable under both static and seismic conditions. The results conclude that EPS Geofoam reduced the vertical stress applied to the pre-existing landslide, but also reduced the lateral earth pressure on a second, lower retaining structure designed to create a flat or leveled back-yard (Mann and Stark, 2007). In conclusion, the project was a success due to the use of the lightweight EPS Geofoam as a backfill material, which resulted in cost savings associated with a smaller wall. Figure 2.16 displays an image of the EPS Geofoam field installation. Note that the EPS Geofoam blocks must be installed adjacent to one another.
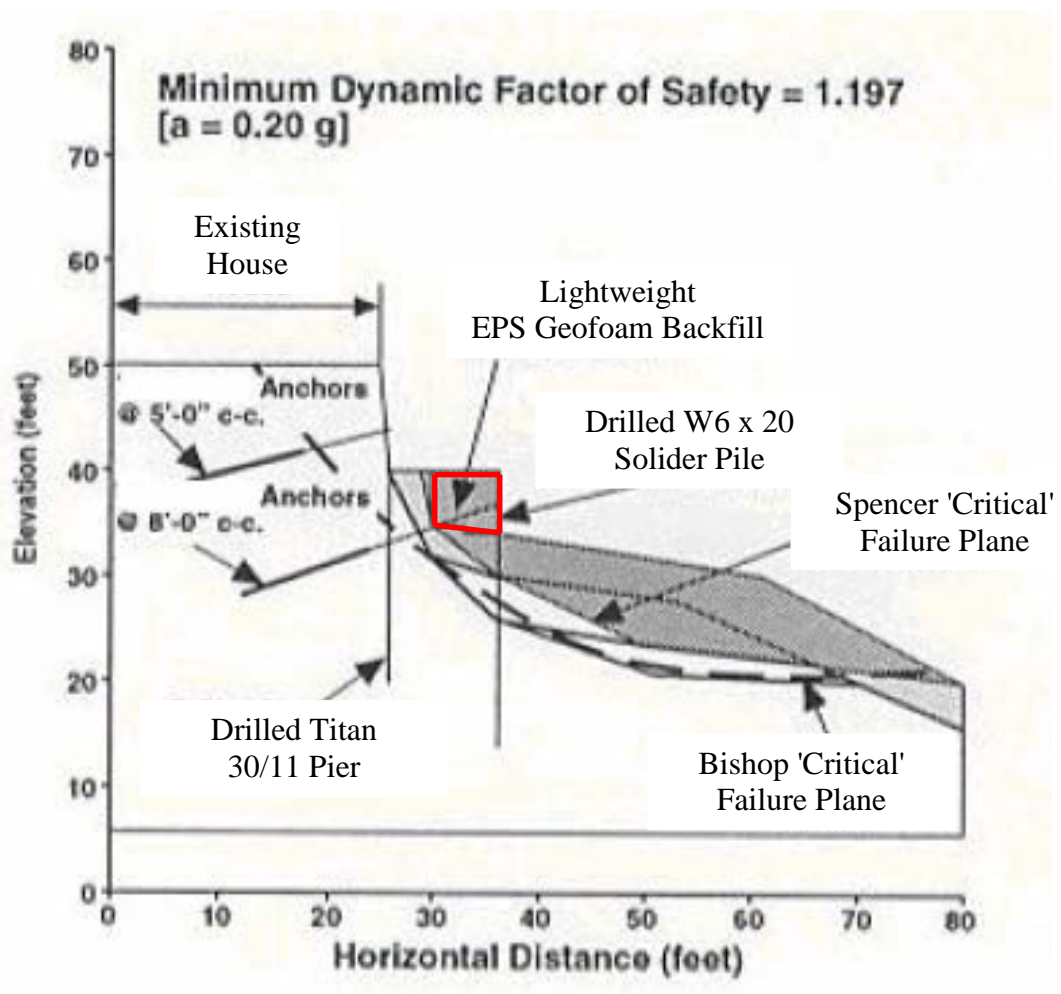
Figure 2.15: Cross-section used in a stability analyses using EPS Geofoam as lightweight fill material (Mann and Stark, 2007)

Figure 2.16: EPS Geofoam block field installation (Mann and Stark, 2007)

Negussey (2007) performed a critical review of EPS Geofoam engineering properties by examining 30 years of field and laboratory data and case studies. EPS Geofoam behavior were quantified using data from unconfined compression tests, density variations, creep tests, field observations, sample size effects, interface pressure distributions, and contact surface details. The summary provided useful insight on the influence of EPS Geofoam density on engineering properties, and its ability to provide a good index for selecting design parameters and classification of EPS Geofoam. In general, both the strength and Young's modulus of EPS Geofoam increased with increasing density (Negussey, 2007). Negussey (2007) argued that the potential for creep deformations was exaggerated and design Young's modulus values were underestimated when based on small laboratory tests. Therefore Negussey (2007) concluded that an increase in the design Young's modulus, coupled with a better understanding of EPS

Geofoam creep behavior, could justify using lower EPS Geofoam densities and less expensive grades of EPS Geofoam.

Arellano and Stark (2009) examined EPS Geofoam for roadway embankments. The study focused on the load-bearing deformation characteristics of the EPS Geofoam embankment while examining the design and costs aspects of the project. Uniaxial compression, creep, and cyclic stress-strain test data were collected as part of this study. The results indicated that the higher the required elastic limit stress, the greater the required block density. However, the cost of the EPS Geofoam increases with increasing density (Arellano and Stark, 2009). The authors highlighted the advantage of using a deformation-based design when using EPS Geofoam for roadway embankments. This is done by calculating stresses and strains within the EPS Geofoam's mass which allows the selection of EPS Geofoam block type to be optimized by selecting blocks with the lowest density that would yield the required elastic limit stress (Arellano and Stark, 2009). The selection of EPS Geofoam blocks with the lowest possible density will yield a cost-efficient EPS Geofoam embankment. Arellano et al. (2010) presented a framework for the EPS Geofoam design guideline that included appropriate material and construction standards for the use of EPS Geofoam block as lightweight fill in slope stability applications with a focus on the two failure modes presented in Figure 2.17 and the ability to handle both internal and external stability (Arellano et al., 2010). Figure 2.18 outlines the recommended design procedure if the existing or proposed roadway is located within the existing or anticipated slide mass, and the existing or anticipated slide mass is located below the roadway. If the roadway is located outside the limits of the existing or anticipated slide mass, or the existing or anticipated slide mass is located above the

roadway, the modified design procedure is modified as shown in Figure 2.19. Figure 2.20 displays a design-selection diagram that aids in selecting the correct design procedure (i.e. Figure 2.18 and Figure 2.19).

The proposed design guideline for EPS block Geofoam for slope stabilization serves as a blueprint for the use of other types of lightweight fills in slope stability applications (Arellano et al., 2010). This study confirmed that EPS block Geofoam is a viable lightweight fill material that can provide a safe and economical solution for slope stabilization and repair (Arellano et al., 2010).

(a)   (b)
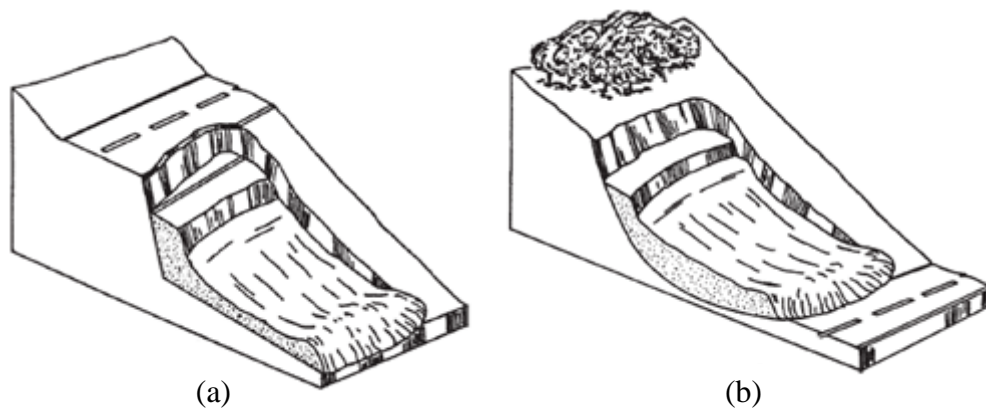
Figure 2.17: Failure modes considered in design procedure: (a) slide above roadway; and (b) slide below roadway (Arellano et al., 2010)
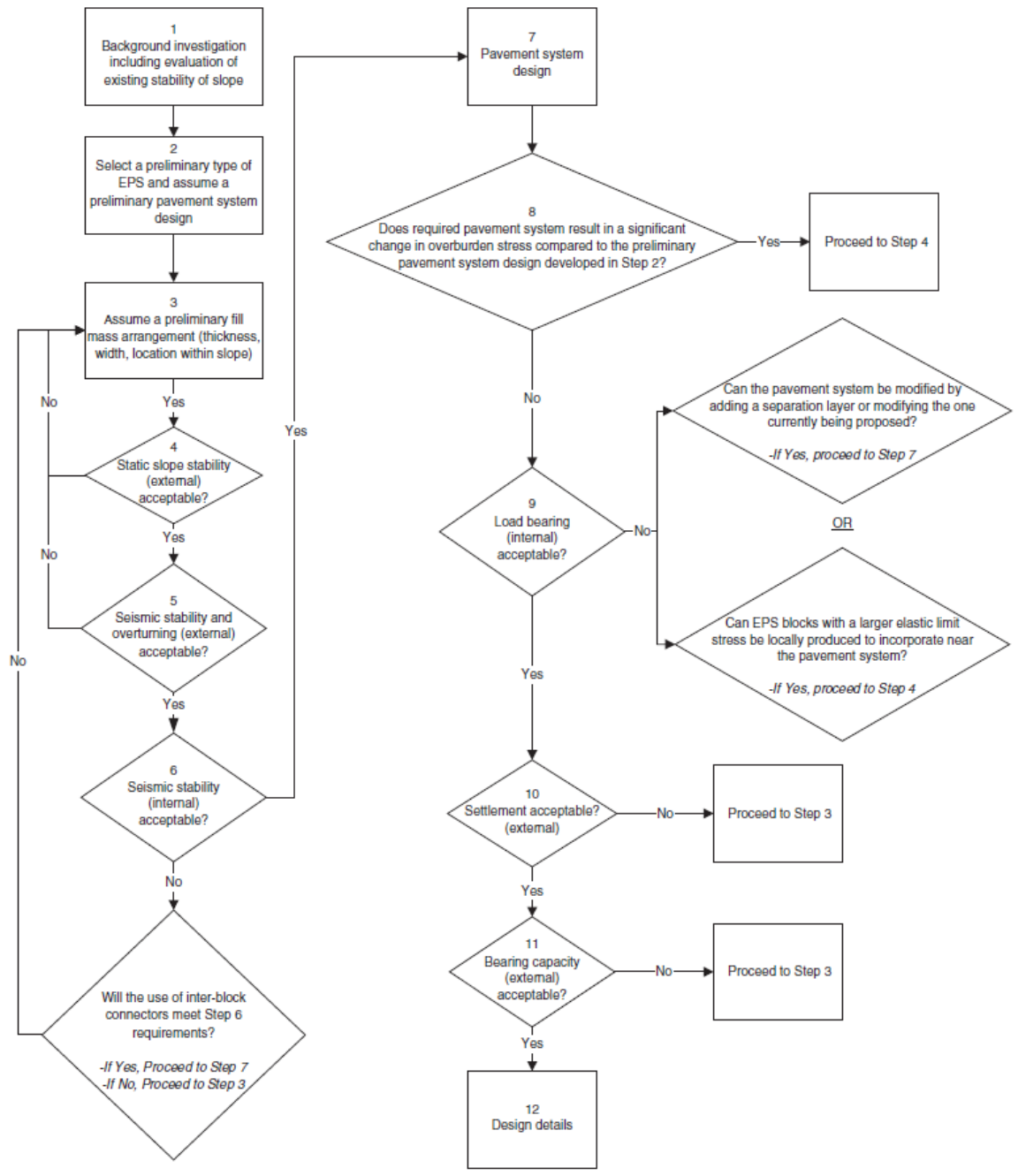
Figure 2.18: Recommended design procedure by Arellano et al. (2010) for roadway failures repaired with EPS blocks – Part A (roadway with sliding mass)
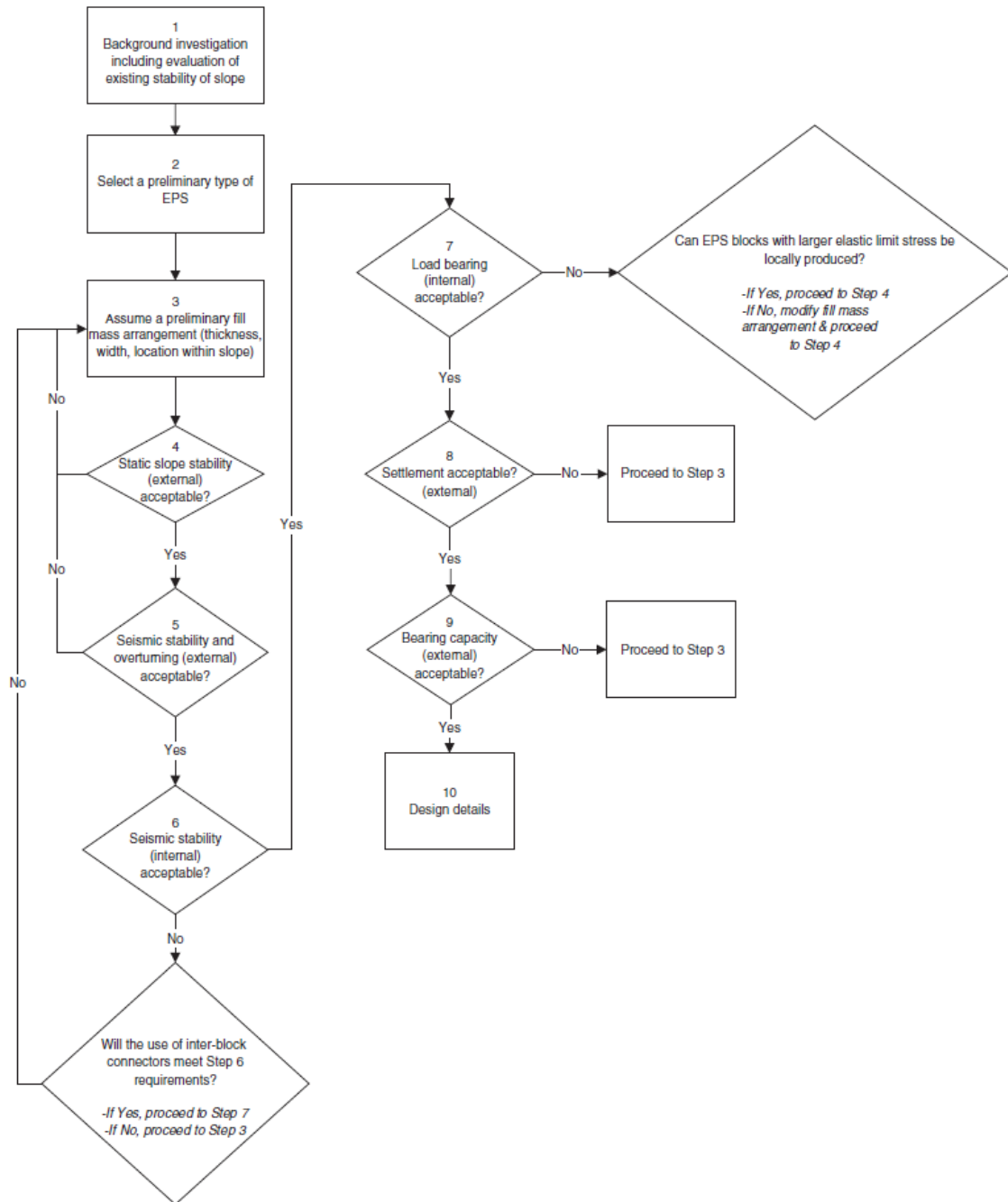
Figure 2.19: Recommended design procedure by Arellano et al. (2010) for roadway failures repaired with EPS blocks – Part B (roadway outside of sliding mass)
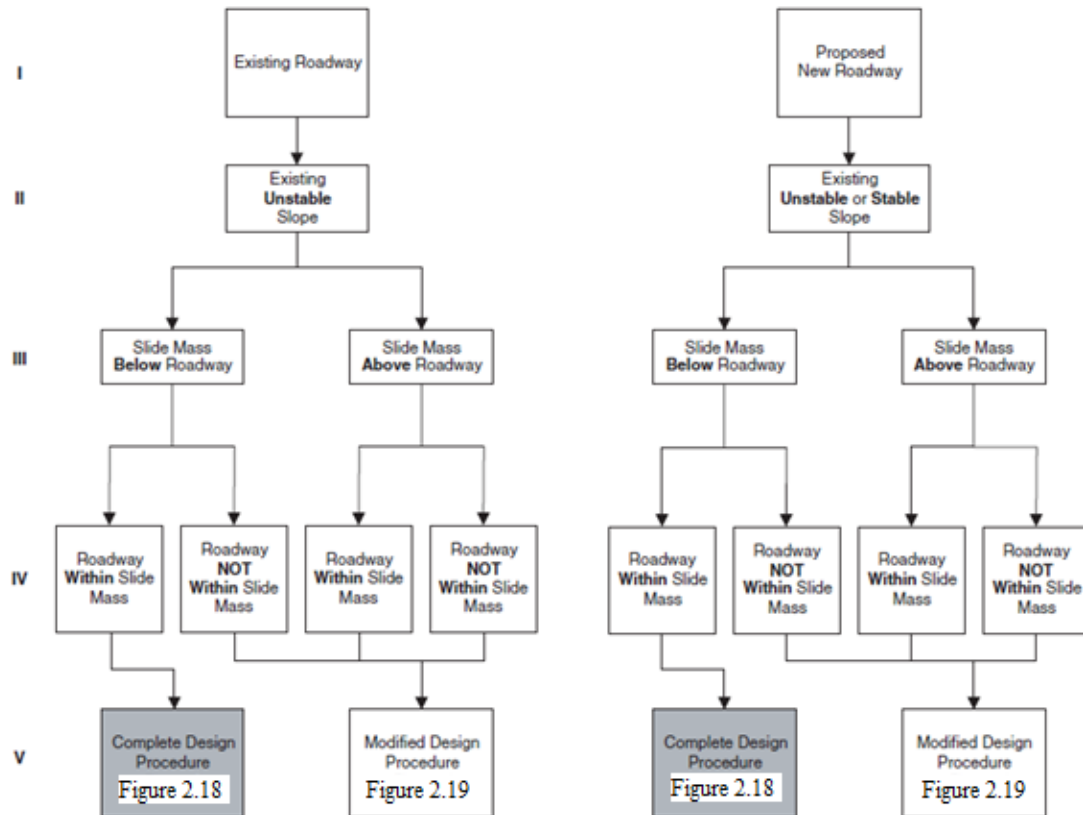
Figure 2.20: Design selection diagram to apply design procedure by Arellano et al. (2010) for roadway failures repaired with EPS blocks

Newman et al. (2010) performed a numeric investigation to assess the use of EPS Geofoam in highway embankments. This study was associated in part to a reconstruction project located along I-15 in Salt Lake City, Utah. This reconstruction project included the widespread use of EPS Geofoam as lightweight embankment material at the location of important utility crossings and at locations in close proximity to existing buildings to help minimize possible consolidation settlements. Figure 2.21 displays an image of one of the embankment sites of this reconstruction project and Figure 2.22 displays a typical cross-section view of an EPS Geofoam embankment that was monitored long-term. The results of the field measurements from magnet extensometers and vibrating wire pressure

cells were utilized in the numerical model. Fast Lagrangian Analysis of Continua (FLAC) was the finite-difference program used to estimate the complex stress distribution, displacements, and strains that developed at select locations within the EPS Geofoam embankments (Newman et al., 2010). The authors used a bilinear elastic constitutive model for the EPS Geofoam produce reasonable estimates of gap closure, block seating, and the subsequent elastic compression of the EPS Geofoam embankment at higher stress levels. The EPS Geofoam material had a density of 18 kg/m^3 and a Poisson's ratio of 0.103 (Bartlett et al., 2001; Benchmark Foam, Inc., 2003). After monitoring three field areas of the EPS Geofoam embankment over a four-year time period, there was no indication of excessive settlement, and the project proved to be a successful implementation of EPS Geofoam embankments (Newman et al., 2010).

Figure 2.21: Typical EPS Geofoam embankment construction on the I-15 reconstruction Project in Salt Lake City (Newman et al., 2010)
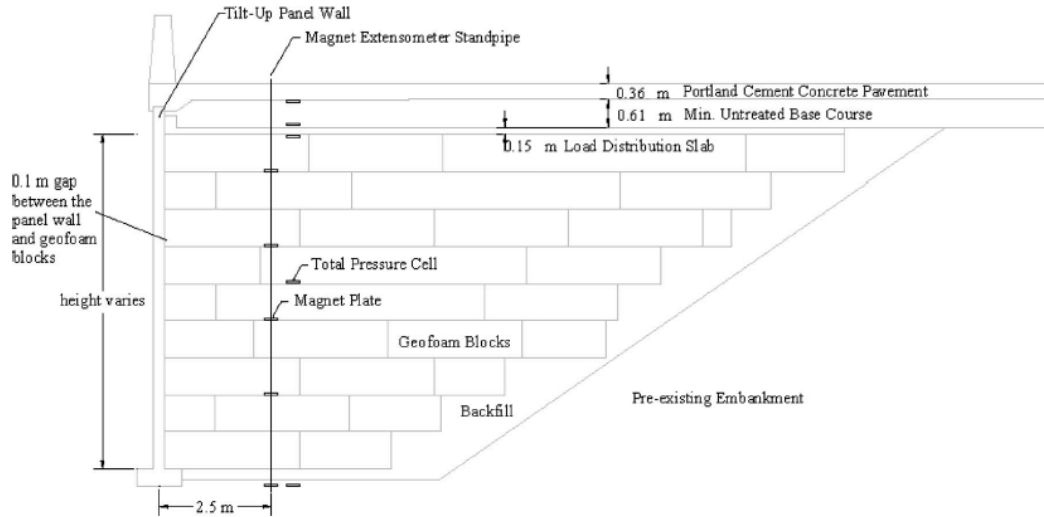
Figure 2.22: Typical cross-section view and of the EPS Geofoam embankment reconstruction project along I-15 in Salt Lake City (Newman et al., 2010)

Horvath (2010) assessed the emerging trends in failures involving EPS Geofoam block fills. Issues related to internal stability, external stability, construction, and post-construction were examined. Many successful infrastructure projects indicated that EPS Geofoam is a reliable geotechnology when properly designed, specified, supplied, and constructed (Horvath, 2010). The author emphasized the need to disseminate existing knowledge to all people involved in the design, supply, construction, and ownership of fills incorporating EPS Geofoam (Horvath, 2010). Based on literature review provided, it was concluded that EPS Geofoam is a successful construction material in terms of strength and durability over the life of the embankment structure.

When road embankments are constructed across deposits of soft clay or peat, both bearing capacity and settlement issues can be resolved with the use of EPS Geofoam blocks as a fill material according to Frydenlund and Aaboe (1988). EPS Geofoam blocks are manufactured at a low unit density equal to 20 kg/m^3, but have been found actually be designed assuming values closer 100 kg/m^3 for stability and settlement control to

handle increases in water content over the service life. Importantly, the low unit density makes it feasible for an individual worker to handle an entire EPS Geofoam block (i.e. requiring a lifting force of approximately 300 N), and for a single crane to handle the weight of a truckload of EPS Geofoam. The significantly lower weight plays an important role in reducing transportation costs relative to other lightweight fill materials.

The durability of EPS Geofoam was also investigated by Frydenlund and Aaboe (1988). The authors assessed long-term durability by retrieving samples from existing fills. EPS Geofoam exhibited little to no decay because polystyrene is a chemically stable compound. When long-term samples were retrieved from existing fills in general, the EPS Geofoam showed no signs of strength reduction, but did indicate a slight increase in compressive strength. EPS Geofoam also displayed good resistance to biological destruction from bacteria and enzymes, and authors concluded it did not pose a threat to major attacks from animals because the EPS Geofoam does not represent a source of nourishment (Frydenlund and Aaboe, 1988). While EPS is not fire resistant, sufficient quantities of oxygen necessary to enable a fire are usually unavailable particularly for projects where EPS Geofoam blocks are covered by a concrete slab and/or soil cover.

Frydenlund and Aaboe (1988) reported that the unconfined compressive strength of a 5 cm by 5 cm by 5 cm cube should have a mean value of at least 100 kN/m^2, and no single measurement should fall below 80 kN/m^2. The sides of each EPS Geofoam blocks are manufactured at 90° angles, and each block must have a minimum thickness of 0.5 m, unless otherwise specified. Deviation from the specified dimensions should be within 1%, and the evenness of the block surface measured with a 3 m straightedge should be within 5 mm (Frydenlund and Aaboe, 1988).

2.2.2 Recycled Tire Bales

Similar to the PET bales compressed at an MRF, recycled tires are compressed into bales using a baler and then contained with steel straps. The process for bale fabrication is described in more detail in Chapter 3. Figure 2.23 displays the typical dimensions of a recycled tire bale (Winter et al., 2009). Recycled tire bales can be utilized in various applications as described in this section.

Winter et al. (2009) investigated the key features of recycled tire bales for use in slope failure remediation. Each tire bale was comprised of approximately 100-115 vehicle tires compressed into a lightweight block of mass equal to approximately 800 kg with a density of about 500 kg/m^3 (Winter et al., 2009). The bales were approximately 1.3 m by 1.55 m by 0.8 m in dimensions and were secured by five galvanized steel tie-wires running around the length and width of the bale. A bale porosity approximately equal to 62% and a permeability approximately equal to 0.02 m/s and 0.2 m/s through the length and depth, respectively, for drainage applications (Winter et al, 2009). Furthermore, the process of generating tire bales consumes approximately 1/16 of the energy required to shred a similar mass of tires (Winter et al., 2009). This project used a bale-to-bale friction angle of approximately 25° under dry conditions by Zornberg et al. (2004), discussed next. For a volume equal to 100 m^3, approximately 6,000 tires in the form of more than 50 tire bales would be required. These are likely to require slightly over two, eight-hour, two-man shifts to manufacture. The authors examined the issues related to drainage, excavation boundary conditions, tire bale placement, and tire bale alignment. The study concluded that geotechnical engineers can repair slope failures

using tire bales, and the cost is comparable to that of conventional materials (Winter et al., 2009).
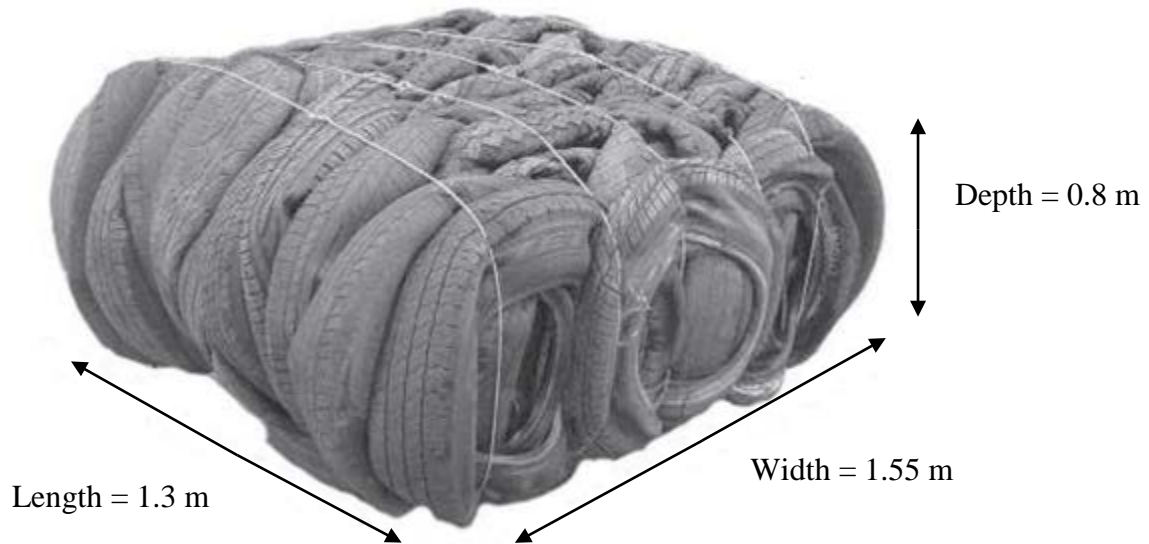
Figure 2.23: Dimensions of a typical tire bale (Winter et al., 2009)

Zornberg et al. (2004) assessed the feasibility and mechanical properties of tire bales used in highway applications. The tire bales assessed had approximate dimensions of 0.75 m by 1.4 m by 1.5 m, but the authors noted that a variety of sizes were produced dependent upon the baler and operation. The unit weight of a tire bale was reported at approximately 5.5 kN/m^3. Compressibility tests were performed on three tire bales. For each tire bale, three vertical deformation measurements were made by gages equal distances around the sample coupled with a vertical load cell. The test results indicated that the tire bales tested did not have a peak strength at stress levels of less than 815 kPa, and produced a Young's modulus of 400 kPa (Zornberg at al., 2004). The authors found that the lateral movement at low stress levels was likely restricted by the combination of

compression during baling, vertical orientation of the tires in the bale, and the restraint from the wire ties. Additionally, unconfined creep evaluations were performed on a tire bale, and the results of the examination produced a displacement rate of 0.005 % strain per day at 1,000 hours for the tire bale. A modified direct shear test examined the tire bale interface by: 1) vertically stacking two tire bales with the tire treads in each tire bale oriented in the same direction; 2) restraining the upper bale from moving laterally; and, 3) measuring the force required to pull out the bottom tire bale, which was supported by a steel plate moving on low friction rollers. Modified direct shear tests were conducted at normal loads of 9 kN, 18 kN, and 27 kN. The results produced a friction angle equal or greater to 25° with a cohesion of 2.4 kPa. Zornberg et al. (2004) concluded that compacted tire bales systematically placed as the core of highway embankments is another technically feasible use of scrap tires.

LaRocque et al. (2005) examined the interface shear strength between 1-ton tire bales to be utilized in an embankment application. Figure 2.24 shows a schematic of tire bales being utilized for slope stabilization. This figure shows a potential slip surface which goes through the zone of the embankment with tire bales. LaRocque et al. (2005) measured the shear strength of the tire bales by means of direct shear testing. Due to the size of the bales, the authors had to construct their own direct shear testing apparatus. The apparatus applies a normal load on the tire bales while simultaneously applying a lateral shear load to slide a 1-ton bale over the top of two 1-ton bales. Figure 2.25 shows a schematic view of the direct shear-testing equipment. Figure 2.26 shows direct shear test results in terms of horizontal shear force as a function of shear displacement for a test conducted using a normal (vertical) load of 20 kN. The results indicated that a significant

shear resistance can develop between the stacked tire bales. A horizontal resistance between bales exceeding 54 kN was measured when the applied vertical load was only 20 kN (LaRocque et al., 2005). The calculated friction angle from Figure 2.28 is 20º which is lower than the previous study by Zornberg et al. (2004) that reported a friction angle of 25º. Based on this study, the results were expected to provide a good alternative for stabilization of shallow slopes (LaRocque et al., 2005).

Soil cover and/or Pavement Structure

Tire Bales

Granular Base

Potential Failure Surface
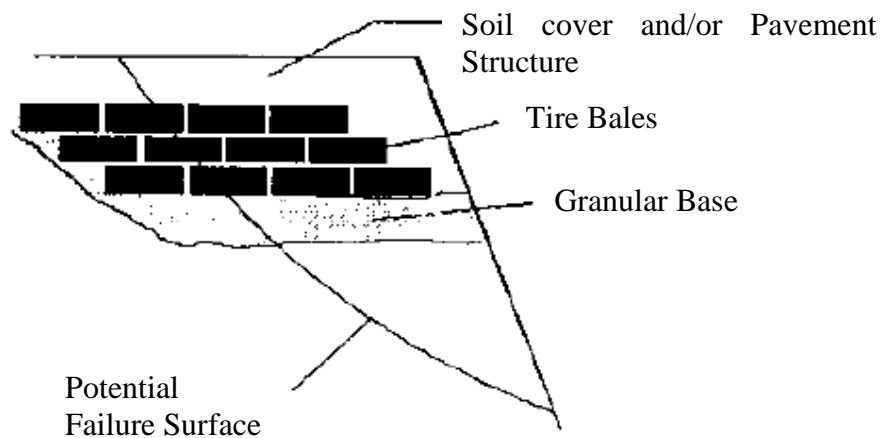
Figure 2.24: Schematic of a recycled tire bale configuration for use in a slope stability applications (LaRocque et al., 2005)
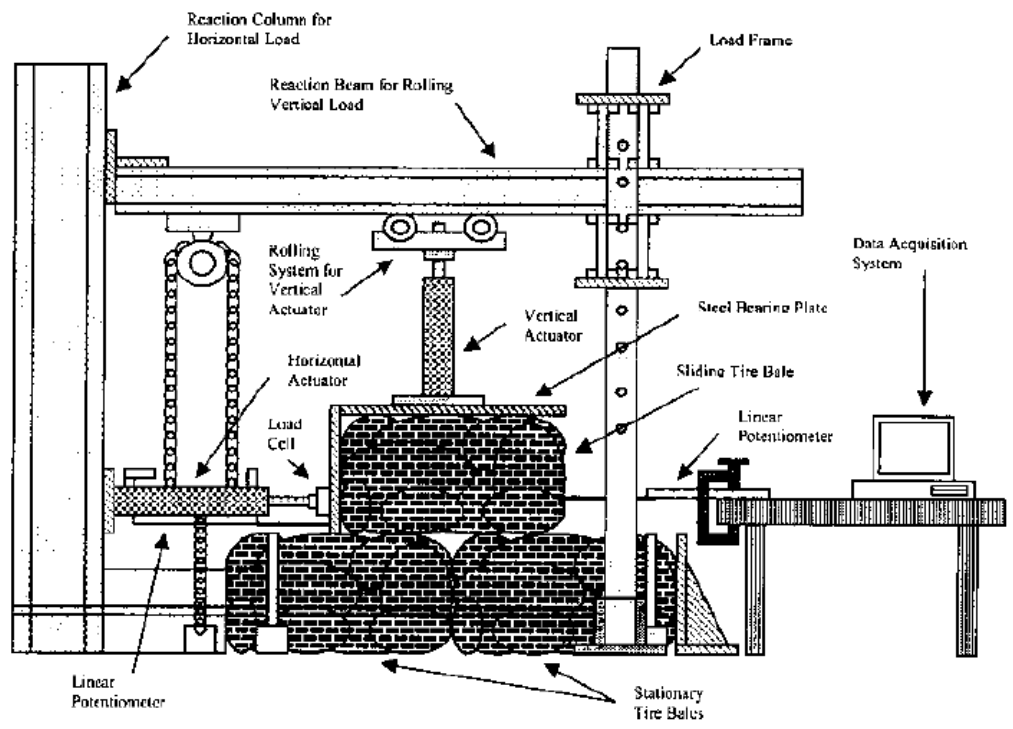
Figure 2.25: Direct Shear Testing Equipment Utilized for the Recycled Tire Bales (LaRocque et al., 2005)
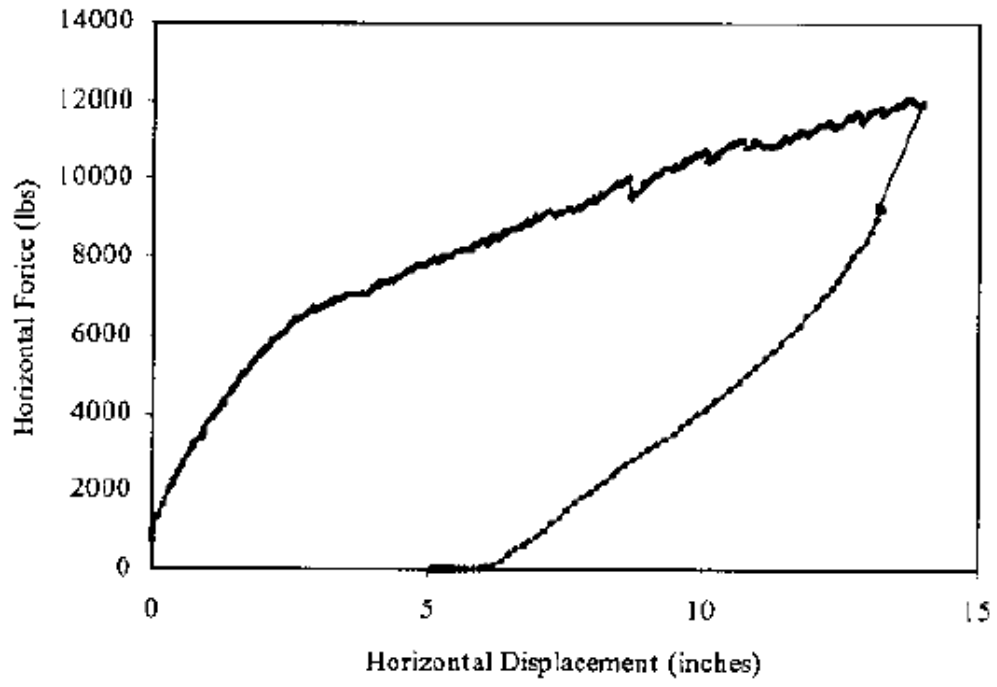
Figure 2.26: Horizontal force versus shear displacement for the full-scale recycled tire bale test (LaRocque et al., 2005)

2.3 Review of Comparable Materials Group 2 Materials - Reinforcing Inclusions

The recycled materials reviewed in this section serve as reinforcing inclusions in the soil that provide tensile strength to a material (i.e. the soil) that has no tensile strength. Studies associated with recycled plastic fibers and plastic pins will be reviewed.

2.3.1 Fibers of Recycled Plastic

Hoare (1979) performed triaxial compression tests on dry, angular, crushed sandy gravel reinforced with strips of polypropylene/nylon fabric (66 mm x 7 mm) and twisted polypropylene chopped fibers (50 mm long). Results indicated that the reinforced test specimens exhibited a higher level of strength compared to unreinforced specimens when specimens were compacted to the same porosity using identical preparation methods (Hoare 1979).

Gray and Ohashi (1983) developed a mechanistic model to characterize the effects of plastic strip reinforcement. Figure 2.27(a) displays a schematic of the soil reinforcement mechanism for a soil reinforced with plastic strips. The model indicates that the plastic strips develop tension in the shear zone resulting from the anchorage that develops at the soil-reinforcement interface outside the shear zone (Gray and Ohashi, 1983). The tension in the plastic strips was found to increase the overall shear strength of the soil, even after the peak strength was reached (Gray and Ohashi, 1983). As part of the same study, Gray and Ohashi (1983) conducted direct shear tests on sand reinforced with natural and synthetic fibers to validate the predictions of the mechanistic model. The results correlated with the findings of the model, and they observed that the Mohr-Coulomb failure envelopes for the reinforced sand were bilinear. Figure 2.27(b) displays the Mohr-Coulomb failure envelopes for the unreinforced and reinforced sand. Note that

the reinforcing inclusions increased the friction angle of the sand until the critical confining stress (σ_c') was reached (Gray and Ohashi, 1983).
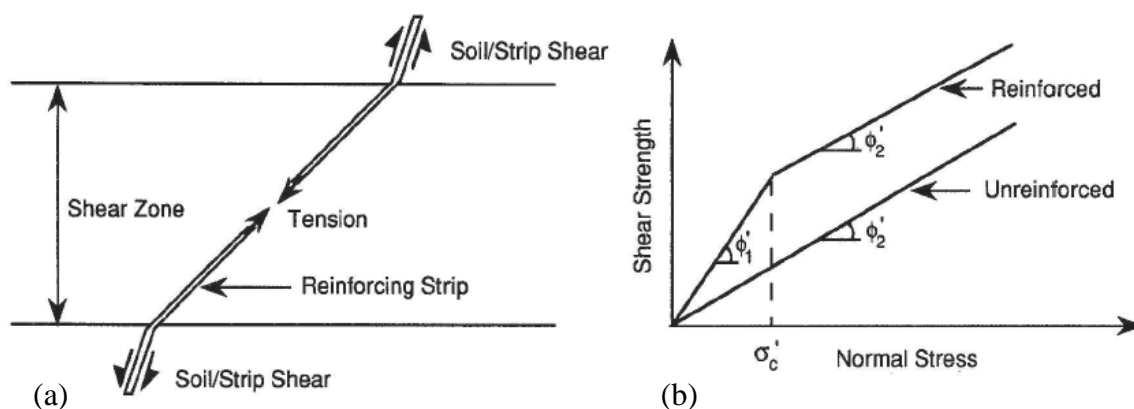
Figure 2.27: Soil reinforced with plastic strips: (a) Schematic of the soil reinforcement mechanism; and (b) Mohr-Coulomb failure envelopes for unreinforced and reinforced sand (Gray and Ohashi, 1983)

Gray and Al-Refeai (1986) performed triaxial compression tests to compare the stress-strain response of dry Muskegon sand reinforced with continuous, oriented fabric layers in comparison to randomly distributed discrete fibers. The amount of reinforcement and the magnitude of the confining stress was varied. The reinforcing inclusions consisted of circular disks of a geotextile cut from fabric sheets. The number of reinforcements varied from one to six discs per layer, spaced equally across the height of the specimens. It was determined that the discrete fiber inclusions improved the strength, increased the axial strain at failure, and reduced the post-peak loss of strength in most cases (Gray and Al-Refeai, 1986). The existence of a critical confining stress was common to both systems, and the failure curves exhibited the same bi-linear shape observed by Gray and Ohashi (1983). The authors reported that the fiber-reinforced samples failed along a classic planar shear plane in comparison to the fabric-reinforced sand, which failed by bulging between layers.

Maher and Gray (1990) utilized discrete, randomly-oriented fiber reinforcements in sands to evaluate the effect of different fiber inclusions within materials that have varying soil properties. The authors developed a stochastic model, based on statistical theory of strength for composites, that was able to predict the impact of fiber contribution on strength under static loads (Maher and Gray, 1990). The results indicated that the sand-fiber composite had either a curved linear or a bi-linear failure envelope with a break that occurred at the critical confining stress. The magnitude of the critical confining stress decreased with an increase in sand gradation, particle angularity, and fiber aspect ratio, but increased with an increase in fiber modulus (Maher and Gray, 1990). Changes in particle size and the reinforcement content did not affect the critical confining stress.

Lawton et al. (1993) reinforced their soil specimens by incorporating multi-oriented geosynthetic inclusions (discontinuous polypropylene elements) within a compacted soil. Triaxial compression tests were conducted to examine effects on shear strength as a function of reinforcement, surface roughness, and the orientation of the reinforcing elements. The reinforcement was most effective when placed in layers and in quantities sufficient to cover the entire cross section of the specimen (Lawton et al., 1993).

Benson and Khire (1994) mixed strips of high-density polyethylene (HDPE) with Portage sand to determine the California Bearing Ratio (CBR), secant modulus, resilient modulus, and shear strength of the composite soil. The aspect ratios (length/width) of the strips were four, eight and 12. In most cases, the resistance to deformation, the CBR, the secant modulus, the resilient modulus, and the shear strength of the HDPE reinforced sand increased (Benson and Khire, 1994), but the effects of the reinforcement depended

on the aspect ratio of the HDPE strips. The largest increases were observed with HDPE strips that had an aspect ratio of eight while HDPE strips with an aspect ratio of 4 actually made the soil weaker. In general, more dilation was observed when the percentage of reinforcement increased. Increased dilation was likely caused by enlargement of the shear zone that occurred as the strips were mobilized during shear (Benson and Khire, 1994).

Consoli et al. (2002) performed unconfined compression tests, splitting tensile tests, and saturated drained triaxial compression tests with local strain measurements to examine the benefit of utilizing randomly-distributed polyethylene terephthalate (PET) fibers. The fibers were acquired from recycled plastic material and used with and without rapid hardening Portland cement to improve the engineering behavior of uniform fine sand. PET fiber reinforcement improved the peak and ultimate strength of both cemented and uncemented soil, but the initial stiffness was not significantly changed by the inclusion of the fibers (Consoli et al., 2002). The positive effects of fiber length were not detected by either the unconfined compression tests or the split cylinder tests, indicating that the confining stress had an effect on the results and further triaxial tests were needed to understand fiber reinforced soil behavior (Consoli et al., 2002).

Zornberg (2002) conducted an analysis of fiber-reinforced soil using a discrete approach involving the independent characterization of soil specimens and the fiber specimens separately (Zornberg, 2002). The experimental testing program included tensile testing of the fibers and triaxial testing of unreinforced and reinforced test specimens. Fiber-induced distributed tension was proportional to the fiber content and the fiber aspect ratio while failure was characterized by pullout of individual fibers

(Zornberg, 2002). Zornberg (2002) concluded that the discrete framework accurately predicted the contribution of randomly distributed fibers for the various soil types, fiber aspect ratios, and fiber contents.

Sobhan and Mashnad (2003) investigated the mechanical behavior of a soil-cement-fly ash composite reinforced with recycled HDPE plastic strips that were obtained from postconsumer milk and water containers. The research was conducted to evaluate the compressive, split tensile, and flexural strength characteristics of the material, and to determine how effectively the recycled plastic strips would enhance the toughness characteristics of the composite. The results indicated that the use of fiber reinforcement significantly increased the post-peak load-carrying capacity of the mix and the fracture energy. It was concluded that the lean cementitious mix with recycled materials was a viable, civil-engineering construction material (Sobhan and Mashnad, 2003). However, flexural fatigue testing was needed to evaluate the resilient properties and the fatigue durability of the material (Sobhan and Mashnad, 2003).

Viratjandr (2006) examined the use of fiber-reinforced soils and the slope stability analysis of reinforced foundation soils. The results indicated that the model can predict the behavior of fiber-reinforced sand, and the developed yield criterion was capable of capturing the strain hardening effect observed during their experimental testing. In addition, it was noted that future work must be conducted to develop a comprehensive model for fiber-reinforced soil over a large stress range.

Dutta and Rao (2007) developed a regression model for predicting the behavior of sand mixed with recycled plastic. They performed triaxial compression tests with strain measurements on sand mixed with recycled Low Density Poly-Ethylene (LDPE)

and HDPE plastic strips and the results indicated the energy-absorption capacity of sand mixed with HDPE/LDPE plastic strips was influenced by aspect ratio, strip content, and confining pressure (Dutta and Rao, 2007).

Babu and Chouksey (2011) examined the use of recycled plastic strips as reinforcement in various soil types to assess the stress-strain-pore water response. Index testing, unconfined compression tests, one-dimensional compression tests, and triaxial compression tests were conducted. The strength of the soil was improved and compressibility reduced significantly with the addition of the plastic strip reinforcement (Babu and Chouksey, 2011).

Okoro et al. (2011) focused on examining the consolidation characteristics of soils stabilized with lime, coal combustion product (fly ash), and recycled plastic. Recycled plastic materials were mixed with soil and heated to approximately $275^{\circ}C$ to attain a uniform fused mix. The percentage of reinforcement was varied and the consolidation behavior (i.e., compression and swell indices) of each specimen was examined. The results indicated that soils stabilized with Class C fly ash, lime and recycled plastic reinforcement reduced the compressibility of soil (Okoro et al., 2011).

2.3.2 Recycled Plastic Pins

Loehr et al. (2000 and 2004) and Parra et al. (2003) examined the use of recycled plastic pins in slope stability applications for roadway embankments. The plastic pins can be fabricated with a wide variety of cross sections and lengths such that they can penetrate past the anticipated failure surface. The recycled plastic pins were manufactured from recycled plastics and industrial waste consisting primarily of HDPE with trace amounts of sawdust, fly ash, and other waste materials (Bowders et al., 2003). During the manufacturing process, the waste streams were pulverized, blended together, heated until partially melted, and then compressed into molds of specified shape and dimensions to form the plastic pins (Loehr et al., 2000). A total of seven 10 cm by 10 cm square pins with 1.2 m and 2.4 m lengths were driven at the site. Given the lateral resistance of the individual pins, the mechanics of a stability analysis for slopes reinforced with structural members is relatively straightforward and well established due to the mechanics of mechanically stabilized earth retaining structures. Although, recycled reinforcing inclusion materials have not been examined for this purpose. For this reason, Loehr et al. (2000) determined the resisting forces provided by each reinforcing member. Using a limit equilibrium analysis for slope stability analysis, the recycled plastic pins served as members that added resisting force to the soil along the assumed slope failure plane. Figure 2.30 comes from a different study conducted by Parra et al. (2003) displays a schematic of generic recycled plastic pins installed within a typical slope. The pins were driven into the slope to intersect the critical failure plane displayed in Figure 2.30. Based on the results, it was determined the failure was commonly located in the soil around or between the reinforcing members, and failure of the reinforcing members

(bending or shear) resulted from excessive stresses imposed by the retained soil (Loehr et al., 2000).
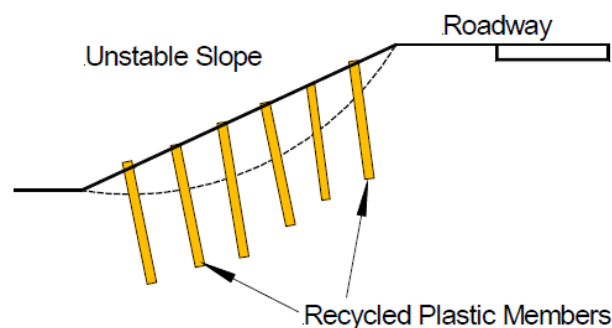
Figure 2.28: Schematic of a slope reinforced with recycled plastic pins (Parra et al., 2003)

Loehr et al. (2004) examined field studies conducted by the Kentucky Department of Transportation (DOT) and Missouri DOT to compare the use of recycled railroad ties and recycled plastic pins, respectively. The results of the field installations highlighted three main issues. First, a widely accepted design procedure for slopes reinforced in-place with recycled materials was needed. Second, the capacity of the recycled members including consideration of potential impacts of first use of the materials and the long-term durability of the materials under field exposure and loading conditions needed to be addressed. Lastly, potential creep of the members under sustained load needed consideration (Loehr et al., 2004).

Three field demonstrations sites were stabilized using recycled plastic reinforcements to demonstrate the effectiveness of the stabilization scheme and to evaluate the load transfer mechanisms between the soil and reinforcement (Parra et al., 2003). The field demonstrations utilized the configuration previously displayed in Figure 2.30. Each site was instrumented with stain gages on the plastic pins, slope inclinometers,

and standpipe screened piezometers to measure the bending moments for each reinforcing member, the change in inclination of the slope, and pore pressure changes within the slope, respectively. In conclusion, the field sites demonstrated the effectiveness of using recycled plastic reinforcement for the stabilization of surficial slope failures (Parra et al., 2003).

Bowders et al. (2003) attempted to examine and develop suitable specifications for accepting and rejecting recycled plastic pins for the same application. They evaluated the compressive strength, strain rate effects, modulus of elasticity, flexural strength, flexural modulus, creep behavior, and installation behavior of recycled plastic pins manufactured by compression and extrusion processes using LDPE, HDPE, and HDPE/fiberglass materials. In general, the member strength and stiffness appear to be poor surrogates for establishing the drivability of the recycled plastic pins (Bowders et al. 2003). It was determined that drivability was considerable significant factor associated with the practical implications of the material, and additional work was being pursued to identify alternative surrogate properties that may be more representative of drivability (Bowders et al., 2003).

2.4 Review of Comparable Group 3 Materials - Recycled Particulate Materials

While the previous section reviewed recycled materials that behave as reinforcing inclusions, this section reviews recycled materials that are particulate in nature (i.e., recycled glass particles, recycled Styrofoam beads, and tire derived aggregate).

2.4.1 Recycled Glass

Reddy (1999) explored the use of recycled glass crushed into glass cullet for backfill material behind retaining structures. Experimental tests were conducted to measure the index properties, hydraulic conductivity, durability, compatibility, shear strength, thermal conductivity, and chemical resistance in addition to a cost analysis associated with use of this material. The results demonstrated that glass cullet is a feasible alternative to conventional granular soils when used as backfill material for retaining structures (Reddy, 1999). The glass cullet exhibited higher permeability, equal or higher friction angles, and lower specific gravities and unit weights in comparison to sand (Reddy, 1999).

Wartman et al. (2004) examined the use of crushed soil as a remedy to improve the engineering characteristics of fine-grained, marginal materials (e.g. kaolin, quarry fines). The same authors explored the extent to which soil blending could enhance the cohesive behavior of crushed glass. The index properties, hydraulic conductivity, compaction behavior, optimum moisture content, and shear strength measured from direct shear and consolidated drained triaxial tests was evaluated for crushed glass blends. The results indicated that the cohesive strength of the crushed glass increased 50-100 % with the addition of the fine-grained soils (Wartman et al., 2004). However, the increase

in cohesive strength was accompanied by a 20% to 45% decrease in frictional strength even though friction angle remained above 35° (Wartman et al., 2004).

Grubb et al. (2006) conducted laboratory tests on crushed glass-dredged material blends to evaluate the optimum moisture content, compaction behaviors, workability, triaxial shear strength, and consolidation time requirements. The mixture consisted of crushed glass mixed with dredged soil material from the Schuylkill River, composed primarily of high plasticity silts (MH) according to the Unified Classification System. In conclusion, the range of properties obtainable by crushed glass-dredged material blends offered the designer material property versatility by using different proportions of each ingredient depending upon the properties needed to optimize the design (e.g. whether strength, settlement, or drainage was most important) (Grubb et al., 2006).

In addition to their laboratory investigation, Grubb et al. (2006) utilized the crushed glass-dredged material blends at three field sites to explore the feasibility of using the material in embankments and other structural fill applications. The results illustrated significant geotechnical improvements of the dredged material from the addition of crushed glass. Grubb et al. (2007) then compared the performance of bulkheads with conventional backfills to bulkheads that leveraged recycled materials. The layered system was comprised of Tire Derived Aggregate (TDA), crushed glass, and dredged material fines. The results clearly illustrate that recycled backfills introduced significant economic and technical advantages including a simplified construction sequence, improved backfill properties, and a reduction in the weight of the backfill (Grubb et al., 2007).

Ooi et al. (2008) examined the shear strength characteristics of recycled glass compared to other recycled materials and virgin aggregates. The initial results indicated

that the recycled glass performed better than recycled asphalt pavement during the California Bearing Ratio (CBR) tests, but the recycled glass performed worse than virgin aggregates. The direct shear results indicated that the relative density had a considerable impact on the internal friction angles. The measured friction angles ranged from 31° – $61°$ (Ooi et al., 2008). When designed properly, recycled glass has the potential to be used in other foundation and ground improvement applications (Ooi et al., 2008).

2.4.2 Styrofoam Beads

Oh et al. (2002) examined the bearing capacity characteristics of lightweight material manufactured using recycled Styrofoam beads. In order to evaluate of the bearing capacity, the subsurface was divided into two layers. The upper part was constructed using lightweight fill material (Styrofoam beads) and the lower part consisted of a soft clay. The mixing rates of waste Styrofoam in the upper part varied between 40%, 50%, and 60%. The use of Styrofoam minimized the stress increment, increased the bearing capacity, and reduced the settlement over the life of the structure. The results indicated that the lightweight Styrofoam fill material increased the ultimate bearing capacity by more than two times in comparison to compacted, weathered soil (Oh et al., 2002).

2.4.3 Tire Derived Aggregate (TDA)

Two hundred and fifty million tires are discarded every year while almost 30% of these scrap tires wind up in overcrowded landfills while thousands more are left in empty lots and illegal dumps (Bernal et al., 1996). Tire derived aggregate (TDA) is categorized by the aggregate size of the material, which can vary depending on the manufacturing technique. The American Society for Testing and Materials (ASTM) (2012) define the dimensions of tire chips (1.2 cm - 5 cm.), the dimensions of tire shreds (5 cm - 30.5 cm.), and the dimensions of tire granulated rubber (0.042 cm - 1.2 cm). Tire fragments have been classified in construction practice as Type A or B. Type A and Type B TDA contain tire fragments with maximum lengths of 8 in. and 18 in., respectively (see Table 2.3 for specifications). The manufacturing process requires sharp knives to shear tires into a predefined size (Humphrey, 2003). However, the manufacturing process does not produce homogeneous mixtures of TDA with size classifications specified in Table 2.3, therefore, TDA may contain any proportion of tire shreds, chips or granulated rubber (Finney et al., 2013). The type of TDA produces for various projects will depend upon the type of reduction process utilized.

Table 2.3: Type A and Type B specifications for the TDA used in project experiments (Scardaci et al., 2012)

Parameter Tested	Type A TDA Specification	Type B TDA Specification
Maximum (Max.) Percent Free Steel (%)	1	1
Max. Longest Shred (in.)	8	18
Max. Weight of Shreds >12 in. of total (%)	0	10
Maximum Passing No. 4 sieve (0.187 in.) (%)	5	1
Maximum Number of Sidewall Shreds in Mixture	1	1
Max. Weight of Shreds >2 in. wire exposed (%)	10	10
Max. Weight of Shreds >1 in. wire exposed (%)	25	25

The constituents of these TDA mixtures can vary considerably, depending upon the compositional components of a rubber tire. Table 2.4 summaries the percentage of constituents of a typical rubber tire (Dodds et al, 1983). Notice the significant amount of Copolymer with minor amounts of Sulfur. However, Amoozegar and Robarge (2006) discovered that components of a typical tire from the Goodyear Tire Company significantly vary from that of a typical tire. Table 2.5 summarizes the results of Amoozegar and Robarge (2006). Notice the difference between the percentage in Table 2.4 and 2.5. Figure 2.29 illustrates a picture of roadway construction utilizing TDA in a geotechnical application. Notice the length of the zone and the quantity of recycled tires required for this particular application. Figure 2.30 illustrates a close up of Type B TDA. Notice the angular edges and shapes associated with the processed recycled material.

Table 2.4: The compositional components of a typical rubber tire (Dodds et al., 1983)

Component	Weight %
Styrene Butadiene Copolymer	62.1
Carbon Black	31
Extender Oil	1.9
Zinc Oxide	1.9
Stearic Acid	1.2
Sulfur	1.1
Accelerator	0.7
Total	99.9

Table 2.5: Components of a typical tire from the Goodyear Tire Company (Amoozegar and Robarge, 2006)

Component	Weight %
Carbon Black	28
Synthetic Rubber	27
Natural Rubber	14
Steel Wire	10
Extender Oil	10
Other Petrochemicals	4
Organic Fabric	4
Sulfur, Zinc Oxide and Other Compounds	3
Total	100

Figure 2.29: Type B TDA utilized in roadway construction (CalRecycle, 2015)

Figure 2.30: Image of Type B TDA (CalRecycle, 2015)

2.5 Summary

This chapter divided the studies reported in the literature into three main groups: 1) a group that summarized studies associated with generating lightweight fill 'zones', 2) a group that summarized studies associated with including reinforcing 'inclusions', and 3) a group that summarized studies associated with the use of recycled 'particulate materials'. The Group 1 studies are more closely tied to the proposed technology. As a result, Table 2.6 has been generated to summarize the information reported in Section 2.2 and clearly identify the key data in addition to the gaps in the available knowledge. Table 2.6 attempts to summarize critical properties including unit weight, shear strength, and deformation behaviors for each study introduced in the literature review for the most comparable technologies, which include the EPS Geofoam block and tire bales.

Table 2.6: Summary of studies involving slopes with reinforcing zones

Reference	Inclusion Zone Type	Dimensions	Unit Weight (kN/m^3)	Shear Strength	Deformation Properties	Description
Horvath (1994)	EPS Geofoam	50 mm^3	0.21	unknown	E = 8750 kPa	Review of EPS Geofoam (Fig. 2.9)
Jutkofsky et al. (2000)	EPS Geofoam	0.6 m x 1.2 m x 2.4 m	0.20	Interface friction angle: Peak ϕ = 40.5° Residual ϕ = 34.8°	unknown	New road embankment with EPS Geofoam zone (Fig. 2.12)
Elragi et al. (2000)	EPS Geofoam	0.37 m^3 0.84 m^3	0.15 0.29	unknown	E = 5100 kPa E = 16000 kPa	Sample size effect of EPS Geofoam (Fig. 2.13)
Mann and Stark (2004)	EPS Geofoam	1.2 m x 1.2 m x 2.4 m	0.35	unknown	E = 310 kPa	Repair of failed slope. EPS Geofoam coupled with solider pile and anchors (Fig. 2.15)
Newman et al. (2010)	EPS Geofoam	0.82 x 1.2 x 4.9	0.18	Interface friction angle: ϕ = 35°	E = 1700 - 2700	Embankment reconstruction along I-15 (Fig. 2.22)
LaRocque et al. (2005)	Tire Bale	unknown	unknown	Interface friction angle: ϕ = 20°	unknown	Direct shear testing of tire bales (Fig. 2.28)
Winter et al. (2009)	Tire Bale	0.8 m x 1.3 m x 1.55 m	4.45	Interface friction angle: ϕ = 35°	unknown	Slope stabiliztion with the use of tire bales
Zornberg et al. (2004)	Tire Bale	0.75 m x 1.4 m x 1.5 m	5.50	Interface friction angle: $\phi \geq$ 25° Cohesion: 2.4 kPa	E = 400 kPa / Creep (at 1000 hrs) = 0.005 %strain/ day	Report on feasibliity and mechanical properties of tire bales

CHAPTER 3: CHARACTERIZATION OF RECYCLED POLYETHYLENE
TEREPHTHALATE (PET) PLASTIC BALE MATERIAL

3.1 Introduction

This chapter will provide an overview of the PET plastic bale test material. A description and a summary of the characterization, including laboratory tensile examination, conducted on the PET bale constituents will be presented within the chapter. Petrochemicals (plastics) are utilized in everything from medical equipment to the armored vests used in military applications, and to package a vast majority of the food and beverages sold domestically. There are seven types of plastics designed to package certain consumer goods. A coding system that identifies the resin content of bottles and containers commonly found in the residential waste stream using a system of numbers on the bottom of all plastic containers was developed in 1988 by the Society of the Plastics Industry, a plastics industry trade association (EPA, 2012). For example, water and soda are packaged in PET or Type 1 plastic containers, while milk containers are manufactured from high density Polyethylene (HDPE) or Type 2 plastic containers. Consumers of these products can use the numbers labeled on the containers to identify materials that can be recycled. Figure 3.1 lists the seven types of plastic with each respective code number and the typical products manufactured with each type.

Figure 3.1: Plastic resin codes (ASTM, 2008)

Recent studies have shown that various forms of plastic are negatively affecting global environmental systems and their inhabitants (e.g., Shaw and Mapes, 1979; Day, 1980; Balazs, 1985; Day 1986; Day and Shaw, 1987; Wallace, 1985; Fowler, 1987; Ryan, 1987; Ryan, 1990; Robards, 1993; Bjorndal et al., 1995; Laist, 1997; Mato et al., 2001; Moore et al., 2001). These environmental systems are required to sustain life on this planet and must be preserved by any means necessary if the proceeding generations are to live on a habitable planet. The proposed geotechnical application for PET bales as a lightweight fill if successful will provide a viable alternative to recycling these materials.

3.2 Polyethylene Terephthalate (PET) Bale Manufacturing and Material Description

Polyethylene Terephthalate, commonly referred to as PET or PETE (Type 1 plastic), is the most widely used plastic in modern domestic society. PET is a thermoplastic polymer resin, first patented in 1941 by John Rex Whinfield, James Tennant Dickson, and their employer, the Calico Printers' Association of Manchester (Whinfield and Dickson, 1941). Since 1941, PET has been used in applications ranging from sailcloth to children's toys. PET is commonly utilized in the beverage and food packaging industry because of its high mechanical strength, inexpensive production costs, and the ability to inexpensively transport large quantities of liquid and food (Keeler and Burke, 2009). PET has no centerline porosity so fluid absorption and leakage is negligible. PET is a proprietary material so the constituents have been protected under the patent laws of the United States (Keeler and Burke, 2009). As a result, the plastic manufacturers are not required to disclose what the explicit constituents of their product are, as they are referred to as proprietary ingredients.

PET is utilized to package liquids in the form of a bottle and was patented in 1973 by Nathaniel Wyeth (Wyeth, 1973). Major food corporations are using this patent to package their beverages, and publicly treated water is also being bottled in PET bottles for convenience. A recent study illustrates that the U.S. consumes 1,500 plastic PET water bottles every second (EPA, 2012). The same study indicates that only 20% of these bottles are recycled at an MRF via curbside collection. At an MRF, all plastics are segregated into the seven plastic types by an optical laser that evaluates the density of each item. The collected material is baled and transported to a manufacturer of post-consumer plastic products to process the material. While the MRF processes bales for

each type of plastic show in Figure 3.1, only Type 1 PET plastic bales were evaluated as part of this study due to the abundance of this type material in comparison to the other types.

The PET bales produced from the MRF contain only Type 1 plastic, and primarily consists of bottles, containers, and food packaging. The process of sorting the Type 1 plastic from the other types can be automated, with an optical laser evaluating density, or manual, with visual inspection. This process will depend upon the supply produced from the MRF's curbside collection. A larger MRF will accommodate a large population (i.e., Charlotte, NC) and will have an automated processing system. In contrast, a smaller MRF that accommodates a much smaller population (i.e., Denver, NC) will have a manual system.

Dependent upon the type of baler and operations at the MRF, the PET bales produced from each MRF fluctuate in dimensions and unit weight. The dimensions of each PET bale correlate to the specifications of the baler. The PET bales donated for this study from Charlotte ReCommunity MRF were produced from a Badger two-ram baler. The dimensions of the bales are approximately 78 cm by 117 cm by 155 cm. For each MRF, all types of plastic bales have approximately the same dimensions because they are compacted, compressed, and baled from the same equipment. In addition, all plastic bales are wrapped with 12-gage steel wires as the bale is extruded from the baler. The number of wires used on each bale is dependent upon the unit weight of the bale. A higher unit weight requires more steel wires to keep the bale compressed. The MRF uses a range between five to nine 12-gage steel wires for each bale depending upon the unit weight, but the type and number of steel wires is dependent upon the MRF.

For the Charlotte ReCommunity MRF, the unit weight of a PET bale fluctuates between 2.36 kN/m^3 and 3.93 kN/m^3 depending upon the supply. Variations in the unit weight values of the PET bales are due to fluctuations in the amount of consumer goods that are recycled each day, collected from curbside collection, and processed by the municipal MRF. A higher daily supply of recycled PET constituents will correlate to PET bale unit weight values that replicate the highest range of bale unit weights, 3.93 kN/m^3, and a lower daily supply will correlate to PET bale unit weight values that replicate the lowest range of bale unit weights, 2.36 kN/m^3. The unit weight values are inversely proportional to the void space within each PET bale. While the weight of the material in each bale may vary slightly depending upon the daily supply, the volume of the bale remains constant because it correlates to the specifications of the baler at the select MRF.

Table 3.1 summarizes the physical properties of the PET bales donated by Charlotte ReCommunity MRF for this study. The range of unit weight values for the PET bales donated for this research was between 2.77 kN/m^3 to 3.61 kN/m^3. The table also displays the dimensions, weight, unit weight, and number of straps for each bale, which correlates to the daily supply of PET constituents processed by the MRF at the time each bale is processed. Although there is a variance in the unit weight of PET bales, the range of values is not outside of a normal range expected for a fill material.

Table 3.1: Summary of physical properties of recycled PET bales from MRF

Bale Number	Dimensions (cm)	Weight (kN)	Unit Weight (kN/m^3)	Number of Straps
1	80.1 x 125.4 x 161.9	5.15	3.17	8
2	81.2 x 120.6 x 157.1	4.26	2.77	7
3	78.6 x 118.1 x 156.4	4.14	2.85	7
4	79.5 x 119.2 x 157.8	3.95	2.64	6
5	80.6 x 121.8 x 159.3	5.65	3.61	9

Figures 3.2 and 3.3 provide photographs of a typical recycled PET bale from this facility. Note that each bale was secured with 12-gage steel wire, which was removed (see Figure 3.3) to retrieve the individual test specimens for the tensile tests described herein. The individual PET plastic constituents were randomly selected but represent a variety of bottles, containers, and food packaging.

Figure 3.2: Photograph of a recycled PET bale from the MRF

Figure 3.3: Recycled PET bale after the straps were cut

Table 3.2 summarizes the physical, mechanical, and thermal properties of a virgin PET block in accordance with the American Society for Testing and Materials (ASTM) testing standards noted in the last column of this table. The displacement rate used to measure the tensile strength from ASTM D638 (2015) was 5 mm/min. The displacement rates selected for the evaluation of tensile strength for the PET bale constituents were 1.27 mm /min and 12.7 mm/min.

Table 3.2: Summary of key properties of typical PET plastic (Plastic Products Inc., 2014)

Physical Properties	Value	Units	ASTM Test Method
Density	1.38	g/cc	D792
Water absorption, 24 h	0.10	%	D570
Mechanical Properties		Units	ASTM Test Method
Tensile Strength at break	79.29	MPa	D638
Tensile Modulus	2757	MPa	D638
Elongation at break	70	%	D638
Flexural Strength	103.4	MPa	D790
Flexural Modulus	2757	MPa	D790
Rockwell Hardness	R117	----	D785
Coefficient of Friction, 275 kPa	0.19/0.25	Static/Dynamic	----
Thermal Properties		Units	ASTM Test Method
Heat Deflection	175	^{o}F	D648
Melting Point	490	^{o}F	----
Coefficient of Linear Thermal Expansion	9.9×10^{-5}	cm/cm/- ^{o}F	D696
Range for Thermal Exp.	50 - 250	^{o}F	----

Figure 3.4 illustrates a photograph of four constituents of the PET bale prior to testing that were evaluated as part of this study. Note the different shape, integrity, and surface irregularities across each specimen. These irregularities will be discussed in the next section.
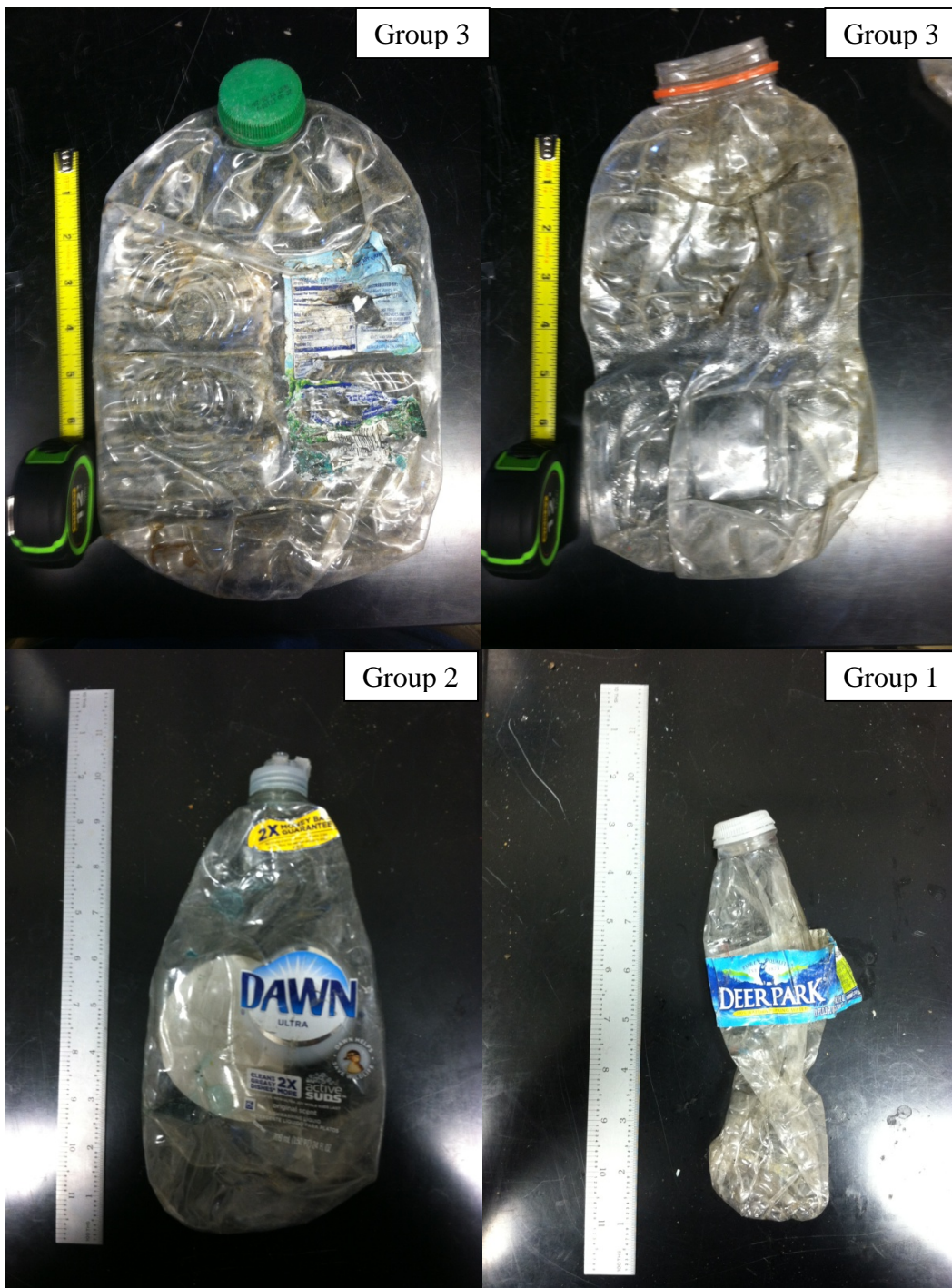
Figure 3.4: Photographs of individual PET bale constituents prior to testing

3.2.1 PET Bale Constituent Variability

The full-scale constituents shown in Figure 3.4 are denoted by Groups 1, 2 and 3, which correlate to the bulk thickness and integrity of the PET bale constituents. Group 1 represents the lowest bulk thickness and integrity, Group 2 represents the medium bulk thickness and integrity, and Group 3 represents the highest bulk thickness and integrity for all full-scale PET constituents. Note on Figure 3.4 that each specimen had different shape, size, compression deformities, surface textures, and included varying caps, cap shapes, cap sizes, and cap integrity. All of these combined variables are random within a typical PET bale and are unpredictable due to the stochastic nature of the curbside collection and bailing process. The only consistent variable between all full-scale PET constituents, regardless of the MRF, is the chemical composition of each constituent that constitutes Type 1 plastic or Polyethylene Terephthalate (PET).

The thickness of virgin PET is approx. 0.05 mm - 2 mm, but the bulk thickness of the material was measured as part of this research. The bulk thickness of full-scale PET constituents can range between 2.3 mm to 12.5 mm for all groups (1/2/3). However the bulk thickness is more representative of the PET full-scale constituents because the baling process at the MRF deforms each PET constituent to a random shape and size within the bale. The resulting sizes and compression deformities must be documented to illustrate the wide variance in the PET full-scale constituents so the bulk thickness is more representative of the recycled PET than the thickness of virgin PET.

Table 3.3 summarizes the categories of groups, percentage of those groups, types of products, and bulk thickness ranges associated with each groups that were measured during the tensile strength tests for 200 specimens. Approximately 50%, 29%, and 23.5%

of the specimens that were examined were represented by Group 1, Group 2, and Group 3 constituents, respectively. The variability in the bulk thickness of the full-scale constituents is due to the wide variety of sizes, shapes, compaction deformities, and surface textures that are randomly collected by curbside collection and compacted by the baler at the MRF. Additionally, there is a wide variance in the full-scale constituents because each constituent is manufactured to different specifications. Each consumer goods manufacturer has different products to package, different marketing strategies, and varying budgetary constraints that dictates these changing specifications.

Table 3.3: Summary of the three groups of recycled PET bale constituents from 200 specimens

Group	Corresponding Types of Products	Material Bulk Thickness (mm)
1 (47.5%)	Lightweight Water Bottles Fresh Produce (Berries / Fruit) Lightweight Beverage Containers	2.3 - 4.96
2 (29%)	20 oz. Beverage Containers (Soda/Juice) 2 - 3 Liter Beverage Containers (Soda)	3.45 - 7.68
3 (23.5%)	Salad Dressing Containers Condiment Containers Cleaning Product Containers	4.31 - 12.55

3.2.2 PET Bale Chopped Group 1 Constituents

In order to determine the effects of the wide amount of variance apparent in the full-scale PET bale constituents, the constituents were systematically processed. Due to the bulk thickness of Group 2 and 3 full-scale PET constituents, Group 1 constituents were the only type of PET bale constituents that could be successfully processed using the method described herein. Group 1 constituents were cut into square pieces (1.98 cm^2) using a commercial strength paper cutter. The top, bottom, and cap pieces were removed from the collective batch to ensure consistency. Thousands of full-scale Group 1 PET bale constituents were reduced into identical shape and sizes to create the test specimens for two experimental phases. The compression deformities and surface textures of the chopped constituents were held as constant as possible to provide the least amount of variance within the collective batch of PET bale chopped Group 1 constituents.

These chopped constituents were utilized to create testing specimens for the 1D compressive and triaxial compression testing experimental phases. Chopped specimens were generated for the 1D compression experimental phase to understand the effects of particle size, which will be discussed in the Section 4.2. Chopped specimens were generated for the triaxial compression experimental phase to ensure particle-particle interaction within the specimen and maintain an acceptable particle size to specimen diameter ratio. The triaxial compression tests dictated the size of the chopped pieces. The 15.24 cm triaxial chamber diameter required a particle size that was 1/6 the diameter of the test specimen to ensure particle-particle interaction within the specimen, which will be discussed in Section 4.4.

3.3 Tensile Strength Test Configuration and Procedure

The constituents of a typical PET plastic bale were evaluated to determine the range of tensile strengths associated with the bales donated by the Charlotte ReCommunity MRF. The tensile behavior and strength of compressed PET plastic constituents retrieved from one of the recycled PET bales was evaluated as part of this study. The individual PET test specimens were placed in buckets located in a laboratory at room temperature to air dry for at least 48 hours prior to testing. Due to the limitations of the tensile machine available only PET plastic test specimens with a width of 203 mm, a length of 609 mm, and bulk thickness of 32 mm were tested. All PET plastic test specimens fell within these dimensional requirements.

Each PET plastic test specimen was prepared using a consistent process. Figure 3.5(a) displays a photograph of a test specimen prior to any modifications. As part of the specimen preparation process, the top and bottom of each test specimen was cut off to ensure a solid grip on the recycled material. Subsequently, a line was marked on each end of the test specimen approximately 50.8 mm from each end to ensure that the grips had a sufficient grip area (See Figure 3.5(b)). Thick cardstock paper was wrapped around the ends of the test specimen to provide guidance as the grips were positioned on the test specimen, and to ensure that the grips would hold the specimen in place during the test without damaging the material (see Figure 3.5(c)). For each test specimen the final length, width, and bulk thickness were measured inside the test area (outside grip areas) at the top, middle, and bottom locations utilizing precision calipers.
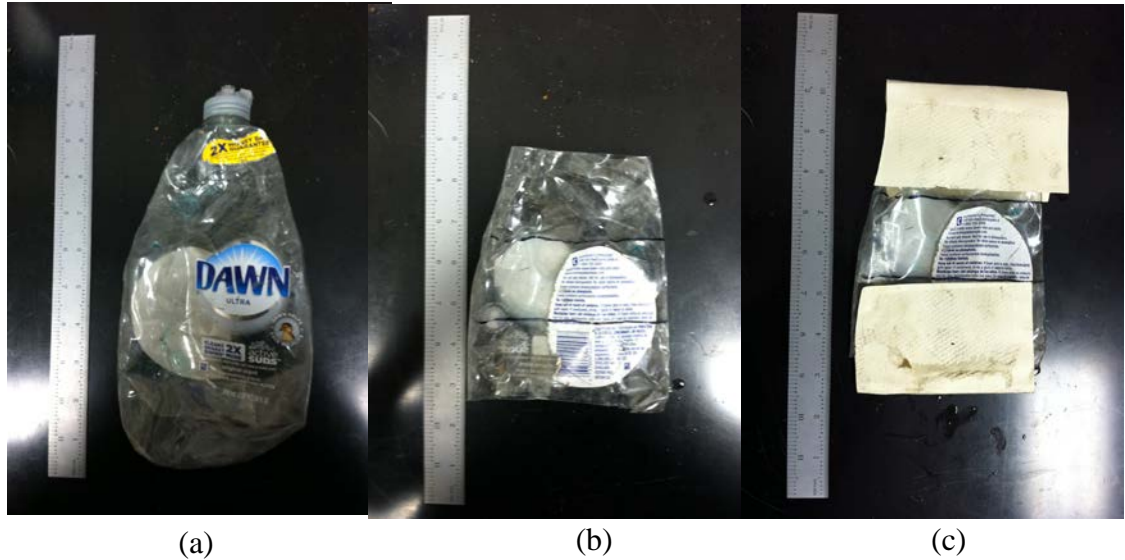
Figure 3.5: Recycled PET Group 2 test specimen: (a) from the bale; (b) with top and bottom removed; and (c) with thick card stock grip covers

The tensile tests were carried out using the United Testing Systems (UTS) tensile machine shown in Figure 3.6. The wide-width hydraulic testing grips used in this experimental component are shown in Figure 3.7. The hydraulic test grips were operated using compressed air from the building supply. Each test was installed between the grips displayed in Figure 3.7. The tensile load was measured using a calibrated 222 kN capacity load cell and the sample elongation was tracked with a linear variable differential transformer (LVDT) that had a stroke equal to 1041 mm. The fixed base of the UTS machine used two actuators to pull the top grip from the bottom grip.
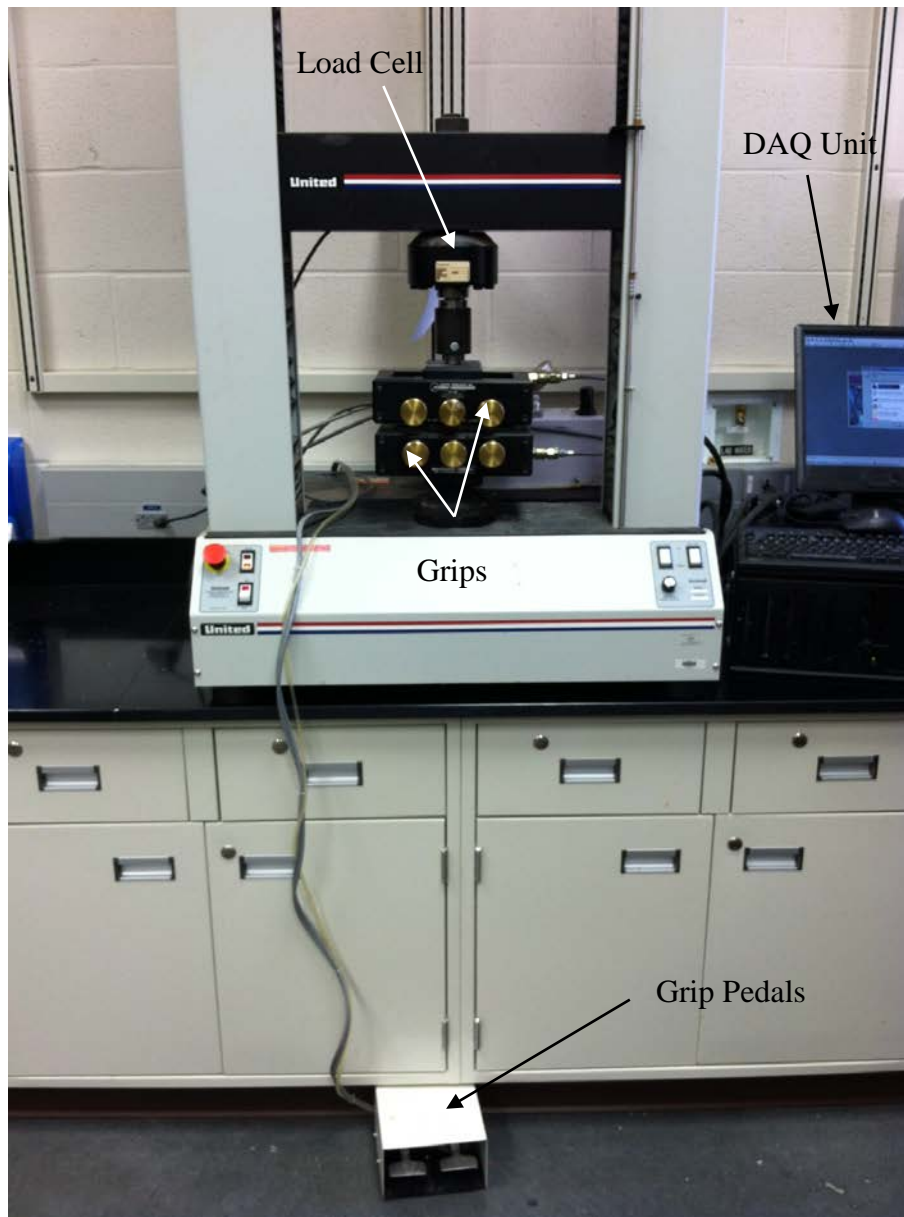
Figure 3.6: United Testing System (UTS) tensile machine
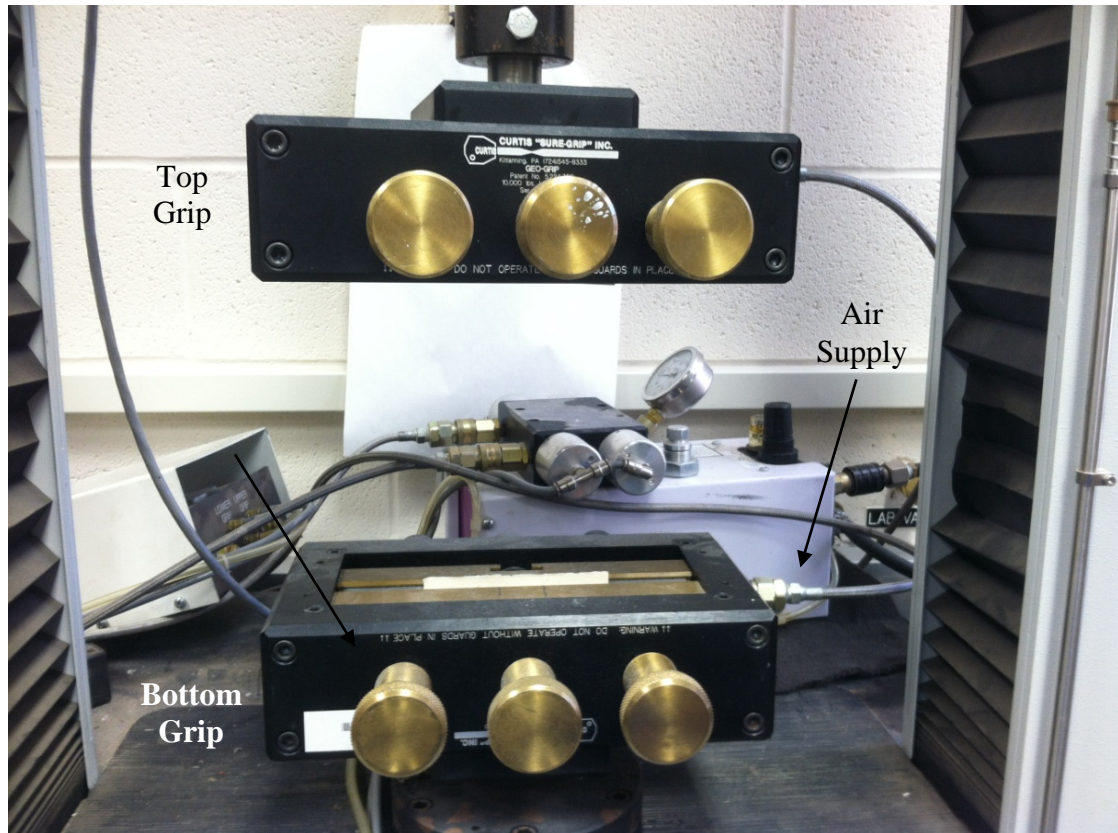
Figure 3.7: Curtis hydraulic grips

The wide-width hydraulic grips applied a contact pressure of 17.23 MPa at the ends of each tensile test specimen. This level of contact was established based on a preliminary study conducted to determine the right level of contact for the PET plastic to prevent the test specimens from slipping out of the grips, and not too high to prevent the grips from tearing specimens at this grip interface. The UTS machine was capable of conducting tests at displacement rates ranging from 1.27 cm/min to 12.7 cm/min. PET plastic constituents were tested at the highest and lowest rates to determine the effects of displacement rate (if any). One hundred tensile strength tests were conducted on random PET plastic test specimens for each displacement rate (a total of 200 tests). Figure 3.8

displays representative pictures of several tensile tests in progress which shows the
typical failure mechanism.
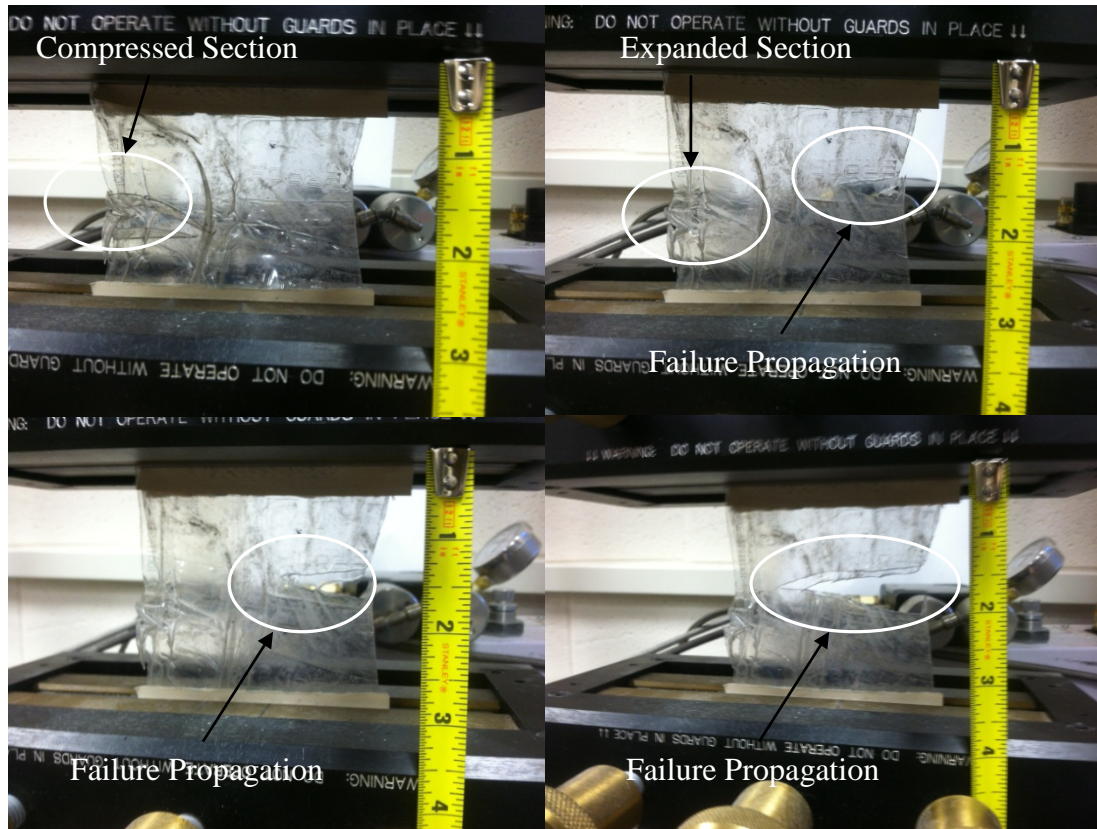
Figure 3.8: Photographs of different recycled PET plastic test specimens during tensile
strength tests

The axial strain was computed as follows:

$$\varepsilon = \Delta L / L_o \qquad\qquad\qquad [3.1]$$

Where:

ε = Axial strain
ΔL = Change in specimen length
L_o = Initial specimen length

The average cross sectional area of each test specimen was calculated using the average of at least three measurements of the initial width and bulk thickness. The width and bulk thickness were measured at three different locations for each test specimen to acquire the average. The nominal tensile stress was computed using as follows:

$$\sigma = T / A_{AVG} \qquad\qquad\qquad [3.2]$$

Where:

σ_t = Nominal tensile stress
T = Tensile force from load cell
A_{AVG} = Average specimen area using average initial width and thickness

3.4 Tensile Strength Results and Discussion

During the test specimen selection process, there appeared to be three visually different groups of PET plastic bottles. Table 3.3 summarizes the three groups and includes a description of the packaging types that fall within each. Figures 3.9 - 3.11 display representative photographs of a post failure conditions for Group 1 bottles (e.g., 0.47 L lightweight water bottle), Group 2 bottles (e.g., 2 L soda bottle), and Group 3 bottles (e.g., 3.78 L orange juice container), respectively. The location of the post failure rupture and the direction of these failures are labeled in these photographs. In all cases the tensile rupture consistently propagated inward from the exterior of the specimens.
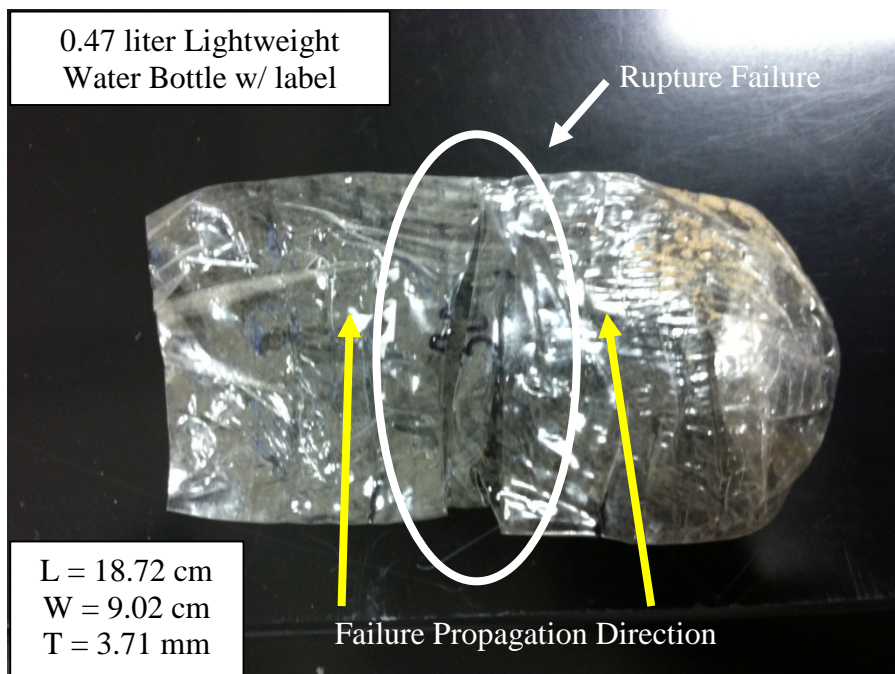
Figure 3.9: Post failure condition for Group 1 specimen

Figure 3.10: Post failure condition for Group 2 specimen
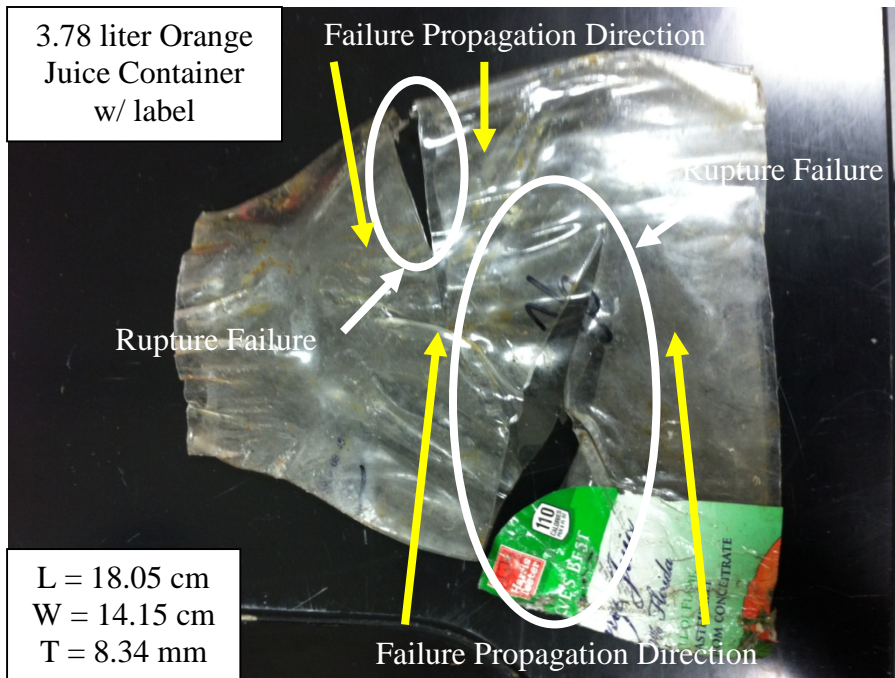
Figure 3.11: Post failure condition for Group 3 specimen

All data was processed to generate the stress-strain relationships for the randomly selected test specimens tested at two different displacement rates. Figure 3.12 displays the stress-strain curves for all tensile tests conducted at the displacement rate of 1.27 mm/min. Figure 3.13 shows the stress-strain curves for all tests conducted at the displacement rate of 12.7 mm/min. Each figure displays 100 tests performed for each displacement rate. Figure 3.12 and 3.13 have stress-strain curves presented with lines of different colors to denote each bottle group listed in Table 3.3. The color lines used were blue, green, and red which correspond to Groups 1, 2, and 3, respectively. All data sets exhibit a significant amount of variance in the failure conditions. The variance in the stress-strain results displayed in Figures 3.12 and 3.13 can be explained by the wide variance of shapes, sizes, compression deformities, and surface textures that were tested from the 200 specimens. These differences in the full-scale constituent's physical characteristics are due to the stochastic nature of the recycled PET consumer goods

obtained from the population of the Greater Charlotte-Mecklenburg Area acquired through daily curbside collection. Additionally, the random collection, compaction, and bailing process by the MRF provides additional variances to the stress-strain results for all of the full-scale PET constituents.

In Figure 3.12, corresponding to the low displacement rate of 1.27 mm/min, one of the test specimens exhibited a tensile failure equal to 251 MPa at an axial strain level equal to 21.6%. In contrast the softer response measured for a test specimen that exhibited a tensile failure equal to 81.1 MPa at an axial strain level equal to 91.2%. (both tests shown in Figure 3.12). Both of these extreme test's failure values are shown in Figure 3.12 as solid black circles. In Figure 3.13, corresponding to the high displacement rate of 12.7 mm/min, one of the strongest test specimens exhibited a tensile failure at a strength equal to 174 MPa at an axial strain level equal to 16.5%. In contrast, one of the lower strength specimens showed a tensile failure at 11.6 MPa at an axial strain level equal to 85%. In accordance with the data presented in Table 3.2, the tensile strength at break for typical PET plastic is 79.3 MPa at 70% elongation, tested at a displacement rate equal to 5 mm/min (Plastic Products, Inc. 2014). This identifier is labeled in Figure 3.12 and Figure 3.13 using dashed lines as a reference point for comparison to the data measured in this study.
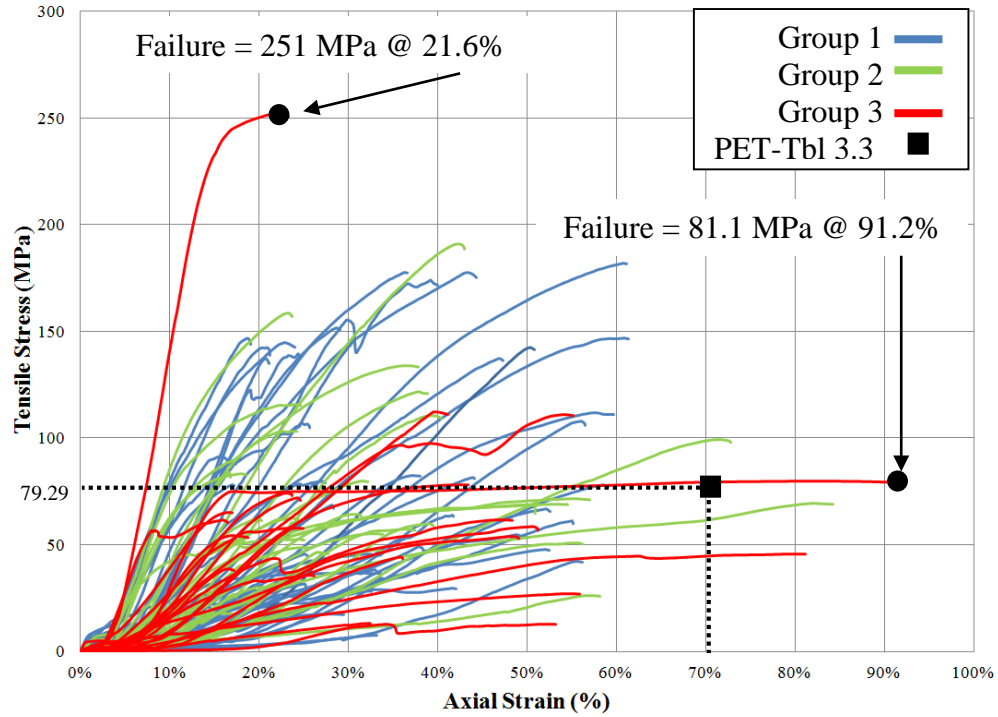
Figure 3.12: All tensile test results using the high displacement rate of 1.27 mm/min
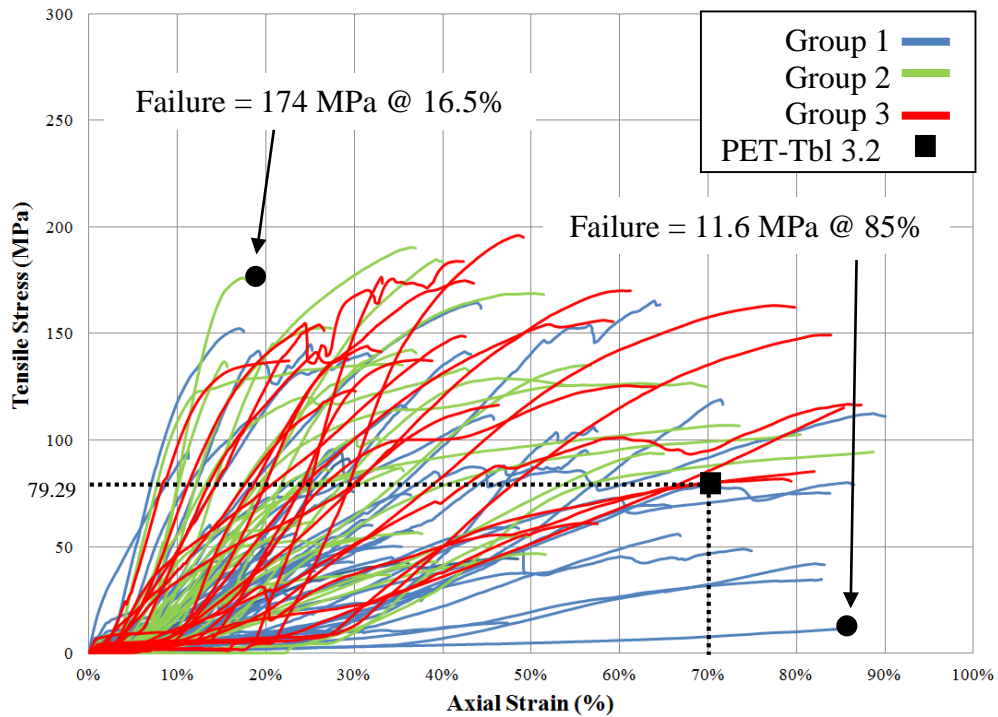
Figure 3.13: All tensile test results using the low displacement rate of 12.7 mm/min

Table 3.4 summarizes the minimum, maximum, and average stress and strain values at failure for all test specimens including both displacement rates and all three Groups. The higher bulk thickness specimens and the maximum values of stress at failure correlate to Group 3 constituents. The average strains at failure exhibited by all groups for each displacement rate range from 36.24% to 53.50%, illustrating the ductile characteristic of the full-scale PET constituents.

Table 3.4: Summary statistics: minimum, maximum, and average stresses and strains at failure for each displacement rate and each Group

Group	Avg. Bulk Thickness (mm)	Displacement rate (cm/min)	Min. (MPa)	Max. (MPa)	Avg. (MPa)	Min. (%)	Max. (%)	Avg. (%)
			Stress at Failure			Strain at Failure		
1	3.63		7.55	182.14	85.47	14.46	61.33	36.24
2	5.57	1.27	17.93	190.81	75.67	14.95	84.28	38.70
3	8.43		12.62	251.57	67.3	16.51	97.12	44.70
1	3.27		11.64	165.1	72.34	11.19	90.04	41.84
2	4.96	12.7	52.12	142.27	87.13	15.56	88.73	43.28
3	9.17		60.93	196.51	138.82	22.63	87.31	53.50

The data displayed in Figures 3.12 and 3.13 shows high variability in terms of tensile strength (peak values of stress-strain curves), the shape of stress-strain curves, the initial stiffness, and the strain to failure. There does not appear to be any notable trends between Groups 1, 2, or 3. Each of these plots shows a horizontal dashed line at a tensile stress equal to 79.29 MPa, which corresponds to the average tensile strength reported for PET plastic in Table 3.2. The average tensile strength value reported in this table was

acquired from tests carried out in accordance with ASTM D638 (Plastic Products Inc., 2014) using plastic test specimens that were machined into a dog bone shape from plastic stock shapes or from injection molding. Approximately 34% of the tensile tests conducted using the slower displacement rate (Figure 3.12) exceeded this average tensile strength and approximately 61% of the tensile tests conducted using the faster displacement rate (Figure 3.13) exceeded the same tensile strength. The plots also show a dashed vertical line at a tensile elongation or axial strain equal to 70%, which corresponds to the elongation at break reported in Table 3.2.

Tensile strength tests typically involve the use of an extensometer to measure the axial strain of the specimen. Due to the variable shape and surface of the bottle specimens tested in this study, it was not possible to use an extensometer. The axial strain values reported in Figures 3.12 and 3.13 are average axial strains computed using the crosshead vertical displacement, which may have errors associated with machine compliance at high stress levels and the possible slippage at the grips of the plastic bottle ends. The initial, flat portion of select stress-strain curves displayed in Figures 3.12 and 3.13 indicate that some tests likely experienced grip slippage. Approximately 4% of the tensile tests carried out using the slow displacement rate (Figure 3.12) and approximately 17% of the tests performed at the faster displacement rate (Figure 3.13) exceeded the average ultimate axial strain or elongation value reported in Table 3.2. For both displacement rates, the recycled PET test specimens produced a larger percentage of specimens that exceeded the average tensile strength as compared to the percentage of test specimens that exceeded the average axial strains.

There could be a number of factors contributing to the wide range of tensile test results. First, tensile stress was based on the initial specimen cross sectional area, which was dependent upon the average measurements of the specimen bulk thickness and width. However, the specimen cross section was not a solid PET plastic material. It was a compressed bottle that is composed of two irregular plastic surfaces that lack consistency, smoothness, and are not in perfect contact. Therefore, these test specimens have a non-uniform cross section that was difficult to measure or characterize. Additionally, the reported tensile stresses do not include cross sectional area variations due to Poisson's effects or sample necking. They are more closely related to nominal tensile stresses since they do not include an area correction that reflects variations in the specimen cross section. Disregarding this effect was conservative since the actual tensile stresses would be higher if the true cross sections were utilized. The main reason for the wide range of tensile test results was likely tied to the fact that the PET bottle constituents were extracted from an actual bale, resulting in a wide range of initial material conditions, ages, deterioration levels, types, geometries. Additionally, the effects of the compression process at the MRF may also be different for each bottle based on their initial geometry, condition, and position within the baling machine.

3.5 Tensile Strength Testing Summary

Chapter 3 describes the test material, the manufacturing process and the characteristics of the bales utilized to generate test specimens in this study, and this tensile test evaluation was conducted to confirm tensile strength properties of the compressed PET bottles within an actual PET bale. The results also served to characterize the variability of the bottle types and conditions within a bale. The large amount of variance displayed in the stress-strain results was due to the variations in shape, size, compression deformities, and surface textures of the full-scale PET constituents. While it is beneficial to measure the characteristics of the bale constituents, it is more likely that the performance of an embankment outfitted with lightweight recycled PET bales would depend on the bottle-to-bottle shear strength should a failure plane intercept a PET bale.

CHAPTER 4: EVALUATION OF SHORT-TERM 1D COMPRESSION, INTERFACE DIRECT SHEAR, AND TRIAXIAL SHEAR STRENGTH TESTING ON RECYCLED PET PLASTIC

4.1 Introduction

This chapter will described the testing protocol and provide a discussion of the results acquired from three independent experimental evaluations designed to assess the properties and behaviors of recycled PET bale constituents for use in the proposed application. The three evaluations include: 1) short-term, one-dimensional (1D) compression, 2) direct shear interface testing, and 3) triaxial shear strength testing.

Short-term, 1D compression tests were conducted on recycled PET bale constituents to determine the short-term deformation characteristics of the proposed PET plastic material. A suite of 42 test specimens were examined using two test cylinder diameter sizes (22.86 cm and 45.27 cm), two initial sample unit weights (2.36 kN/m^3 and 3.93 kN/m^3), two load applications methods (continuous and segmented), and two recycled PET bale constituent particle sizes (full-bottle and chopped). The varying effects of specimen size, unit weight, load application method, and constituent size were evaluated.

The direct shear interface evaluation was conducted to assess plastic to plastic interface friction shearing against each other with two sheets of PET material (circular

with a diameter of 6.35 cm) with a modified direct shear test configuration to accommodate a plastic on plastic shear interface evaluation. Nine test specimens were examined using a 0.01 cm/sec displacement rate, three test specimen orientations/textures (flat, ribbed-aligned, and ribbed-orthogonal), and three normal stresses (50 kPa, 100 kPa, and 200 kPa). The varying effects of each specimen configuration with varying normal loads were evaluated to determine the interface frictional behavior of the recycled PET material.

The triaxial shear strength tests were conducted using chopped recycled PET plastic bottle constituents to determine the shear strength of the recycled. The 24 test specimen test matrix evaluated five unit weights (0.79 KN/m^3, 1.57 KN/m^3, 1.73 KN/m^3, 1.89 KN/m^3, and 2.36 KN/m^3), five axial displacement rates (0.02 mm/min, 0.2 mm/min, 1 mm/min, 5 mm/min, and 10 mm/min), four isotropic confining pressures (17.24 kPa, 34.47 kPa, 51.71 kPa, and 68.95 kPa), and two sample testing conditions (saturated and dry). The effects of unit weight, displacement rate, and saturation level were evaluated. This chapter is divided into three main sections to summarize the testing protocol and results for each testing protocol.

While the tensile strength tests presented in Chapter 3 and most of the short-term compression tests in this chapter were conducted using full-bottle recycled PET constituents, select short-term compression tests and all triaxial shear strength tests were conducted on test specimens prepared using chopped recycled material to meet the necessary particle size to test cylinder diameter ratio for the purpose of minimizing boundary effects and enabling particle-to-particle-interactions within the PET test specimen. However, the results from the full-bottle PET test specimens will be compared

to the results generated from chopped test specimens to document differences in behavior (if any).

4.2 Short-Term, 1D Compression Testing

1D compression tests were conducted to assess the short-term deformation characteristics of recycled PET material constituents from a recycled PET bale. In an attempt to evaluate a variety of constituents from the bale, two different configurations of 1D compression were evaluated across two unit weights. All short-term, 1D compression tests were conducted at a fixed displacement rate equal to 3.81 cm/min. There were a total of 42 tests performed; 24 test specimens were examined using a 22.86 cm diameter test cylinder and 18 specimens were examined using a 45.72 cm diameter test cylinder. The data were utilized to plot the stress-strain relationship and determine the constrained modulus (M_s) for the material, which provided the information necessary to compute the compressibility parameters, K and n. The next section describes the test material and test configuration.

4.2.1 Short-Term, 1D Test Configuration and Procedure

Chapter 3 discusses the recycled PET bale configuration, constituents, and the variability of the constituents in more detail. A random selection of PET bale constituents were utilized to capture the variations within a recycled PET bale. For the chopped test specimens, recycled Category 1 constituents (defined in Chapter 3) were reduced to 1.98 cm^2 square pieces using a commercial strength paper cutter, ensuring that each piece was exactly 2.54 cm across each diagonal. This reduction process was performed to achieve an acceptable particle size to specimen diameter ratio. Figure 4.1 displays a photograph of the chopped Category 1 material, prior to specimen preparation. Note that all bottle

tops such as they are shown in the upper left corner of this photograph were removed in all cases to create consistency within the test specimen. Additionally, any irregular deformations or surface textures of the chopped constituents were removed for consistency.

Figure 4.1: Chopped pieces of a Category 1 recycled PET bale constituent

Both 22.86 cm and a 45.72 cm diameter steel test pipe were utilized to assess the effects (if any) related to boundary conditions. Full bottle constituents were test in both cells. Chopped constituents were only tested in the larger cell. Because the steel test cylinders were not standard for those tests, a test specimen preparation and testing protocol process was developed for each test specimen type. Applied axial loading was measured in all short-term compression tests were conducted using a calibrated 445 kN Pacific compression canister load cell. The sample change of height was measured using

a Measurement Specialties string potentiometer with a full stroke range of 1270 mm. Specifications for all sensors used in the 1D compression tests are included in Appendix A.

Figures 4.2 and 4.3 display a schematic and a photograph of the 22.86 cm diameter testing apparatus, respectively. The inside diameter of the steel pipe is 22.86 cm, and the pipe has a wall thickness equal to 1.27 cm. Because the steel pipe was open at the bottom, a 5.08 cm thick steel plate was positioned underneath the steel pipe during each test to provide a stable foundation for the apparatus and too close the open end.

For the 22.86 cm diameter test configuration, the piston was hydraulically operated using a fixed displacement control rate equal to approximately 3.81 cm/min for all tests. A careful trial and error process for a pneumatic system achieved a constant displacement rate which was held constant using the hydraulic pressure panel. The string potentiometer was attached to the piston arm at a fixed location. The piston head compressed into the load cell, transferring the compressive force from the piston head into the wood cap and steel disc displayed in Figure 4.2. Subsequently, the wood cap and 2.5 cm thick steel disc slid inside the steel test cylinder. The additional cap and disc were required to ensure that the actuator had enough stroke to account for the necessary deformation of the PET material.

The recycled PET sample of compressed full bottles were initially placed loosely up to a height of 15.24 cm measured from the base. The initial stage of the test compacted in the caps until the PET sample reached the target unit weight. For the initial target weight of 2.36 kN/m^3 the loose plastic had to be compressed to a height of 15.24 cm. For an initial target weight of 3.93 kN/m^3 the sample was compressed to a height of 15.24

cm. However, the weight of the specimen was increased to approximately 70 N, as compared to 40 N for the lower unit weight, thus resulting in a higher unit weight. The load was applied using a pressure panel regulated by the air pressure in the building. The load cell and the potentiometer enabled the data acquisition unit to collect force and displacement data for each test specimen.
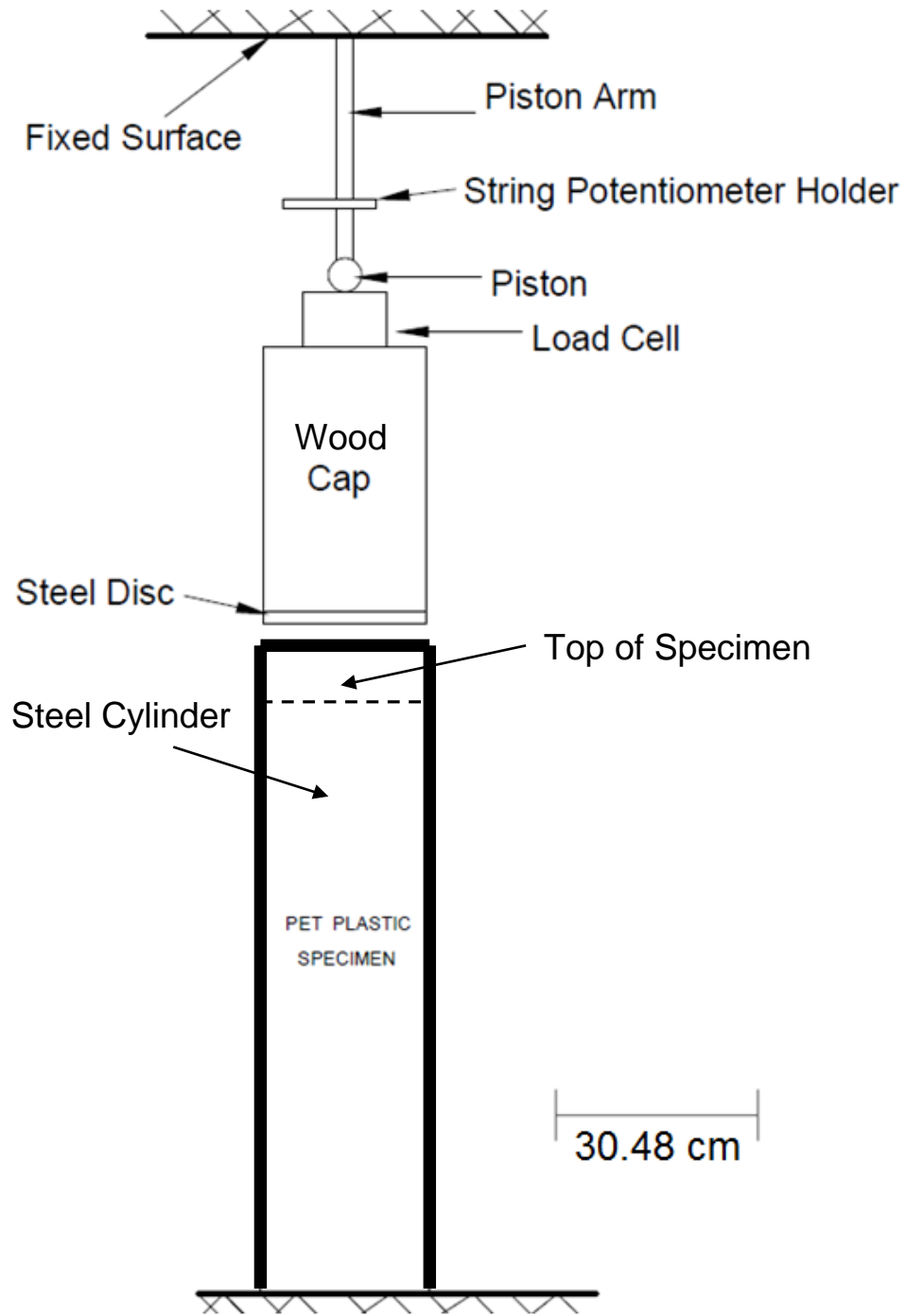
Figure 4.2: Schematic of the 22.86 cm inside diameter test configuration for the short-term, 1D compression test

Figure 4.3: Photograph of the 22.86 cm inside diameter test configuration for the short-term, 1D compression test

Figures 4.4 and 4.5 display a schematic and photograph of the 45.72 cm diameter test cylinder, respectively. The steel test cylinder had an inside diameter equal to 45.72 cm with a wall thickness equal to 2.54 cm. The string potentiometer was attached to the top of the steel cap. The hydraulic piston was applied to the load cell using a fixed displacement control rate equal to approximately 3.81 cm/min, identical to the previous configuration. The valve setting on the hydraulic piston necessary to maintain this rate was determined using an iterative process. The load cell was installed between the top of the steel cap and the load actuator, which had a 25.4 cm stroke. The two 15.24 cm thick steel caps displayed in Figure 4.4 were utilized to help the material deform uniformly. The recycled PET material did not reach the target unit weight until the steel caps were 15.24 cm from the base of the testing cylinder, which resulted in a 15.24 cm specimen height for all test specimens. The results acquired using the larger diameter cylinder (Figure 4.5) will be compared to the results acquired using the smaller cylinder (Figure 4.3) to assess boundary condition effects (if any).
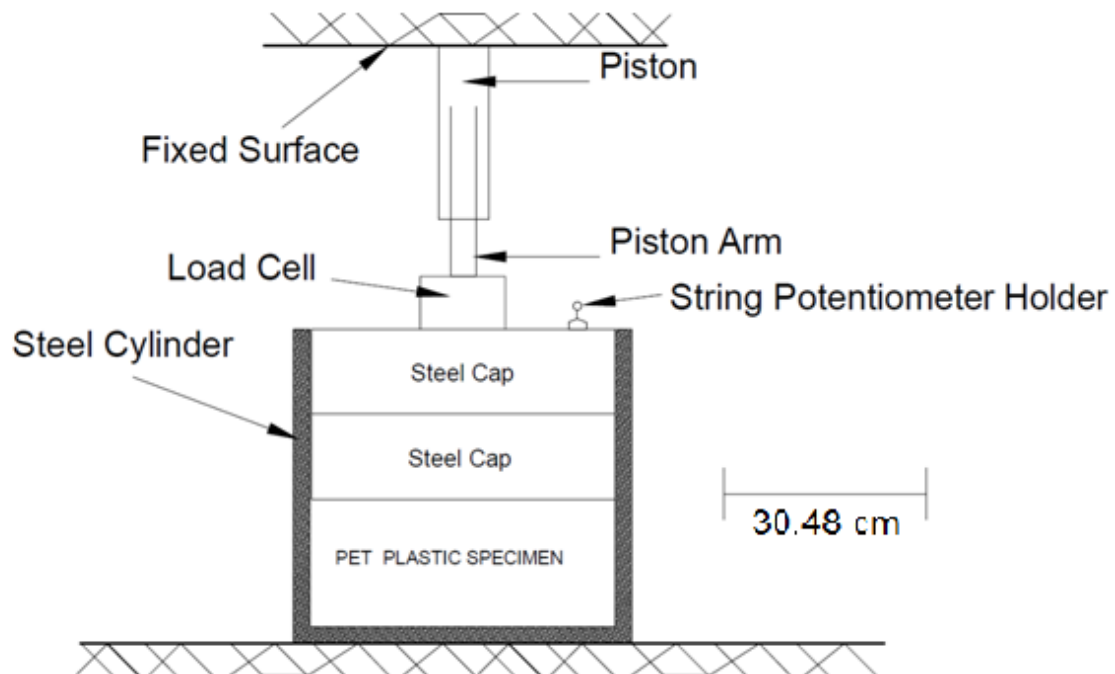
Figure 4.4: Schematic of the 45.72 cm inside diameter test configuration for the short-term, 1D compression test
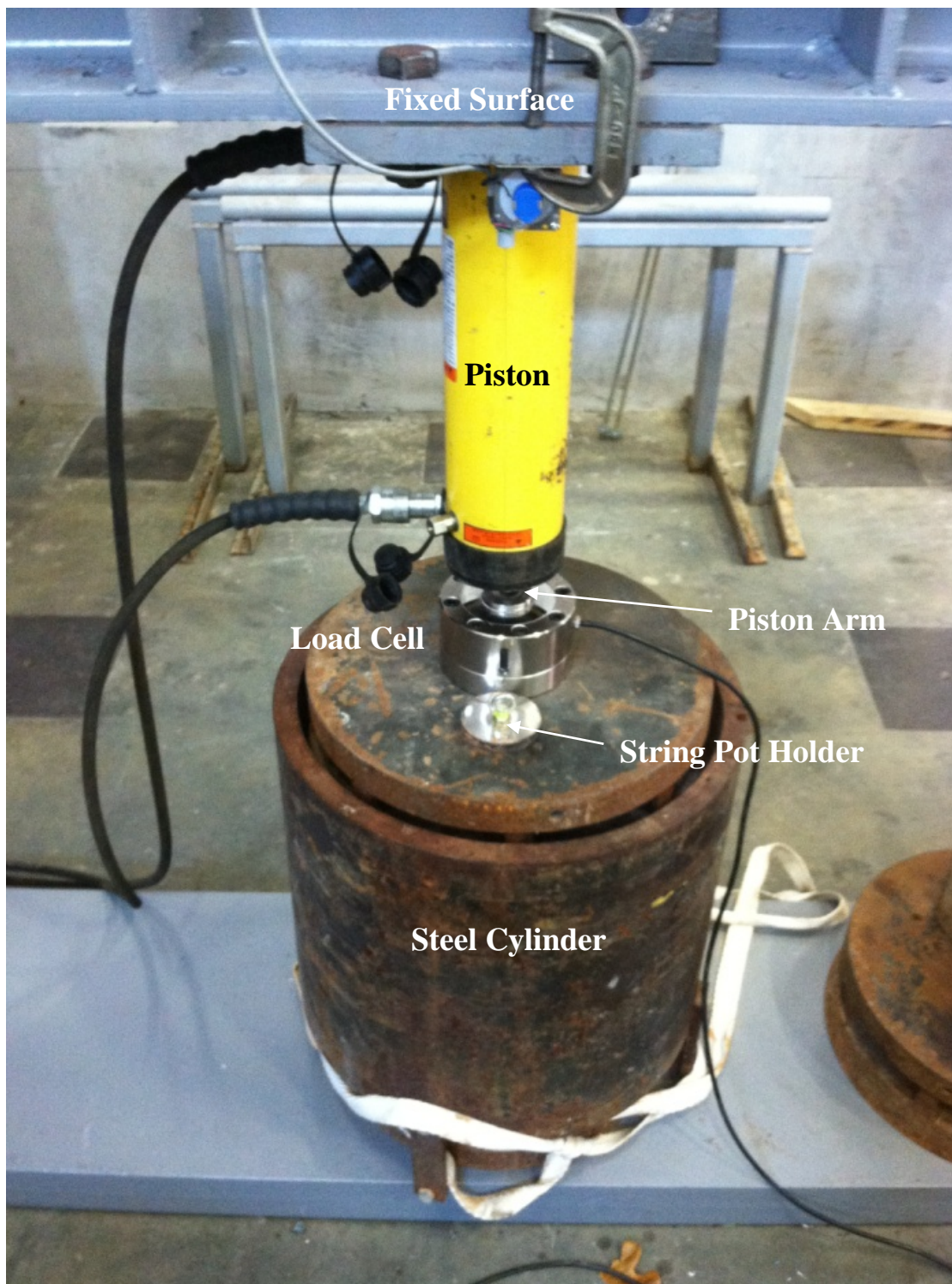
Figure 4.5: Photograph of the 45.72 cm inside diameter test configuration for the short-term, 1D compression test

Two independent load application methods were utilized to evaluate the stress-strain behaviors during each short-term 1D compression test. In the first method (referred to as M1 in subsequent tables and charts), a continuous increasing load was applied beyond the pressure threshold required to ensure the two target unit weights (2.36 kN/m^3 and 3.93 kN/m^3) to simulate an MRF bale (with unit weights ranging from 2.36 kN/m^3 to 3.93 kN/m^3). In the second method (referred to as M2 in subsequent tables and charts), a continuous load was applied until the required pressure threshold was achieved, the load was removed, and then the load was re-applied using the M1 method. In other words, the M2 method included a pre-stressing phase prior to the primary compression phase. Figure 4.6 displays the vertical loading scheme for each method as a function of elapsed time.

Two independent target unit weights (2.36 kN/m^3 and 3.93 kN/m^3) representing the minimum and maximum unit weights for a compacted PET bale at the Charlotte MRF, respectively, were examined inside the 22.86 cm diameter test cylinder and the 2.36 kN/m^3 was evaluated inside the 45.72 cm diameter test cylinder. The short-term 1D compression text matrix is provided in Table 4.1. While Tables 4.2 and 4.3 display the measured unit weights for each test using the 22.86 cm and 45.27 cm diameter test cylinders, respectively.
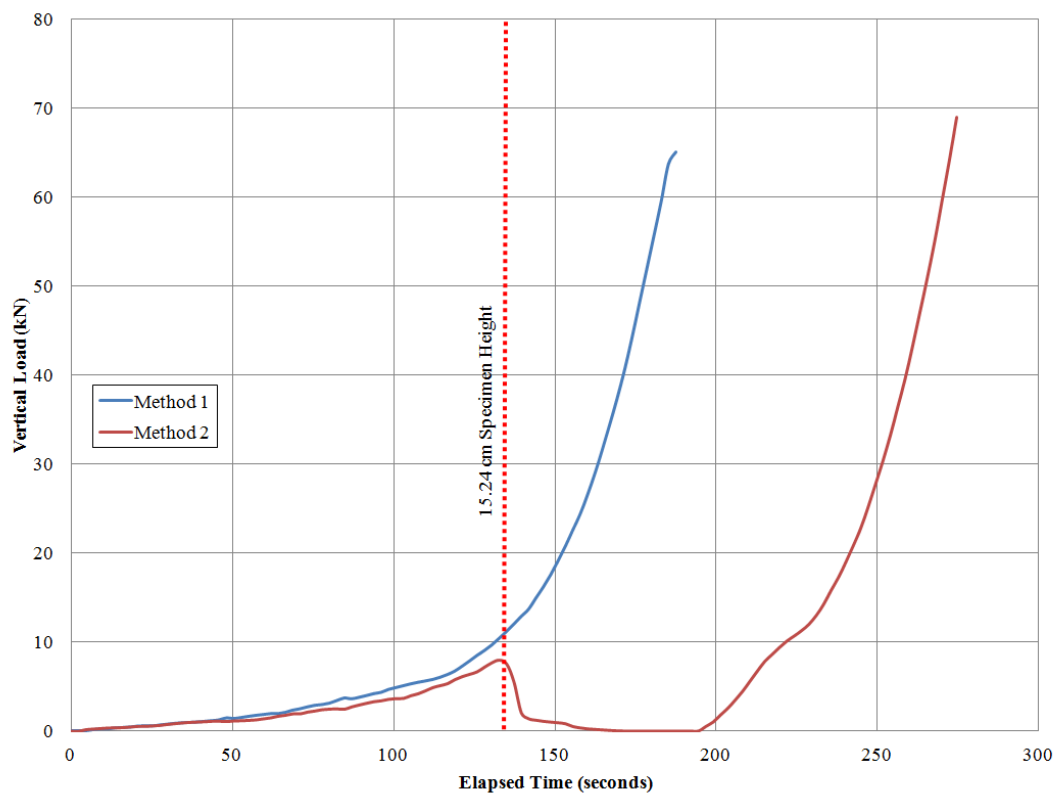
Figure 4.6: Representative vertical load as a function of elapsed time for Method 1 (M1) and Method 2 (M2) during the short-term, 1D compression tests (Test ID: C1-22-2.36-M1-F & C7-22-2.36-M2-F)

Table 4.1: Short-term, 1D compression test matrix

Test ID	Inside Diameter (cm)	Target Unit Weight (kN/m^3)	Disp. Rate (cm/min)	Load Method	No. [3] Specimens	PET Sample Size
C1-22-2.36-M1-F through C6-22-2.36-M1-F	22.86	2.36[(1)]	3.79	M1	6	Full-Bottle
C7-22-2.36-M2-F through C12-22-2.36-M2-F			3.80	M2	6	Full-Bottle
C13-22-3.93-M1-F through C18-22-3.93-M1-F		3.93[(2)]	3.81	M1	6	Full-Bottle
C19-22-3.93-M2-F through C24-22-3.93-M2-F			3.83	M2	6	Full-Bottle
C25-45-2.36-M1-F through C30-45-2.36-M1-F	45.27	2.36[(1)]	3.81	M1	6	Full-Bottle
C31-45-2.36-M2-F through C36-45-2.36-M2-F			3.82	M2	6	Full-Bottle
C37-45-2.36-M1-C through C42-45-2.36-M1-C			3.80	M1	6	Chopped

[1]Weight = approx. 40 N
[2] Weight = approx. 70 N
[3] Specimen height = 15.24 cm

Table 4.2: Unit weight measurements for all 22.86 cm test specimens (short-term, 1D compression tests)

Test ID	Target Unit Weight (kN/m^3)	Measured Unit Weight (kN/m^3)	Average Unit Weight (kN/m^3)
C1-22-2.36-M1-F	2.36	2.38	2.35
C2-22-2.36-M1-F		2.33	
C3-22-2.36-M1-F		2.36	
C4-22-2.36-M1-F		2.37	
C5-22-2.36-M1-F		2.36	
C6-22-2.36-M1-F		2.35	
C7-22-2.36-M2-F	2.36	2.35	2.36
C8-22-2.36-M2-F		2.36	
C9-22-2.36-M2-F		2.38	
C10-22-2.36-M2-F		2.37	
C11-22-2.36-M2-F		2.34	
C12-22-2.36-M2-F		2.35	
C13-22-3.93-M1-F	3.93	3.95	3.94
C14-22-3.93-M1-F		3.93	
C15-22-3.93-M1-F		3.95	
C16-22-3.93-M1-F		3.94	
C17-22-3.93-M1-F		3.91	
C18-22-3.93-M1-F		3.93	
C19-22-3.93-M2-F	3.93	3.90	3.93
C20-22-3.93-M2-F		3.94	
C21-22-3.93-M2-F		3.93	
C22-22-3.93-M2-F		3.95	
C23-22-3.93-M2-F		3.92	
C24-22-3.93-M2-F		3.94	

Table 4.3: Unit weight measurements for all 45.27 cm test specimens (short-term, 1D compression tests)

Test ID	Target Unit Weight (kN/m^3)	Measured Unit Weight (kN/m^3)	Average Unit Weight (kN/m^3)
C25-45-2.36-M1-F		2.38	
C26-45-2.36-M1-F		2.34	
C27-45-2.36-M1-F	2.36	2.34	2.36
C28-45-2.36-M1-F		2.34	
C29-45-2.36-M1-F		2.36	
C30-45-2.36-M1-F		2.38	
C31-45-2.36-M2-F		2.37	
C32-45-2.36-M2-F		2.34	
C33-45-2.36-M2-F	2.36	2.36	2.35
C34-45-2.36-M2-F		2.36	
C35-45-2.36-M2-F		2.37	
C36-45-2.36-M2-F		2.34	
C37-45-2.36-M1-C		2.38	
C38-45-2.36-M1-C		2.35	
C39-45-2.36-M1-C	2.36	2.34	2.36
C40-45-2.36-M1-C		2.38	
C41-45-2.36-M1-C		2.36	
C42-45-2.36-M1-C		2.37	

The necessary weight of the randomly selected recycled PET plastic constituents required to achieve the target unit weight was poured into the test cylinder before the cylinder caps were placed on top of the material. Figures 4.7 and 4.8 display photographs of the full-bottle constituents inside the 22.86 cm and 45.75 cm test cylinders, respectively. Prior to testing, the orientation of the extension and cap were checked to make sure they were orthogonal to the testing cylinder to ensure uniform compression. The pipe threads at the top of the cylinder displayed in Figure 4.7 did not interfere with the tests.

Figure 4.7: Photograph of the 22.86 cm diameter testing cylinder prior to 1D compression
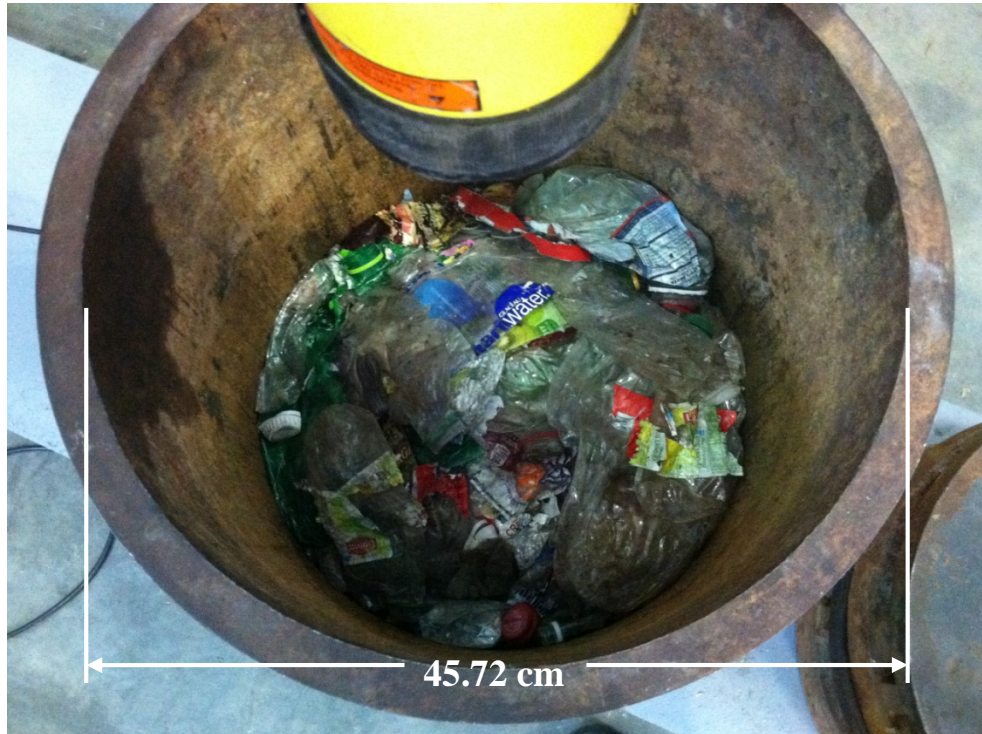
45.72 cm

Figure 4.8: Photograph of the 45.72 cm diameter testing cylinder prior to 1D compression

4.2.2 Short-Term, 1D Compression Results and Discussion

A total of 42 recycled PET bale test specimens were tested using a fixed displacement control rate equal to approximately 3.81 cm/min to evaluate short-term, 1D compressive behaviors (see Table 4.1). For the smaller 22.86 cm diameter test cylinder, two different load application procedures (M1 and M2) were evaluated using the minimum and maximum MRF bale unit weights, each test was conducted using full-bottle constituents, and 6 repetitions of each test were conducted for a total of 24 tests. For the 45.72 cm diameter cylinder, both load application procedures (M1 and M2) were evaluated using only the minimum unit weight value (2.36 kN/m^3) , using the full-bottle and chopped constituents, and 6 repetitions of each were completed for a total of 12 tests.

The M1 procedure was then repeated 6 times using the lower unit weight with the chopped pieces to determine the impact of 'particle size'.

As shown in Table 4.1, a total of 42 short-term 1D compression tests were conducted. The initial length of each test specimen was recorded, and the force-displacement data collected using the load cell and string potentiometer that were converted to the data acquisition unit.

The axial strain of the test specimen was calculated using the sample change of height as follows:

$$\varepsilon = \Delta H \, / \, H_o * 100 \qquad\qquad\qquad [4.1]$$

Where:

      ε = Axial strain (%)
      ΔH = Change in specimen height (cm)
      H_o = Initial specimen height (cm)

The applied compressive stress was computed using the recorded applied compressive force and the specimen's cross-sectional area as follows:

$$\sigma = F/A \qquad\qquad\qquad [4.2]$$

Where:

      σ_c = Compressive stress (MPa)
      F = Compressive force (MN)
      A = Contact area (m^2)

The compression constrained modulus (M_s) is used to describe the compressibility of a material under 1D compression. The constrained modulus computed using Equation 4.3 represents the slope of a secant line on the stress-strain curve. Since the compression curves are non-linear, the constrained modulus is a function of the stress values selected to compute the change in compressive stress. Typically the higher stresses yields higher constrained moduli. Figure 4.9 displays a schematic of the constrained modulus relationships with the stress-strain curve. Using the stress-strain curve the constrained secant modulus was calculated as follows:

$$M_s = \Delta\sigma \, / \, \Delta\varepsilon \tag{4.3}$$

Where:
   M_s = Constrained secant modulus increment from σ_o to σ_n (kPa)
   $\Delta\sigma$ = Change in compressive stress (kPa)
   $\Delta\varepsilon$ = Change in axial strain from stress increment from σ_o to σ_n
   σ_o = Seating load normal stress = 10 kPa (constant for all tests)
   σ_n = Applied vertical normal stress = 120 kPa (constant for all tests)
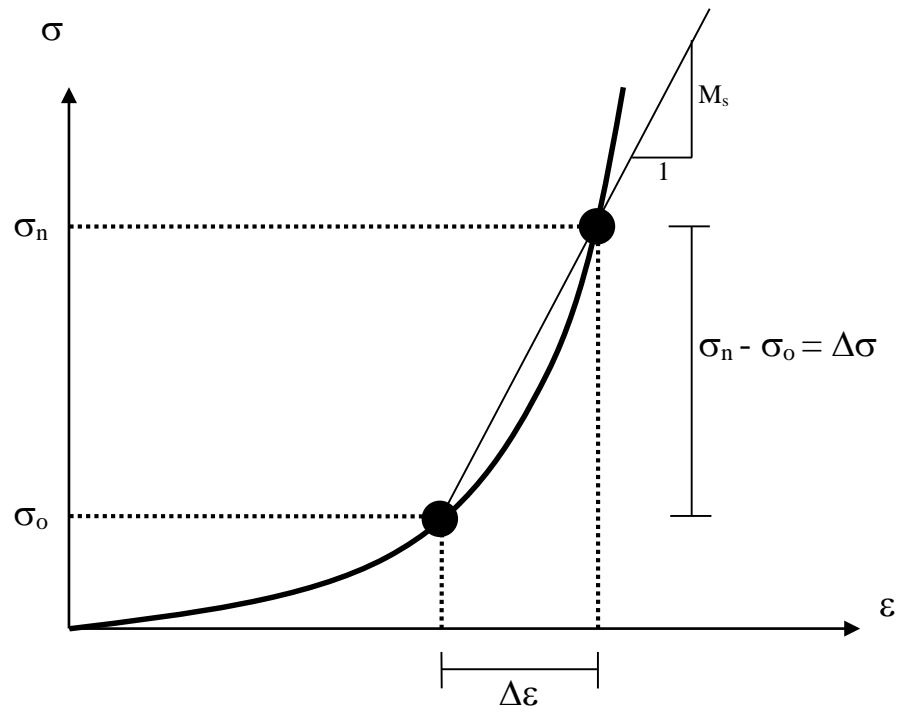
Figure 4.9: Schematic 1D compression stress-strain curve and the definition of the constrained secant modulus

4.2.2.1 Influence of Test Method (M1 versus M2)

To illustrate possible differences associated with the loading schemes (M1 and M2), Figures 4.10(a) and 4.10(b) display the stress-strain relationships for the 22.86 cm inside diameter test specimens loaded using both M1 and M2 methods for the specimens prepared using unit weights equal to 2.36 kN/m^3 and 3.93 kN/m^3, respectively. Recall that the M1 load application procedure (designated by the solid blue curves in Figure 4.10) involved a continuous increase in pressure while the M2 load application procedure (designated by the red dashed curves in Figure 4.10) involved loading the bale constituents to the target unit weight, releasing the load, and then reapplying it. All 12 specimens in Figure 4.10(a) were tested until a maximum axial strain of approximately 62% to 71% was reached. In Figure 4.10(b), the 3.93 kN/m^3 unit weight test specimens reached a maximum strain at approximately 35% - 53%. Recall that each test specimen contained a random variation of PET bale constituents installed in random orientations, which could account for the variations in measured stress-strain relationships. There does not appear to be a significant difference in the trends exhibited between the two different loading methods (M1 and M2) in either Figure 4.10(a) and 4.10(b), respectively. Using the predetermined stress values for the seating load normal stress and applied vertical stress, reported from Tatlisoz et al. (1997), the average constrained moduli for loading Methods 1 and 2 for a unit weight of 2.36 kN/m^3 were calculated as 449 kPa and 537 kPa, respectively. While the average constrained moduli for the unit weight of 3.93 kN/m^3 for loading Methods 1 and 2 for a unit weight of 2.36 kN/m^3 were calculated as 1158 kPa and 1048 kPa, respectively.
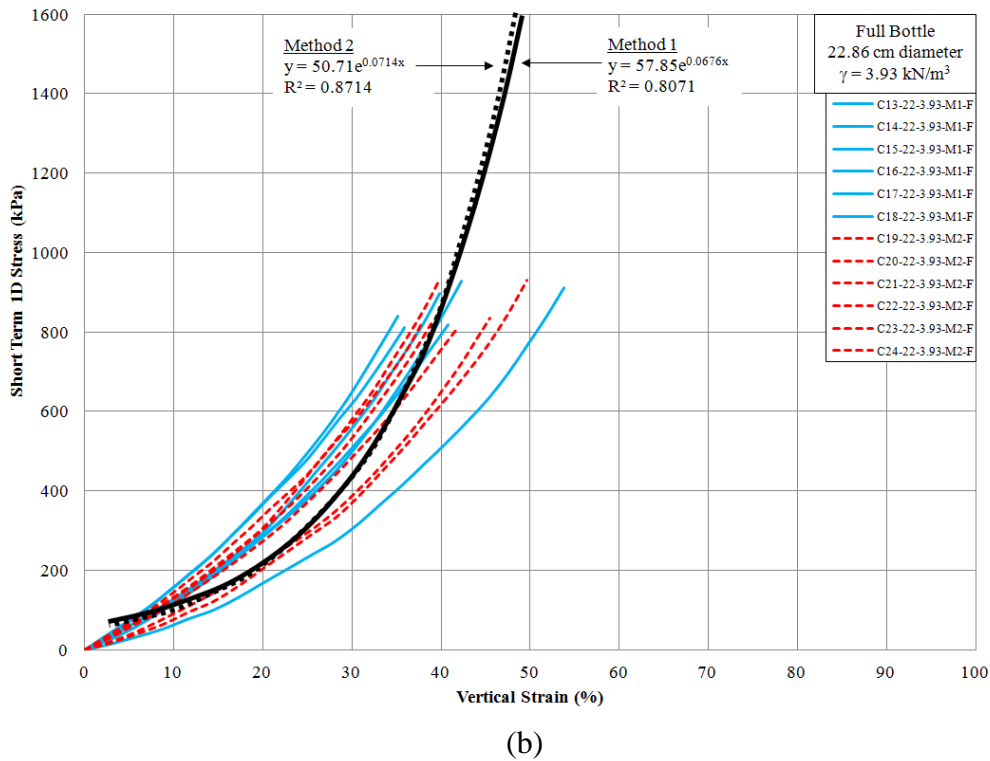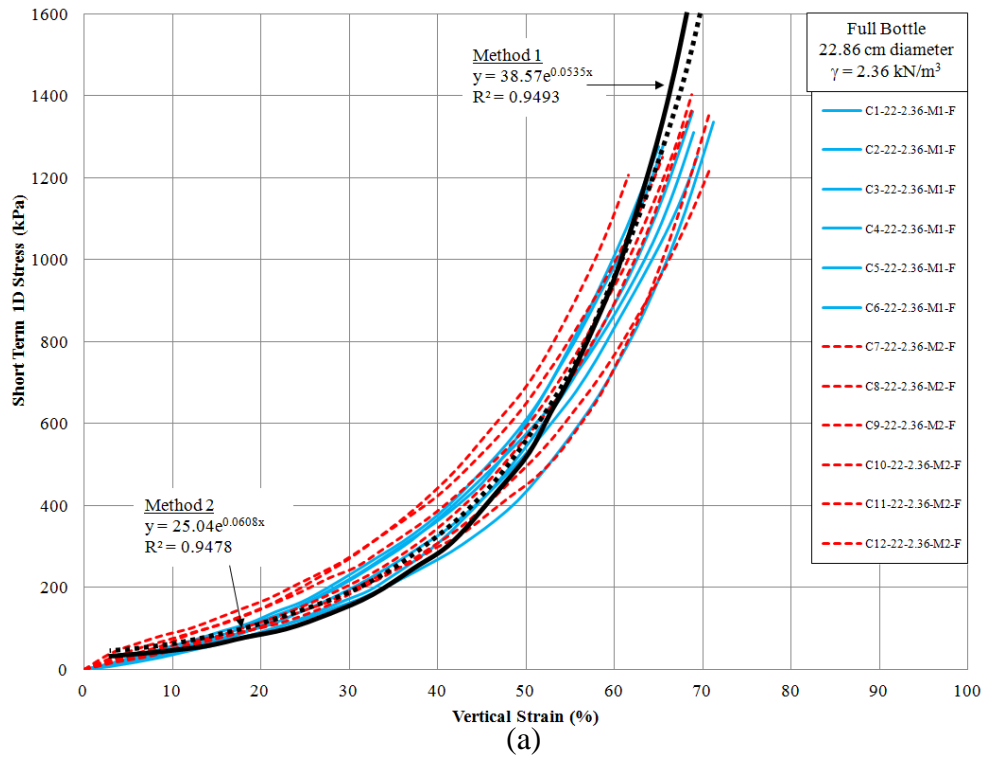
Figure 4.10: Comparison of the loading schemes (M1 and M2) using the full bottle, short-term, 1D compression stress-strain results from the 22.86 cm diameter test cylinder: (a) 2.36 kN/m^3 target unit weight; and (b) 3.93 kN/m^3 target unit weight

The regression lines shown in Figure 4.10 are exponential and the best fit equations are summarized in Table 4.4.

Table 4.4: Summary of exponential regression of 1D compression test for M1 and M2 loading schemes

Figure Number	Unit Weight (kN/m^3)	Equation of Exponential Regression	Coefficient of Correlation (R^2)
10(a)	2.36	$\sigma = 38.57e^{0.0535\varepsilon}$	0.9493
10(a)	2.36	$\sigma = 25.04e^{0.0608\varepsilon}$	0.9478
10(b)	3.93	$\sigma = 57.85e^{0.0676\varepsilon}$	0.8071
10(b)	3.93	$\sigma = 50.71e^{0.0714\varepsilon}$	0.8714

σ = Compressive stress (kPa)
ε = Axial strain (%)

4.2.2.2 Influence of Test Specimen Diameter (22.86 cm versus 45.72 cm)

To illustrate possible effects associated with a difference in test specimen diameter, Figure 4.11 illustrates the stress-strain relationships for the 22.86 cm and 45.72 cm diameter, full-bottle, 2.36 kN/m^3 unit weight test specimens, prepared using the M1 loading scheme. The test specimens prepared inside the 22.86 cm diameter cylinder are designated by the solid purple curves while the test specimens prepared inside the 45.72 cm diameter cylinder are designated by the dashed green curves on Figure 4.11. All 12 test specimens reached maximum axial strains ranging from 62% to 71%. While the larger test cylinder encompasses a wider range of results in Figure 4.11, it is hypothesized that the wider variance in the test results for the larger test specimens are associated with the increased variability in the test specimen due to the increase in test material needed to generate those test specimens. The variability of the full-scale PET constituents (discussed in Section 3.2.2) added an increased level of variance to the results acquired using the larger test specimen diameter. In other words, more material incorporates more variability. Using the predetermined stress values for the seating load normal stress and applied vertical stress, reported from Tatlisoz et al. (1997), the average constrained moduli for test specimen diameter of 22.86 cm and 45.72 cm were calculated as 611 kPa and 512 kPa, respectively.
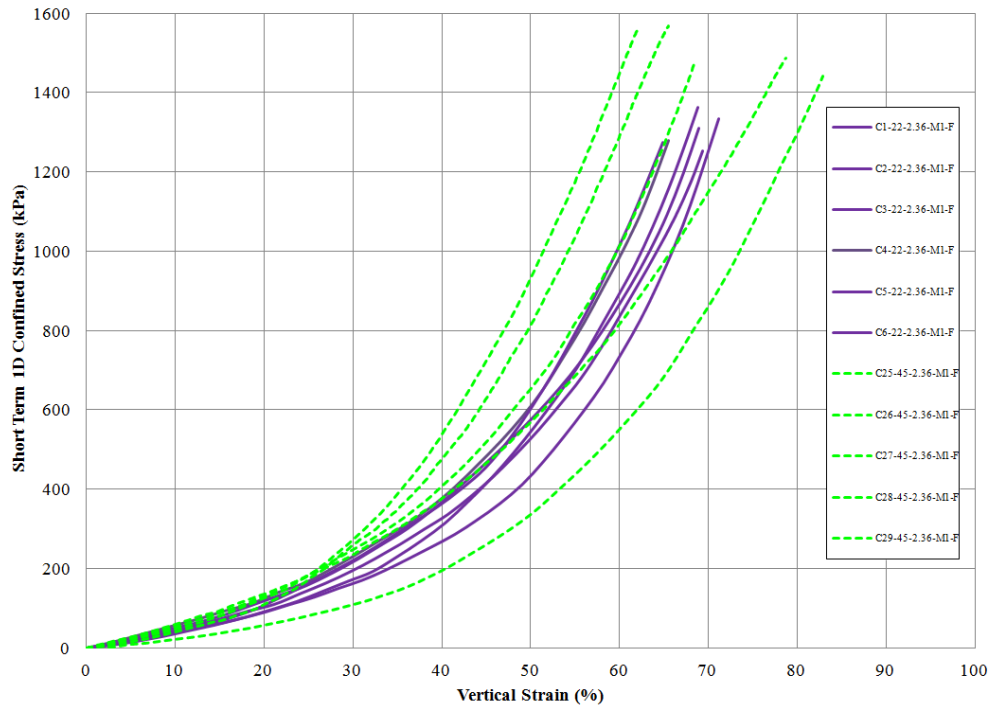
Figure 4.11: Comparison of test specimen size using the full bottle, short-term, 1D compression stress-strain results for test specimens prepared at a 2.36 kN/m^3 target unit weight for 22.86 cm and 45.72 cm diameters, loaded using the M1 loading procedure

4.2.2.3 Influence of Specimen Constituents (Full-bottle versus Chopped)

To illustrate possible effects associated with particle size and shape, Figure 4.12 illustrates the stress-strain relationships for the full-bottle and chopped test specimens prepared in the 45.72 cm diameter test cylinders at a 2.36 kN/m^3 target unit weight, loaded using the M1 procedure. The full-bottle constituents are represented by the solid blue curves while the chopped constituents are represented by the dashed yellow curves. All 12 test specimens reached a maximum strain at ranges between 62% and 82%. While the full-bottle test specimens encompass a slightly wider range of results in comparison to the chopped test specimen, the trends appear to be relatively consistent. The full-bottle constituents introduced more variability into the results due to their variations in size, shape, and the roughness of each constituent with the test specimens in comparison to the consistency created by chopping the constituents into square pieces that are all relatively the same size and similar in texture. Using the predetermined stress values for the seating load normal stress and applied vertical stress reported from Tatlisoz et al. (1997), the average constrained moduli for test specimen constituents of full-bottle and chopped were calculated as 531 kPa and 495 kPa, respectively.
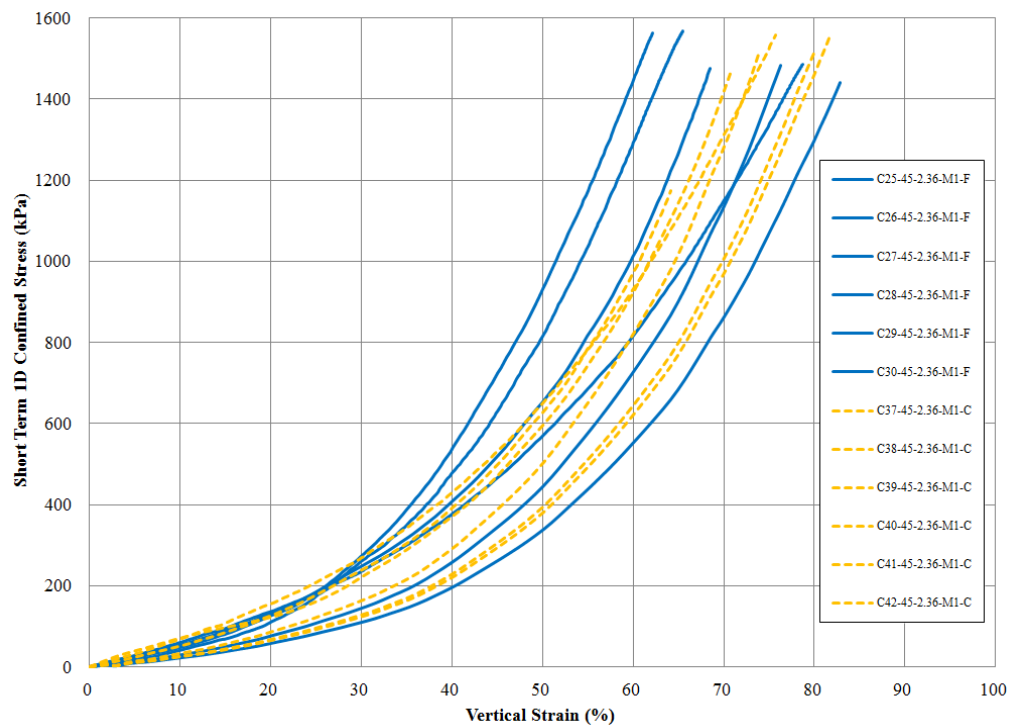
Figure 4.12: Comparison of particle size/shape (full bottle versus chopped) using short-term, 1D compression stress-strain results for full-bottle and chopped particle test specimens prepared in the 45.72 cm diameter test cylinder at a 2.36 kN/m^3 target unit weight, loaded using the M1 loading procedure

4.2.2.4 Influence of Unit Weight (2.36 kN/m^3 versus 3.93 kN/m^3)

To illustrate the differences associated with unit weight, Figure 4.13 displays the stress-strain relationships for the test specimens prepared in the 22.86 cm diameter test cylinder using the M1 loading procedure for both target unit weights (2.36 kN/m^3 and 3.93 kN/m^3). The test specimens associated with the lower 2.36 kN/m^3 unit weight are displayed with solid yellow lines while the data from the test specimens prepared at the 3.89 kN/m^3 target unit weight are displayed using dashed green lines. All 12 test specimens reached a maximum strain at approximately 35% - 72% under the applied load. With the exception of one test, the data separated into distinct groups for each unit weight. Using the predetermined stress values for the seating load normal stress (σ_o = 10 kPa) and applied vertical stress (σ_a = 120 kPa) similar to those selected and reported by Tatlisoz et al. (1997), the average constrained moduli for unit weights equal to 2.36 kN/m^3 and 3.93 kN/m^3 were approximately 539 kPa and 1,222 kPa, respectively.
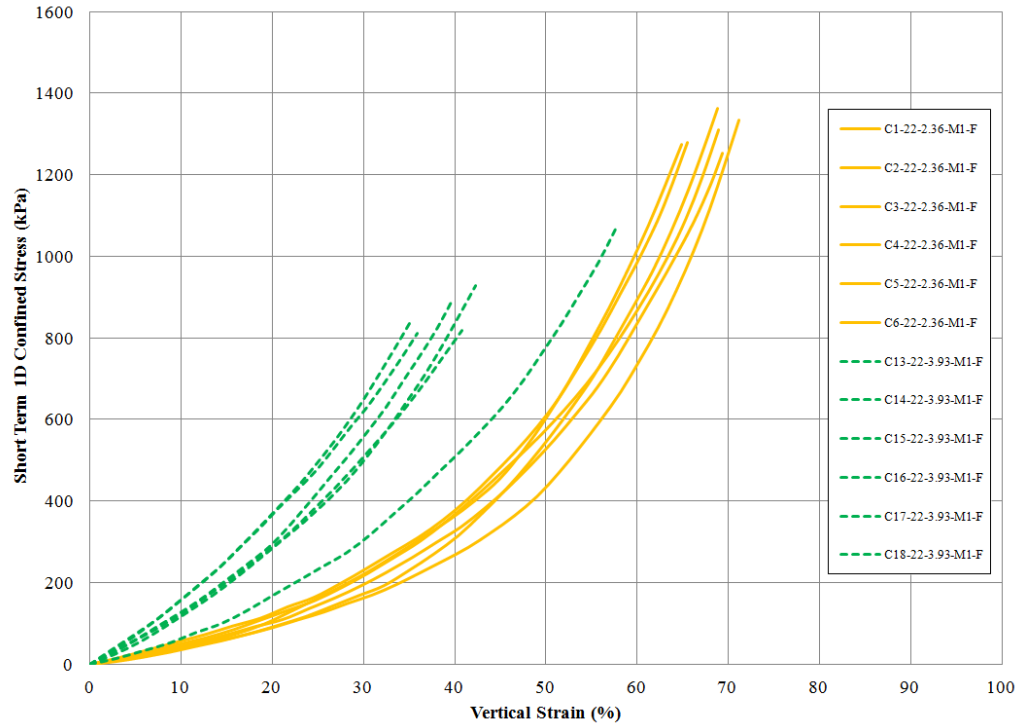
Figure 4.13: Comparison of unit weight using short-term, 1D compression stress-strain results from full-bottle test specimens prepared in the 22.86 cm diameter test cylinder, loaded using the M1 procedure

4.2.3 Short-term, 1D Compression Testing Summary

The deformation characteristics of full-bottle and chopped recycled PET bale constituents were examined using a short-term, 1D compression test configuration. Two independent test specimen sizes were evaluated using two different loading methods to determine the short-term, stress-strain behavior and constrained material modulus of the PET bale material. All tests specimens were prepared using a consistent process as described in this chapter. The figures in this attempt to illustrate possible effects associated with 1) load application procedure (M1 versus M2), 2) test specimen diameter (22.86 cm versus 45.72 cm), 3) particle size/shape (full-bottle versus chopped), and 4) the effect of the target unit weight (2.36 kN/m^3 and 3.93 kN/m^3).

Based on the results displayed in Figures 4.10, the different load application method did not appear to have a noticeable influence in the results. Regarding specimen diameter, there was more variability in the data acquired from the larger 45.72 cm diameter test specimens relative to the smaller diameter test specimens. It is assumed that an increase in volume of the randomly selected, full-bottle constituents also increased the variability in the compression results. According to data presented in Figure 4.12, data collected from test specimens prepared using chopped Category 1 constituents displayed less variance in comparison to the data collected from full-bottle test specimens. It is important to note that the full-bottle constituents were randomly selected from all three Categories of PET plastics and contained a high degree of variability in size, shape, and texture while chopped test specimens were generated using PET Category 1 constituents only. Additionally, the data from the larger 3.93 kN/m^3 target

unit weight test specimens displayed in Figure 4.13 produced stiffer results in comparison to the lower 2.36 kN/m^3 target unit weight test specimens.

Table 4.5 displays the constrained moduli for soils as reported by Tatlisoz et al. (1997) for comparison with the constrained moduli calculated as part of this study. Constrained moduli determined during this study ranged from 495 kPa to 1222 kPa. The higher values (1222 kPa) were associated with test specimens that had the largest unit weight (3.93 kN/m^3) while the lower constrained moduli (495 kPa) were associated with Group 1 chopped test specimens. Constrained moduli for recycled PET material is at least 10 times less than that of soils, four times less than EPS Geofoam, but was comparable to compacted tire shreds and chips.

Table 4.5: Summary of constrained moduli for soils, EPS Geofoam, TDA, and recycled PET

Performed Study	Material Type & Influence Factor	Constrained Modulus [4] (kPa)
Tatlisoz et al. (1997)	Compacted Sand (SP)	100,000
	Compacted Sandy Silt (ML)	16,000
	Compacted Clay (CL)	10,000
Negussesy and Jahanandish (1993)	EPS Geofoam	4,000
Strenk et al. (2007)	Compacted Tire Chips (12-50mm)	253 - 485
	Compacted Tire Shreds (50-305 mm)	130 - 373
Garbini (Current Study)	Loading Scheme M1[1,5]	1158 (Fig. 10a)
	Loading Scheme M2[2,5]	1048 (Fig. 10b)
	22.86 cm test specimen[1,5]	611 (Fig. 11)
	45.72 cm test specimen[1,5]	512 (Fig. 11)
	Full-bottle constituent[5]	531 (Fig. 12)
	Chopped constituent[5]	495 (Fig. 12)
	Unit weight of 2.36 kN/m^3 [3,5]	539 (Fig. 13)
	Unit weight of 3.93 kN/m^3 [3,5]	1222 (Fig. 13)

Notes: [1] Unit weight of 2.36 kN/m^3

         [2] Unit weight of 3.93 kN/m^3

         [3] Test specimen diameter of 22.86 cm

         [4] Computed for seating load $\sigma_o = 10$ kPa and applied load $\sigma_a = 120$ kPa.

         [5] PET plastic bale constituents

4.3 Interface Direct Shear Behaviors of Recycled PET Plastic

A modified direct shear testing device was utilized to carry out interface shear test to assess the interface friction and shear behavior of the PET bale, plastic to plastic. To evaluate a variety of constituents from the bale, three different recycled PET bale test specimen textures were identified and evaluated. The three textures identified were: 1) flat on flat, 2) ribbed on ribbed with ribs aligned to each other, and 3) ribbed on ribbed with ribs orthogonal to each other. Interface shear tests were conducted at a constant displacement rate of 0.01 cm/sec using three normal stress levels of: 50 kPa, 100 kPa, and 200 kPa. Each of the three defined interface texture conditions were evaluated at each of the three normal stress levels, resulting in a total of nine tests performed. The interface behavior was carried out in general accordance to ASTM D5321 (2015) using a modified direct shear apparatus. This section provides a description of the test set-up and procedure followed by a presentation and discussion of the test results.

4.3.1 Interface Direct Shear Test Configuration and Procedure

Photographs of the front and side of the modified direct shear machine and data acquisition unit are shown in Figures 4.14(a) and 4.14(b). Figures 4.15 (a) and 4.15(b) show the vertical and horizontal load cells, respectively. The modified direct shear machine had a maximum horizontal displacement equal to 10 mm.

(a)   (b)
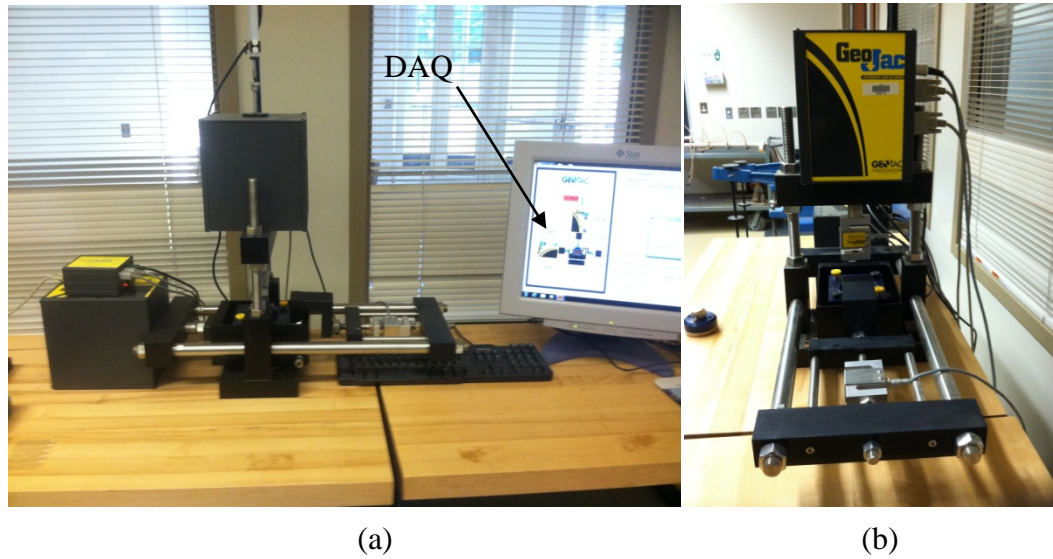
Figure 4.14: Geotac direct shear apparatus: (a) front-view; and (b) side-view

(a)   (b)
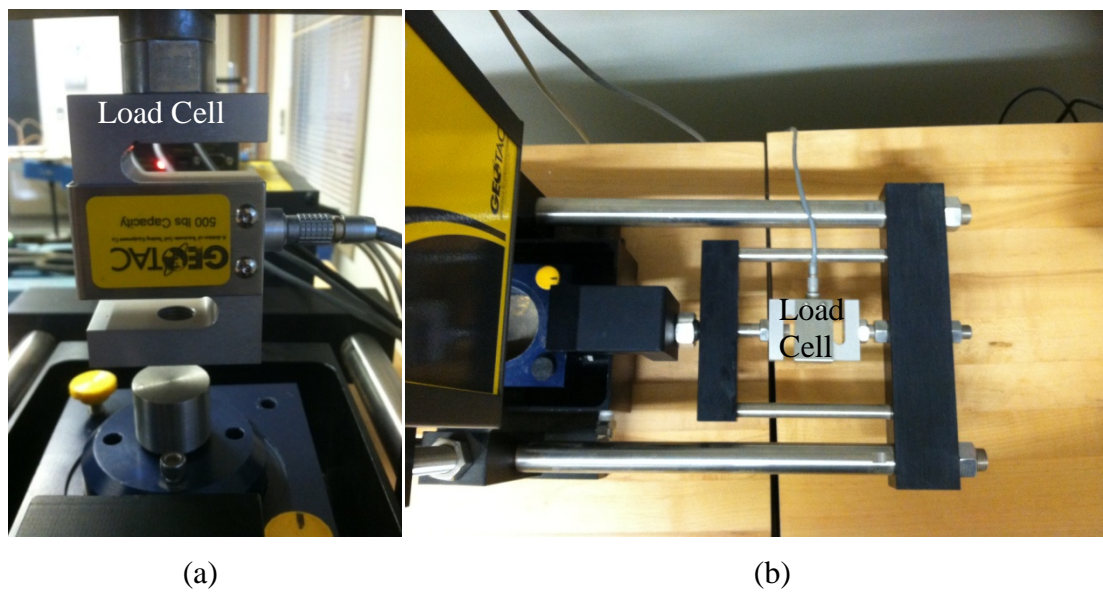
Figure 4.15: Geotac load cells: (a) vertical; and (b) horizontal

The front and side of the direct shear box are shown in Figures 4.16 (a) and 4.16(b), respectively. The gap screws allow the user to create a gap between the top and bottom portions of the cell to prevent contact between the top and bottom of the shear box during the test. A gap was set at 1 mm to ensure the plastic to plastic interface. The

load head, labeled in Figure 4.22(a) and Figure 4.22(b), sits on top of the test material, and provides a platform for the ball bearing to apply the normal load. The load head also helps distribute the normal load across the top of the test specimen.
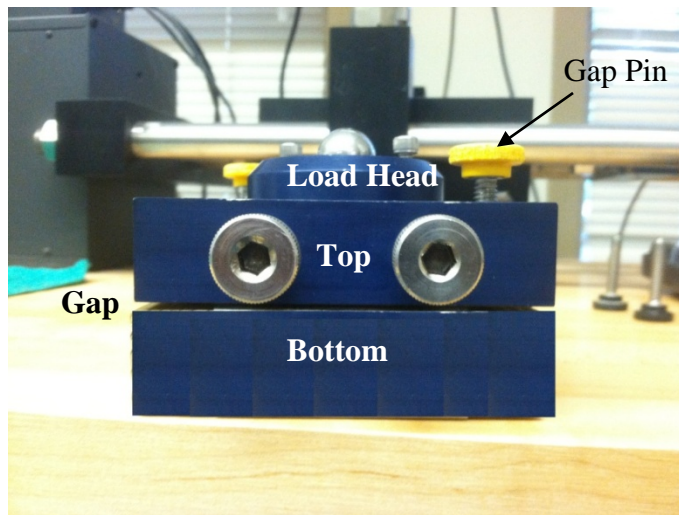
(a)

(b)

Figure 4.16: Geotac direct shear test box: (a) front-view; and (b) side-view

The shear box described above sits inside a bottom box assembly which is shown in Figure 4.17. The four raised portions inside this bottom box help keep the lower half of the shear box locked in place.
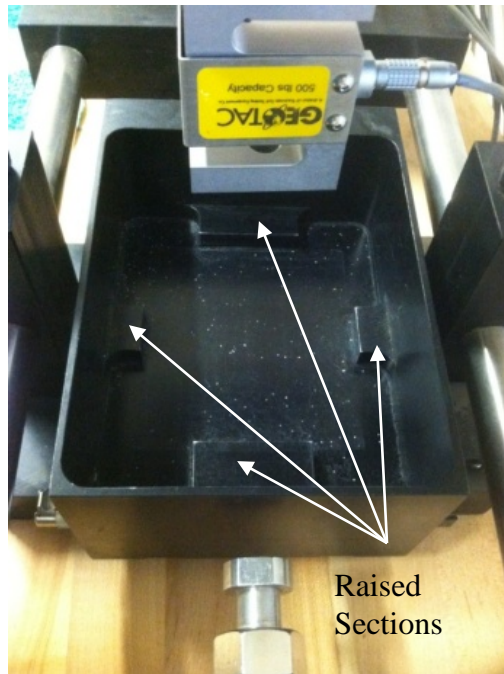
Figure 4.17: Direct shear base assembly without the base plate and test box

Representative PET bale test constituents were retrieved from a recycled PET bale. Figure 4.18(a) displays a photograph of a recycled PET constituent that would be considered relatively flat. To enhance flatness of these types of specimens, a 0.22 kN weight was placed on top of the extracted pieces for a two day period to flatten any potential curvatures and/or irregularities. The samples were in the 6.35 cm wide by 20 cm long. Figure 4.18(b) displays a photograph of a recycled PET constituent that would be utilized for either the ribbed-orthogonal and/or the ribbed-aligned textures. Both the front and/or back of the bottle could be utilized to trim test specimens for this test using the same dimensions. This identification and trimming process was repeated to extract six flat, nine ribbed-aligned, and three ribbed-orthogonal pieces for a total of 18 pieces to generate nine plastic-to-plastic test specimens. Table 4.6 summarizes the test program based on the top and bottom textures in each of the nine test specimens.

(a)   (b)
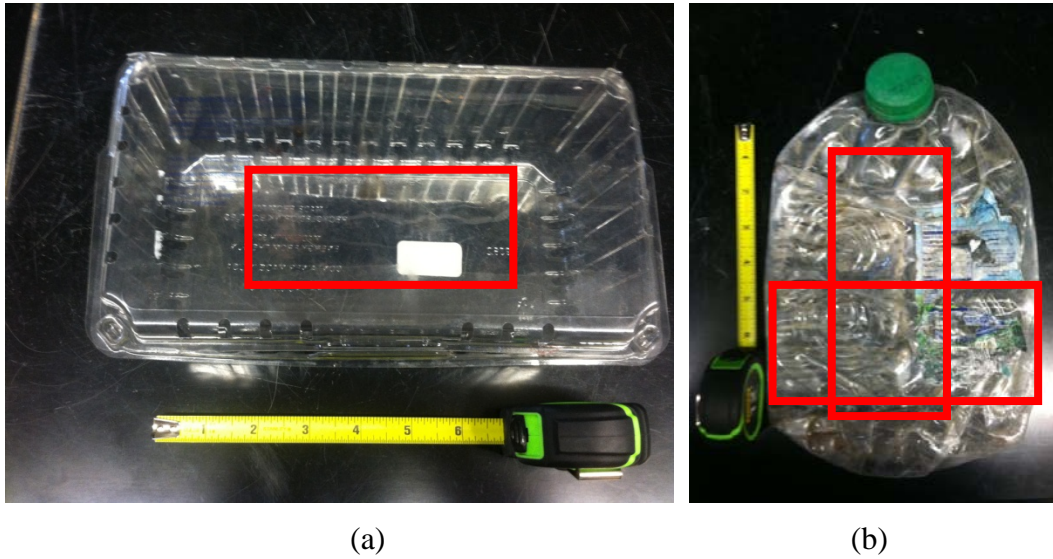
Figure 4.18: PET bale constituents utilized for the direct shear tests: (a) flat; and (b) ribbed-aligned and ribbed orthogonal

Table 4.6: Summary of interface test program bottle texture configurations

Configuration	Top Texture (No. of Pieces)	Bottom Texture (No. of Pieces)	No. of Specimens
Flat	Flat (3)	Flat (3)	3
Ribbed-Aligned	Ribbed-Aligned (3)	Ribbed-Aligned (3)	3
Ribbed Orthogonal	Ribbed-Aligned (3)	Ribbed-Orthogonal (3)	3

The modified direct shear apparatus used a wood block that fit tightly in the bottom of the direct shear box between the raised nubs displayed in Figure 4.19. The wood block was used as a platform for the bottom piece of the plastic specimen. This wood block replaced the bottom half of the normal direct shear test box. Figure 4.19 shows the wood block installed in the base of the direct shear assembly with (a) flat PET plastic piece, (b) ribbed-aligned PET plastic piece, and (c) ribbed-orthogonal piece on top of the block. The black lines shown in these photographs are added to improve clarity and highlight location of specimen edges and ribs, if any.

(a)   (b)

(c)
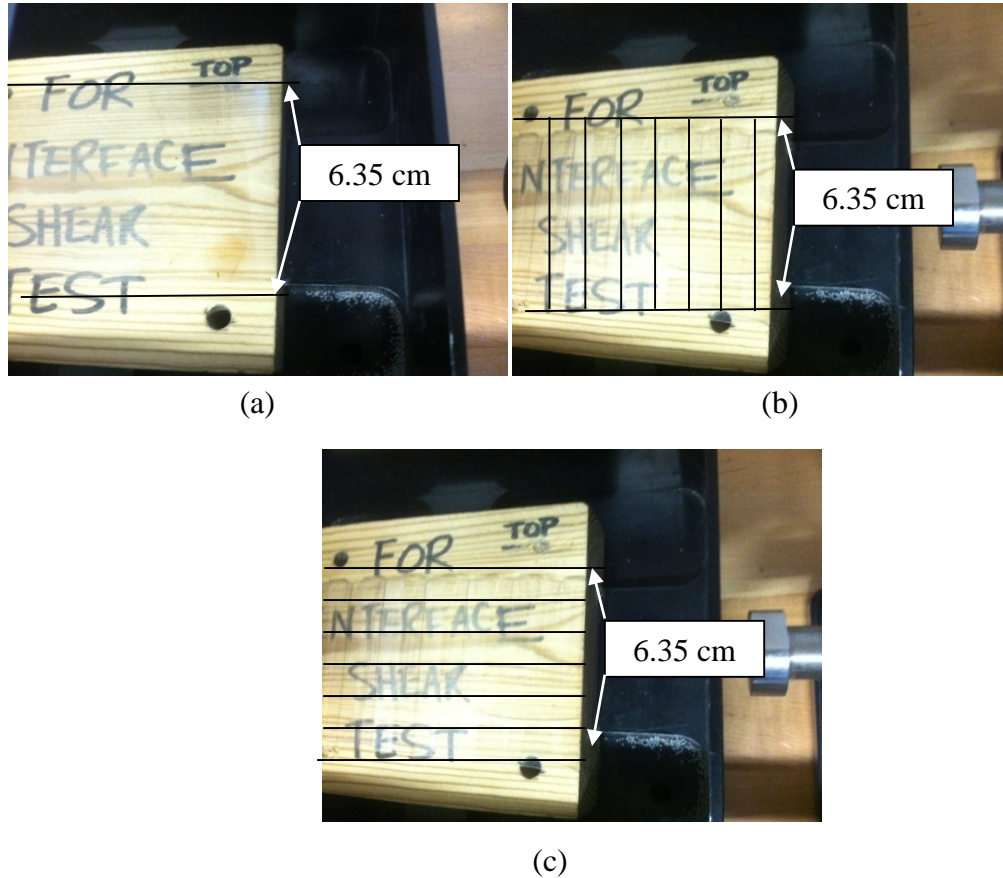
Figure 4.19: Photographs of the bottom PET plastic pieces on the wood block base: (a) flat; (b) ribbed-aligned; and (c) ribbed-orthogonal

The top shear box also required a modification. For the top shear box a circular block of wood was fit tightly inside the top half of the direct shear test box as shown Figure 4.17. Figure 4.20 displays photographs of the top half of the direct shear test box (turned upside down) with (a) a flat PET plastic piece and (b) a PET plastic piece that will be utilized for the ribbed-aligned and ribbed-orthogonal test specimens. The orientation of the ribs displayed in Figure 4.20(b) remains the same for both the ribbed-aligned and ribbed-orthogonal tests. Figure 4.20(c) shows the circular (diameter = 6.35 cm) installed in the top shear box prior to testing.

(a)   (b)   (c)
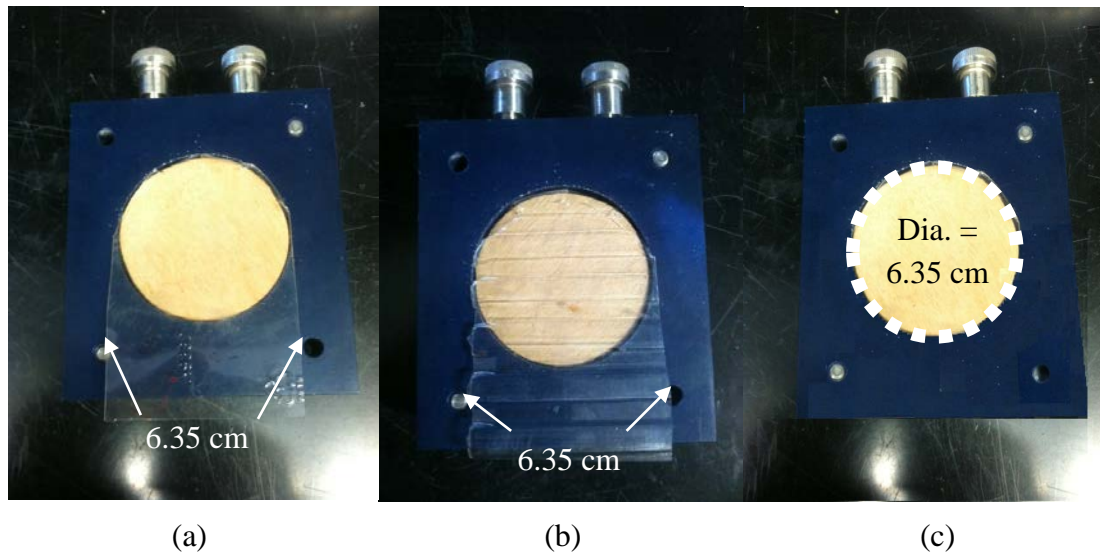
Figure 4.20: Photographs of the top PET plastic pieces adjacent to the top half of the direct shear test box: (a) flat PET piece; (b) ribbed-aligned and ribbed-orthogonal PET piece; and (c) circular test specimen prior to testing

The modified direct shear test box configuration, outside of the direct shear base assembly, is shown in Figures 4.21(a) and 4.21(b). The two pieces of PET plastic are positioned against each other between the base block and the top half of the cell. However, the bottom piece was wedged between the wood block and the shear base assembly to prevent movement of the bottom piece during each direct shear test. The

gap pins were utilized to create a 2.1 mm gap since the thickness of each plastic piece, i.e. top and bottom, was 1.05 mm, but were backed out after creating the gap. This height was selected to ensure contact between the top and bottom pieces of the recycled PET plastic.

(a)   (b)
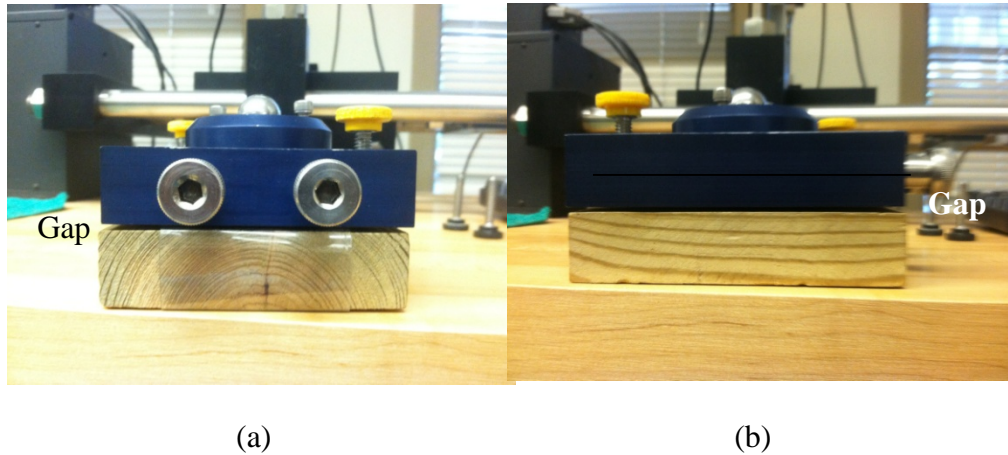
Figure 4.21: Assembled top and bottom portion of the modified direct shear box: (a) parallel to direction of shear; and (b) orthogonal to direction of shear

The final test matrix for the interface shear study is shown in Table 4.7. During each test the shear force was monitored using the horizontal load cell connected to the data acquisition unit. The nominal shear stress and nominal normal stress were computed as follows:

The nominal shear stress of the test specimen was calculated as follows:

$$\tau = F_s / A \tag{4.6}$$

Where:
τ = Nominal shear stress (kPa)
F_s = Shear force (kN)
A = Contact area between specimens (m^2)

Table 4.7: Interface direct shear test matrix

Test ID	PET Plastic Orientation	Normal Stress (kPa)	Displacement Rate (cm/sec)
D1-Flat-50	Flat	50	0.01
D2-Flat-100		100	
D3-Flat-200		200	
D4-Ribbed Aligned-50	Ribbed-Aligned	50	
D5-Ribbed Aligned-100		100	
D6-Ribbed Aligned-200		200	
D7- Ribbed Orthogonal-50	Ribbed-Orthogonal	50	
D8- Ribbed Orthogonal-100		100	
D9- Ribbed Orthogonal-200		200	

The nominal normal stress of the test specimen was calculated as follows:

$$\sigma_{n} = F_n / A \hspace{6cm} [4.7]$$

Where:

σ_n = Nominal Normal stress (kPa)

F_n = Normal Force (kN)

A = Contact area between specimens (m^2)

4.3.2 Interface Direct Shear Test Results

For the flat texture, Figure 4.22(a) displays shear stress as a function of horizontal displacement for all three normal loads. Figure 4.22(b) displays the vertical displacement as a function of horizontal displacement for each normal load. The shear stress versus horizontal displacement plots showed a gradual increase of shear stress as a function of horizontal displacement. The test at the lowest normal stress of 50 kPa the curve did not show a well-defined peak. The curves for the normal stresses of 100 kPa and 200 kPa showed peak shear stresses of 26.12 kPa and 39.74 kPa, respectively. The peak interface shear stresses for the test with normal stresses of 100 kPa and 200 kPa occurred at horizontal displacement of 7.33 mm and 6.33 mm, respectively. The interface shear behavior showed small dilation as denoted by the vertical displacement of about 0.1 mm that was recorded in all three tests.
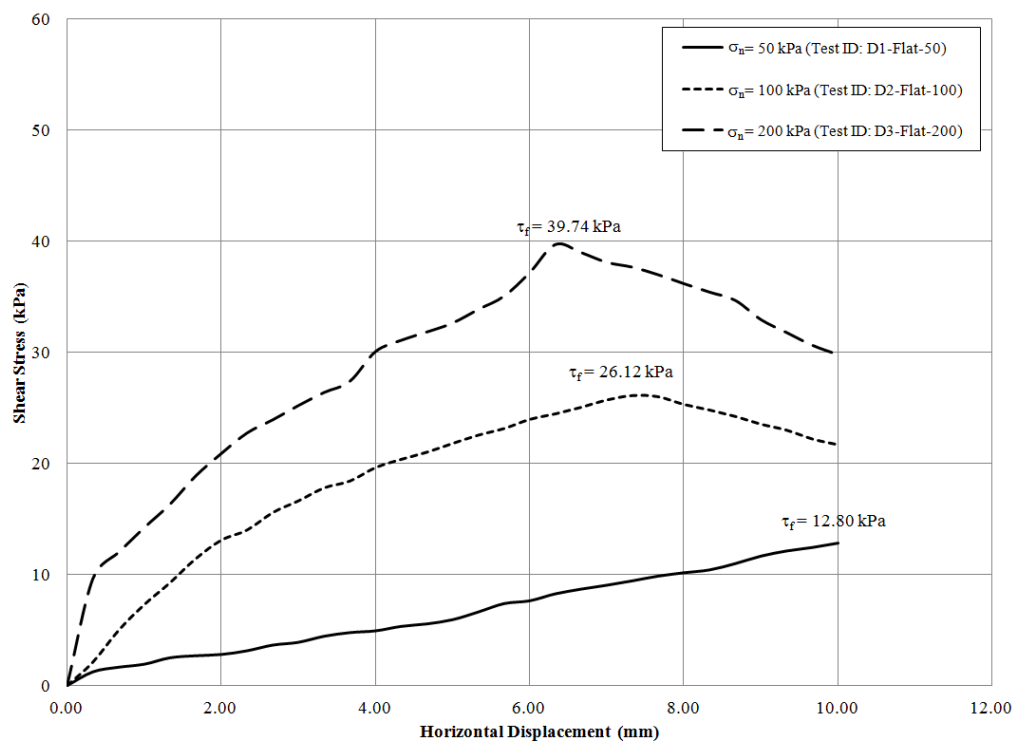
(a)
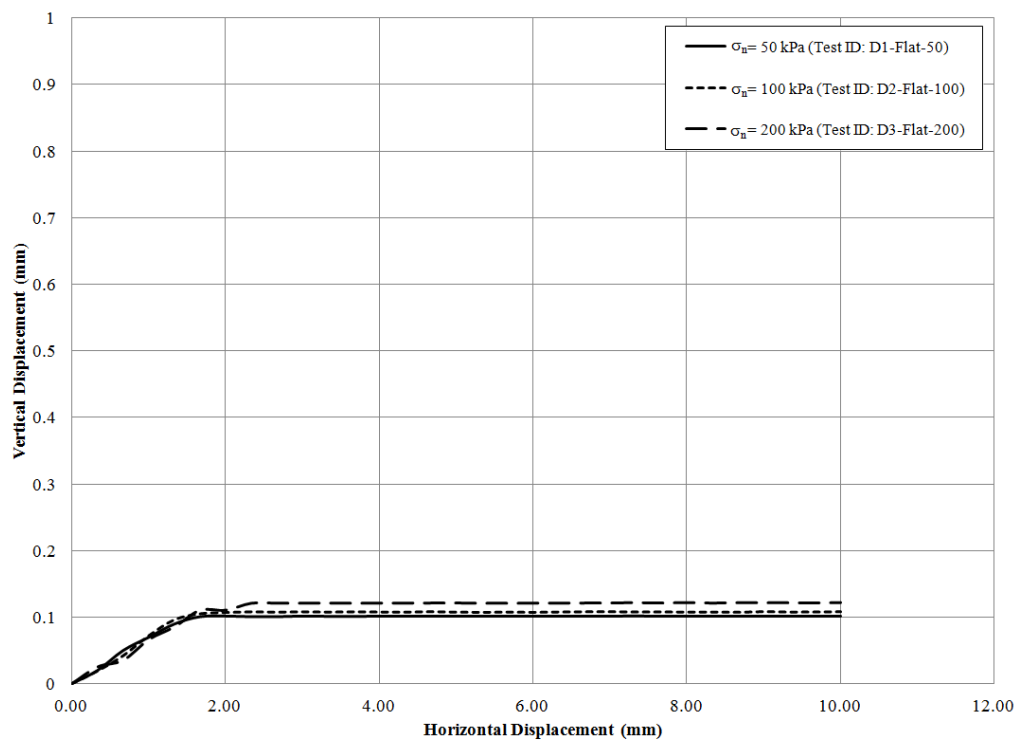
(b)

Figure 4.22: Interface shear tests for flat texture PET plastic test specimens: (a) shear stress as a function of horizontal displacement; and (b) vertical displacement as a function of horizontal displacement

For the ribbed-orthogonal texture, Figure 4.23(a) displays shear stress as a function of horizontal displacement for all three normal loads while Figure 4.23(b) displays the vertical displacement as a function of horizontal displacement for each normal load. The shear stress versus horizontal displacement plots showed a gradual increase of shear stress as a function of horizontal displacement. The test at the lowest normal stress of 50 kPa the curve did not show a well-defined peak. The curves for the normal stresses of 100 kPa and 200 kPa showed peak shear stresses of 28.91 kPa and 42.06 kPa, respectively. The peak interface shear stresses for the test with normal stresses of 100 kPa and 200 kPa occurred at horizontal displacement of 8.33 mm and 5.66 mm, respectively. The interface shear behavior showed small dilation as denoted by the vertical displacement of about 0.15 mm that was recorded in all three tests. In addition, all ribbed orthogonal test specimens illustrate and a bilinear relational between horizontal displacement as function of shear stress until the pronounced peak is reached. The slopes of each linear section shows the first segment has a greater slope, from 0 mm to approximately 0.4 mm, as compared to the slope of after 0.4 mm horizontal displacement.
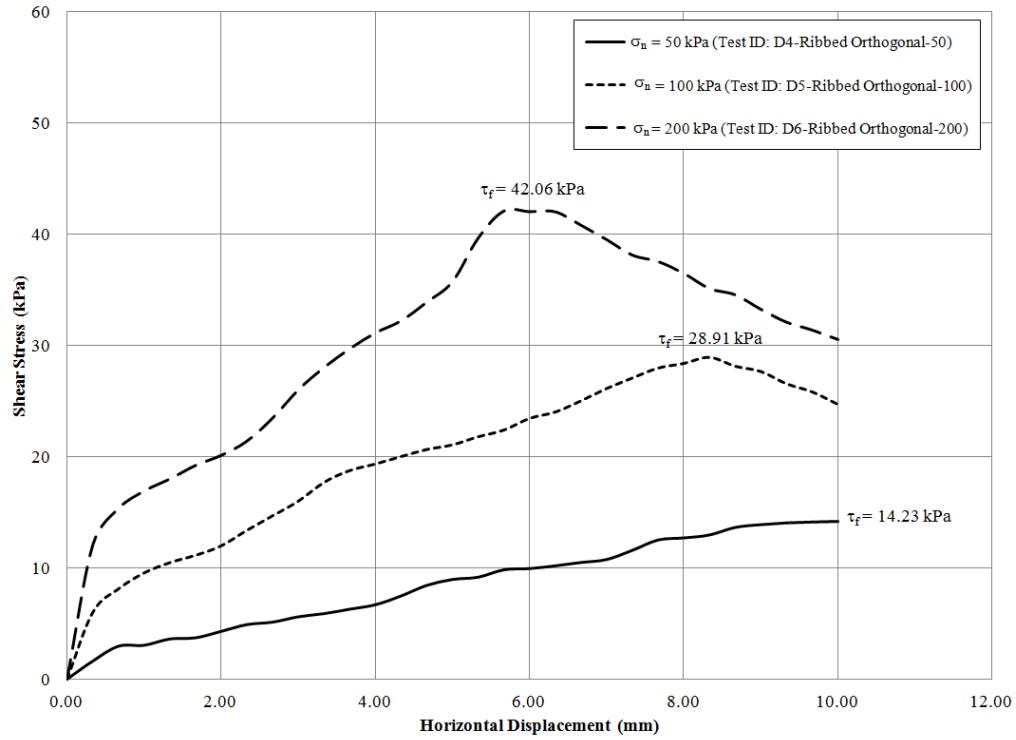
(a)
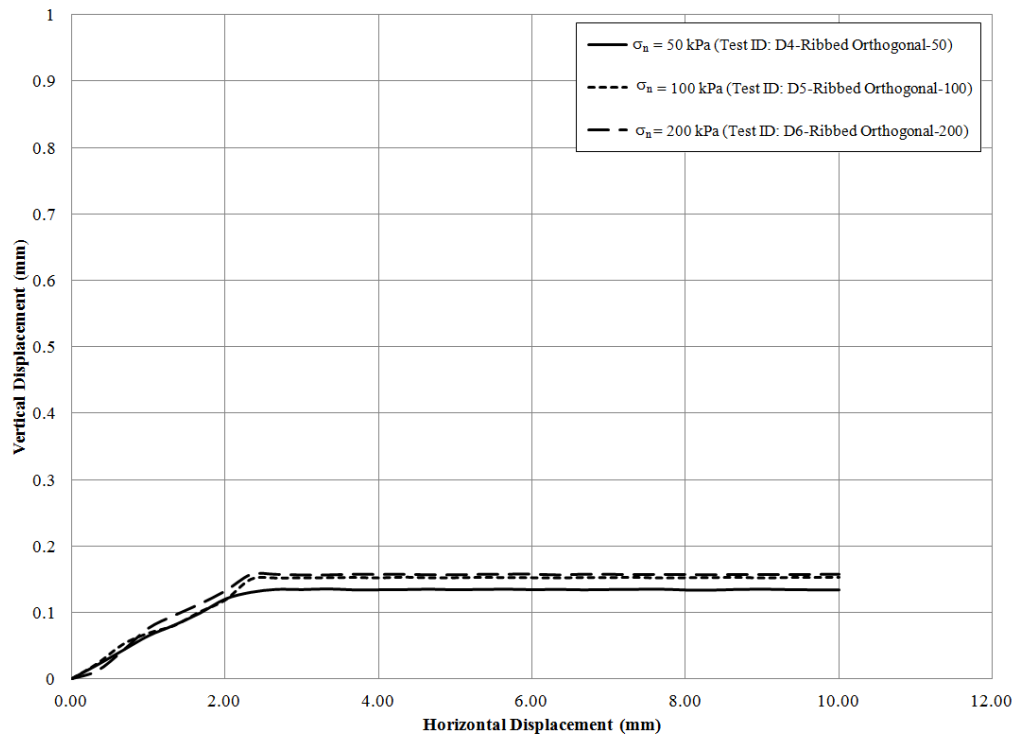
(b)

Figure 4.23: Interface shear tests for ribbed-orthogonal PET plastic test specimens: (a) shear stress as a function of horizontal displacement; and (b) vertical displacement as a function of horizontal displacement

For the ribbed-aligned texture, Figure 4.24 (a) displays shear stress as a function of horizontal displacement for all three normal loads while Figure 4.24(b) displays the vertical displacement as a function of horizontal displacement for each normal load. The shear stress versus horizontal displacement plots showed a gradual increase of shear stress as a function of horizontal displacement. The curves for the normal stresses of 50 kPa, 100 kPa and 200 kPa showed peak shear stresses of 19.42 kPa, 36.99 kPa, and 58.29 kPa, respectively. The peak interface shear stresses for the test with normal stresses of 50 kPa, 100 kPa, and 200 kPa occurred at horizontal displacement of 8.33 mm, 6.66 mm, and 5 mm, respectively. The interface shear behavior showed small dilation as denoted by the vertical displacement of about 0.17 mm that was recorded in all three tests. Similar to Figure 4.23, the ribbed-aligned test specimens tested with a normal stress of 100 kPa and 200 kPa illustrated the same bilinear relational between horizontal displacement as function of shear stress until the pronounced peak is reached. The slopes of each linear section for the 100 kPa and 200 kPa test specimens illustrate the first segment has a greater slope, from 0 mm to approximately 0.4 mm, as compared to the slope of after 0.4 mm horizontal displacement.
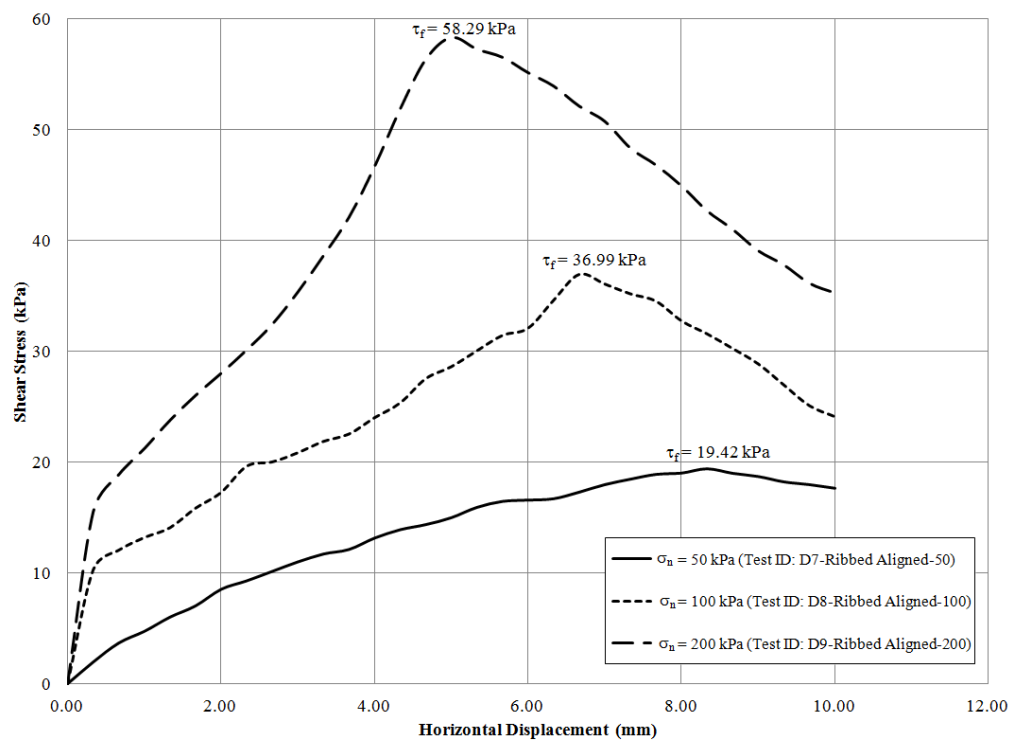
(a)
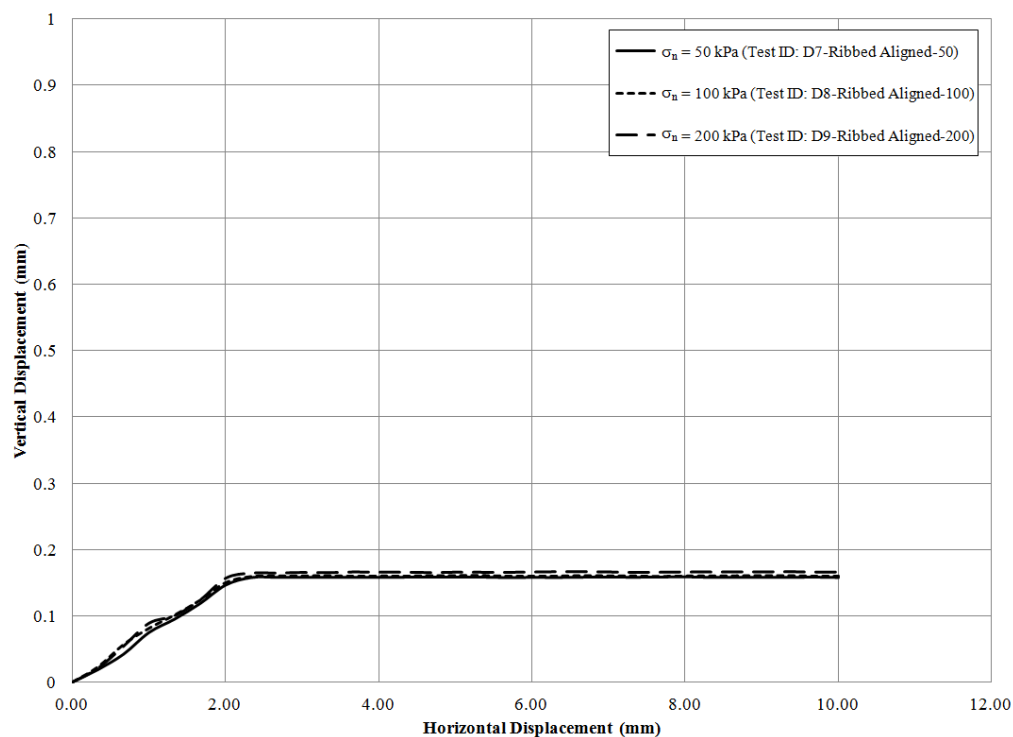
(b)

Figure 4.24: Interface shear tests for ribbed-aligned PET plastic test specimens: (a) shear stress as a function of horizontal displacement; and (b) vertical displacement as a function of horizontal displacement

To help compare the interface shear behavior of the three texture types, Figures 4.25 through 4.27 show these plots corresponding to the three normal stress levels considered. For the flat and ribbed-orthogonal configurations, subjected to a normal load of 50 kPa, the specimens produced a linear relationship without reaching a well-defined peak shear stress (except for ribbed-aligned texture). However, the specimens tested under the 100 kPa and 200 kPa normal stress levels produced well defined peaks where the specimen illustrated a decrease in shear stress beyond these peaks.

Figure 4.31 compares the stress level of 50 kPa for all configurations. The similarities between the three series are that all produce shear stress values under 20 kPa. However, the differences between the three series shows that the ribbed aligned configuration was only series to produce a pronounced peak at a displacement of 8.33 mm.
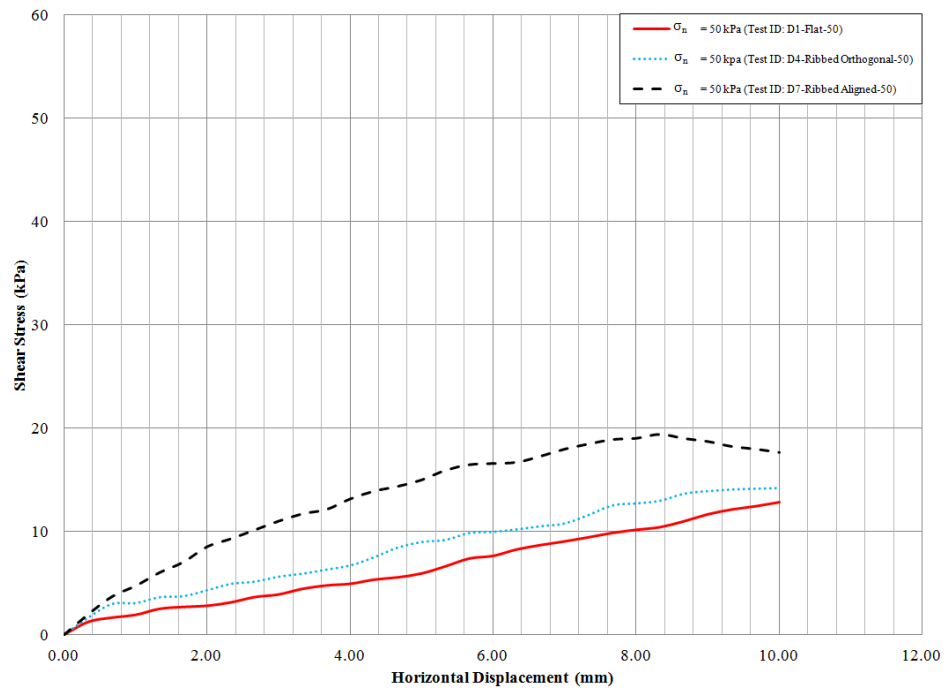
Figure 4.25: Shear stress as a function of horizontal displacement for recycled PET plastic at 50 kPa stress level

Figure 4.26 compares the stress level of 100 kPa for all configurations. The similarities between the three series are that all produce shear stress values under 40 kPa, and that all three series produced a pronounced peak above a stress level of 20 kPa. However, the ribbed orthogonal and ribbed aligned configurations shows a bilinear relational between horizontal displacement as function of shear stress until the pronounced peak is reached. In addition, the slopes of each linear section illustrate the first segment has a greater slope, from 0 mm to 0.4 mm, as compared to the slope of after 0.4 mm horizontal displacement.
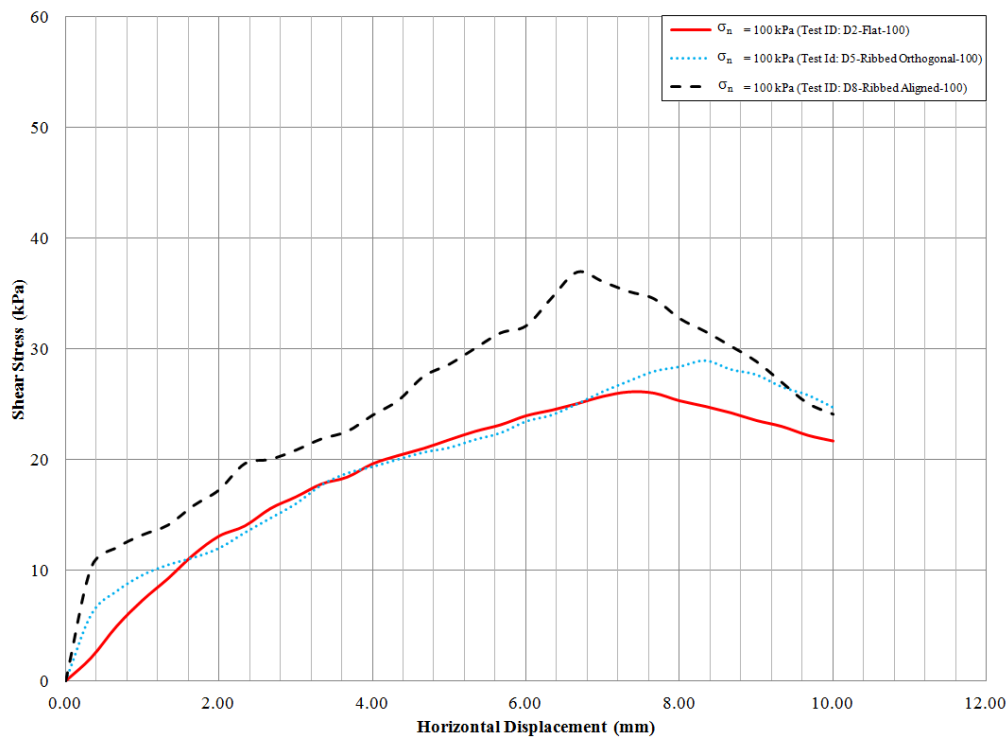
Figure 4.26: Shear stress as a function of horizontal displacement for recycled PET plastic at 100 kPa stress level

Figure 4.27 compares the stress level of 200 kPa for all configurations. The similarities between the three series are that all produce shear stress values under 60 kPa. Similar to Figure 4.26, each series produced a pronounced peak above 39 kPa and the curves change slope at the 0.4 mm horizontal displacement mark. The slopes of these relationships ascend from the configurations of flat, ribbed orthogonal, and ribbed aligned with the latter producing the highest slope. The flat and ribbed orthogonal configurations produced similar slopes after the 0.4 mm horizontal displacement.
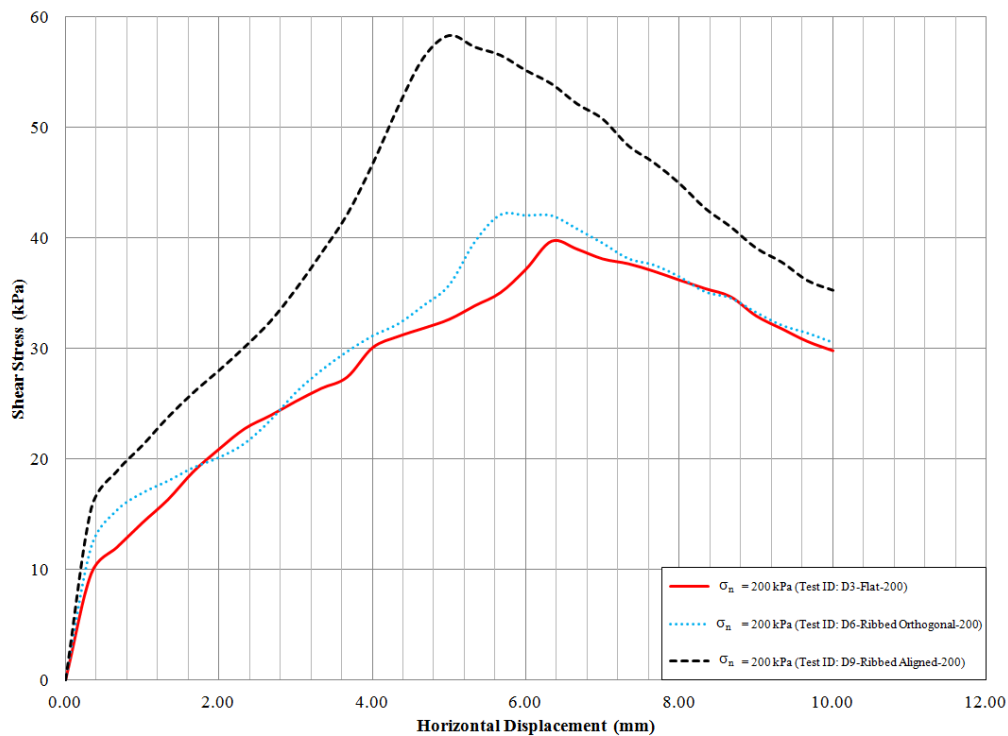
Figure 4.27: Shear stress as a function of horizontal displacement for recycled PET plastic at 200 kPa stress level

The following three figures shows that in each stress level the ribbed aligned reached a pronounced peak with the smallest horizontal displacement as compared to the other two configurations (flat and ribbed orthogonal). This indicates the ribbed aligned configuration exhibits a stiffer response as compared to the other configurations. Across all stress levels the ribbed aligned configuration reached the pronounced peak with second smallest horizontal displacement suggesting that this is the second stiffer response. The flat configuration did not produce pronounced peaks for the stress levels of 50 kPa and 100 kPa, but exhibited a peak with the 200 kPa stress level.

All tests were carried out to a maximum horizontal displacement equal to 10 mm. The maximum shear stresses recorded for all test specimens are summarized in Table 4.8. However, as mentioned before, the specimens examined under the flat configuration under normal loads of 50 kPa and 100 kPa did not reach a maximum value therefore the value reported corresponds to the value at the end of the test. Figure 4.28 displays the shear strength values as a function of the applied normal stress. This plot also shows the linear regression line obtained for each set of tests. The linear regressions shown correspond to an intercept of zero which yields coefficient of correlation (R^2) values of 0.90, 0.85, and 0.91 for the flat, ribbed orthogonal, and ribbed aligned, respectively. The resulting angles of internal friction for the flat, ribbed-orthogonal, and ribbed-aligned test specimen configurations were 12.0°, 12.9°, and 17.3°, respectively.

Table 4.8: Summary of the direct interface shear test results

Test Specimen ID	Test Specimen Orientation	Normal Stress (kPa)	Shear Strength (kPa)	δ (degrees)
D1-Flat-50	Flat	50	12.8[1]	12.0°
D2-Flat-100		100	26.12[1]	
D3-Flat-200		200	39.74	
D4-Ribbed Orthogonal-50	Ribbed-Orthogonal	50	14.23	12.9°
D5-Ribbed Orthogonal-100		100	28.91	
D6-Ribbed Orthogonal-200		200	42.06	
D7-Ribbed Algined-50	Ribbed-Aligned	50	19.42	17.3°
D8-Ribbed Algined-100		100	36.99	
D9-Ribbed Algined-200		200	58.29	

Notes: [1] Specimen did not reach maximum shear stress, but the value at the end of displacement was recorded
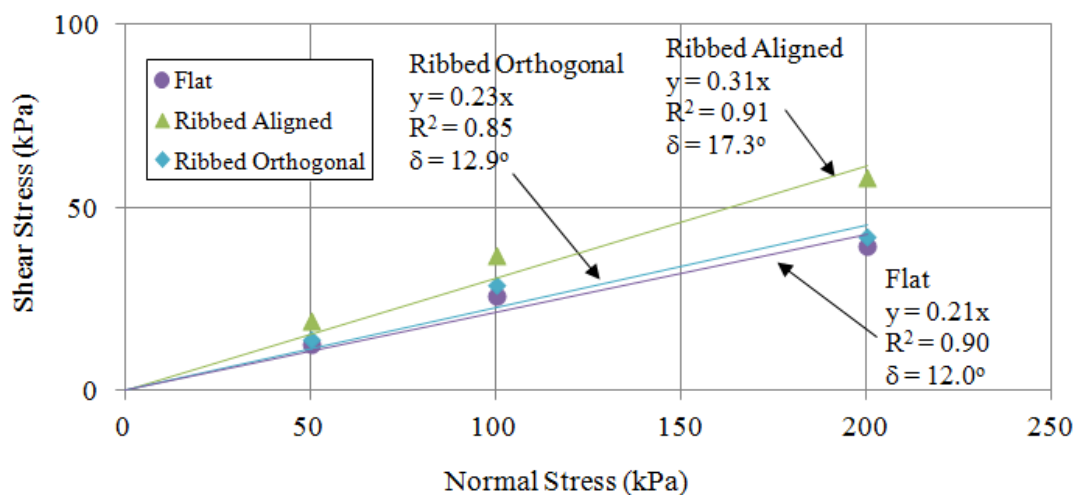
Figure 4.28: Interface shear strength as a function of applied normal stress for all recycled PET plastic test specimens evaluated during direct shear testing

Figure 4.29 shows the same data in Figure 4.28, but has included a linear regression line for y-intercept of zero (solid line) and a linear regression line that determines the y-intercept as a function of data points (dashed line). The three intercepts for the flat, ribbed orthogonal, and ribbed aligned were 5.99, 7.66, and 8.77, respectively.
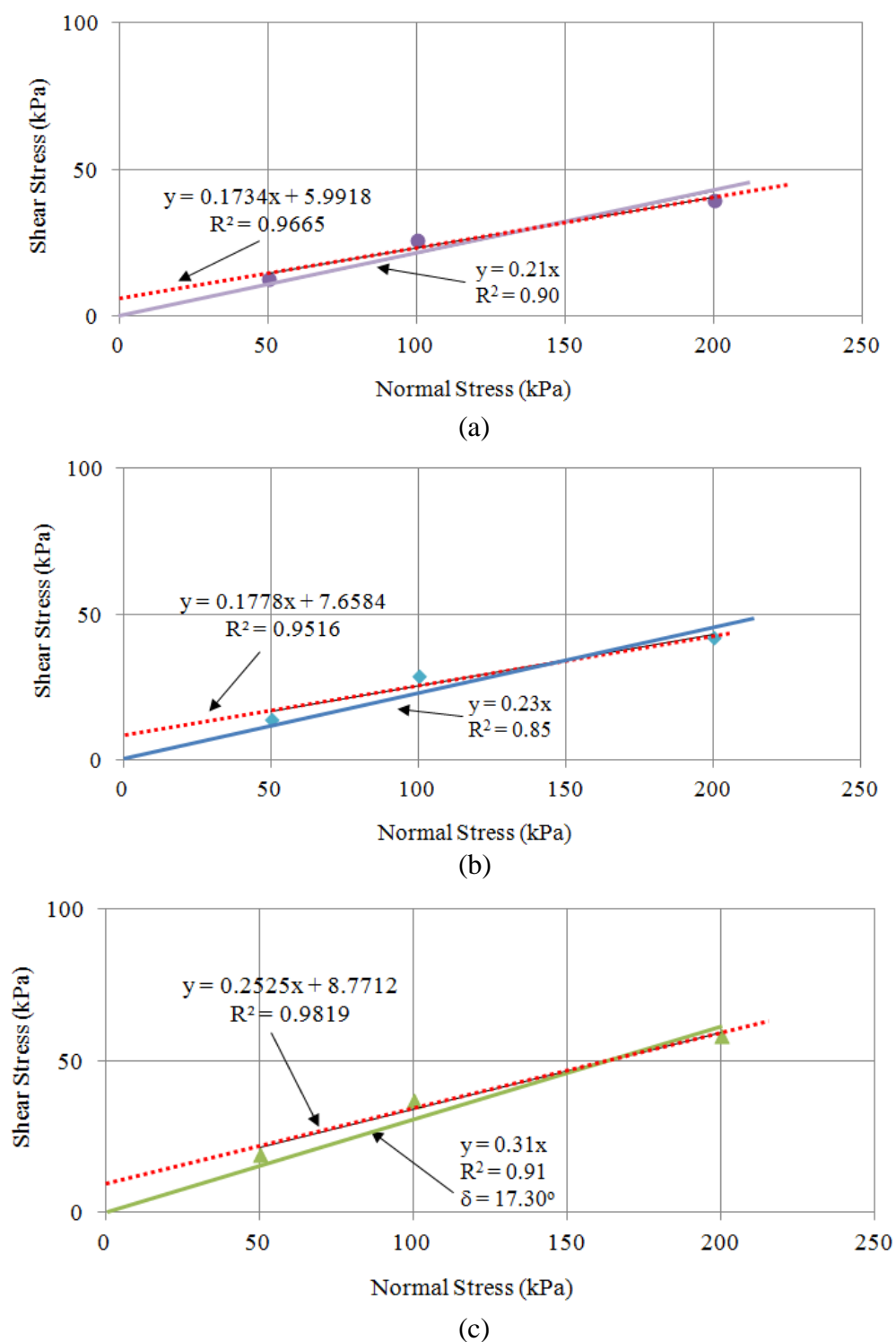
Figure 4.29: Interface shear strength as a function of applied normal stress for each configuration of recycled PET plastic test specimens evaluated during direct shear testing: (a) flat; (b) ribbed orthogonal; and (c) ribbed aligned

4.3.3 Interface Direct Shear Test Summary

Nine direct shear test specimens were examined using three different PET plastic textures/orientations (flat, ribbed-orthogonal, and ribbed-aligned), each tested at three normal loads. The standard direct shear test method ASTM D5321, (2015) was modified to determine the interface shear behavior of the recycled PET plastic materials using constituents from a recycled PET bale.

The data was processed to generate plots of interface shear stress as a function of horizontal displacement. All test specimens were tested at a displacement rate of 0.01 cm/sec. Seven out of the nine test specimens exhibited a peak shear stress with a bi-linear relationship that also develops during the triaxial testing that is presented as part of this study.

The interface friction angles measured during this study are summarized in Table 4.8 for each group of tests, and compared to data reported by Shooter and Tabor (1952), which are summarized in Table 4.9. Shooter and Tabor (1952) also used a modified the standard direct shear test method by utilizing hemispherical plastic sliders (top and bottom) with a displacement rate equal to 0.01 cm/sec and applied normal stress equal to 50 kPa, 100 kPa, and 200 kPa. Shooter and Tabor (1952) tested five plastic types and all with a 'flat' texture. As shown in Table 4.9 this study reported an interface friction angle of 14° for flat polyethylene. This value compares very well with the 12° interface friction angels obtained in this project for flat PET bottles.

Table 4.9: Coefficient of friction values for plastic-on-plastic adopted from Shooter and Tabor (1952)

Reference	Type of Plastic/ Configuration	δ (degrees)
Shooter and Tabor (1952)	Virgin Polyethylene	14.0
Garbini (Current Study)	Recycled PET/Flat	12.0
	Recycled PET/Ribbed-orthogonal	12.9
	Recycled PET/ Ribbed-aligned	17.3

4.4 Triaxial Compression Testing

Triaxial compression testing was conducted to assess the shear strength and stress-strain behavior of the same recycled PET material collected from actual PET bales. The triaxial test program included five different unit weights, five independent axial displacement rates, and two different test specimen preparation/testing conditions (i.e., dry and saturated). Each test condition was repeated to evaluate variability in the results. This resulted in a total of 24 triaxial tests were conducted for this component of this study. Results were utilized to determine the friction angle and to evaluate the stiffness and stress-strain behavior of the material. This section provides a description of the test set-up and procedure, followed by a presentation and discussion of the test results.

4.4.1 Triaxial Compression Test Configuration and Procedure

The triaxial compression tests were carried out using a 15.24 cm diameter triaxial cell with a 50 kN ELE load frame shown in Figure 4.30. The main components of the triaxial test apparatus are shown in Figure 4.30. ELE load frame had a load platen where the triaxial cell is placed. This load platen moves upwards at the specified vertical displacement rate.
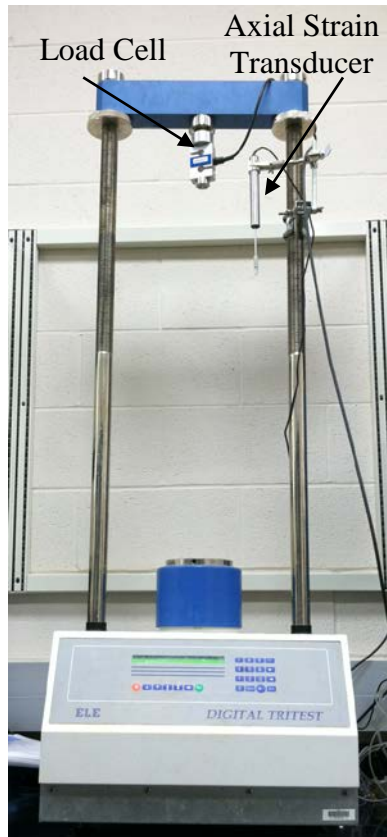
Figure 4.30: ELE load frame

All tests were performed in general accordance with the ASTM D7181 (2015). Both dry and saturated test specimens were evaluated under drained conditions. The force and displacement were measured directly using the data acquisition unit while the volume changes were recorded manually using the appropriate burettes on the pressure panel. The load was measured using an Interface force transducer with a 4.45 kN capacity (Figure 4.31). Displacement was measured using a calibrated ELE axial displacement transducer with a 7.62 cm stroke (Figure 4.32). Specifications for each sensor used during triaxial testing is presented in Appendix A.

Figure 4.31: Interface triaxial force transducer

Figure 4.32: ELE axial strain transducer

Due to the relatively large size of the plastic bottles in a typical PET bale compared to a 15.24 cm diameter triaxial test specimen, it was necessary to conduct the triaxial compression tests using chopped plastic PET bottle constituents. Sample plastic bottles were cut into 1.98 cm^2 squares (2.54 cm diagonals) to comply with the ASTM D7181 (2015) requirement requiring the maximum particle size within a triaxial sample to be $1/6^{th}$ the diameter of the test specimen. For the triaxial testing, PET plastic bottle constituents were processed until enough PET material was produced to meet the target unit weight for each test specimen. Figures 4.33(a) and 4.33(b) display photographs of a bale constituent before and after it was processed, respectively. The amount of processed material needed to create a test specimen for a triaxial test is shown in Figure 4.34, which was a typical 18,927 cm^3 (5 gallon) bucket. The testing material was air dried at room temperature for at least one week prior to triaxial testing.
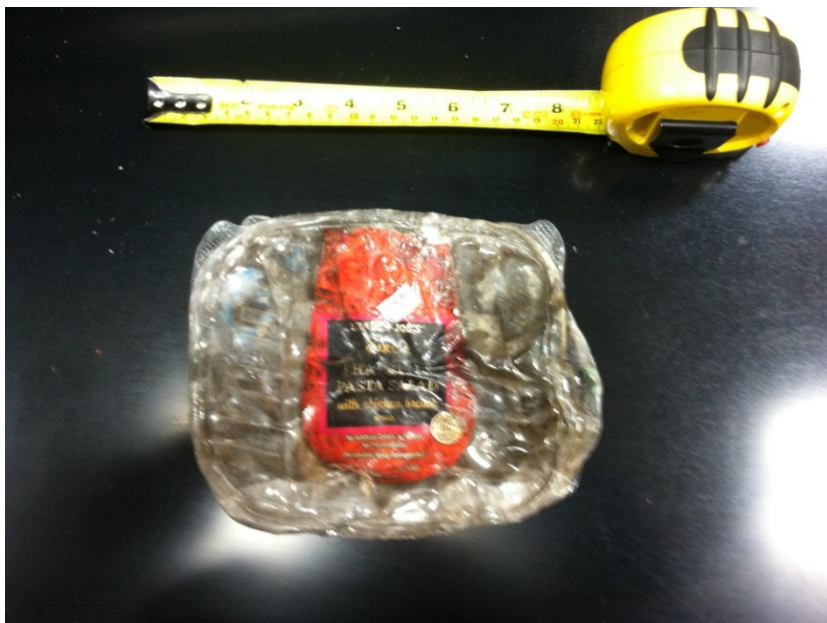
(a)

(b)

Figure 4.33: Category 1 recycled PET bale constituent: (a) before a reduction in size; and (b) after it was chopped

Figure 4.34: PET bale material processed in quantity for the preparation of triaxial test specimens

A special test specimen preparation procedure was developed to consistently generate the chopped plastic pieces, particularly due to the sharp edges of the chopped pieces which required use of three latex membranes that were carefully secured to the triaxial base using three O-rings. The triple membrane was stretched around a typical test specimen preparation mold and secured on the outside of the mold with three additional O-rings as displayed in Figure 4.35. Figure 4.35 displays the triaxial test specimen preparation procedure at the various stages of the process. A small vacuum pressure equal to 5 kPa was applied to the exterior of the membranes to conform the membranes to the specimen preparation mold. The chopped recycled PET plastic material pieces were placed inside the cell in ten layers. The weight of each layer was recorded and carefully tamped to reach the target unit weight for the test specimen. The process was repeated until the unit weight of the test specimen was achieved.
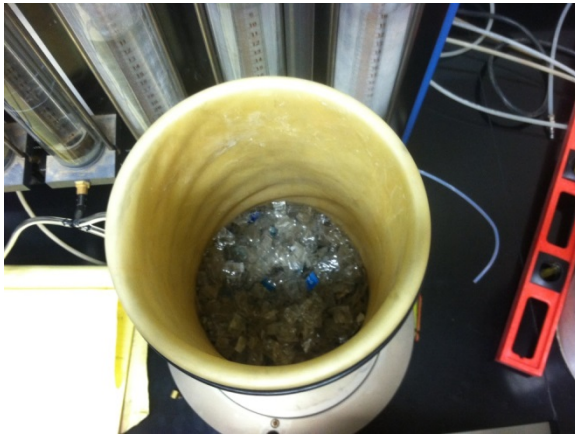
(a)   (b)

(c)   (d)

Figure 4.35: Triaxial test specimen preparation procedure: (a) first layer; (b) multiple layers with tamper; (c) final layer; and (d) completed test specimen

The height of the test specimen was measured at the four cardinal directions while the circumference of the specimen was measured using a pi-tape at eight uniform locations along the length of the test specimen. Using the volume measurement and target unit weight, the precise weight of chopped recycled PET material was added or removed as needed to achieve the desired unit weight. This was an iterative process that was repeated and recalculated using the weight and volume to ensure that the unit weight of the test specimen was within a tolerance of +/- 1%. A typical triaxial test specimen was

approximately 7 cm in diameter by 39 cm in length. The triaxial compression tests involved five different unit weights equal to 0.79 kN/m^3, 1.57 kN/m^3, 1.73 kN/m^3, 1.89 kN/m^3, and 2.36 kN/m^3. For the larger unit weight test specimens, zip ties had to be used instead of O-rings to better seal the test specimen. In these cases, the final test specimen typically had a larger diameter than the triaxial specimen mold as displayed in Figure 4.35(d).

After the triaxial test specimen was prepared and the cell chamber was installed, the piston arm was secured into the top cap and fastened to the triaxial apparatus using three rods that screw in evenly around the triaxial chamber. The triaxial cell ports were connected to the pressure panel to allow the specimen to release any water that potentially leaked in from the triaxial chamber fluid. Water was pumped into the triaxial chamber and a valve was opened at the top of the triaxial chamber to ensure no pressure accumulated during the filling process. The triaxial chamber was completely filled with fluid so that volume change could be monitored using the pressure panel as changes occurred in the triaxial chamber fluid during the isotropic compression and shear phases of the triaxial test. If any leaking occurred during the filling process of the triaxial chamber, the test specimen was terminated, and the process was repeated.

After chamber filling, a confining stress was applied to each test specimen. For tests involving the dry test specimen conditions, the triaxial compression test specimen was monitored during the initial isometric compression phase (i.e., while the confining stress was applied) to determine the bulk modulus of the material. The confining pressure was applied to the chamber gradually using small stress increments of 1.38 kPa. This small pressure increment ensured that the sample did not experience a volume change

greater than 25 mL which corresponded to the maximum volume that could be measured using the volume change burettes. Following each cell pressure increment, the changes in test specimen volume and height were recorded until the target confining pressure was achieved. Any change in the volume of the confining fluid as measured by the triaxial panel was proportional to the change in the volume of the test specimen. After each target confining pressure level was reached (i.e. 17.24 kPa, 34.47 kPa, 51.71 kPa, and 68.95 kPa), the final volume change was recorded, and the piston arm was locked to ensure the specimen did not vertically rebound. At this point the test specimen was installed in the triaxial compression apparatus (see Figure 4.30) prior to initiating the shearing phase of the triaxial compression test. Figure 4.36(a) displays an image of the triaxial test prior to testing, and Figure 4.36(b) displays an image of the triaxial specimen during testing.

(a)   (b)
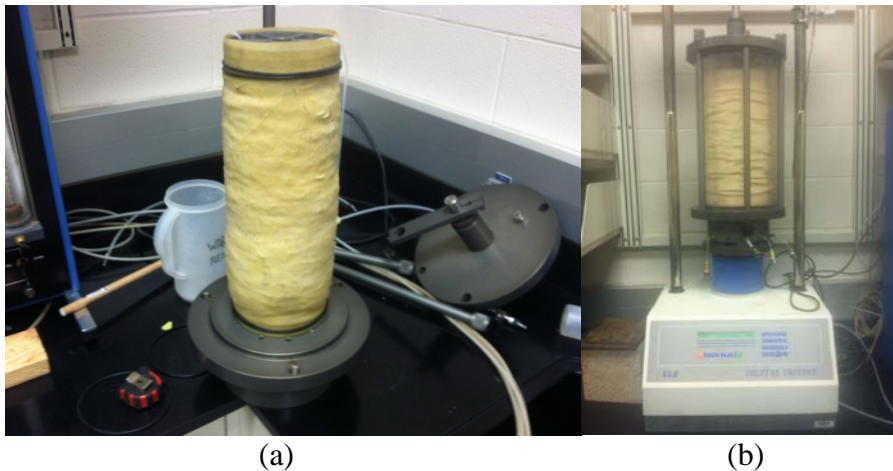
Figure 4.36: Triaxial specimen: (a) prior to testing; and (b) during testing

For triaxial tests involving saturated specimen conditions, the same process was repeated until the triaxial chamber cell was installed. Saturation of the test specimen was accomplished by applying a 5kPa back pressure to drive air into solution and forcing de-aired water through the system while maintaining the vacuum. The back pressure was applied by simultaneously increasing the chamber and back pressure in steps with the specimen drainage valves open so that de-aired water from the burette connected to the top and bottom of the specimen was allowed to flow into the specimen. To ensure test specimens were saturated, a calculation of the pore pressure Parameter B (B-value) was performed in accordance with ASTM D7181-11 (2015) to ensure a B-value was at least 0.95. The pore pressure Parameter B of the saturated test specimen was calculated as follows:

$$B = \Delta u \: / \: \Delta \sigma_3 \tag{4.8}$$

Where:

Δu = change in the specimen pore pressure that occurs as a result of a change in the chamber pressure when the specimen drainage valves are closed
$\Delta \sigma_3$ = isotropic change in the chamber pressure

This procedure was repeated until the pore pressure Parameter B successfully reached the minimum value of 0.95.

After back pressure saturation specimen were isotopically consolidated to four effective consolidation stress levels of 17.24 kPa, 34.47 kPa, 51.71 kPa, and 68.95 kPa. Consolidation involved recording sample volume change using a burette at increasing elapsed times of 0.1 min, 0.2 min, 0.5 min, 1 min, 2 min, 4 min, 8 min , 15 min, 30 min, 1 hr., 2 hr., 4 hr., 8 hr., and 24 hours). Once the specimen reach equilibrium under the prescribed confining pressure, the shearing phases was initiated.

After effective confining pressure, for dry and saturated samples, the triaxial chamber was carefully aligned within the load frame to ensure pure axial loading was applied and prevent the application of lateral force to the piston during shearing. The axial load piston was slowly moved into contact with the load frame until a small seating load of 0.1 kN was applied. During shearing, the chamber pressure was kept constant while the axial load piston advanced downward against the specimen cap. Drainage was permitted during shear, and volume changes were monitored and recorded using the volume change burette. Deformations and volume changes were monitored at increments of axial strain of 0.1% up to 1% strain, and every 1%, thereafter. Sufficient readings were collected to ensure complete definition of the stress-strain curve. The axial loading was applied until at least 15% axial strain was reach. Final values of load, deformation, and volume change were recorded.

Table 4.10 summarizes the triaxial test matrix conducted as part of this study. The four target effective confining pressures were 17.24 kPa, 34.47 kPa, 51.71 kPa, and 68.95 kPa.   Initially, each test was prepared at a single unit weight of 2.36 kN/m^3 and the triaxial test was repeated three times for each of the four confining pressures above, resulting in the first 12 triaxial tests (Phase 1) listed in Table 4.10. The displacement rate

used for the initial test was 10 mm/min which corresponds to an axial strain of 3.42% strain/min.

The second phase of this test matrix (test numbers 13 - 16) used the same displacement rate and a constant effective confining pressure of 17.24 kN/m^3. However, tests investigated influence of unit weight which ranged from 0.79 kN/m^3 to 2.36 kN/m^3 to capture the typical range of PET bale unit weight values generated at the regional MRF.

The third phase of this test matrix, test numbers 17 – 20, four different displacement rates were evaluated ranging from 0.02 mm/min to 10 mm/min while keeping the unit weight and the effective confining pressure constant at 2.36 kN/m^3 and 17.24 kPa, respectively.

The fourth and final phase of the text matrix, involved tests 21 through 24, which were carried out to investigate the influence of saturation. Tests for this phase were carried out at a unit weight of 2.36 kN/m^3 and a displacement rate of 0.03 mm/min.

As shown in Table 4.10, 20 specimens were examined under dry conditions compared to the four specimens examined under saturated conditions. The reason the majority of the specimens were examined under dry conditions was due to the amount of time required to prepare, consolidate, and axially load a test specimen. A saturated specimen took at least four to six times longer to examine than a dry specimen.

Table 4.10: Triaxial test matrix of triaxial compression experimental program[1]

Parameters of each Triaxial Test Phase	Test ID	Initial Unit Weight[2] kN/m³	Disp. Rate mm/min	Disp. rate %/min	Cell Pressure kPa
Dry Triaxial[3] Constant Unit Weight Constant Displacement rate *Confining σ Varies* **(PHASE 1)**	T1-2.36-10-17.24-D	2.36	10	3.42	17.24
	T2-2.36-10-17.24-D				
	T3-2.36-10-17.24-D				
	T4-2.36-10-34.47-D				34.47
	T5-2.36-10-34.47-D				
	T6-2.36-10-34.47-D				
	T7-2.36-10-51.71-D				51.71
	T8-2.36-10-51.71-D				
	T9-2.36-10-51.71-D				
	T10-2.36-10-68.95-D				68.95
	T11-2.36-10-68.95-D				
	T12-2.36-10-68.95-D				
Dry Triaxial[3] *Unit Weight Varies* Constant Displacement rate; Constant σ **(PHASE 2)**	T13-1.89-10-17.24-D	1.89			17.24
	T14-1.73-10-17.24-D	1.73			
	T15-1.57-10-17.24-D	1.57			
	T16-0.79-10-17.24-D	0.79			
Dry Triaxial[3] Constant Unit Weight *Displacement rate Varies* Constant σ **(PHASE 3)**	T17-2.36-5-17.24-D	2.36	5	1.71	
	T18-2.36-1-17.24-D		1	0.34	
	T19-2.36-0.2-17.24-D		0.2	0.07	
	T20-2.36-0.02-17.24-D		0.02	0.01	
Saturated CD Triaxial[4] Constant Unit Weight Constant Displacement rate *Confining σ Varies* **(PHASE 4)**	T21-2.36-0.03-17.24-W		0.03	0.012	
	T22-2.36-0.03-34.47-W				34.47
	T23-2.36-0.03-51.71-W				51.71
	T24-2.36-0.03-68.95-W				68.95

Notes: [1] All samples prepared using chopped PET bottles.

[2] Average initial total unit weight reported.

[3] Triaxial compression test on dry samples. Test procedure similar to a CD triaxial test, but sample not 'consolidated'. Sample volume change <u>computed</u> based on variation of volume of the water in the triaxial cell chamber.

[4] Triaxial compression test on saturated samples. Test procedure used corresponds to CD triaxial test where sample is consolidated. Sample volume change <u>measured</u> by means of volume variation of sample pore water.

The triaxial compression data during the shearing phase involved computing the deviator stress using the correct area as follows:

$$\sigma_d (\varepsilon) = \frac{P(\varepsilon)}{A_{corr}(\varepsilon)} \qquad [4.9]$$

Where:

$P(\varepsilon)$ = measured applied deviator load at strain ε
$A_{corr}(\varepsilon)$ = corrected cross-sectional area at strain ε

The corrected area was computed using the ratio of the sample volume at a given axial strain to the sample height at the same axial strain. The equation for the corrected area is as follows:

$$A_{corr}(\varepsilon) = V_c - \Delta V_\varepsilon) / (H_c - \Delta H_\varepsilon) \qquad [4.10]$$

Where:

A = cross-sectional area for a given applied load
V_c = volume after compress (dry specimen) or after consolidation (saturated specimen)
ΔV_ε = change in volume form beginning of shear to any strain
ΔH_ε = change in height from beginning of shear to any strain

The deviator stress was also corrected for membrane, particularly given that three latex membranes were used in each test. The member correction of the deviator stress is as follows:

$$\Delta(\sigma_1 - \sigma_3) = (4E_m t_m \varepsilon) / D_c \qquad [4.11]$$

Where:

$\Delta(\sigma_1 - \sigma_3)$ = correction to be subtracted from the measured principal stress difference (deviator stress)
$D_c = (4A_c/\pi)^{0.5}$ diameter of specimen after consolidation
E_m = Young's modulus for the membrane material
t_m = thickness of the membrane
ε = axial strain (decimal form)

4.4.2 Triaxial Compression Test Discussion and Results

4.4.2.1 Phase 1 Testing - Repeatability

Figures 4.37 through 4.40 display isotropic stresses as a function of volumetric strain during the initial compression phase of the first 12 triaxial tests (Phase 1 tests in Table 4.10) conducted using confining pressures equal to 17.24 kPa, 34.47 kPa, 51.71 kPa, and 68.95 kPa, respectively. The constant variables are labeled in the upper right corner of each figure and the calculated moduli are displayed on each respective figure. The data indicate that the material exhibits a relatively linear relationship between isotropic confining stress and volumetric strain during the application of the cell pressure.

Linear regressions were included for each figure to evaluate the variability from this trend. The slopes of the each regression line (labeled 'y' in each figure) for the 17.24 kPa, 34.47 kPa, 51.71 kPa, and 68.95 kPa applied confining pressures were 2.7116, 2.7074, 2.4937, and 2.4959, respectively. The coefficients of correlation (R^2) were 0.8372, 0.9213, 0.9286, and 0.9062 for the same four confining pressures, respectively. Regardless of the applied confining pressure, the material exhibited consistent behavior. The initial stiffness for each series of confining pressures produced bulk moduli values ranging from 260 kPa to 285 kPa, which are significantly lower than other building materials. For example, for all the positive volumetric strain represents a loss of volume in the specimen.
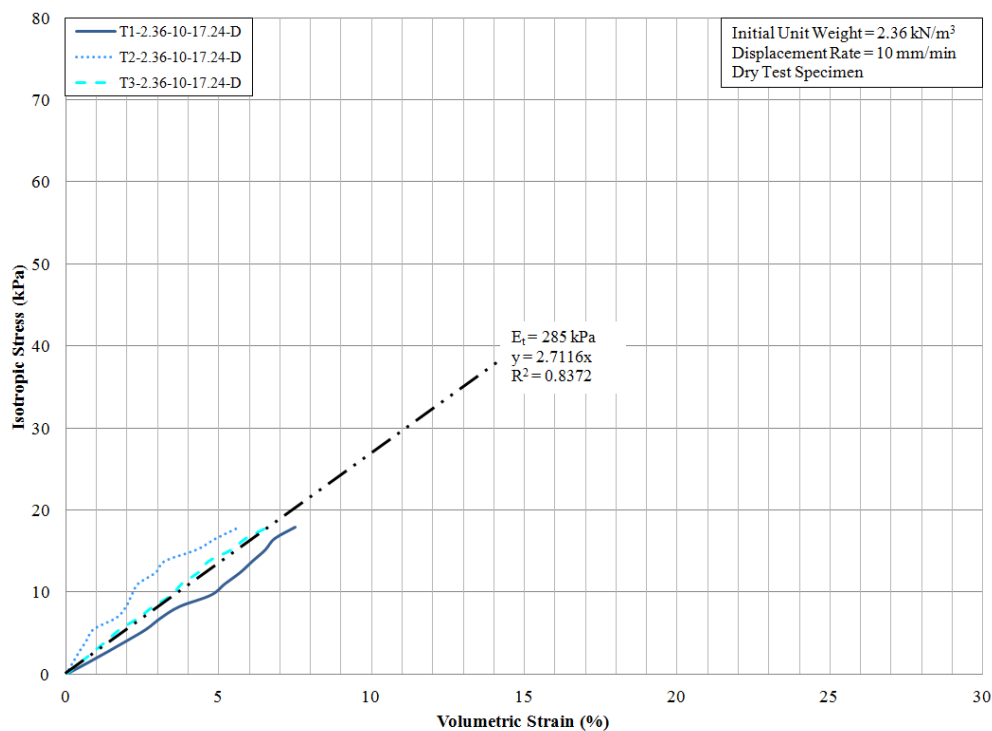
Figure 4.37: Isotropic stress as a function of volumetric strain for the 17.24 kPa confining pressure and unit weight of 2.36 kN/m³
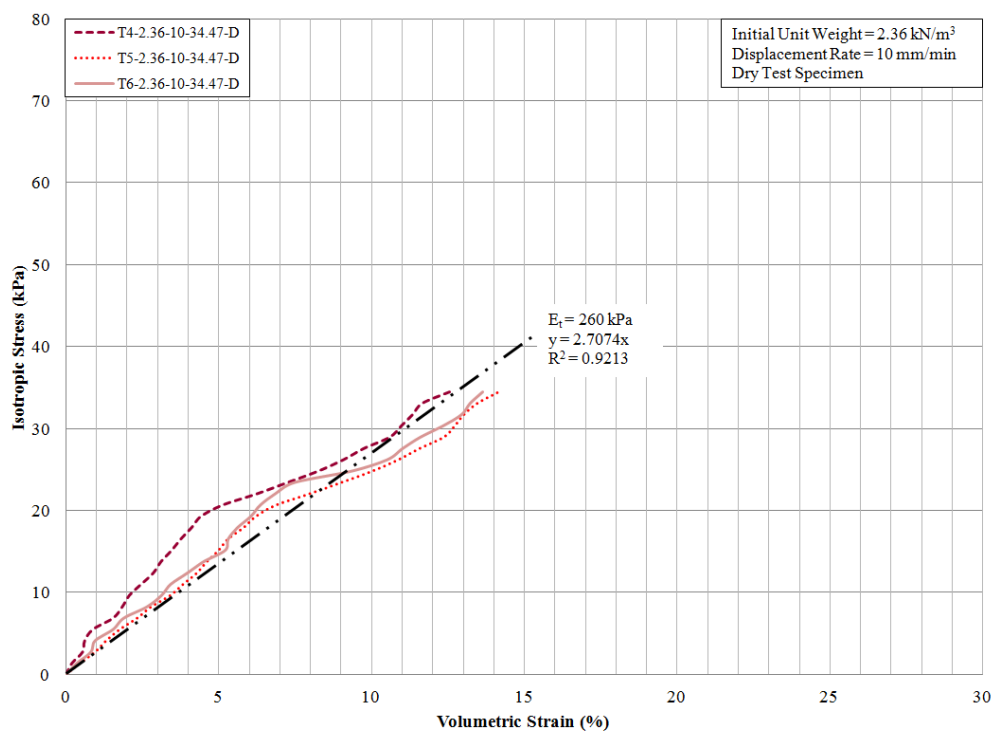
Figure 4.38: Isotropic stress as a function of volumetric strain for the 34.47 kPa confining pressure and unit weight of 2.36 kN/m³
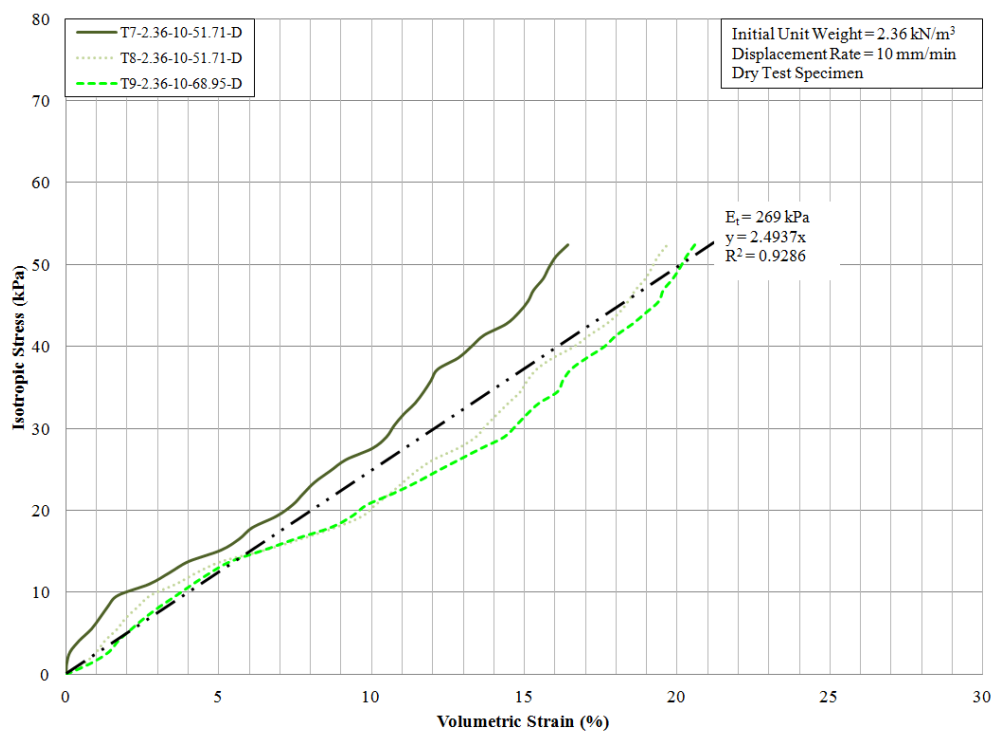
Figure 4.39: Isotropic stress as a function of volumetric strain for the 51.71 kPa confining pressure and unit weight of 2.36 kN/m^3
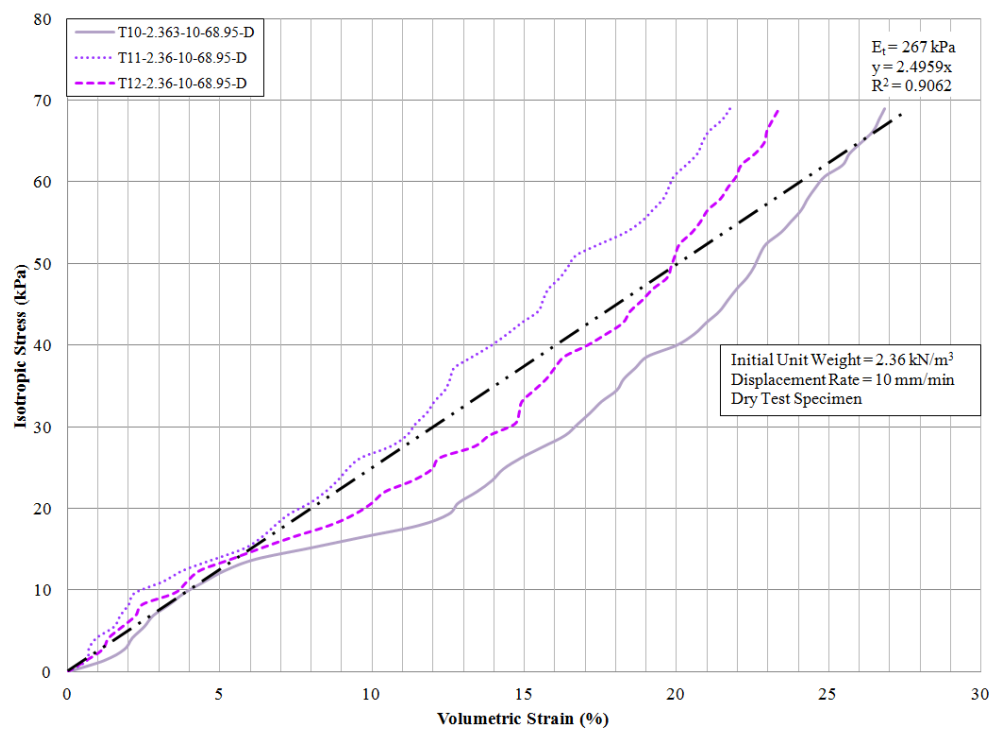
Figure 4.40: Isotropic stress as a function of volumetric strain for the 68.95 kPa confining pressure and unit weight of 2.36 kN/m^3

While Figures 4.41 to 4.44 display results for each confining stress, respectively, holding unit weight constant at 2.36 kN/m^3, Figure 4.41 displays isotropic stress as a function of volumetric strain for five different unit weight values for specimens tested at a 17.24 kPa confining pressure. Unit weights include 2.36 kN/m^3, 1.89 kN/m^3, 1.73 kN/m^3, 1.57 kN/m^3, and 0.79 kN/m^3. The relationship between isotropic compression and volumetric strain for each test specimen remained linear. However, as expected the slope of each curve decreased with decreasing sample unit weight. For example, the test specimen with a unit weight equal to 2.36 kN/m^3 produced a volumetric strain of 7.5% while the test specimen with a unit weight equal to 0.79 kN/m^3 produced a volumetric strain of 14.6%, both with the same confining pressure of 17.24 kPa.
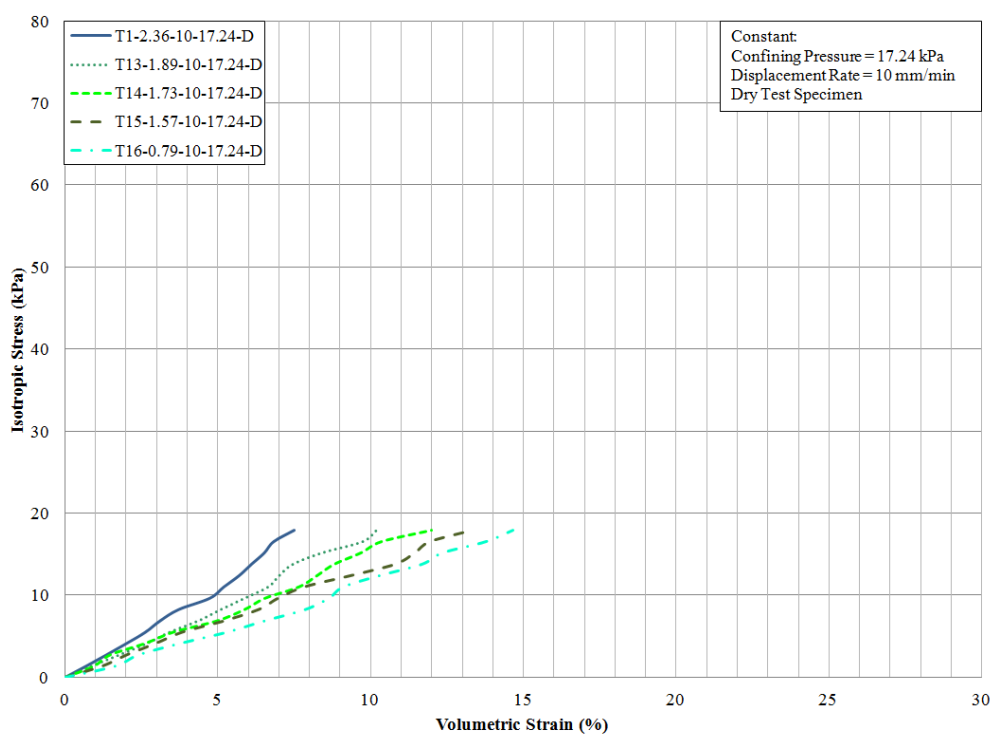
Figure 4.41: Isotropic stress as a function of volumetric strain for test specimens with various unit weights and dry test specimen

For saturated test specimens with a 2.36 kN/m³ unit weight, Figure 4.42 displays isotropic stress as a function of volumetric strain using 17.24 kPa, 34.47 kPa, 51.71 kPa, and 68.95 kPa confining pressures. Similar to Figures 4.40 - 4.44, these data show the same linear relationships exhibited by the dry test specimens. The slope of the linear regression displayed in Figure 4.42 was 2.21, in comparison to the 2.49 - 2.71 range measured from specimens tested dry. A 235 kPa bulk modulus was generated from the data displayed in Figure 4.42 in comparison to the 260 - 285 kPa range generated from the specimens tested dry.
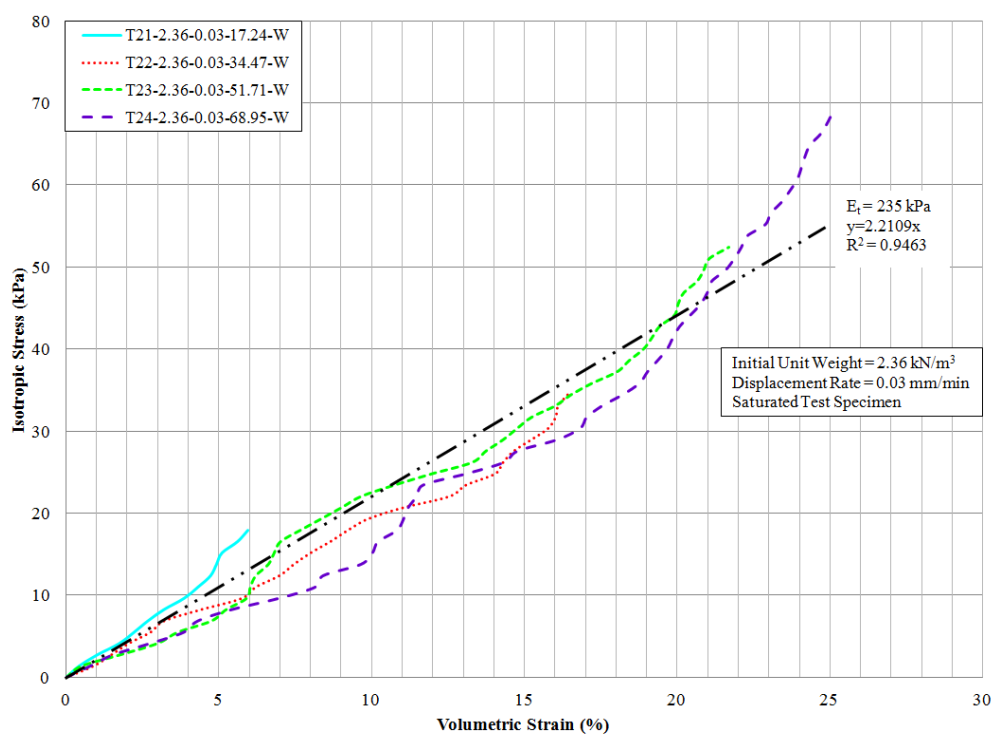
Figure 4.42: Isotropic stress as a function of volumetric strain for saturated testing conditions at a unit weight of 2.36 kN/m³

The triaxial compression test results for Phase 1 are shown in Figures 4.43 through 4.46. In all deviator stress versus axial strain plots the behavior was bilinear. The initial portion of the stress-strain curves extended to axial strain levels of about 0.4%, 0.7%, 0.5%, and 0.4% for the set of tests at effective confining stress levels of 17.24 kPa, 34.47 kPa, 51.71 kPa, and 68.95 kPa, respectively. This is shown graphically in Figure 4.47 where it is clear that the initial tangential Young moduli, E_t, does not show a correlation with confining pressure. This observation is contrary to the typical behavior of granular materials such as soils or other particulate media. This lack of correlation could also be related to the variability of plastic textures and sample unit weights.

The second linear, E_2, portion of the stress-strain curves showed slopes as summarized in Figure 4.50 where it is clear that the initial tangential Young moduli does not show a correlation with confining pressure. The volumetric strain versus axial strain for all 12 triaxial tests of Phase 1 showed a contractive behavior that was fairly linear. The average final volumetric strain recorded at the final axial strain of 15% was -8.2%, -11.14%, -12.03%, and -13.98% for the confining stresses of 17.24 kPa, 34.47 kPa, 51.71 kPa, and 68.95 kPa, respectively. Therefore contractive behavior was found to be greater with increasing confining stress level during Phase 1 tests. There is not a correlation in transition points between E_t and E_2 across all triaxial specimens. However, the axial strain level that represents the transition point between E_t and E_2 across all triaxial specimens ranges between 0.25% and 0.5% axial strain.
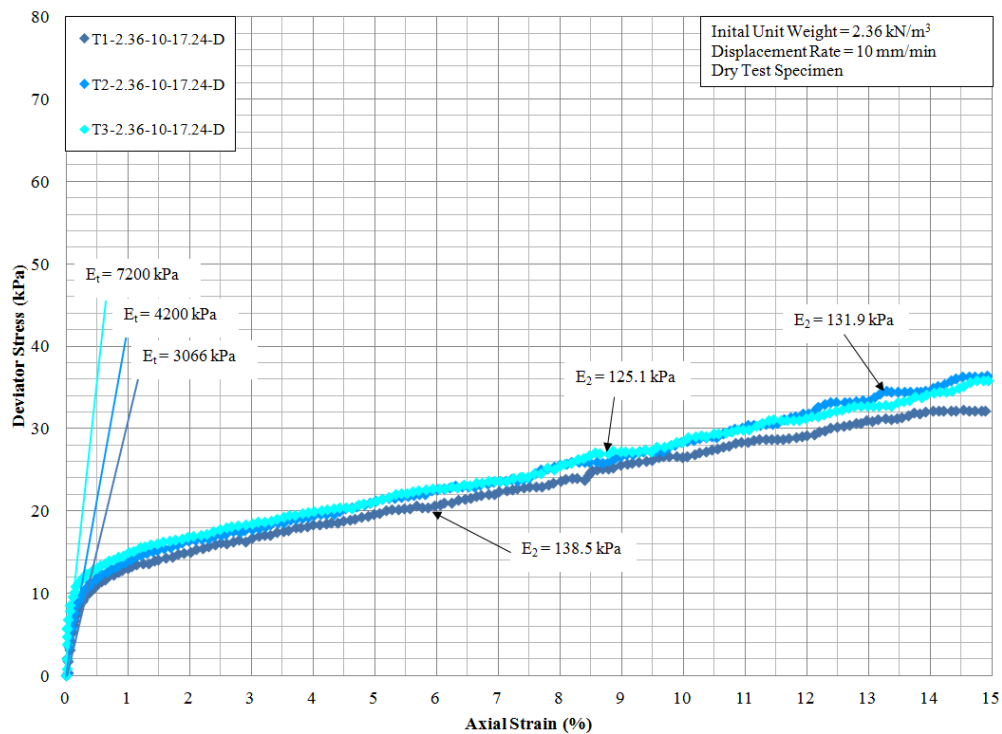
(a)
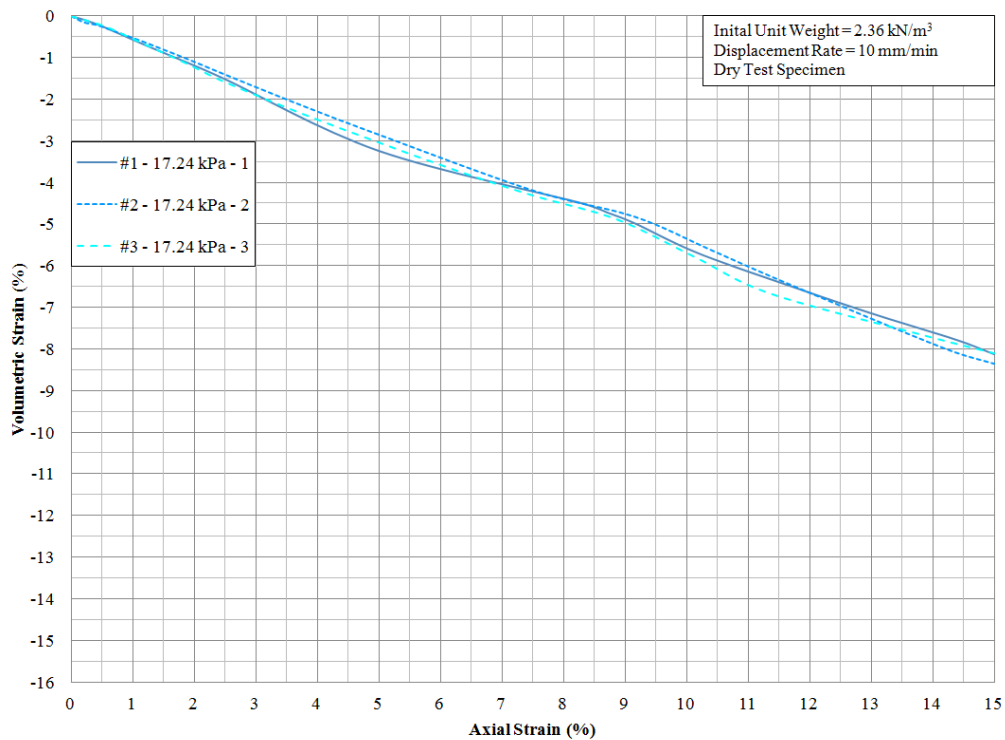
(b)

Figure 4.43: (a) Deviator stress as a function of axial strain for the 17.24 kPa confining stress; and (b) Volumetric strain as a function of axial strain for the 17.24 kPa confining stress
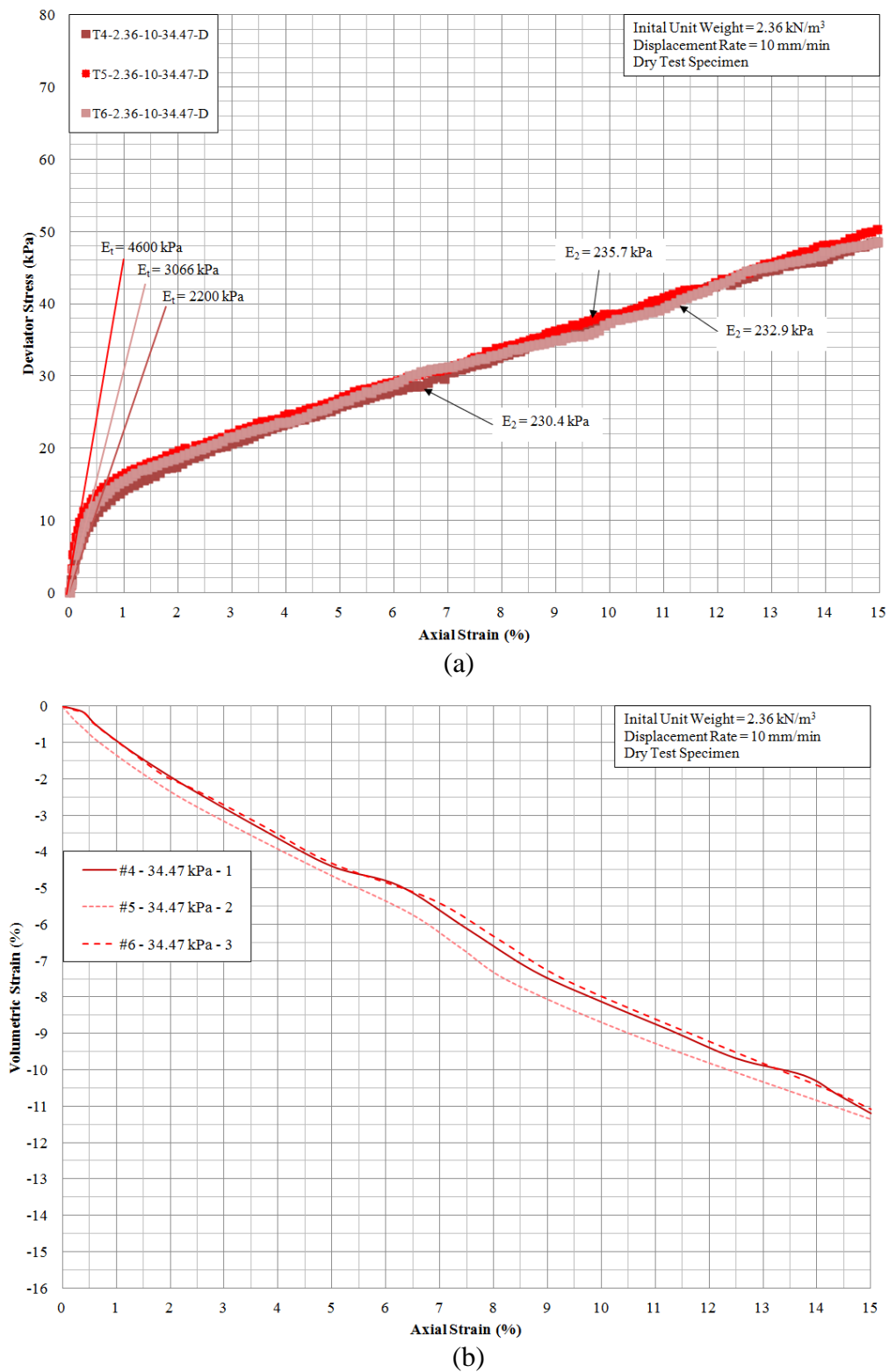
Figure 4.44: (a) Deviator stress as a function of axial strain for the 34.47 kPa confining stress; and (b) Volumetric strain as a function of axial strain for the 34.47 kPa confining stress

(a)

(b)
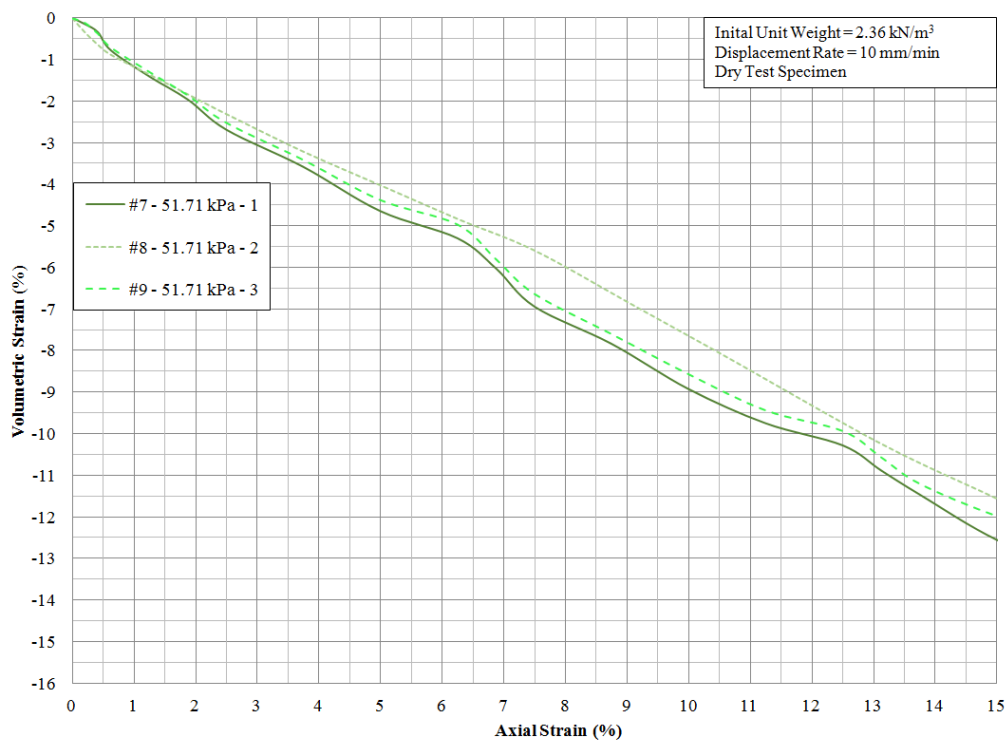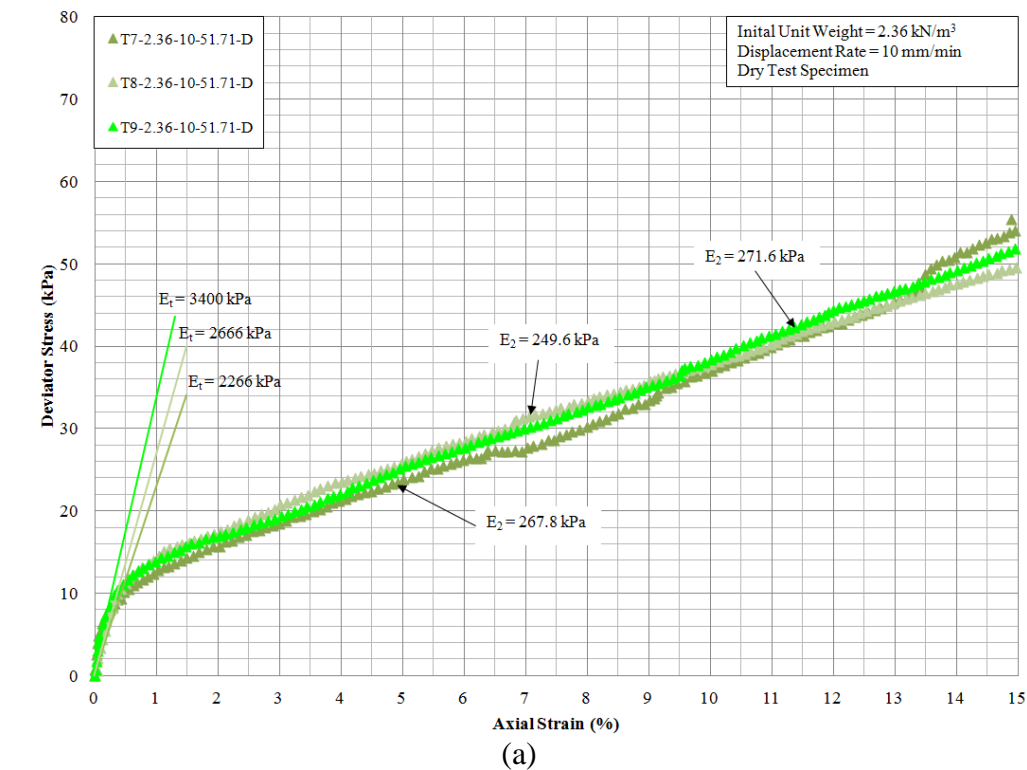
Figure 4.45: (a) Deviator stress as a function of axial strain for the 51.71 kPa confining stress; and (b) Volumetric strain as a function of axial strain for the 51.71 kPa confining stress
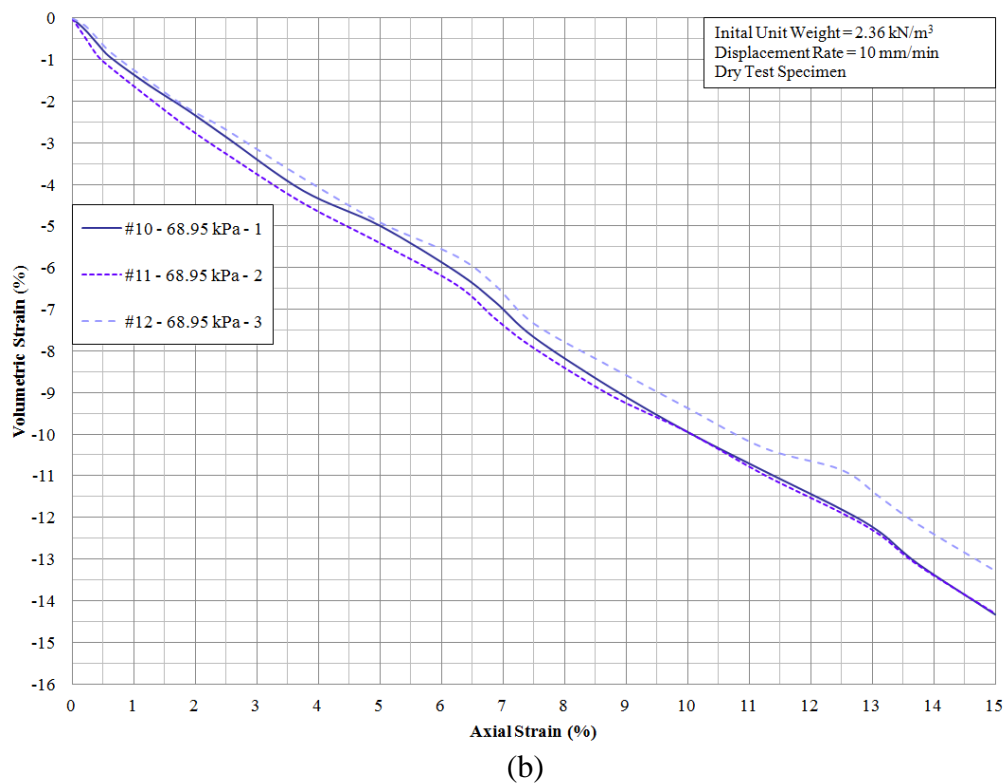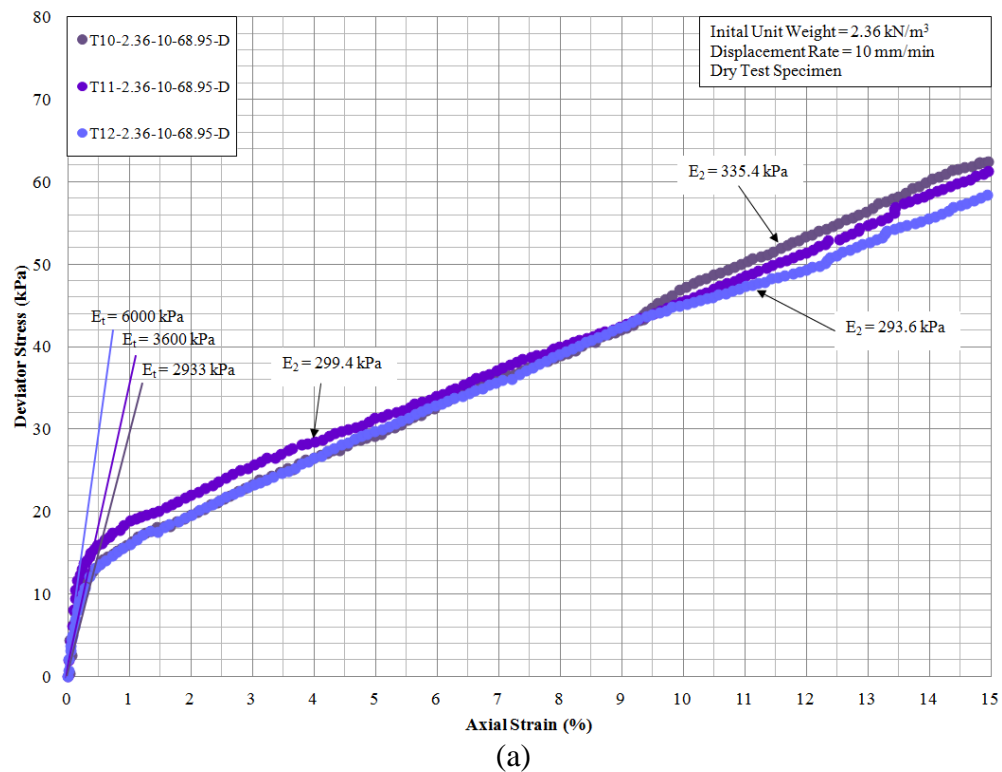
Figure 4.46: (a) Deviator stress as a function of axial strain for the 68.95 kPa confining stress; and (b) Volumetric strain as a function of axial strain for the 68.95 kPa confining stress

Figure 4.47 shows both moduli, E_t and E_2, as a function of each confining pressures (17.24 kPa, 34.47 kPa, 51.71 kPa, and 68.95 kPa). Figure 4.47(a) illustrates the first moduli's relationship. The first moduli does not show a correlation between confining pressure and the first moduli. Figure 4.47(b) displays the second moduli's relationship. The second modulus is proportional to the confining pressure whereas an increase in confining pressure results in an increase in second modulus or stiffness.
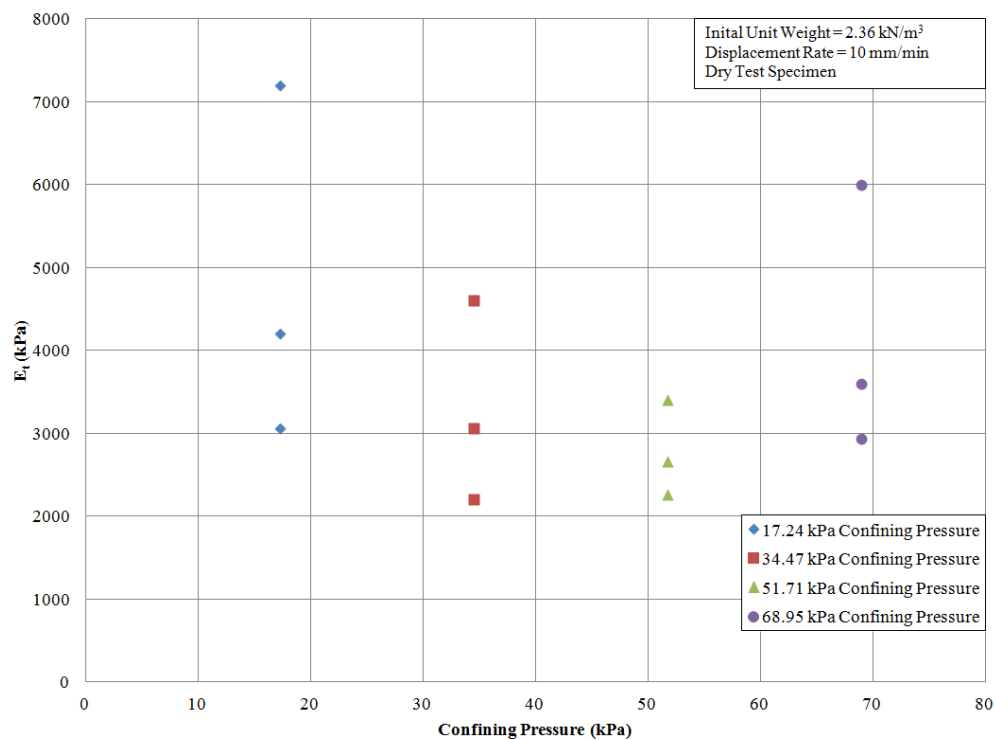
(a)
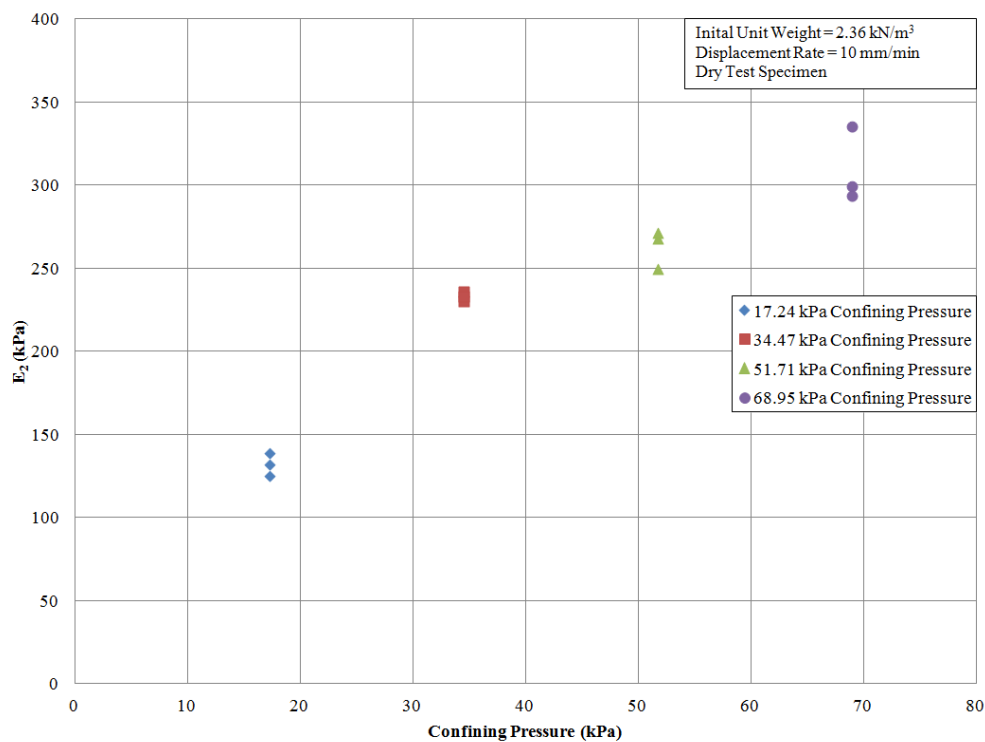
(b)

Figure 4.47: Moduli as a function of 17.24 kPa, 34.47 kPa, 51.71 kPa, and 68.95 kPa confining pressures and for a dry test specimen and a unit weight of 2.36 kN/m^3: (a) First moduli, E_t; and (b) Second moduli, E_2

4.4.2.2 Phase 2 Testing - Unit Weight Variations

Phase 2 of the triaxial testing component involved tests carried out to investigate the influence of the sample unit weight. Including tests from Phase 1 at unit weight of 2.36 kN/m^3 four additional tests were performed with unit weights of 1.89 kN/m^3, 1.73 kN/m^3, 1.57 kN/m^3, and 0.79 kN/m^3. All tests were tested at an effective confining stress of 17.24 kPa and a displacement rate of 10 mm/min. Figure 4.48 (a) illustrates the deviator stress as a function of the axial strain while Figure 4.48(b) illustrates the volumetric strain as a function of the axial strain for test specimens with different unit weights. Figure 4.54(a) displays a decrease in deviator stress proportional to the decrease in the unit weight. For example, the specimen with a unit weight of 2.36 kN/m^3 produced a deviator stress of 32 kPa at 15% axial strain while the specimen with a unit weight of 0.79 kN/m^3 produced a deviator stress of 7 kPa at 15% axial strain. Figure 4.48(b) illustrates that there is an increase in volumetric strain with decreasing sample initial unit weight. This is as expected as a less dense material would experience larger volumetric strains in comparison to a dense material. Furthermore, higher unit weight samples developed higher shear strengths in comparison to the materials with the lower unit weights. Recall that the range of unit weights produced from the MRF was 2.36 kN/m^3 - 3.93 kN/m^3. Similar to the previous figures, the axial strain level that represents the transition point between E_t and E_2 ranges between 0.25% and 0.5% axial strain.
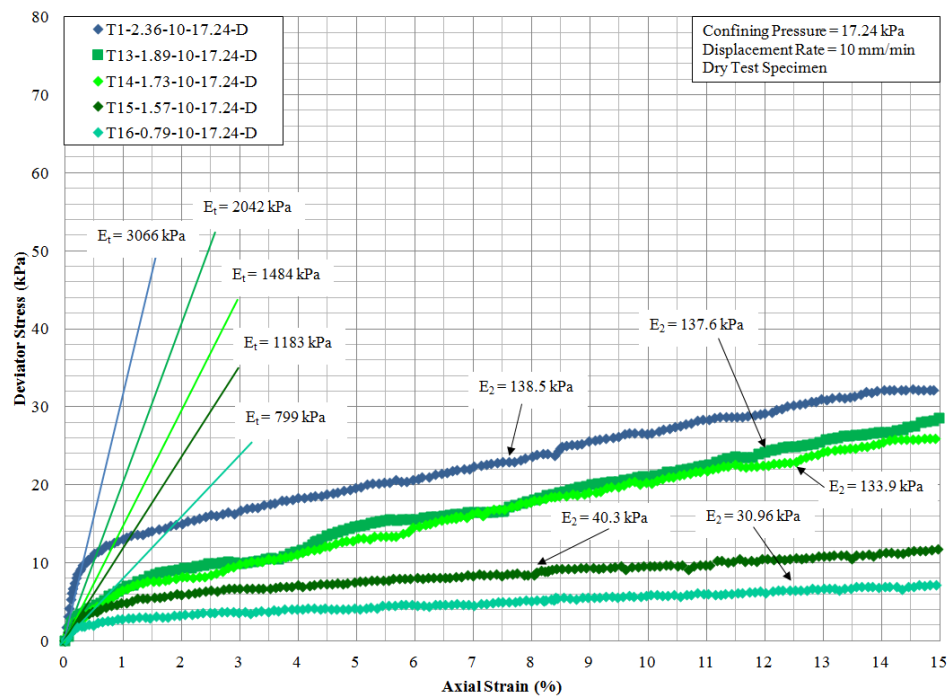
(a)
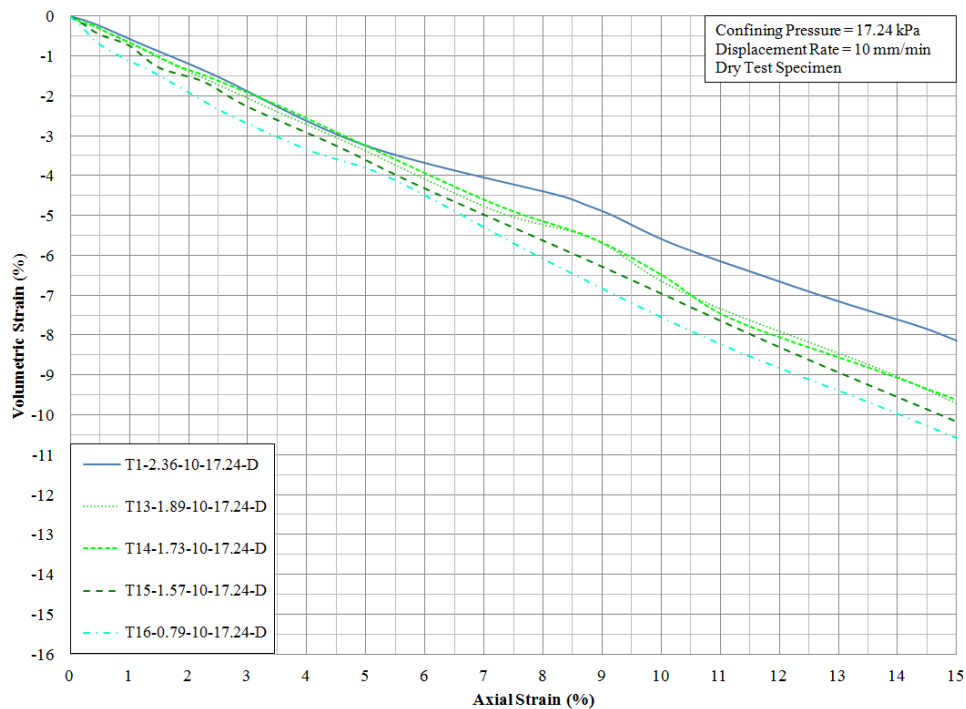
(b)

Figure 4.48: Summary of Phase 2 testing: (a) Deviator stress as a function of axial strain for various unit weight values under a 17.24 kPa confining stress; and (b) Volumetric strain as a function of axial strain for various unit weight values under a 17.24 kPa confining

Figure 4.49 shows the both moduli, E_t and E_2, as a function of each unit weight of 2.36 kN/m^3, 1.89 kN/m^3, 1.73 kN/m^3, 1.57 kN/m^3, and 0.79 kN/m^3.   Figure 4.49(a) illustrates the first moduli's relationship. The first moduli is proportional to the unit weight whereas a decrease in unit weight results in a decrease in first modulus or stiffness. Figure 4.49 (b) displays the second moduli's relationship. The second modulus is proportional to the unit weight whereas an increase in unit weight results in an increase in second modulus or stiffness.
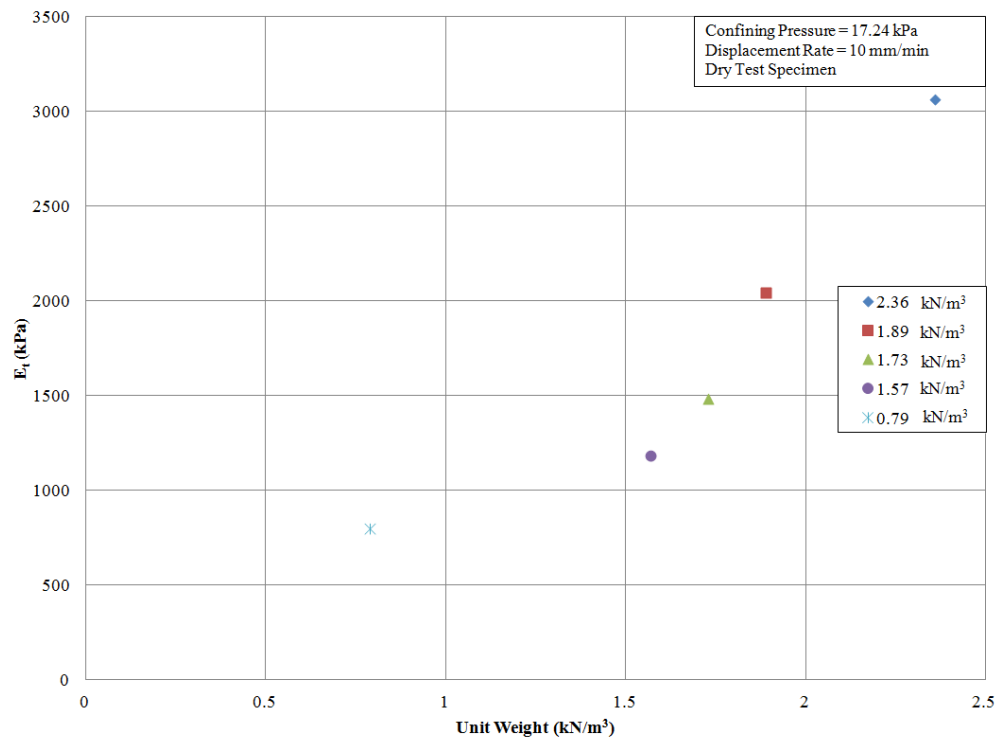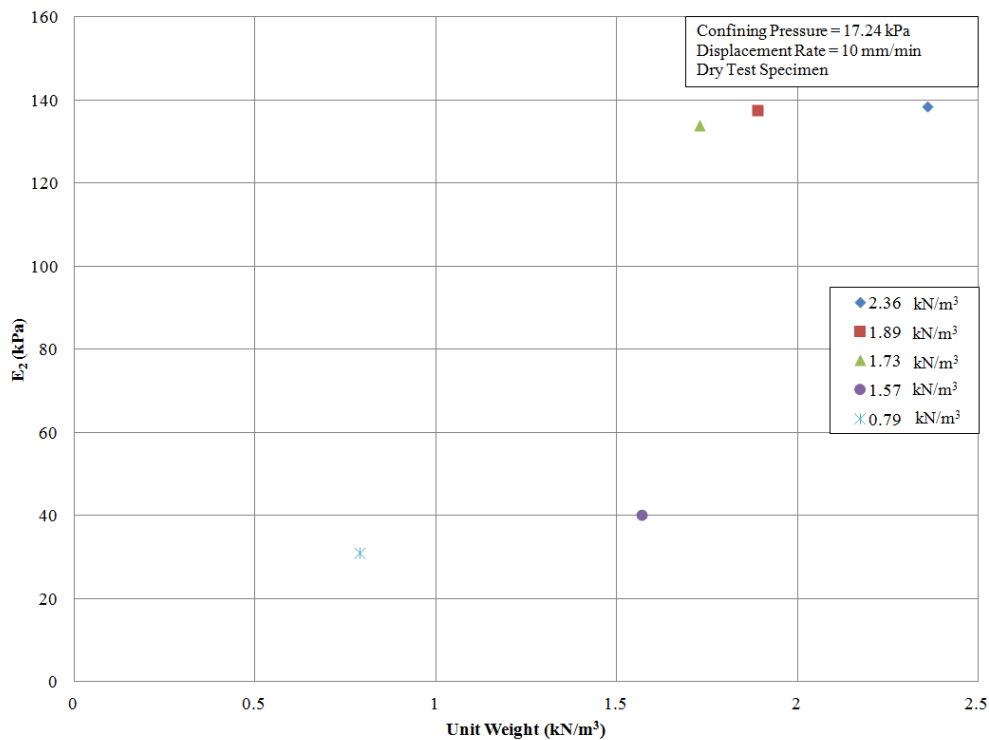
Figure 4.49: Moduli as a function of unit weight of 2.36 kN/m^3, 1.89 kN/m^3, 1.73 kN/m^3, 1.57 kN/m^3, and 0.79 kN/m^3 and with an effective confining pressure of 17.24 kPa: (a) First moduli, E$_t$; and (b) Second moduli, E$_2$

4.4.2.3 Phase 3 Testing - Displacement Rate Variations

Phase 3 of the triaxial testing component involved tests carried out to investigate the influence of the displacement rate. Figure 4.50(a) illustrates the deviator stress as a function of the axial strain while Figure 4.50(b) illustrates the volumetric strain as a function of the axial strain for the tests that varied displacement rate. As mentioned before, the displacement rates were 10 mm/min, 5 mm/min, 1 mm/min, 0.2 mm/min, and 0.02 mm/min with some limitations due to equipment. Figure 4.50(a) indicates that a slower displacement rate produces a lower deviator stress value at failure. For example, the 0.02 cm/sec displacement rate resulted in a deviator stress equal to 12 kPa at 15% strain. The test conducted using a 10 cm/sec displacement rate resulted in a deviator stress equal to 32 kPa at 15% strain. Figure 4.50(b) illustrates a consistent trend for the volumetric strain across the varying displacement rates. These results also produced a variation equal to +/- 5% across the five specimens that were examined. For 10 mm/min displacement rate, there was a -8.2% volumetric strain while the specimen examined using a displacement rate equal to 1 mm/min produced a volumetric strain equal to -8.3%.
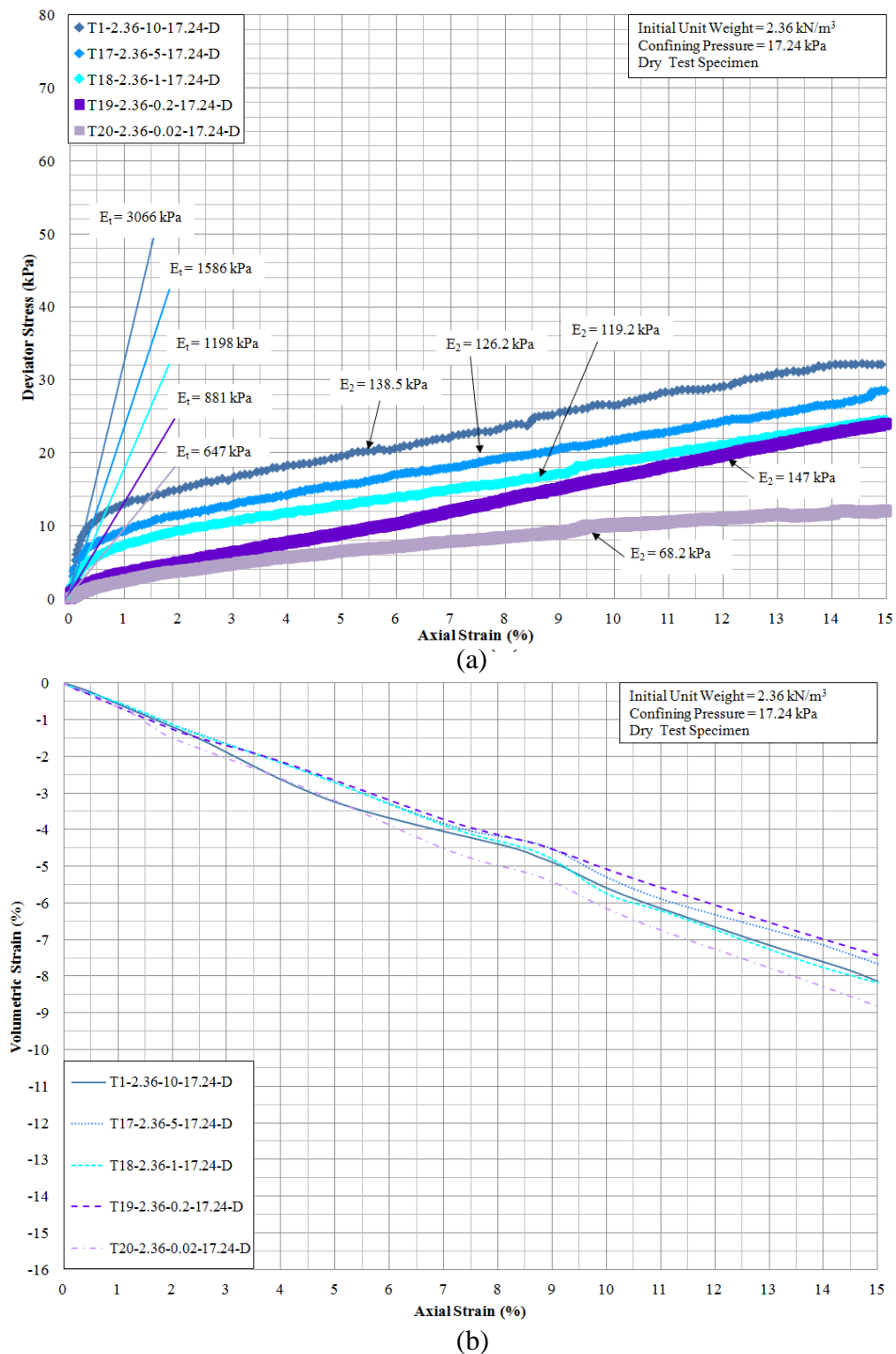
Figure 4.50: Summary of Phase 3 Testing: (a) Deviator stress as a function of axial strain for various displacement rates under a 17.24 kPa confining stress; and (b) Volumetric strain as a function of axial strain for various displacement rates under a 17.24 kPa confining pressure

Figure 4.51 shows the both moduli, E_t and E_2, as a function of each displacement rate of 10 mm/min, 5 mm/min, 1 mm/min, 0.2 mm/min, 0.02 mm/min. Figure 4.51(a) illustrates the first moduli's relationship. The first moduli is proportional to the displacement rate whereas a decrease in displacement rate results in a decrease in first modulus or stiffness. Figure 4.51(b) displays the second moduli's relationship. With the exception of the 0.2 mm/min displacement rate, the second modulus is proportional to the displacement rate whereas an increase in displacement rate results in an increase in second modulus or stiffness.
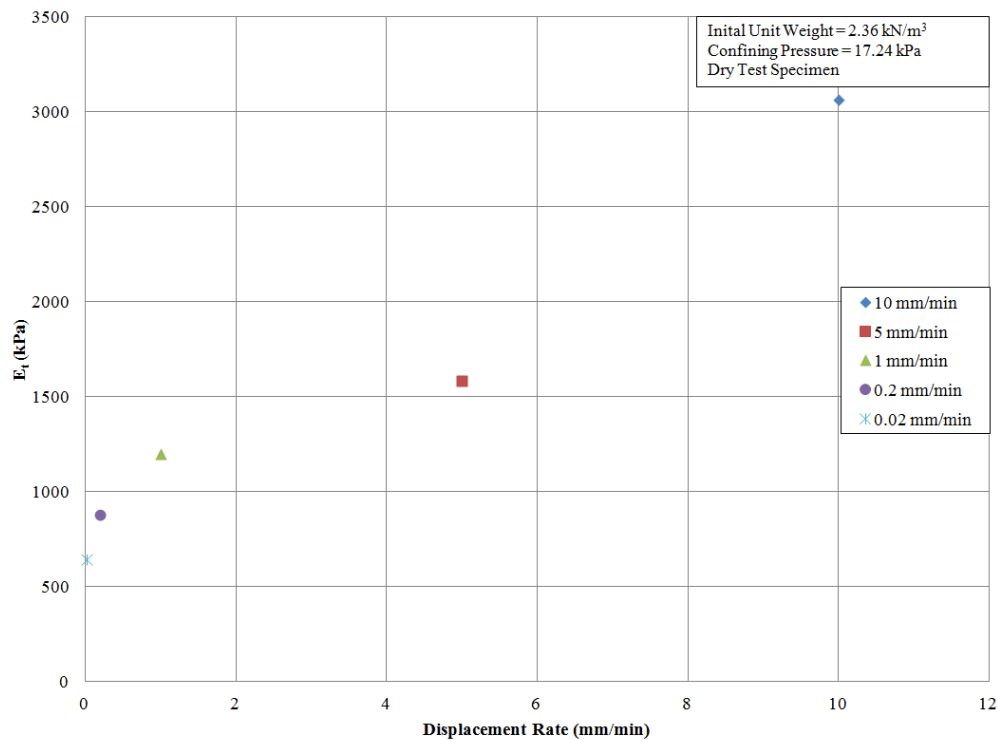
(a)
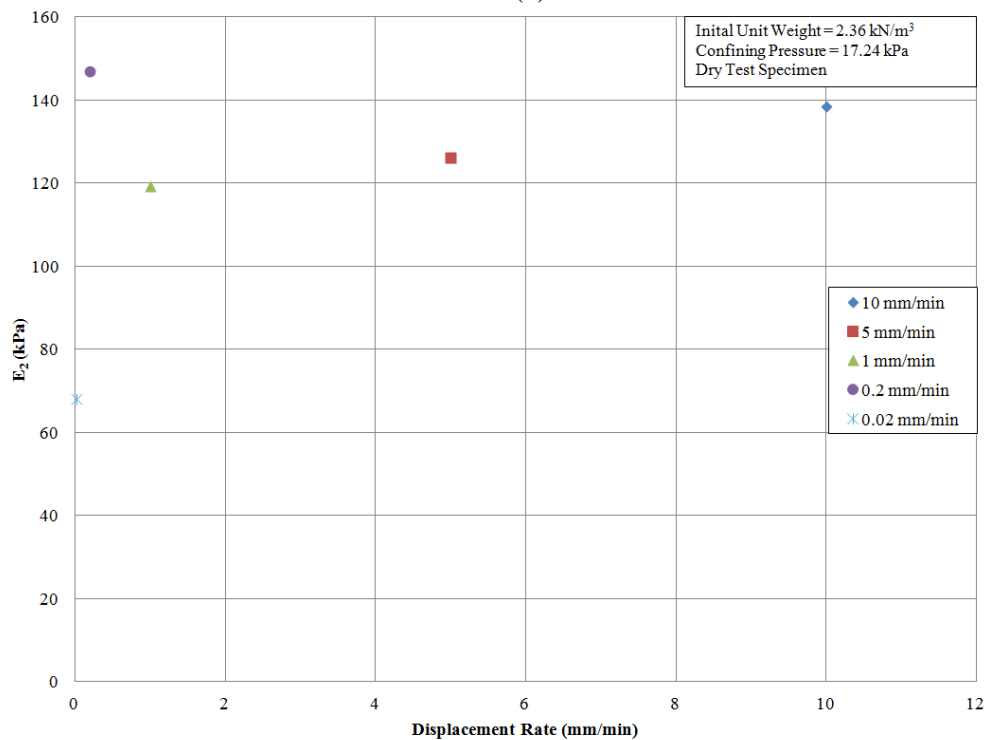
(b)

Figure 4.51: Moduli as a function of displacement rate of 10 mm/min, 5 mm/min, 1 min/mm, 0.2 mm/min, and 0.02 mm/min with an effective confining pressure of 17.24 kPa m^3: (a) First moduli, E$_t$; and (b) Second moduli, E$_2$

4.4.2.4 Phase 4 Testing - Saturation Variation

Phase 4 of the triaxial testing component involved tests carried out to investigate the influence of the saturation. Figure 4.52 shows the deviator stress as a function of the axial strain from zero to 1% to illustrate the variation in initial Young's moduli. For the test specimens tested under saturated conditions, Figure 4.53(a) illustrates the deviator stress as a function of the axial strain while Figure 4.53(b) displays the volumetric strain as a function of the axial strain. There does not appear to be a clear difference between the saturated and dry test specimens however, more experimental examinations are required to validate this hypothesis.

Figure 4.54 displays volumetric strain as a function of axial strain for the saturated testing conditions with a comparable test that had a dry test specimen. The unit weight and displacement rate were 2.36 kN/m^3 and 0.02, respectively. While the dry test specimens were conducted at a 0.02 mm/min displacement rate and the saturated test specimens were performed at a 0.03 mm/min displacement rate, results were similar.
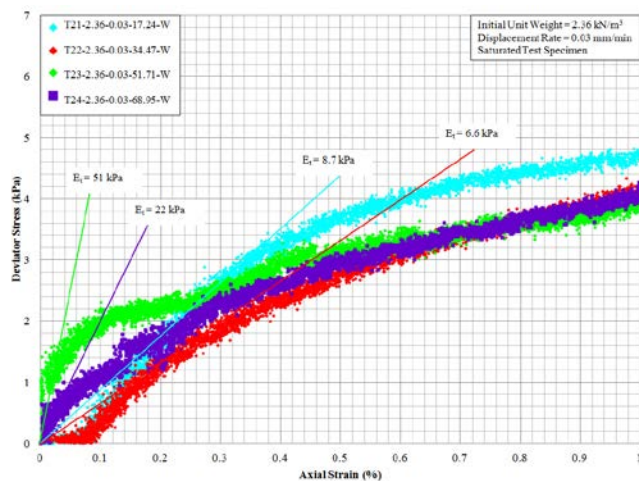
Figure 4.52: Summary of Phase 4 testing with deviator stress as a function of axial strain from 0 to 1%, for saturated testing conditions
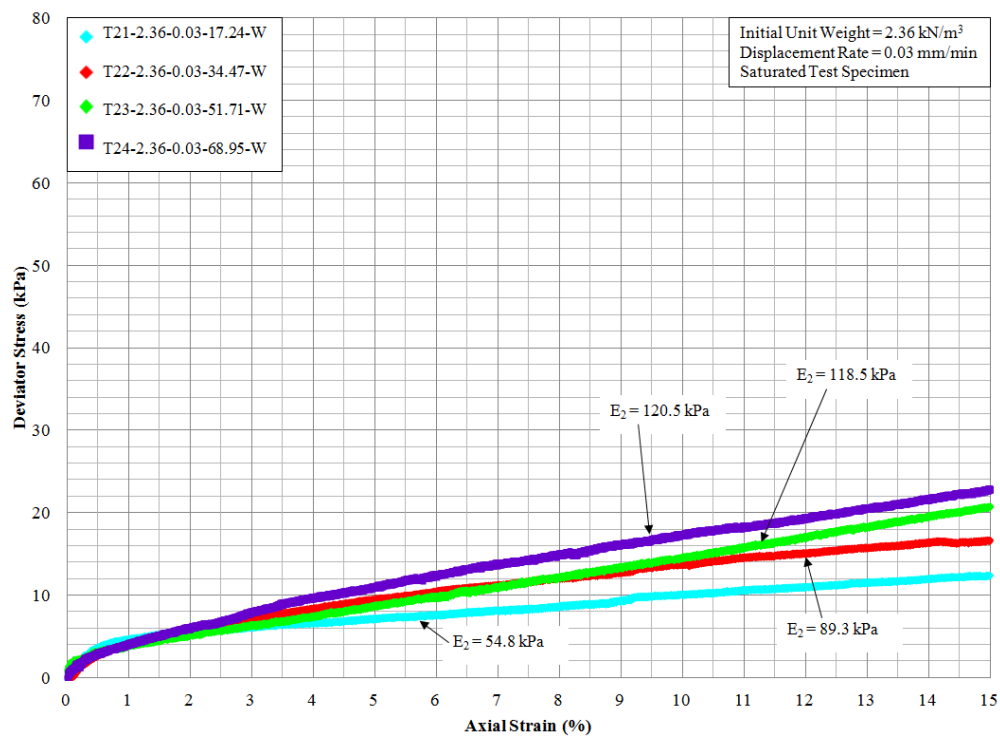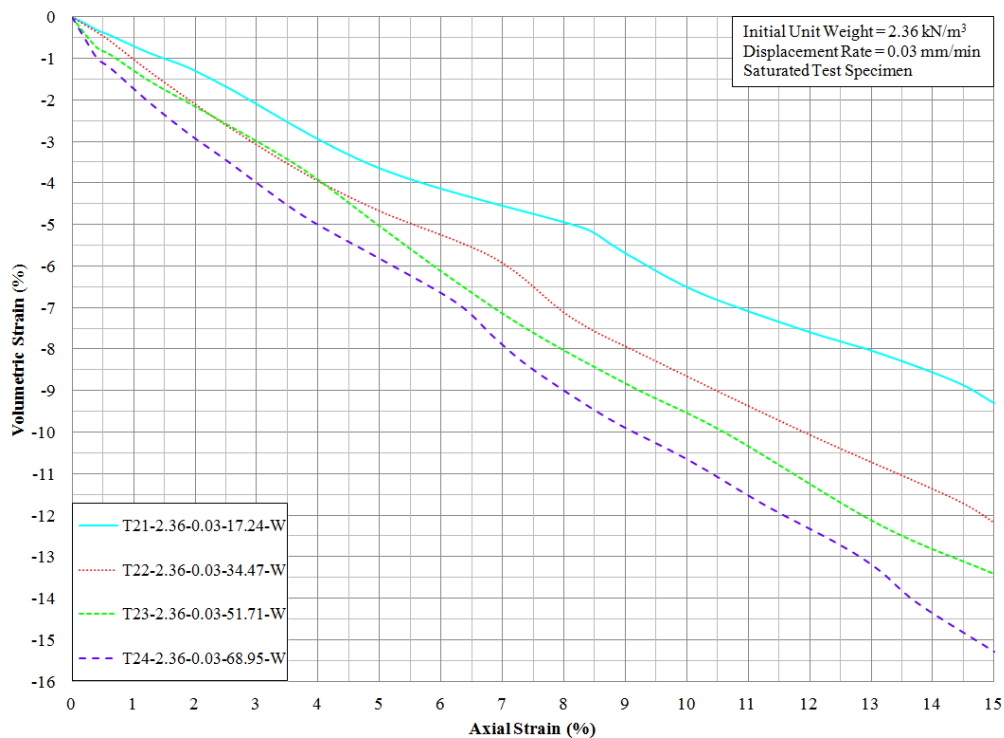
Figure 4.53: Summary of Phase 4 testing: (a) Deviator stress as a function of axial strain for saturated testing conditions; and (b) Volumetric strain as a function of axial strain for saturated testing conditions
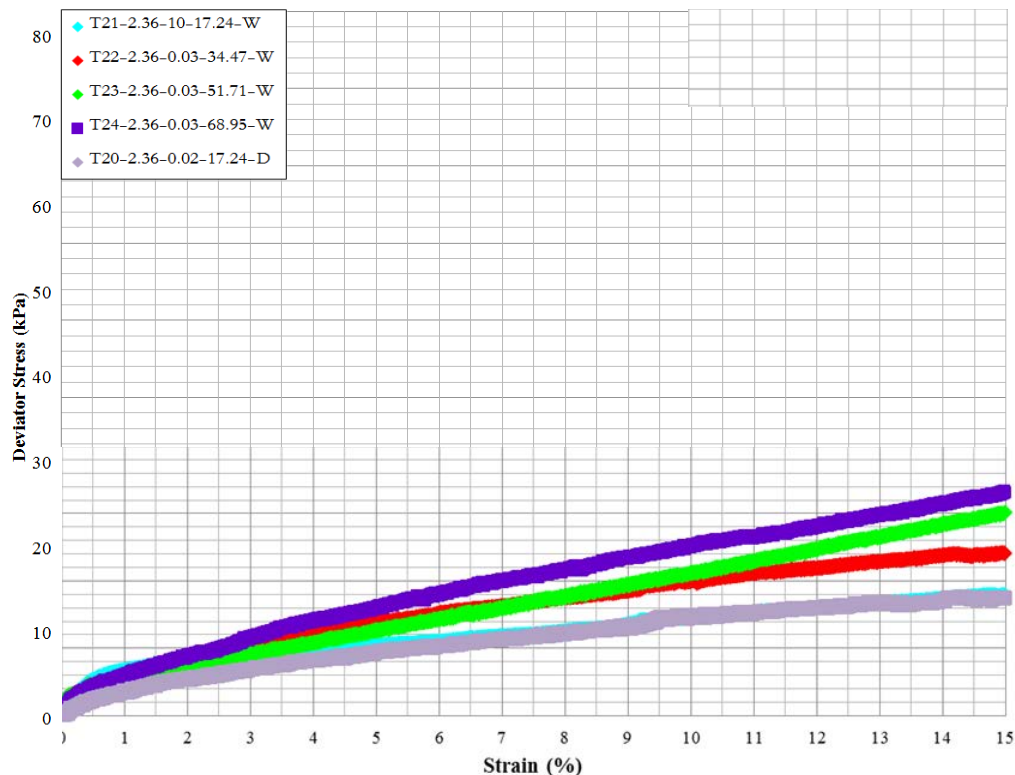
Figure 4.54: Deviator stress as a function axial strain for ASTM D7181 (2015) CD examination with dry specimen at same displacement rate for a unit weight of 2.36 kN/m^3

Figure 4.55 shows the both moduli, E_t and E_2, as a function of each confining pressures (17.24 kPa, 34.47 kPa, 51.71 kPa, and 68.95 kPa) for the saturated specimens. Figure 4.55(a) illustrates the first moduli's relationship. The first moduli does not show a correlation between confining pressure and the first moduli. Figure 4.55(b) displays the second moduli's relationship. For the saturated specimens, the second modulus is proportional to the confining pressure whereas an increase in confining pressure results in an increase in second modulus or stiffness.
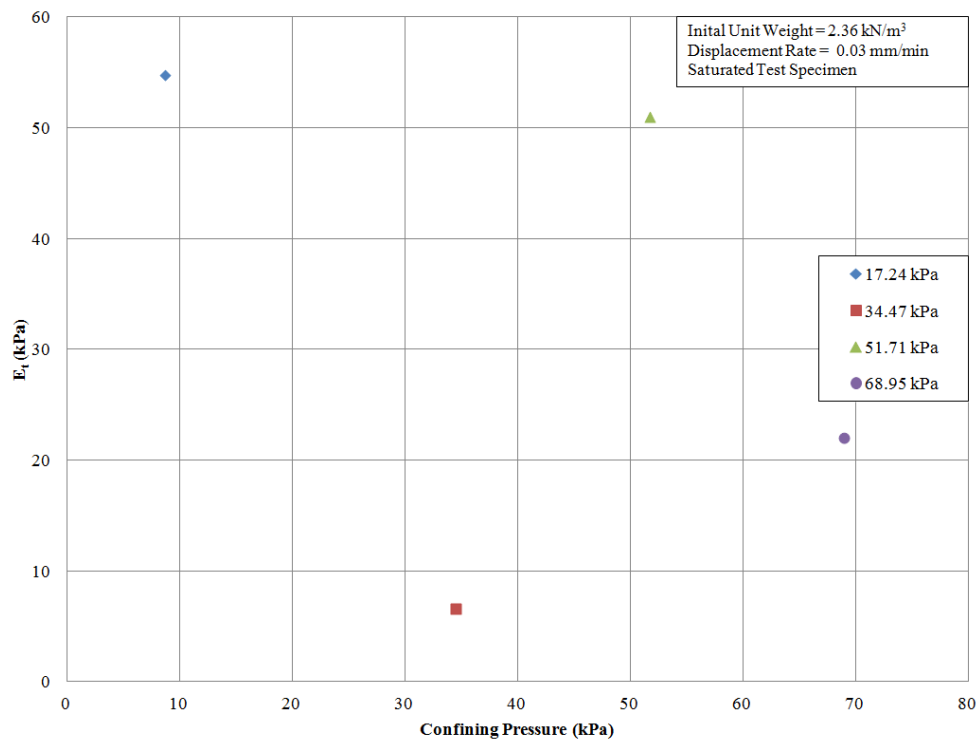
(a)
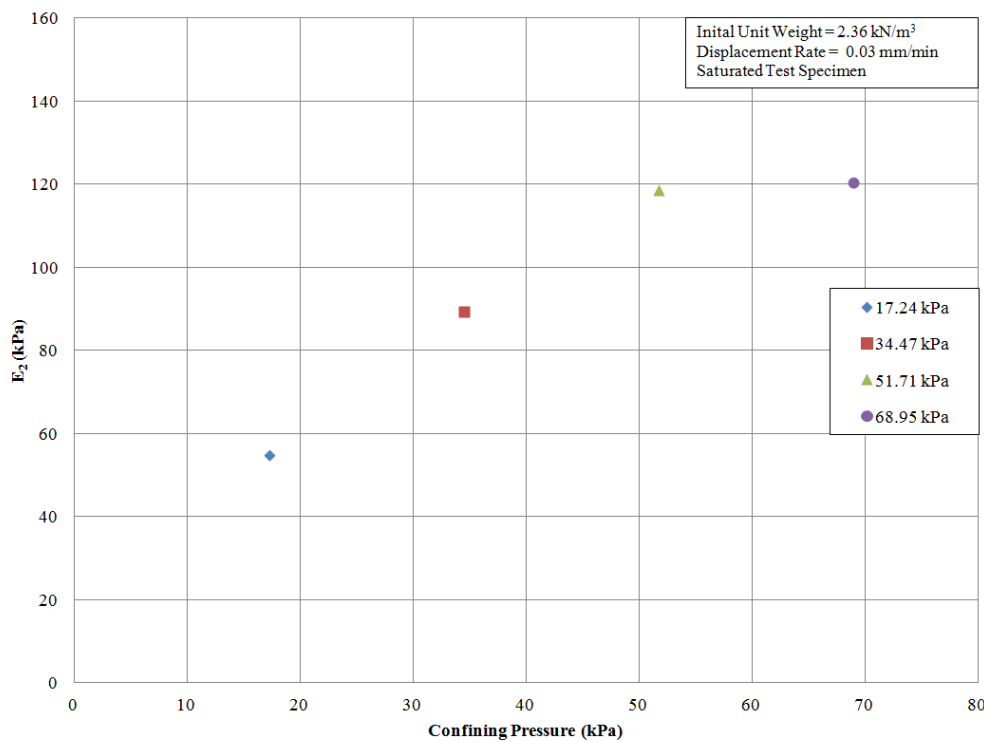
(b)

Figure 4.55: Moduli as a function of 17.24 kPa, 34.47 kPa, 51.71 kPa, and 68.95 kPa confining pressures and for a saturated test specimen and a unit weight of 2.36 kN/m^3: (a) First moduli, E_t; and (b) Second moduli, E_2

4.4.2.5 Shear Strength Characteristics from Triaxial Tests

The stress-strain data were analyzed to develop stress paths in the form of p'-q diagrams. Since the recycled PET plastic material does not have internal cohesion, the intercepts of the linear regressions were forced through zero. In addition, since the material did not exhibit pronounced failure peak or plane during the shearing phase, the shear strength parameters were selected based on a strain based failure criteria evaluated at axial strain levels of 5%, 10%, and 15%. Figures 4.56(a) and 4.56(b) were developed using the corresponding p' and q values from each stress-strain curve at the 5%, 10%, and 15% axial strain levels under dry and saturated conditions, respectively. The linear regression lines displayed in Figure 4.56 correspond to the kf-lines which have a slope inclination (α). The slope of these linear regression as well as the coefficients of linear regression are labeled adjacent to each series in each figure. The effective angle of internal friction (ϕ') was obtained using the following relationship with the angle of inclination from the p'-q diagrams:

$$\sin\phi' = \tan\alpha \qquad\qquad\qquad [4.13]$$

Where:
ϕ' = angle of internal friction
α = angle of inclination of k_f line in a p'-q diagram

Table 4.11 summarizes the shear strength results from the triaxial tests. Note that the friction angle for the axial strain level is significantly less than the friction angle for the larger stain level.
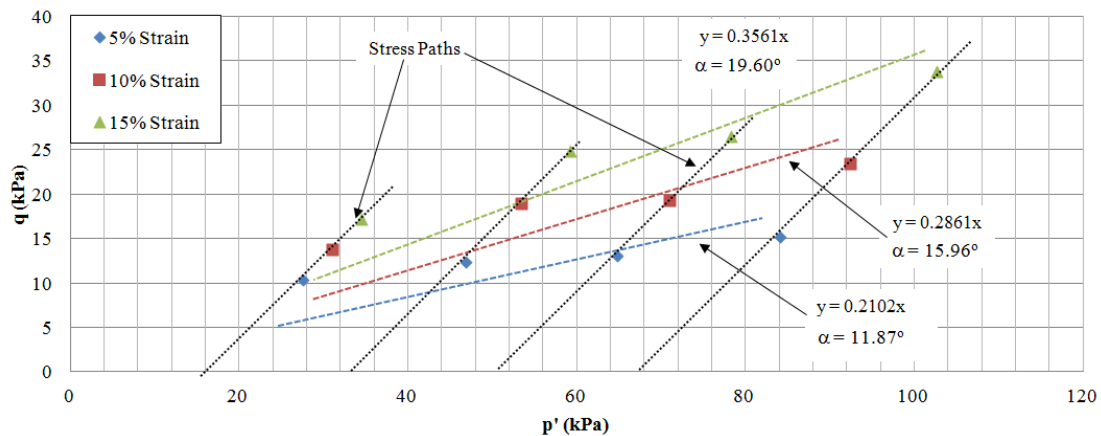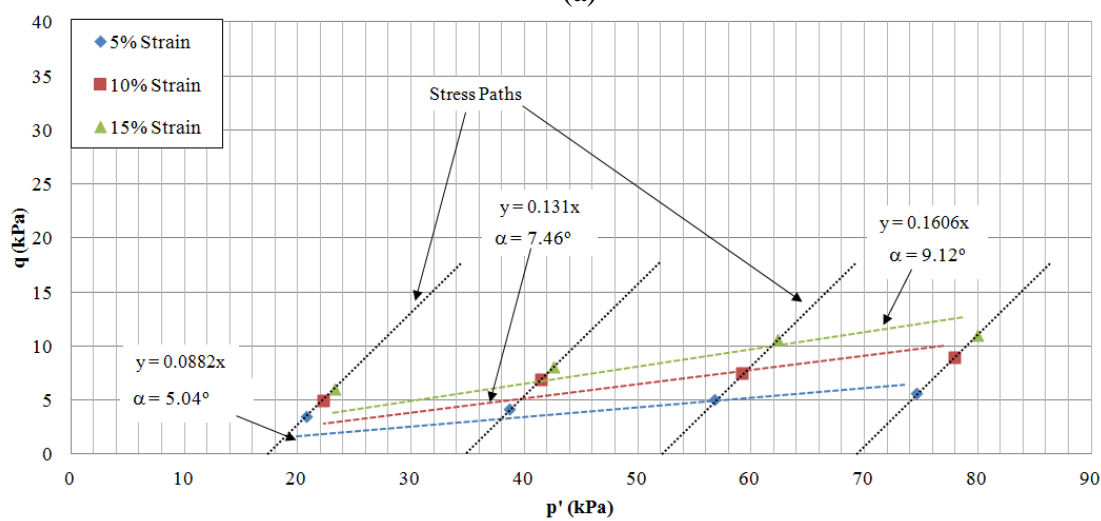
Figure 4.56: Triaxial shear strength p'-q diagrams with stress paths and linear regressions with no cohesion intercept: (a) dry conditions; and (b) saturated conditions

Table 4.11: Summary of the shear strength friction angles from triaxial testing

Strain Level (%)	Initial Unit Weight (kN/m^3)	Friction Angle (ϕ')[1] (degree)	Saturation (%)	Displacement Rate (mm/min)
5		*5.06*	*97.5*	*0.02*
		12.13	0	10
		12.49		
		12.58		
10	2.36	*7.52*	*98*	*0.02*
		16.62	0	10
		16.52		
		16.44		
15		*9.24*	*97*	*0.02*
		20.86	0	10
		20.22		
		19.98		

Notes: [1] Assuming no cohesion intercept

Similar to Figure 4.56, Figure 4.57 illustrates the identical p'-q diagrams for the dry and saturated test specimens, and was constructed to compare the two linear regression methods. The calculated linear regressions could either be forced through the y-intercept of zero or allowed to determine the y-intercept based on the data set. Figure 4.57 incorporated a linear regression that was not forced through a y-intercept of zero (c'=0) and displays apparent cohesion in the material. As indicated in this figure, the values associated with α, the slope of the linear regression, are not representative of the recycled PET's frictional properties yet displays the coefficient of correlations, R^2, above 0.94 for both the dry and saturated test specimens. Figure 4.56 does not show the coefficient of correlation due to the extremely low, if not negative values. However Figure 4.57 displays that the coefficients of correlations are significantly higher when allowing the linear regressions fits to have an apparent cohesion intercept when compared to forcing the y-intercept of zero.
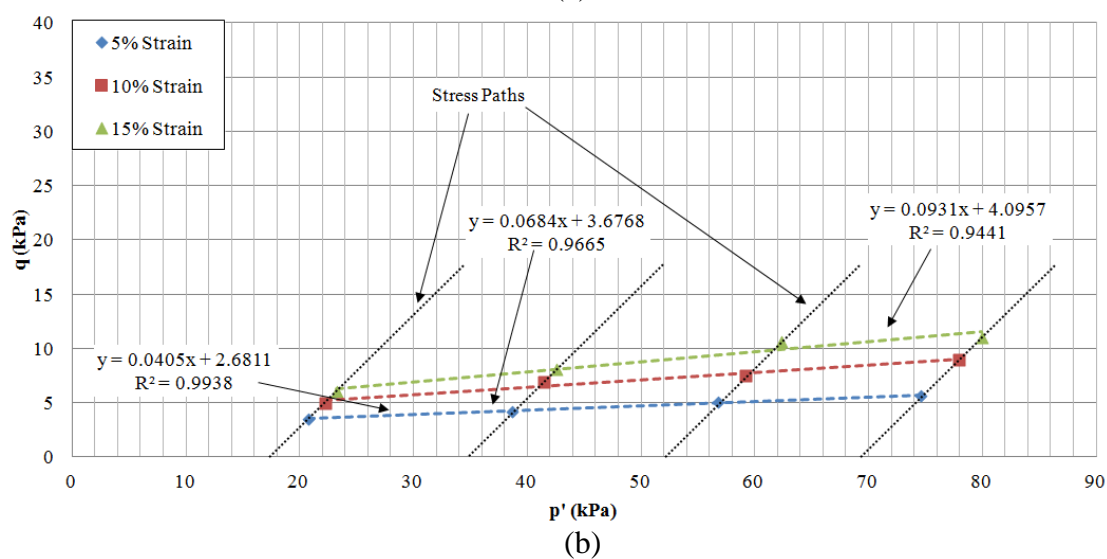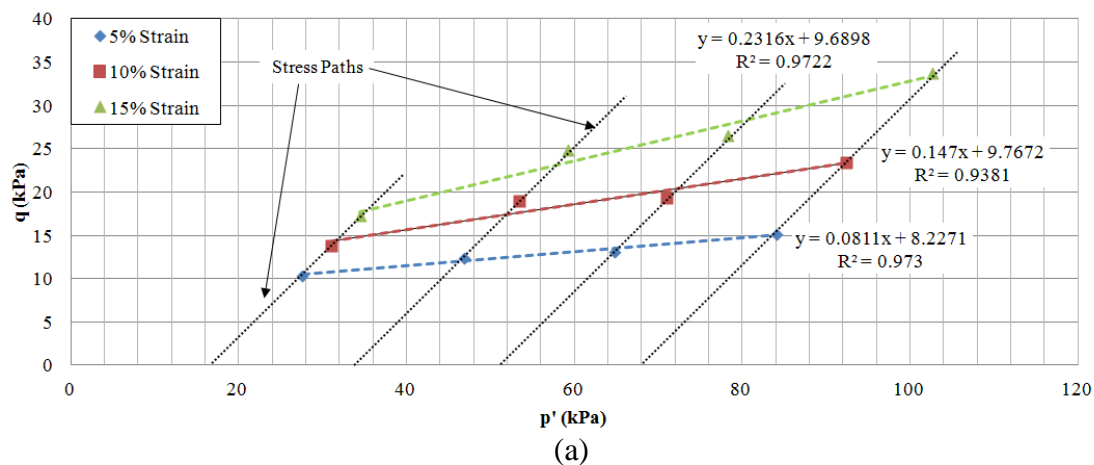
Figure 4.57: Triaxial shear strength p'-q diagrams with stress paths and linear regressions with an apparent cohesion intercept: (a) dry conditions; and (b) saturated conditions

Based on information acquired from the literature, average, minimum and maximum values of friction angle for 60 variations of plastic (including PET) are displayed in Table 4.12. These properties were evaluated using ASTM D1894 (2015). While the plastics were not recycled, they were manufactured specifically for packaging. The friction angles in Table 4.12 vary approximately 20° when all 60 types are considered, but the range narrows to 4° for the PET plastics cited. If failure is assumed at 5% strain, the friction angle calculated from this study and reported in Table 4.11 (12.49°) is similar to the friction angle reported in the literature and displayed in Table 4.12 (12.40°).

Table 4.12: Summary of friction angle for plastics

Performed Study	Plastic Type	Statistic	Friction Angle
Dotmar (2015)	60 types	Average	13.45
		Min	3.43
		Max	23.27
	Virgin PET	Average	12.41
		Min	10.76
		Max	14.04
Garbini (Current Study)	Recycled PET[1,2]	-	5.04
	Recycled PET[1,3]	Average	12.40
		Min	12.13
		Max	12.58

Notes: [1] 5% strain level and no cohesion intercept
[2] Saturated Specimen
[3] Dry Specimen

Figure 4.58 displays a bar graph of the friction angles collected from the literature and summarized in Table 4.12 in addition to the friction angles measured during the current study. All measured friction angles fall within the range of the 60 plastic types displayed in this figure while the average measured friction angle is similar to the PET plastic literature values. For example, the measured values for the 5%, 10% and 15% strain levels were 4.93º, 7.29º, and 9.25º, respectively, while the range of the values from the literature were 3.43º to 23.27º.
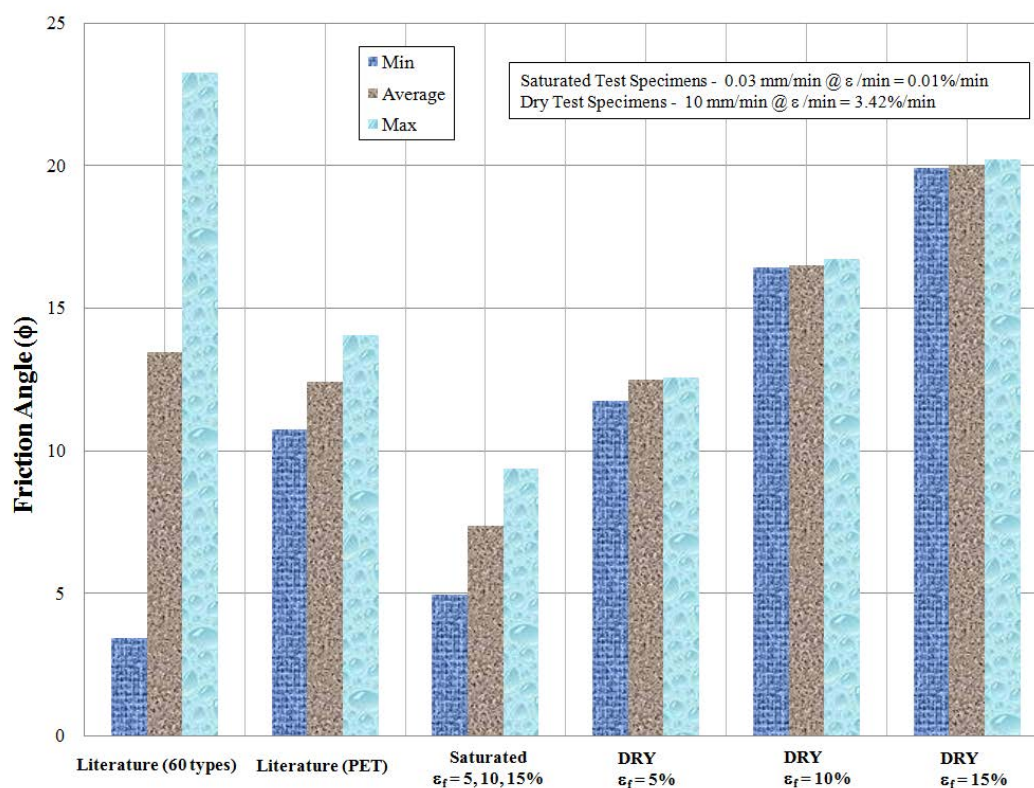
Figure 4.58: PET Friction angle from experimental research and literature review versus literature on plastic, literature on PET, saturated experimental research, and dry experimental research for 5%, 10%, and 15% strain values

4.4.3 Triaxial Compression Testing Summary

Reduced recycled PET constituents were utilized in the examination of the triaxial shear strength behavior to estimate the shear strength behavior of a bale of recycled PET. The reduced pieces were utilized to ensure a particle-particle interaction as a result of specimen's diameter. A modified version of D7181-11 - Standard Test Method for Consolidated Drained Triaxial Compression Test for Soils (2015) was implemented to determine the angle of internal friction between the aggregate pieces of recycled PET constituents. All tests specimens were prepared using a consistent process clearly defined in this chapter. The data was processed to generate the stress-strain relationships for test specimens randomly selected and tested at a variety of testing conditions (Table 4.10). Triaxial examinations were carried out across four independent suite of tests that examined the material's repeatability and the effects of varying the unit weight, displacement rate, and saturated testing conditions.

The results show that the material produces consistent results across four confining pressures (17.24 kPa, 34.47 kPa, 51.71 kPa, and 68.95 kPa) for the material's isotropic, stress-strain, and volumetric change during shearing behavior. In addition, the material's isotropic stress deviator stress, and volumetric change during shearing was proportional to the increase in confining pressure. The recycled PET material's isotropic modulus ranged from 260-285 kPa. The stress-strain curves from the triaxial compression tests exhibited a bi-linear behavior similar to the interface direct shear results.

The initial stress-strain modulus, E_t, produced a range of 6.6 kPa to 7200 kPa. The second moduli, E_2, from the triaxial stress-strain curves produced a range of 54.75

kPa to 335 kPa. The second moduli was also proportional to an increase in confining pressure. There was no correlation between the transition points from E_t to E_2 for all triaxial specimens. However, the axial strain level that represents the transition point between E_t and E_2 across all triaxial specimens ranges between 0.25% and 0.5% axial strain. This range was consistent for each triaxial specimen examined as part of this study. In addition, each failure strain level selected to calculate the friction angle (5%, 10%, and 15%) incorporated these transition points as it occurs during the initial portion of the stress-strain curve for all the triaxial test specimens.

The PET material exhibits an increase in volumetric strain which is proportional to the decrease in unit weight. In addition, the material exhibited an inverse relationship when comparing the deviator stress and the material's unit weight. In comparing dry and saturated test specimens the results indicate the recycled PET material under saturated test specimen produces the same results as compared to the dry test specimen.

The results from the triaxial examinations were analyzed for strain levels of 5%, 10%, and 15% using Figure 4.56 for the saturated conditions, producing a range of internal friction between 5° and 20° (Table 4.11). The friction angle values determined from this study were comparable to the values from the documented literature. Further research is needed to measure the bale-to-bale friction angle using a full-scale direct shear test configuration for comparison to the values reported herein.

CHAPTER 5: LARGE SCALE UNCONFINED COMPRESSION EXPERIMENT

5.1 Introduction

This chapter presents the results of a large scale unconfined compression experiment carried out on a full-scale recycled PET bale to assess its short-term and long-term deformation characteristics. This full-scale experiment was conducted outdoors in the yard of the EPIC Civil and Environmental Engineering department at UNC Charlotte. The full-scale recycled PET bale test specimen was subjected to five static vertical load increments while bale vertical deformations were monitored using string potentiometers over a 21 month time period. Short-term deformations were monitored during the first 48 hours. Long-term creep deformations were evaluated under a constant sustained vertical load during the remaining part of the testing period. This chapter describes the test material, test configuration and instrumentation, and methodology utilized to examine the short-term and long-term compressive behavior of a recycled PET bale. An in-depth presentation and discussion of the results is also included.

5.2 Large-scale Unconfined Compression Test Configuration and Procedure

The full-scale recycled PET bale test specimen utilized in this study, which weighed 5.14 kN, was acquired from the MRF. The length, width, and height of the bale were approximately 169.9 cm, 132.6 cm, and 80.1 cm, respectively, and it had a unit weight equal to 2.85 kN/m^3. This unit weight fell within the target 2.36 kN/m^3 - 3.93 kN/m^3 range reported by the MRF. Variability of the bales is discussed in Chapter 3. The PET bale test specimen was not modified prior to the test described herein.

Due to the size of the PET bale, large loads were required to perform a full-scale unconfined compression test.   In order to provide a stable foundation for the test specimen, three steel beams were set on the pavement and leveled using two steel plates under each beam. The plates were located in the middle section of beams. Figure 5.1 provides a close-up photograph of a steel member being leveled by two steel plates, which were approximately 30.5 cm x 30.5 cm x 2.5 cm in dimension.

Two Steel Plates

Figure 5.1: Photograph of a steel beam being leveled to serve as the foundation for the full-scale PET bale test specimen

The three steel beams were placed with a center to center spacing of 55 cm. After the three beams were in place and leveled, two sheets of treated plywood were positioned on top of the beams to provide a flat solid base to support the recycled PET bale across the three steel beams (see Figure 5.2).   For the purpose of illustrating the irregularities associated with each side of the PET bale, Figure 5.3 displays three photos with different perspectives of the recycled PET bale specimen after it was positioned on the steel beam foundation.

Figure 5.2: Photograph of the steel beam foundation constructed for the full-scale PET bale test specimen

Each PET bale was secured with multiple 12 gage steel wires. The number of wires on each bales typically varies between five and seven, depending upon the unit weight of the bale. Normally for bales from this MRF the higher unit weight bale required more straps. The straps were distributed evenly across the length of the bale. Figure 3.2 displays a close up image of a PET bale with dimensions.   The PET bale for this experiment had six steel straps.

(a)

(b)

(c)

Figure 5.3: Photograph of the full-scale recycled PET bale test specimen:
(a) facing east; (b) facing west; and (c) facing north

After the PET bale specimen was set on the steel beam foundation, two additional sheets of treated plywood were centered on the top to provide a loading surface for the weights (Figure 5.4(a)). Figure 5.4(b) displays the reinforcing steel rebar that was positioned on top of the plywood to provide a convenient method of attachment for the instrumentation (to be discussed in a subsequent section). Five rods of steel rebar (2.54 cm in diameter by 1.8 m in length) were secured across the width of the plywood with fasteners and two additional rods (0.9 m in length) were positioned orthogonally and secured to the ends of the plywood. Figure 5.4(b) displays the rebar configuration and the approximate position of each string potentiometer monitored during the test (Sensors 1-4).

(a)
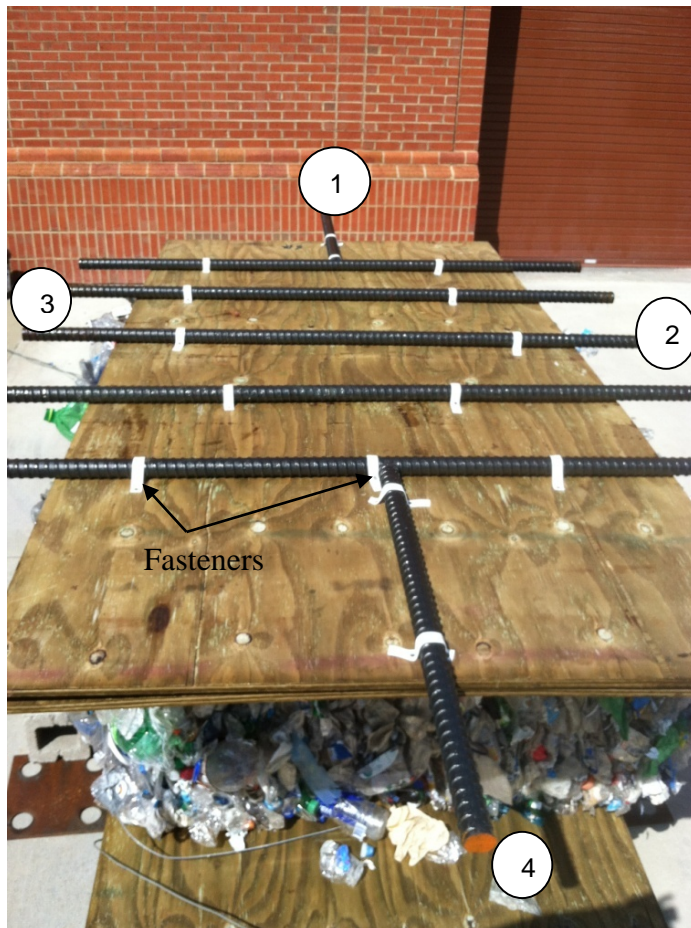
(b)

Figure 5.4: Photographs of the final unconfined compression test configuration prior to loading: (a) PET bale with plywood loading surface; and (b) rebar configuration

Four string potentiometers were attached to the PET bale specimen and monitored using a Hewlett-Packard desktop computer running LabVIEW (Version 8.6) to monitor vertical displacement on the four sides of the PET bale. Data was initially collected every 2 seconds to closely monitor vertical deformation of the PET bale specimen during initial stages of the test which included the application of the different load stages. After two months of data collection, the rate of change in vertical deformations tapered so data was only collected weekly. The specifications for all equipment and sensors utilized is included in Appendix A.

Figure 5.5 displays a close-up photograph of a string potentiometer utilized in this study. Recall that the four potentiometer measurement locations are identified in Figure 5.4(b). Each potentiometer sensor was positioned on a concrete block. The initial sensor setup involved extending the potentiometer string vertically up from the sensor and attached to the corresponding rebar that extended past the plywood platform on top of the PET bale specimen. The potentiometer string is barely visible in the photograph in Figure 5.5 so it has been labeled to improve clarity. Figures 5.6(a) and Figure 5.6(b) display all four string potentiometers from two different angles.
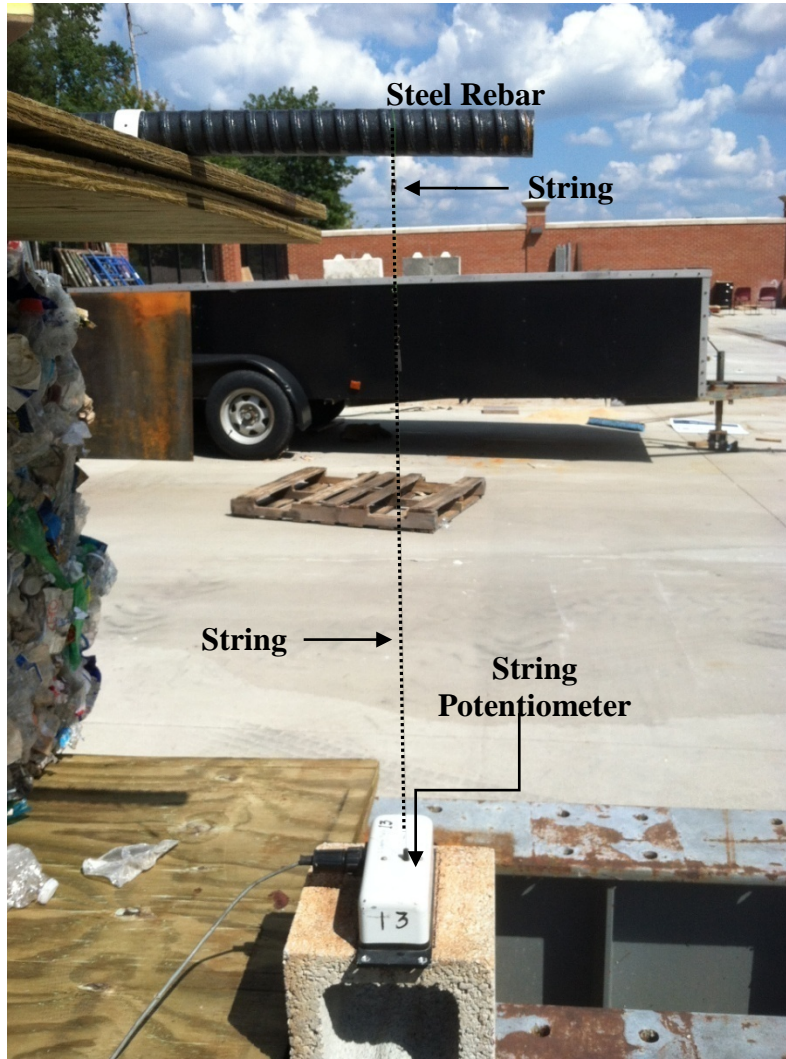
Figure 5.5: Photograph of a string potentiometer installed

(a)

(b)

Figure 5.6: Photograph of the instrumented, full-scale PET bale test specimen: (a) facing south; and (b) facing east

The PET bale test specimen was loaded incrementally to ensure the test configuration remained stable and safe. A large steel member and four large concrete loading blocks were used as dead weight loading to load incrementally the full-scale test specimen. Prior to placement, each load component was weighed using a Cambridge Scale Works floor scale (Model 660). Figures 5.7(a) and 5.7(b) display photographs of the short-term and long-term load configurations, respectively. While the interlocking mechanisms on the tops of the concrete blocks displayed in Figure 5.7(b) provided a surface to better secure the second row of concrete blocks displayed in Figure 5.7(a), the top two concrete blocks displayed in Figure 5.7(a) were removed 90 minutes after they were positioned. It was determined that the load configuration displayed in Figure 5.7(a) was unstable (see Figure 5.8). The inclination of the concrete blocks rotated approximately 4° in that 90 minute time period.

Table 5.1 summarizes the weight of each load component displayed in Figure 5.7, the order in which the loads were added, the cumulative stress level applied on the 2.25 m^2 surface area of the top face of the bale, and the cumulative loading time. For example, the W36 steel member, load 1, was in position for approximately 5 minutes (0.08 hours) before the 1st concrete block, load 2, was added. Outside of the initial plywood and steel rebar placement, there were five major loads added and one major load taken off before the final, long-term load configuration was established. The long-term vertical stress maintained on to the bale was approximately equal to a normal vertical stress of 23 kPa.

(a)

(b)
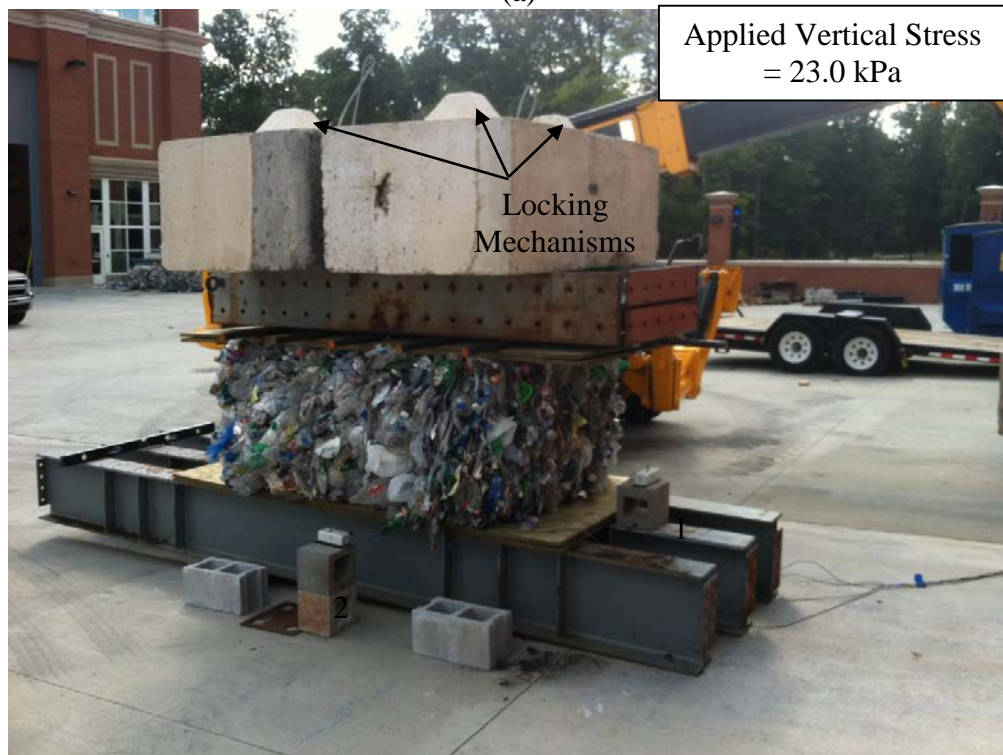
Figure 5.7: Photograph of the loaded PET test specimen: (a) initial 90 minute 42.4 kPa load configuration (σ_v= 42.4 kPa); and (b) long-term 23.0 kPa load configuration (σ_v= 23.0 kPa)

Figure 5.8: Photograph of the loaded PET test specimen exceeding a reasonable angle of inclination

Table 5.1: Summary of the loading scheme for the unconfined compression test conducted on a PET bale

Load Component	Weight Added (kN)	Cumulative Applied Stress [1] (kPa)	Cumulative Time (hr.)
Nothing on Top of Test Specimen	0	0	0
Plywood & Steel Reinforcement	0.7	0.3	1
Load 1 = W36 Steel Member	7.6	3.7	1.017
Load 2 = 1st Concrete Block	21.4	13.2	1.025
Load 3 = 2nd Concrete Block	22.1	23.0	1.117
Load 4 = 3rd Concrete Block	21.9	32.7	1.294
Load 5 = 4th Concrete Block	21.8	42.4	1.5
Unload 6 = 3rd and 4th Concrete Blocks	(-43.7)	23.0	15,330 (21 months)

[1]Applied stress values based on weight of component and loading area of 2.253 m^2

5.3 Short-term, Unconfined Compression Test Results and Discussion

All data presented in this section is representative of the short-term (initial 90 minute) load-displacement data before the last two concrete blocks were removed displayed in Figure 5.7(a). Figure 5.9(a) displays the short-term load-displacement data. While Figure 5.9(b) shows the corresponding loading schedule. For these data, the final applied vertical stress is equal to 42.4 kPa.

Due to the safety concerns and complications associated with the loading process, each load component was monitored carefully before positioning another load. The effects of this loading scheme are visible in Figure 5.9(a). For example, the steel beam was applied at 7.2 sec (0.002 hours). As a result, potentiometer curves displayed in Figure 5.9(a) for sensors 2 and 3 illustrate compression behavior while sensors 1 and 4 illustrate expansion. Each load application generated differential displacements and fluctuations in the average strain as recorded by the four string potentiometers.

Similar to Figure 5.9, Figure 5.10 displays the same data but they are organized in reference to each axis of the bale. The long axis is represented by potentiometers 1 and 4 so the data from these sensors are averaged to depict the long axis curve on this figure. Likewise, the short axis is represented by potentiometers 2 and 3. The data from all four locations are averaged to generate the 'average' curve displayed in Figure 5.10(a). Figure 5.10(a) also illustrates the differential displacements for every applied stress corresponding to each axis (long and short). Differential displacements are likely caused by the variations in the PET bale constituents within the bale medium, which includes randomly compacted Category 1, 2, and 3 recycled constituents as discussed in Chapter 3. For example, sensor 1 measured a 13.6% strain value while the other three sensors

measured strains equal to 4.3%, 3%, and -8.1%. Similar patterns existed during the four

remaining load increments.

(a)
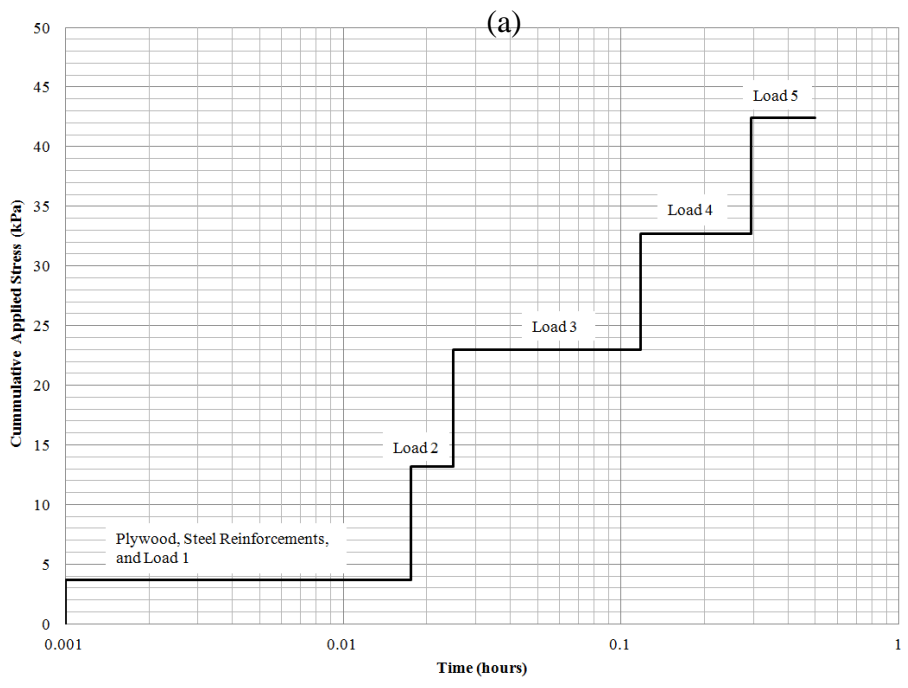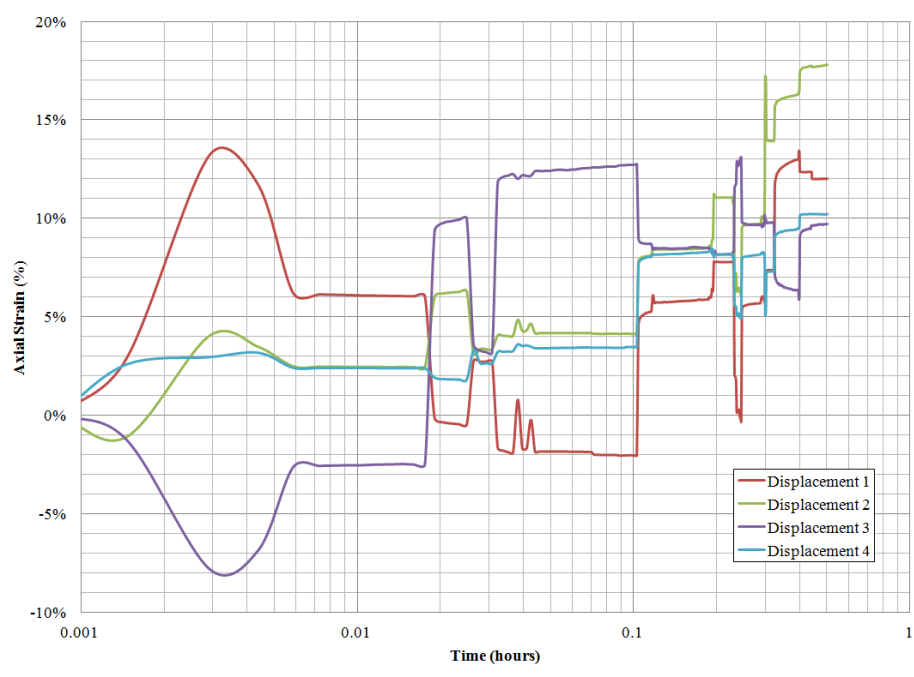
(b)

Figure 5.9: Initial load-displacement data as a function of time during the unconfined compression test, 0 - 90 minutes: (a) strain for sensors 1-4; and (b) cumulative applied stress

(a)

(b)
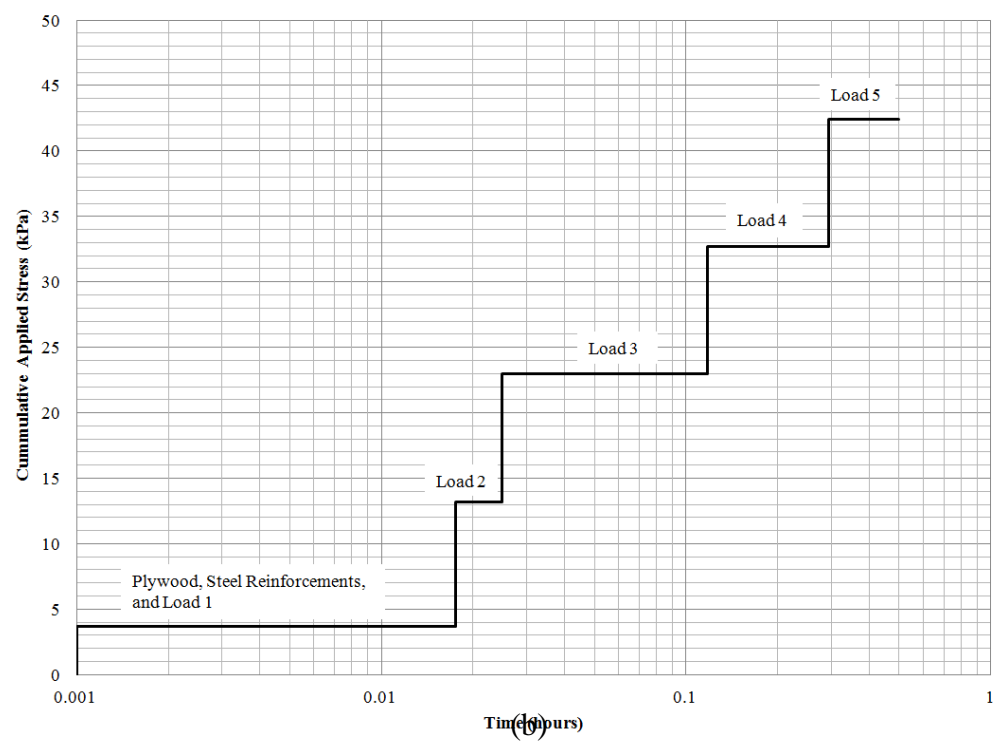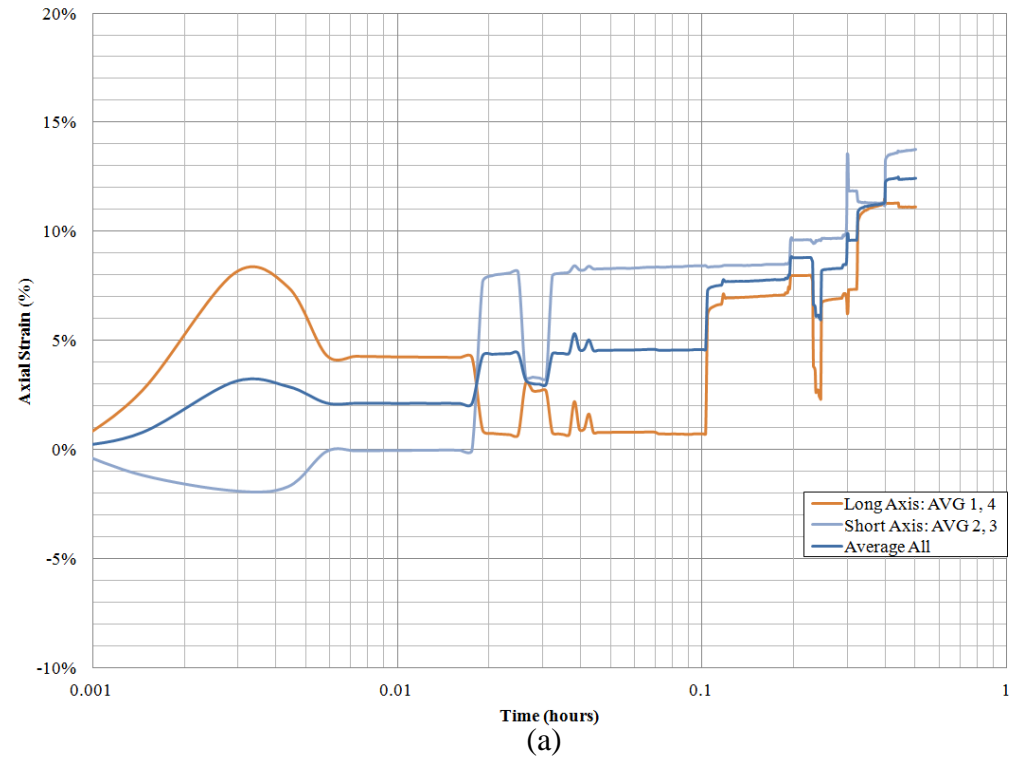
Figure 5.10: Initial load-displacement data as a function of time during the unconfined compression test, 0 - 90 minutes: (a) average strain for the long and short axis; and (b) cumulative applied stress

The solid curve in Figure 5.11 depicts the applied vertical stress as a function of the mean vertical axial strain (i.e., data averaged from all four potentiometers) for the recycled PET bale test specimen during the first 90 minutes of loading. Each part of the solid curve represents one of the applied load increments displayed in Table 5.1. For example, when the W36 steel member was applied to the specimen with an initial height equal to 78.74 cm (Load 1 in Table 5.1), it increased the vertical stress level to 3.4 kPa and caused string potentiometers 1, 2, 3, and 4 to displace 2.46 cm, 4.83 cm, 1.90 cm, and -2.01 cm, respectively. A positive reading is compression and a negative reading is an extension. The average displacement of these four sensors was 1.80 cm and the corresponding average axial strain was approximately equal to 2.28%. A secant Young's Modulus (E) was calculated for each load increment; the secant modulus values are displayed on Figure 5.11 and summarized in Table 5.2.

Figure 5.11 also displays dashed boundary lines above and below the data points. The slopes of these two lines could be viewed as the lower and upper limits of Young's modulus for the unconfined compression behaviors associated with the recycled PET test bale. A third dashed regression line processed through the data displayed in Figure 5.11 depicts an average modulus value equal to 333.3 kPa.
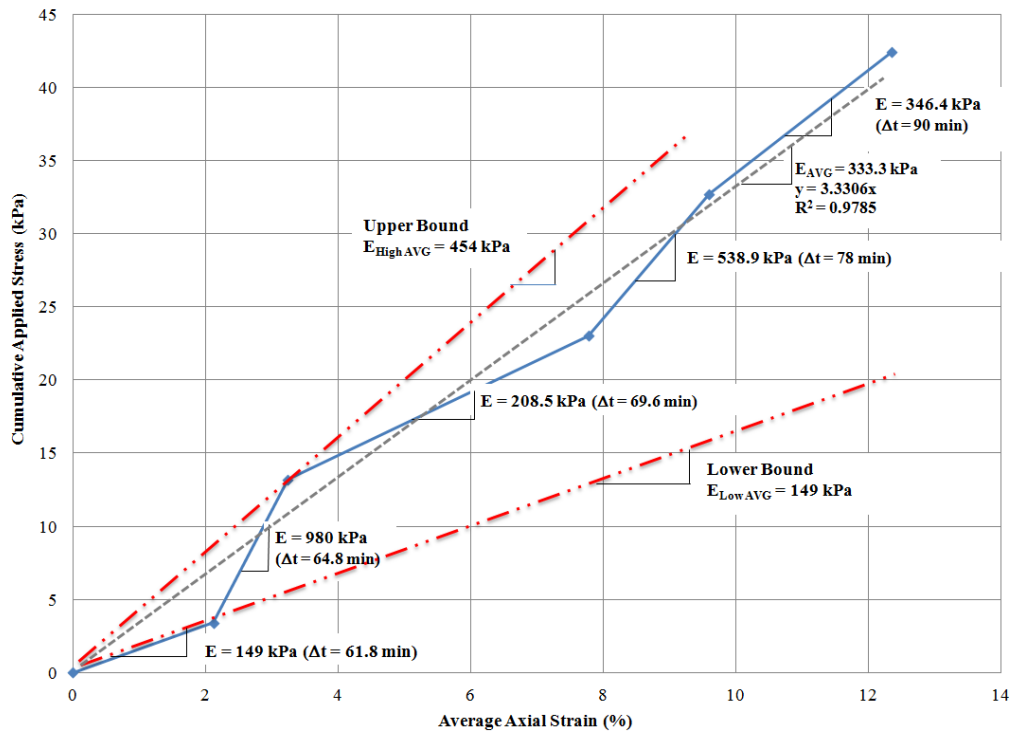
Figure 5.11: Initial applied vertical stress as a function of average axial strain for the PET bale during the full-scale unconfined compression test

Table 5.2: Summary modulus values (E) calculated during the short-term, unconfined compression test

Load Component	Weight Added (kN)	Cumulative Vertical Stress (kPa)	Average Vertical Strain (%)	E (kPa)
Plywood & Rebar	0.7	0.3	0.0	-
				149.0
Load 1	6.9	3.4	2.28	
				980.0
Load 2	22.1	13.2	3.1	
				208.5
Load 3	22	23.0	7.8	
				538.9
Load 4	21.9	32.7	9.6	
				346.4
Load 5	21.8	42.4	12.4	
			Average:	333.3

After the initial total vertical stress was applied to the test specimen, elapsed time of 90 minutes, the data collection intervals were decreased to each hour for the first two weeks of the unconfined compression test. Figure 5.12 illustrates the axial strain as a function of time for the first three days after the initial applied vertical stress displayed in Figures 5.9 and 5.10. Similar to those figures, Figure 5.12(a) and Figure 5.12(b) illustrates the axial strain as a function of time for all four sensors and the averages, respectively. As shown in Figure 5.12, the unconfined compression test shows a sharp increase in axial strain for the first 24 hours after the initial applied vertical stress. After which the rate of change in axial strain gradually decreases as it approaches the 72 hour time stamp.

Table 5.3 summarizes comparable Young's modulus values (E) for other materials obtained under unconfined compression loading. Additionally, according to ASTM D6817, (2015), the minimum unconfined Young's Modulus for EPS40 Geofoam is 580,000 kPa, which is approximately 1740 times higher than the stiffness measured for the PET bale.
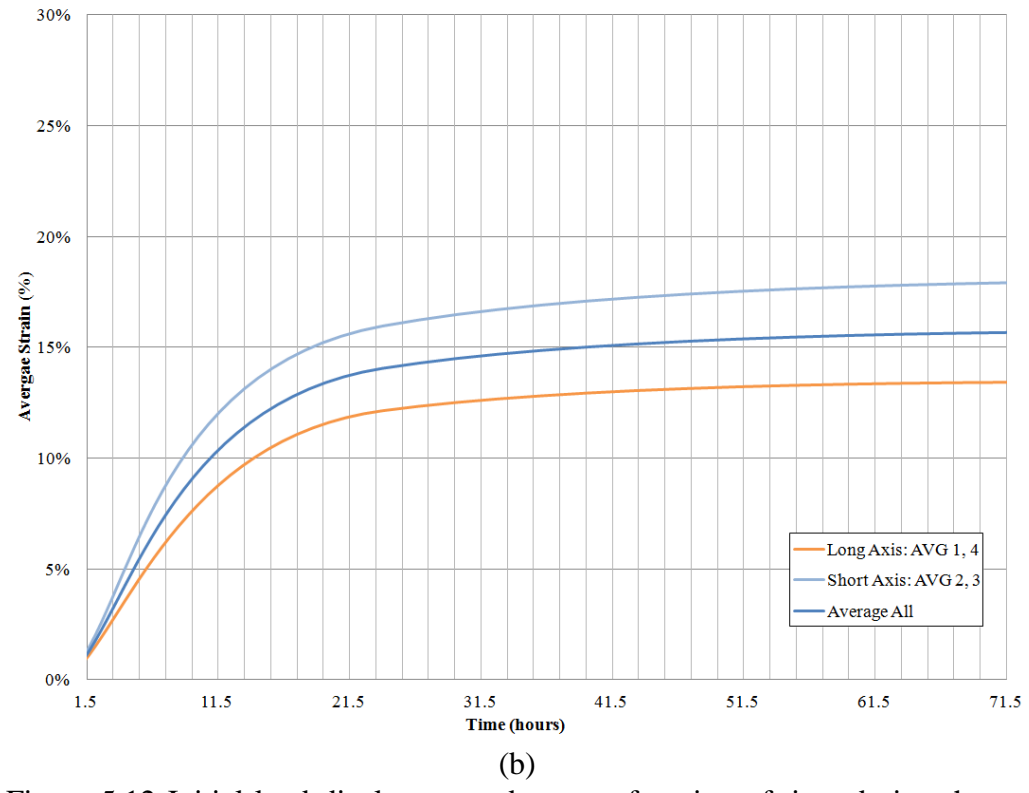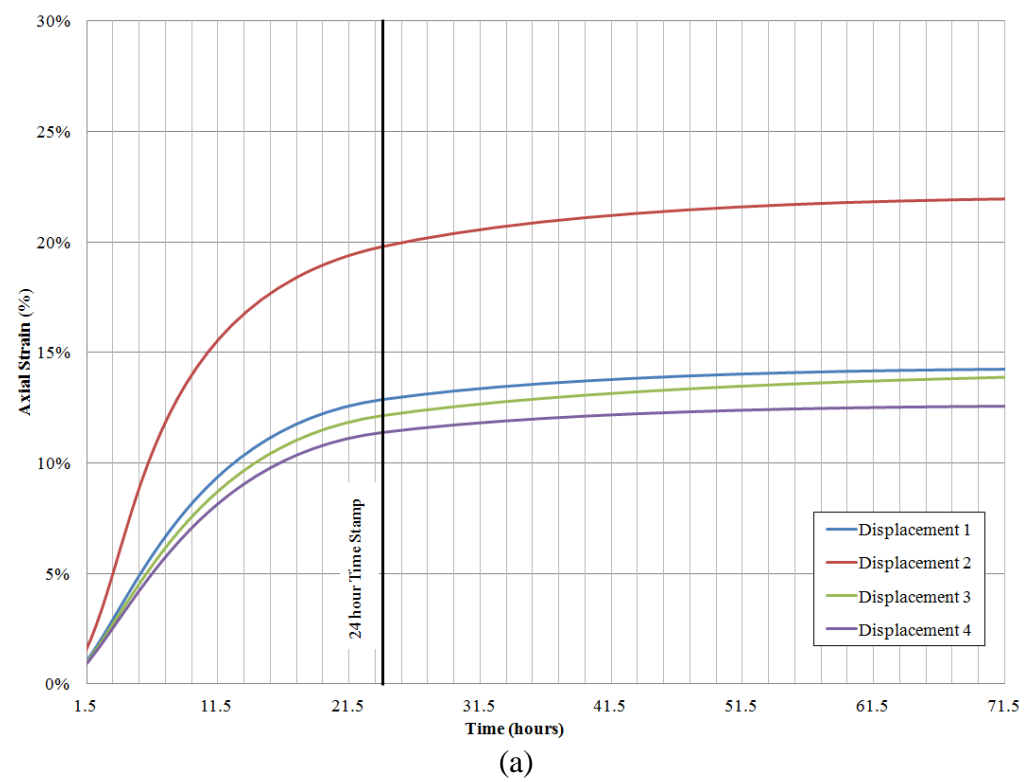
(a)

(b)

Figure 5.12 Initial load-displacement data as a function of time during the unconfined compression test, 1.5 - 71.5 hours: (a) strain for sensors 1-4; and (b) average strain for the long and short axis

Table 5.3: Typical Young's Modulus (E) values for other materials

Material	Young's Modulus (kPa)	Reference
Very Soft Clay	478	Geotechnicalinfo.com, 2012
Soft Clay	4,788	
Medium Clay	19,152	
Stiff Clay	47,880	
Sandy Clay	23,940	
Clay Shale	95,760	
Geofoam	580,000	ASTM D6817(2015)
Low Density Polyethylene	110,316	Matweb, 2012
High Density Polyethylene	799,791	
Wood (along grain)	1.1×10^7	
Recycled PET Bale	333.3	Garbini (Current Study)

5.4 Long-Term, Unconfined Compression Test Results and Discussion

Subsequent to the initial 90 minute time period, long-term unconfined compression data was acquired weekly over the 21 month (15,330 hour) test period. According to Horvath (1994), most creep tests are conducted for at least 10,000 hours for EPS Geofoam material. Two groups of data were retrieved. The data acquisition unit stored the sensor data in a text file of displacement readings for all four potentiometers. This data was used to calculate vertical strain values for the first 15 months of the unconfined compression test. Simultaneously, manual measurements were acquired each week at each of the four potentiometer locations using a plumb bob and tape measure to provide an independent check of the data. The manual measurements were collected for 21 months.

Figure 5.13 displays the long-term, vertical strain measurements from each of the four sensor locations as a function of time over the 15,330 hour (21 month) test period. There is a sharp increase in strain within the first 24 hours (discussed in more detail in the previous section and displayed in Figures 5.12), with a diminishing strain rate

209

thereafter. In Figure 5.13, Sensor 2 illustrates a larger amount of deformation compared to the other sensors. For example, at the one year time stamp (illustrated with a vertical line in Figure 5.13), Sensor 2 exhibited a strain equal to 25.52%, while Sensors 1, 3 and 4 exhibited strains equal to 16.99%, 17.22% and 16.49%, respectively. Sensor 2 exhibited this excess in strain due to the differential settlement that occurred within the recycled PET bale specimen as a result of the heterogeneous properties of the recycled PET bale specimen. An illustration of the uneven settlement is displayed in Figure 5.8. Sensor 2 is located on the right side of this figure.
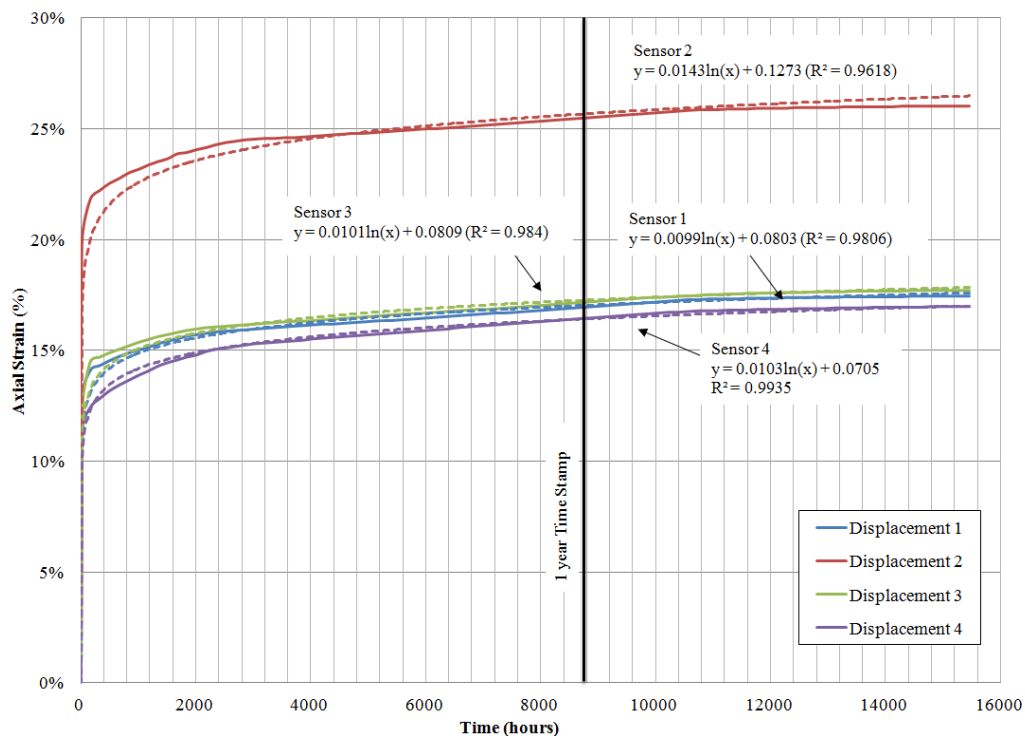
Figure 5.13: Long-term vertical strain for the unconfined compression test conducted on the PET bale test specimen at 23.0 kPa (all 4 sensors individually)

The data from the individual string potentiometers is averaged using all sensors and displayed in Figure 5.14 as described previous for Figure 5.10(a). The shorter test specimen axis (data averaged from Sensors 2 and 3) exhibited larger strain values in comparison to the longer test specimen axis (data averaged from Sensors 1 and 4 displayed on Figure 5.4). The data from all four sensors in Figure 5.4 are also averaged and displayed as a single curve in Figure 5.14. Based on the 'Average' curve, the recycled PET bale test specimen experienced approximately 15% vertical strain during the first 200 hours, approaching 20% strain by the end of the 15,500 hour examination period.
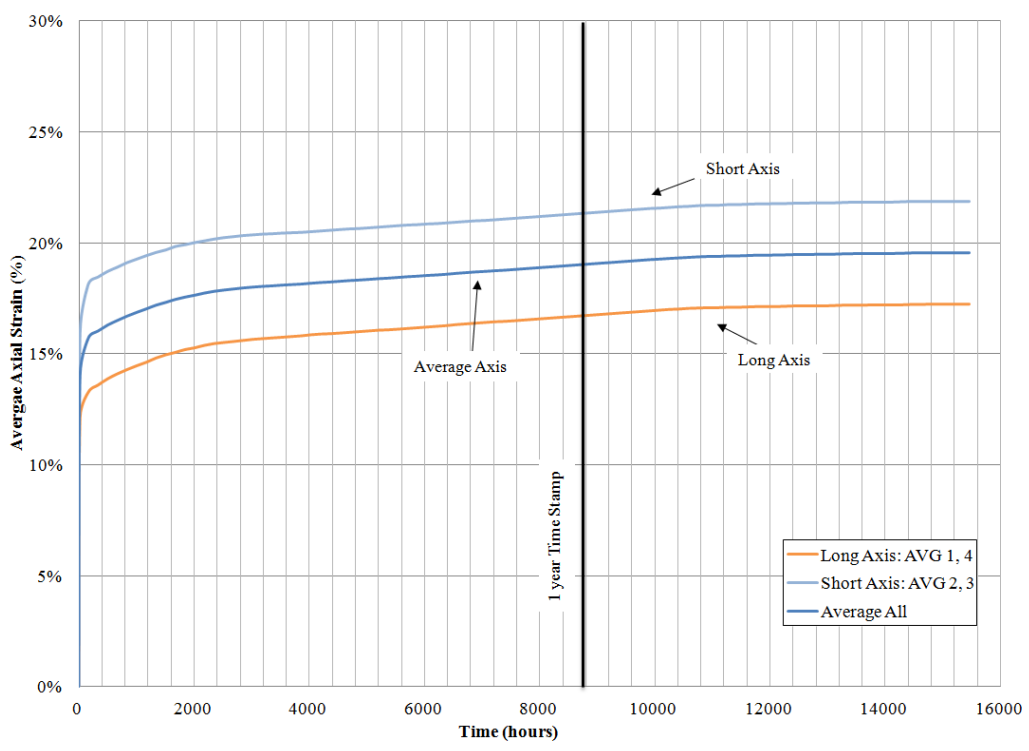
Figure 5.14: Long-term axial strain for the unconfined compression test conducted on the PET bale test specimen (axis and test specimen averages)

The long-term vertical strain data presented in Figure 5.13 and 5.14 are displayed in Figures 5.15 and 5.16 using a logarithmic time scale to better illustrate the trajectory of the deformation behavior for this material.
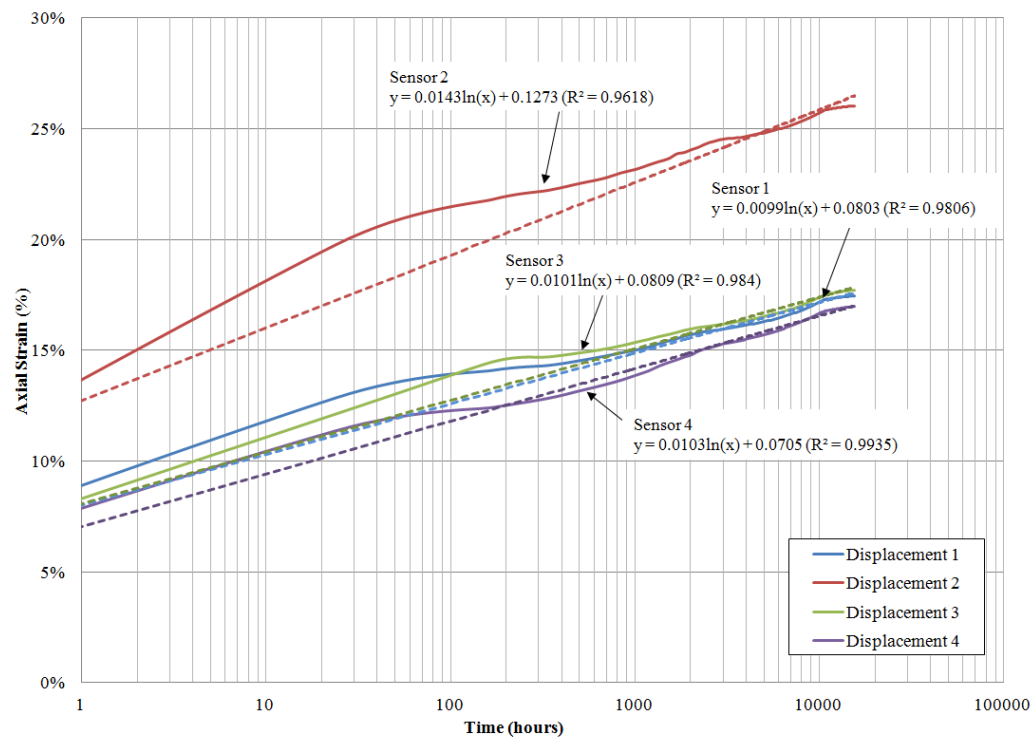
Figure 5.15: Long-term axial strain as a function of time for the unconfined compression test conducted on the PET bale test specimen at 23.0 kPa (all 4 sensors individually using a logrithmic scale)
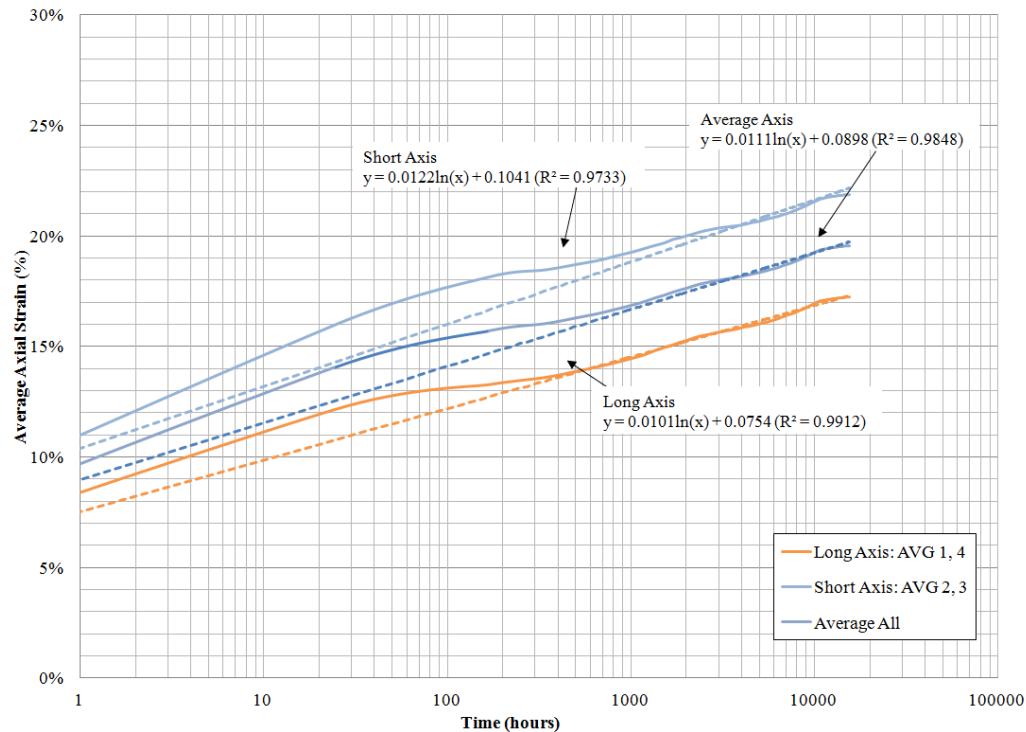
Figure 5.16: Long-term axial strain for the unconfined compression test conducted on the PET bale test specimen (axis and test specimen averages using a logrithmic scale)

Figure 5.17 illustrates the incremental change in strain per week throughout the life of the creep test for each sensor and axis. The incremental change in strain per week was calculated by taking the difference between averages calculated for two consecutive weeks. For example, in two consecutive weeks, the average axial strain measurements were 20% and 30%, respectively. This results in an incremental change in strain equal to 10% after the 2nd week (i.e. 30% - 20% = 10%). Figure 5.17 clearly illustrates that higher strains calculated during the short-term phase of the test period taper off after the 200 hour mark (just after one week of testing).
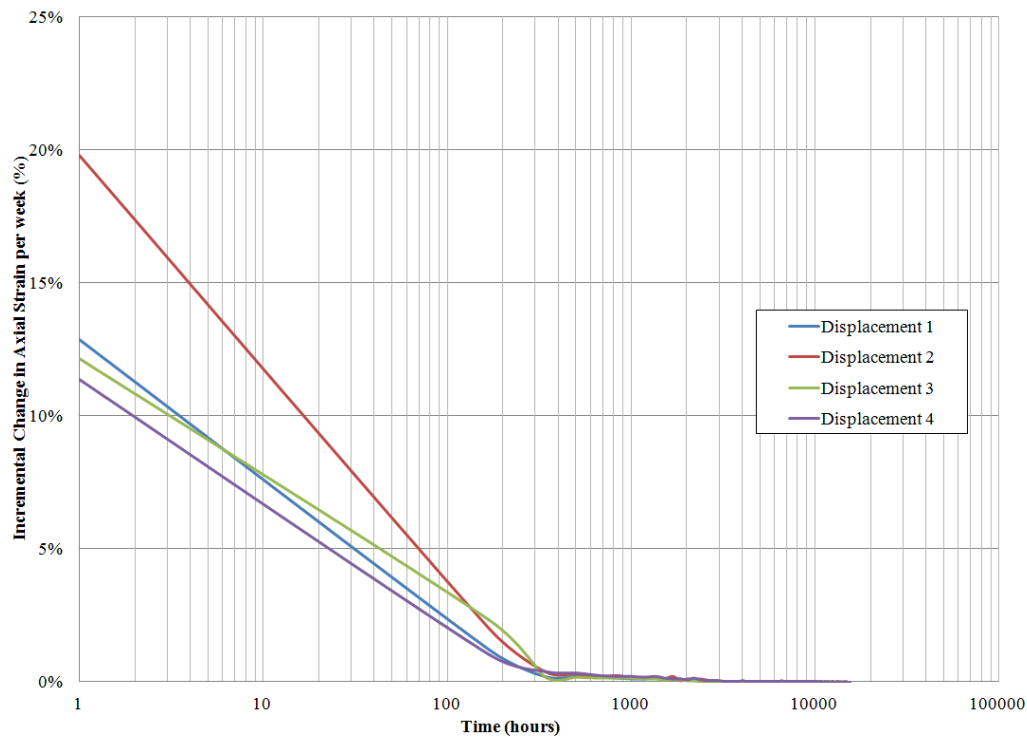
(a)
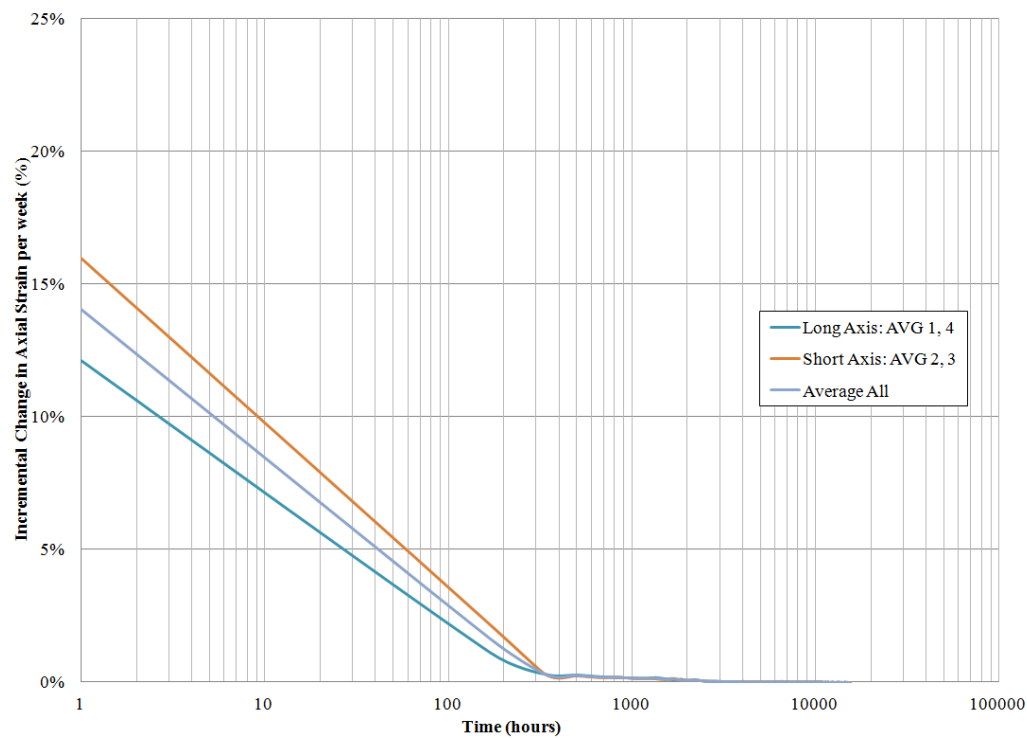
(b)

Figure 5.17: Incremental change in strain per week for the unconfined compression test conducted on the PET bale test specimen: (a) strain for sensors 1-4; and (b) average strain for the long and short axis

Creep compressibility can be quantified using a compression index (C_α), commonly used for clayey soils as follows:

$$C_\alpha = \Delta\varepsilon_{vertical} / \log(t_1/t_2)$$ [4.8]

Where:

C_α = compression index
$\Delta\varepsilon_{vertical}$ = change in vertical strain = ε_{Final} - $\varepsilon_{Initial}$
t_1 = initiation time for the compression index calculation
t_2 = final time for the compression index calculation

The compression index was calculated using the data collected by the four string potentiometers and the manual measurements. In order to do so, the initiation time (t_1) represented by the 1.5 hour mark, corresponding to the end of the short-term phase outlined in Table 5.1. The final time (t_2) is equal to 15,330 hours. The compression index was calculated as 0.02 using the average vertical strain values with a vertical change at the end of the compression evaluation of 7.95% (i.e., 19.55% - 11.6%) for a time interval from 1.5 hours to 15,330 hours.

5.5 Large Scale Unconfined Compression Testing Summary

Data from a full-scale unconfined compression test were analyzed both short-term and long-term to assess the deformation behavior of a recycled PET bale since this material was proposed for use as lightweight fill in embankments. The large scale unconfined compression test involved the application of five load increments up to a maximum compressive stress of 42.4 kPa. The static load induced during this test represented an overburden stress within an embankment, but the test was limited because it was unconfined, which is not represented of in-situ field conditions. The short-term Young's moduli measured during this initial phase of the test ranged from 149 kPa to 538

kPa with an overall average stiffness of 333.3 kPa. This stiffness value is about 1740 times lower than the stiffness associated with EPS Geofoam blocks, commonly used as lightweight fill material for geotechnical applications.

The recycled PET bale experienced significant creep, reaching approximately 20% axial strain over a 21 month test period. The incremental change in axial strain per week decreased exponentially, and tapered off significantly after 200 hours of testing. The compression index for the unconfined compression test measured 0.02, approximately one order of magnitude lower in comparison to the compression indices for soft and hard clay equal to 0.34 and 0.44, respectively (Kaufmann and Shermann, 1964).

While creep behavior was observed during the 21 month test period, it is important to note that an unconfined environment is not representative of in-situ field conditions. A confined test could not be performed at this facility due to testing equipment limitations. Confinement of the PET bales in the subsurface would produce significantly less creep. To fully describe the compressibility of this material, additional confined compression tests on a full-scale bale would be required and multiple tests would speak to the repeatability of the results since there is a wide variety of recycled constituents in each bale, each bale varies slightly in unit weight, and the number of metal straps applied to the outside of the bales during the compaction process vary as well. Based on the results from this study, PET bales are recommended for use as a lightweight fill for non-loading bearing applications only, but further research is needed.

CHAPTER 6: LIMIT EQUILIBRIUM ANALYSES FOR SLOPE STABILITY
APPLICATIONS OF DIFFERENT RECYCLED PET BALE CONFIGURATIONS

6.1 Introduction

A series of slope stability limit equilibrium analyses were conducted using various
PET bale configurations to further assess the feasibility of utilizing PET bales as
lightweight material in embankments. The friction angles determined from the triaxial
compression tests performed on Group 1 PET chopped constituents were used as material
inputs for the slope stability limit equilibrium analyses. While the PET bale constituents
utilized for the triaxial test specimens were processed (i.e., chopped) to create the test
specimens, the measured friction angles from these tests served as conservative estimates
of shear strength since many of the inconsistencies inherent in the full-bottle constituents
that would normally provide additional resistance (e.g., differences in size, shape,
textures, compaction, etc.) were removed by using only Group 1 bottles and by chopping
them into consistently sized squares.

Five PET bale zone configurations were assessed using two slope inclinations and
two types of subsurface soils to determine changes in the factor of safety (FS) of a fixed
failure surface resulting from the inclusion of the proposed lightweight material. It is
important to note that the analysis contained herein consistently uses a pre-defined fixed
failure surface for a more controlled comparison of the FS output. Additionally, this
chapter is divided into two main sections. Initially, the slope was analyzed assuming the

rows of recycled PET bales intersected the slip surface using the various PET bale zone configurations. An in-depth examination of one slope inclination and soil type was also conducted to evaluate the normal, resisting, and driving forces for each slice along the failure surface. Subsequently, the effect of changing the unit weight of the material inside the fixed failure surface was evaluated to determine the effect on the FS due to lightweight fill for comparison of PET bales to other materials. This chapter will present a description of the methodology and software used for the analyses, summarize the soil and slope conditions evaluated, and discuss the results from the limit equilibrium analyses.

6.2 Slope Stability Software and Analysis Configuration

The slope stability analyses conducted herein considered two slope inclinations. The varying PET bale zone configurations for the 2H:1V slope inclination are displayed in Figures 6.1 and 6.2, and the same PET bale zone configurations for the 3H:1V slope inclination are displayed in Figures 6.3 and 6.4. The embankment height was kept constant at 3 m, and the center of the pre-defined circular failure surface was located 30 meters above the toe of the slope with a radius equal to 30 m. This slope stability analyses only considered one circular failure surface so that the failure method through the varying configurations was consistent and all resulting FS values were more comparable. For this reason, it is important to note that the FS values reported in this chapter do not represent the minimum FS value calculated using standard design practices.
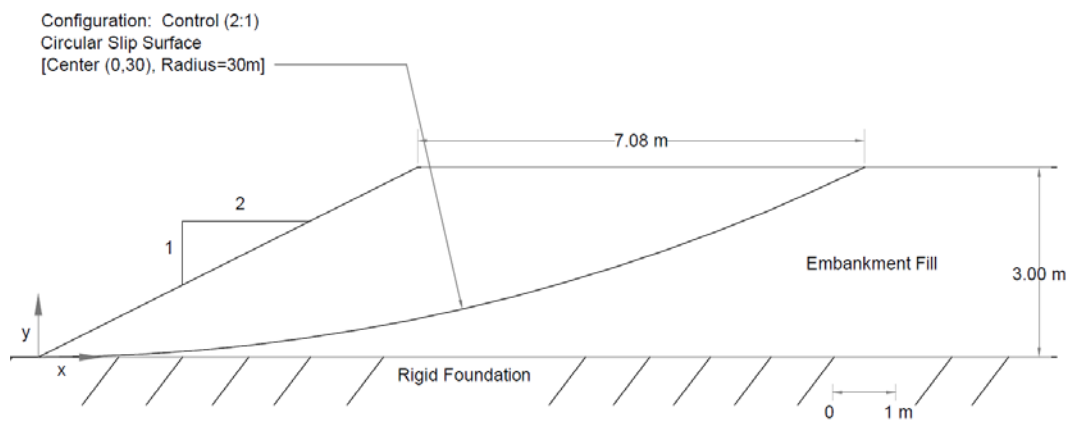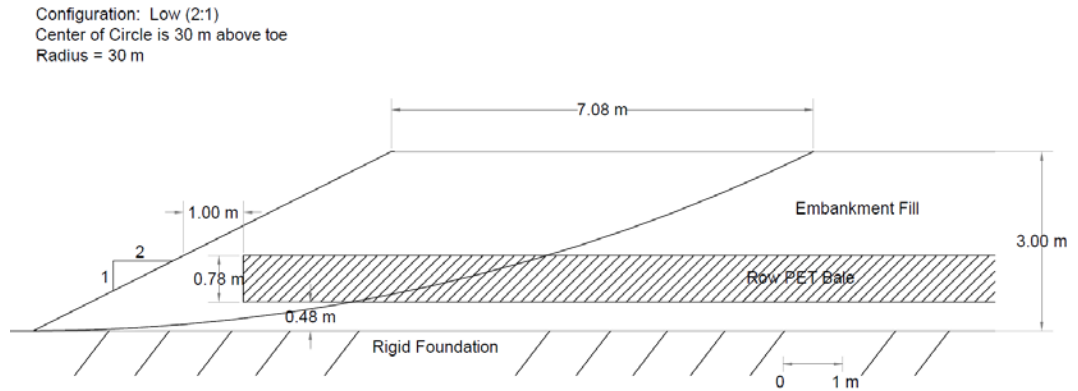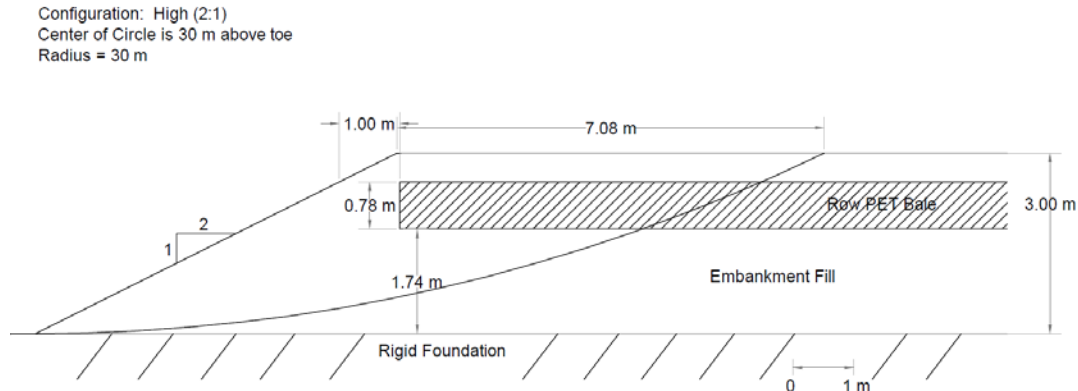
Figure 6.1: Control and single row PET bale configurations for the 2H:1V slope inclination used in the limit equilibrium analyses: (a) control (no inclusions); (b) single row positioned low; and (c) single row positioned high

Figure 6.2: Multiple rows PET bale configurations for the 2H:1V slope inclination used in the limit equilibrium analyses: (a) two distributed rows; and (b) three stacked rows

.
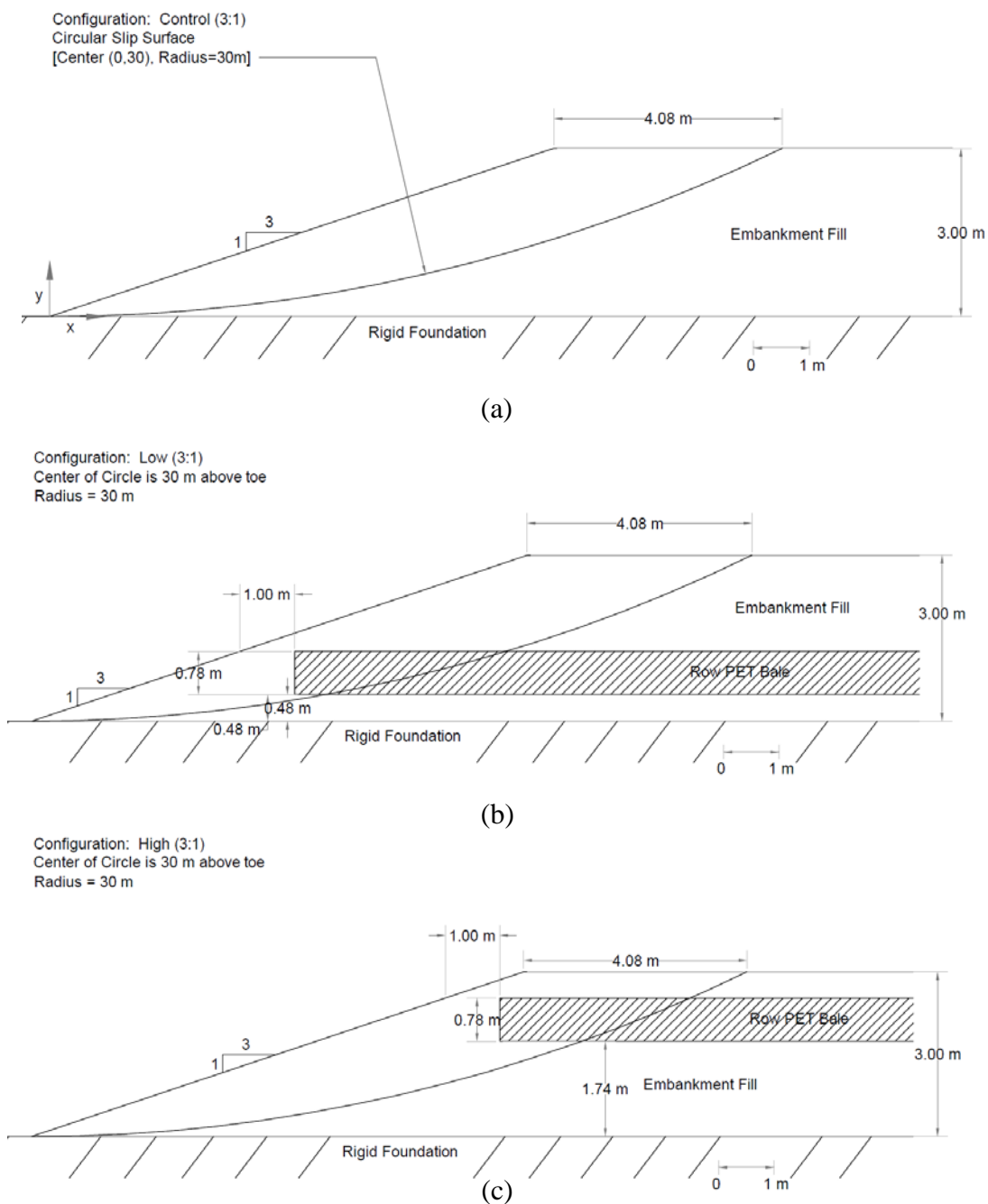
Figure 6.3: Control and single row PET bale configurations for the 3H:1V slope inclination used in the limit equilibrium analyses: (a) control (no inclusions); (b) single row positioned low; and (c) single row positioned high

Configuration: Distributed (3:1)
Center of Circle is 30 m above toe
Radius = 30 m

4.08 m

1.00 m   0.78 m   Row PET Bale

0.48 m   Embankment Fill   3.00 m

Row PET Bale

3
1

0.48 m   Rigid Foundation

0   1 m

(a)

Configuration: Stacked (3:1)
Center of Circle is 30 m above toe
Radius = 30 m

4.08 m

Embankment Fill

1.00 m

Row PET Bale

1.00 m   3.00 m

Row PET Bale

3
1   0.78 m   Row PET Bale

Rigid Foundation

0   1 m

(b)
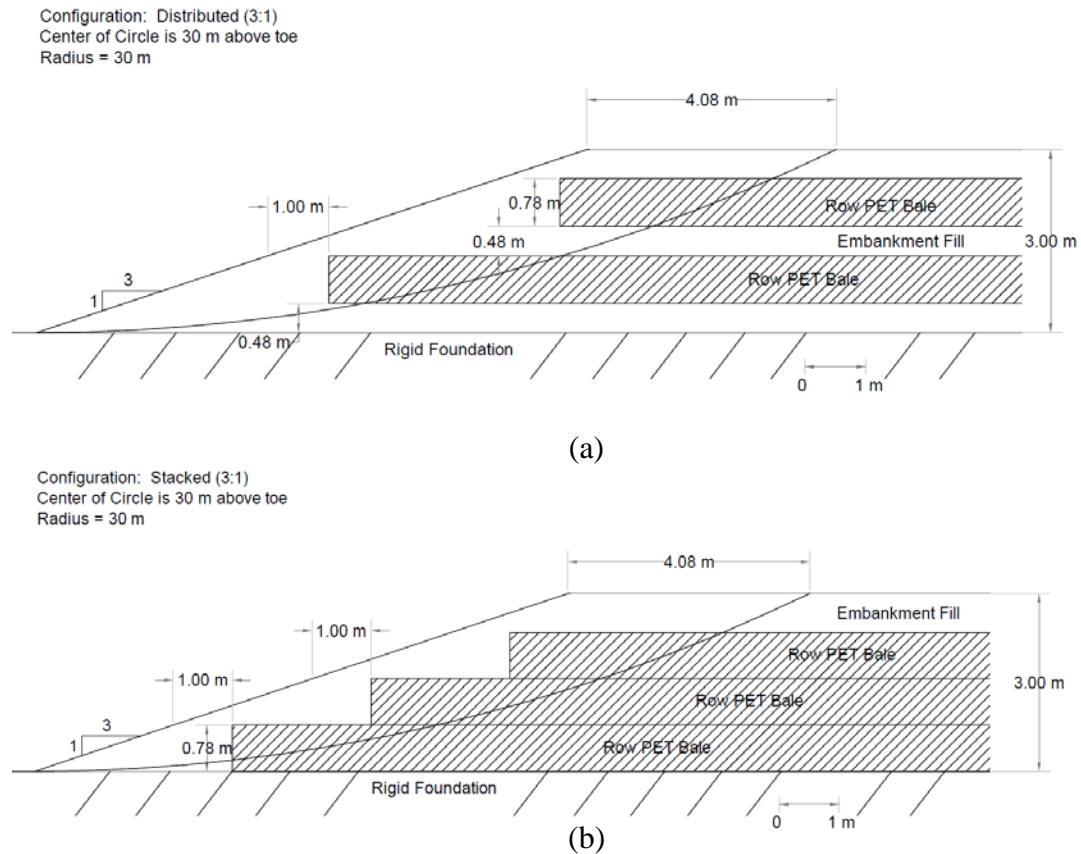
Figure 6.4: Multiple row PET bale test configurations for the 2H:1V slope inclination used in the limit equilibrium analysis: (a) two distributed rows; and (b) three stacked rows

Tables 6.1 and 6.2 summarize the analyses matrix for the 2H:1V and 3H:1V slope inclinations, respectively. For the 2H:1V analyses displayed in Table 6.1, each set of PET bale zone configurations (control, single-high, single-low, distributed, and stacked) is evaluated assuming two different subsurface materials. The first material is a sand with a γ = 18 kN/m³, ϕ' = 35°, and c' = 0 kPa. The second material is a clay with a γ = 19 kN/m³, ϕ' = 20°, and c' = 60 kPa. In both cases, the PET properties were initially defined using a γ = 2.36 kN/m³, ϕ' = 5°, and c' = 0 kPa. Five analyses were completed for each material, and then the same analyses were conducted for each subsurface soil material

assuming a PET $\phi' = 10^o$ and 15° with a c' = 0 kPa (a total of 30 analyses summarized in

Table 6.1). The entire matrix was repeated for the 3H:1V slope inclination in Table 6.2.

Table 6.1: All limit equilibrium cases analyzed for the 2H:1V slope inclination

Configuration	Slope Inclination (H:V)	Soil Type (USCS)	Soil Parameters			PET Bale Parameters		
			γ_t^1 (kN/m³)	ϕ' (°)	c' (kPa)	γ_t^1 (kN/m³)	ϕ' (°)	c' (kPa)
Control	2:1	Sand (SW)	18	35	0	2.36	5	0
High	2:1	Sand (SW)	18	35	0	2.36	5	0
Low	2:1	Sand (SW)	18	35	0	2.36	5	0
Distributed	2:1	Sand (SW)	18	35	0	2.36	5	0
3 rows stacked	2:1	Sand (SW)	18	35	0	2.36	5	0
Control	2:1	Clay (CL)	19	20	60	2.36	5	0
High	2:1	Clay (CL)	19	20	60	2.36	5	0
Low	2:1	Clay (CL)	19	20	60	2.36	5	0
Distributed	2:1	Clay (CL)	19	20	60	2.36	5	0
3 rows stacked	2:1	Clay (CL)	19	20	60	2.36	5	0
Control	2:1	Sand (SW)	18	35	0	2.36	10	0
High	2:1	Sand (SW)	18	35	0	2.36	10	0
Low	2:1	Sand (SW)	18	35	0	2.36	10	0
Distributed	2:1	Sand (SW)	18	35	0	2.36	10	0
3 rows stacked	2:1	Sand (SW)	18	35	0	2.36	10	0
Control	2:1	Clay (CL)	19	20	60	2.36	10	0
High	2:1	Clay (CL)	19	20	60	2.36	10	0
Low	2:1	Clay (CL)	19	20	60	2.36	10	0
Distributed	2:1	Clay (CL)	19	20	60	2.36	10	0
3 rows stacked	2:1	Clay (CL)	19	20	60	2.36	10	0
Control	2:1	Sand (SW)	18	35	0	2.36	15	0
High	2:1	Sand (SW)	18	35	0	2.36	15	0
Low	2:1	Sand (SW)	18	35	0	2.36	15	0
Distributed	2:1	Sand (SW)	18	35	0	2.36	15	0
3 rows stacked	2:1	Sand (SW)	18	35	0	2.36	15	0
Control	2:1	Clay (CL)	19	20	60	2.36	15	0
High	2:1	Clay (CL)	19	20	60	2.36	15	0
Low	2:1	Clay (CL)	19	20	60	2.36	15	0
Distributed	2:1	Clay (CL)	19	20	60	2.36	15	0
3 rows stacked	2:1	Clay (CL)	19	20	60	2.36	15	0

[1] Total unit weight

Table 6.2: All limit equilibrium cases analyzed for the 3H:1V slope inclination

Configuration	Slope Inclination (H:V)	Soil Type (USCS)	Soil Parameters			PET Bale Parameters		
			γ_t^1 (kN/m³)	ϕ' (°)	c' (kPa)	γ_t^1 (kN/m³)	ϕ' (°)	c' (kPa)
Control	3:1	Sand (SW)	18	35	0	2.36	5	0
High	3:1	Sand (SW)	18	35	0	2.36	5	0
Low	3:1	Sand (SW)	18	35	0	2.36	5	0
Distributed	3:1	Sand (SW)	18	35	0	2.36	5	0
3 rows stacked	3:1	Sand (SW)	18	35	0	2.36	5	0
Control	3:1	Clay (CL)	19	20	60	2.36	5	0
High	3:1	Clay (CL)	19	20	60	2.36	5	0
Low	3:1	Clay (CL)	19	20	60	2.36	5	0
Distributed	3:1	Clay (CL)	19	20	60	2.36	5	0
3 rows stacked	3:1	Clay (CL)	19	20	60	2.36	5	0
Control	3:1	Sand (SW)	18	35	0	2.36	10	0
High	3:1	Sand (SW)	18	35	0	2.36	10	0
Low	3:1	Sand (SW)	18	35	0	2.36	10	0
Distributed	3:1	Sand (SW)	18	35	0	2.36	10	0
3 rows stacked	3:1	Sand (SW)	18	35	0	2.36	10	0
Control	3:1	Clay (CL)	19	20	60	2.36	10	0
High	3:1	Clay (CL)	19	20	60	2.36	10	0
Low	3:1	Clay (CL)	19	20	60	2.36	10	0
Distributed	3:1	Clay (CL)	19	20	60	2.36	10	0
3 rows stacked	3:1	Clay (CL)	19	20	60	2.36	10	0
Control	3:1	Sand (SW)	18	35	0	2.36	15	0
High	3:1	Sand (SW)	18	35	0	2.36	15	0
Low	3:1	Sand (SW)	18	35	0	2.36	15	0
Distributed	3:1	Sand (SW)	18	35	0	2.36	15	0
3 rows stacked	3:1	Sand (SW)	18	35	0	2.36	15	0
Control	3:1	Clay (CL)	19	20	60	2.36	15	0
High	3:1	Clay (CL)	19	20	60	2.36	15	0
Low	3:1	Clay (CL)	19	20	60	2.36	15	0
Distributed	3:1	Clay (CL)	19	20	60	2.36	15	0
3 rows stacked	3:1	Clay (CL)	19	20	60	2.36	15	0

[1] Total unit weight

The slope stability analyses were conducted using Slide, Version 6.035 (manufactured by Rocscience). As with most limit equilibrium software, this program allows the input of multiple soil layers, enables the user to define the failure surface type, failure surface location, analysis method, and other analysis parameters/configurations including the number of slices and maximum number of iterations. Table 6.3 summarizes the slope stability analysis program inputs. The Ordinary Method of Slices (Fellenius, 1936) was utilized in all cases without pore pressure complications. For comparison, the modified Bishop method (Bishop, 1955) and Janbu method (Janbu et al., 1956) were evaluated using the same slope geometry, and the results only differed approximately +/- 2%.

Using the Ordinary Method of Slices, the FS was calculated using Equation 6.1.

$$FS = \frac{\sum_{i=1}^{n} \{c'_i l_i + [(W_i/b)\cos\alpha_i - u_i l_i]\tan\phi'_i\}}{\sum_{i=1}^{n} [(W_i/b)\sin\alpha_i]} \qquad [6.1]$$

Where:
   c'_i = effective cohesion at base of slice i
   l_i = length of slice i along failure plane
   W_i = weight of slice i
   b = unit length of the slope
   α_i = angle of inclination of base of slice i with respect to the horizontal
   u_i = pore pressure at center of base of slice i = 0 in all cases
   ϕ'_i = effective friction angle
   i = slice number
   n = total number of slices

Table 6.3: Slope stability analysis program inputs

Variable	Input or Description
Units of System	Metric
Failure Direction	Right to Left
Method of Analysis	Ordinary Method of Slices
Tolerance	0.005
Maximum Number of Iterations	50
Groundwater Analysis	Not Applicable
Surface Type	Circular
Center of Circular Failure Surface	30 m above toe of slope
Radius of Circular Failure Surface	30 m
Soil Strength Type	Mohr-Coulomb

Table 6.4 summarizes the material input parameters for the soil and recycled PET bales. The embankments were modeled assuming a compacted sand (SW) and compacted clay (CL) under the Unified Soil Classification System (USCS). The selected values of unit weight (γ_t), effective friction angle (ϕ'), and effective cohesion (c') are typical. PET bale unit weights vary from 2.36 kN/m^3 - 3.93 kN/m^3 at the regional MRF so the lower end of this range was selected for analysis. Friction angle values ranging from 5° - 20° were measured during the laboratory evaluation so limit equilibrium analyses were conducted using three recycled PET friction angles equal to 5°, 10°, and 15°, which is also displayed in the last column of Tables 6.1 and 6.2.

Table 6.4: Slope stability material input parameters

Material Type (USCS)	γ (kN/m^3)	ϕ' (°)	c' (kPa)
Sand (SW)	18	35	0
Clay (CL)	19	20	60
Recycled PET Bale	2.36	5, 10, 20	0

6.3 Discussion of Results: Recycled PET Bales Intersecting the Fixed Failure Surface

The results displayed in this section were acquired from limit equilibrium analyses conducted assuming all PET bale zone configurations crossed over the pre-defined failure surface. For this reason, the shear strength of the PET bale material served as a critical factor in the resulting FS values.

6.3.1 Fixed Surface FS Results for PET Bale Zones Intersecting the Failure Curve

Table 6.5 presents the previously displayed matrix for 2H:1V slope inclination with final FS results displayed in the last column. Recall that these FS values do not represent the minimum FS for the embankment since only one pre-defined failure surface was analyzed. Table 6.6 presents the same information for the 3H:1V slope inclination.

Table 6.5: Summary of the fixed failure surface FS results for the 2H:1V slope inclination

Configuration	Soil Type (USCS)	Soil Parameters			PET Bale Parameters			Computed OMS FS
		γ_t^1 (kN/m³)	ϕ' (°)	c' (kPa)	γ_t^1 (kN/m³)	ϕ' (°)	c' (kPa)	
Control	Sand (SW)	18	35	0	2.36	5	0	3.2
High	Sand (SW)	18	35	0	2.36	5	0	3.3
Low	Sand (SW)	18	35	0	2.36	5	0	2.1
Distributed	Sand (SW)	18	35	0	2.36	5	0	2.1
3 rows stacked	Sand (SW)	18	35	0	2.36	5	0	1.0
Control	Clay (CL)	19	20	60	2.36	5	0	13.1
High	Clay (CL)	19	20	60	2.36	5	0	14.8
Low	Clay (CL)	19	20	60	2.36	5	0	10.9
Distributed	Clay (CL)	19	20	60	2.36	5	0	12.2
3 rows stacked	Clay (CL)	19	20	60	2.36	5	0	7.2
Control	Sand (SW)	18	35	0	2.36	10	0	3.2
High	Sand (SW)	18	35	0	2.36	10	0	3.3
Low	Sand (SW)	18	35	0	2.36	10	0	2.2
Distributed	Sand (SW)	18	35	0	2.36	10	0	2.3
3 rows stacked	Sand (SW)	18	35	0	2.36	10	0	1.3
Control	Clay (CL)	19	20	60	2.36	10	0	13.1
High	Clay (CL)	19	20	60	2.36	10	0	14.8
Low	Clay (CL)	19	20	60	2.36	10	0	11.3
Distributed	Clay (CL)	19	20	60	2.36	10	0	12.4
3 rows stacked	Clay (CL)	19	20	60	2.36	10	0	7.5
Control	Sand (SW)	18	35	0	2.36	15	0	3.2
High	Sand (SW)	18	35	0	2.36	15	0	3.4
Low	Sand (SW)	18	35	0	2.36	15	0	2.5
Distributed	Sand (SW)	18	35	0	2.36	15	0	2.7
3 rows stacked	Sand (SW)	18	35	0	2.36	15	0	2.0
Control	Clay (CL)	19	20	60	2.36	15	0	13.1
High	Clay (CL)	19	20	60	2.36	15	0	14.9
Low	Clay (CL)	19	20	60	2.36	15	0	11.3
Distributed	Clay (CL)	19	20	60	2.36	15	0	12.8
3 rows stacked	Clay (CL)	19	20	60	2.36	15	0	8.2

Table 6.6: Summary of the fixed failure surface FS results for the 3H:1V slope inclination

Configuration	Soil Type (USCS)	Soil Parameters			PET Bale Parameters			Computed OMS FS
		γ_t^1 (kN/m³)	ϕ' (°)	c' (kPa)	γ_t^1 (kN/m³)	ϕ' (°)	c' (kPa)	
Control	Sand (SW)	18	35	0	2.36	5	0	2.9
High	Sand (SW)	18	35	0	2.36	5	0	2.9
Low	Sand (SW)	18	35	0	2.36	5	0	2.1
Distributed	Sand (SW)	18	35	0	2.36	5	0	1.8
3 rows stacked	Sand (SW)	18	35	0	2.36	5	0	1.1
Control	Clay (CL)	19	20	60	2.36	5	0	15.8
High	Clay (CL)	19	20	60	2.36	5	0	16.5
Low	Clay (CL)	19	20	60	2.36	5	0	13.2
Distributed	Clay (CL)	19	20	60	2.36	5	0	13.2
3 rows stacked	Clay (CL)	19	20	60	2.36	5	0	9.1
Control	Sand (SW)	18	35	0	2.36	10	0	2.9
High	Sand (SW)	18	35	0	2.36	10	0	3.0
Low	Sand (SW)	18	35	0	2.36	10	0	2.2
Distributed	Sand (SW)	18	35	0	2.36	10	0	2.0
3 rows stacked	Sand (SW)	18	35	0	2.36	10	0	1.4
Control	Clay (CL)	19	20	60	2.36	10	0	15.8
High	Clay (CL)	19	20	60	2.36	10	0	16.5
Low	Clay (CL)	19	20	60	2.36	10	0	13.3
Distributed	Clay (CL)	19	20	60	2.36	10	0	13.4
3 rows stacked	Clay (CL)	19	20	60	2.36	10	0	9.4
Control	Sand (SW)	18	35	0	2.36	15	0	2.9
High	Sand (SW)	18	35	0	2.36	15	0	3.0
Low	Sand (SW)	18	35	0	2.36	15	0	2.4
Distributed	Sand (SW)	18	35	0	2.36	15	0	2.4
3 rows stacked	Sand (SW)	18	35	0	2.36	15	0	2.0
Control	Clay (CL)	19	20	60	2.36	15	0	15.8
High	Clay (CL)	19	20	60	2.36	15	0	16.6
Low	Clay (CL)	19	20	60	2.36	15	0	13.6
Distributed	Clay (CL)	19	20	60	2.36	15	0	13.8
3 rows stacked	Clay (CL)	19	20	60	2.36	15	0	10.0

The FS results for the sand (SW) presented in Tables 6.5 and 6.6 were used to generate Figure 6.5 and the averages for all PET material friction angles are presented in Table 6.7. Figure 6.5 displays the computed FS values for both SW embankment slope inclinations. The five PET bale zone configurations are displayed along the bottom of this figure. Recall that each slope inclination considered three different values for the PET friction angle so there are three curves for each slope inclination. For clarity in this figure, the 2H:1V slope inclination iterations are displayed using dashed lines with closed symbols while the 3H:1V slope inclination iterations are displayed using solid lines with open symbols. Based on accepted practice, the FHWA minimum design FS for an embankment is 1.3 (FHWA, 2000), which is represented by the horizontal dashed line in this figure.

Figure 6.5 shows that the FS values for both slope inclinations generally decreased in comparison to the control condition. For the low, distributed, and stacked PET bale zone configurations, the benefits associated with the lightweight unit weight of the PET bales were not enough to compensate for the decrease in the overall resisting moment associated with the low shear strength of PET zones along the fixed failure surface. For both slope inclinations, the lowest FS values were computed for the stacked slope configuration. However, the fixed failure surface FS values increase as the PET bale friction angles increase in all cases.
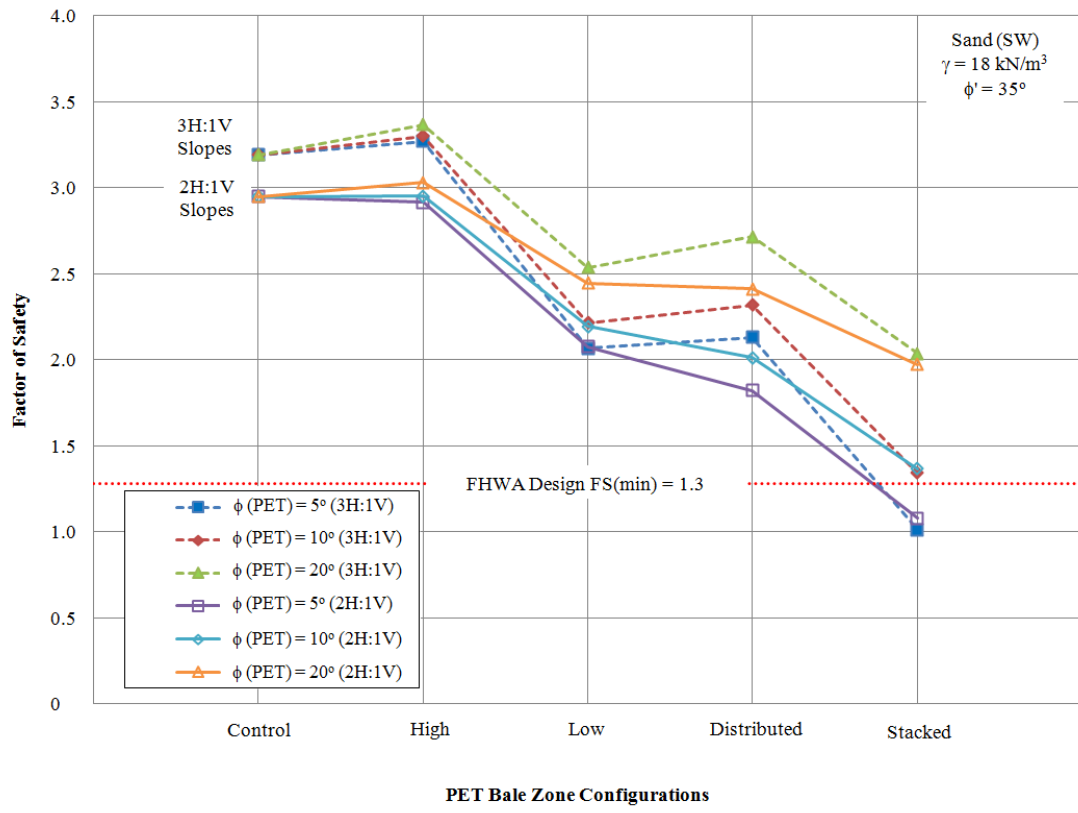
Figure 6.5: Fixed failure surface FS results for both slope inclinations assuming a sand (SW) embankment with intersecting PET bale zone configurations

Table 6.7: Average fixed failure surface FS for each slope configuration assuming a sand (SW) embankment

Slope Inclination	PET Bale Zone Configuration	FS for the SW Embankment
2:1	Control	3.19
	High	3.31
	Low	2.27
	Distributed	2.39
	Stacked	1.46
3:1	Control	2.95
	High	2.97
	Low	2.24
	Distributed	2.08
	Stacked	1.47

The results presented in Tables 6.5 and 6.6 were also presented using the same format in Figure 6.6 and Table 6.8 for the clay (CL) embankment. While there are larger FS values displayed in this figure due to the material inputs utilized and the pre-defined fixed failure surface, recall these values do not represent the minimum FS values normally determined as part of the design of the embankment. The same trends discussed for Figure 6.5 exist in Figure 6.6. The lowest factor of safety values were obtained for the stacked configuration because the effects of the lower shear strength of the PET intersecting the fixed failure surface are maximized in this configuration. For the CL embankment, there is less of a difference in the fixed failure surface FS when the friction angle of the PET is varied.
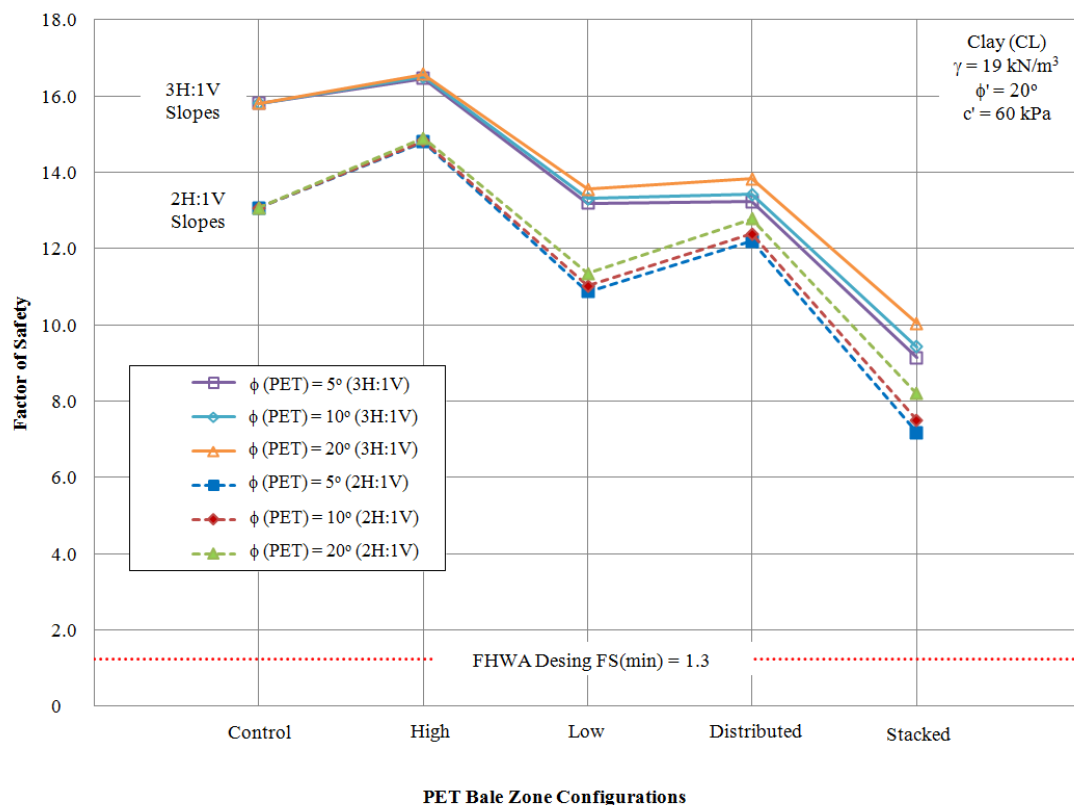
Figure 6.6: Fixed failure surface FS results for both slope inclinations assuming a clay (CL) embankment with intersecting PET bale zone configurations

Table 6.8: Average fixed failure surface FS for each slope configuration, assuming a clay (CL) embankment

Slope Inclination	PET Bale Zone Configuration	FS for the CL Embankment
2:1	Control	13.07
	High	14.84
	Low	11.08
	Distributed	12.45
	Stacked	7.63
3:1	Control	15.81
	High	16.51
	Low	13.35
	Distributed	13.49
	Stacked	9.54

Figures 6.7 displays the normalized FS ratios ($FS_{control}/FS_{other}$) for both subsurface materials and all PET bale zone configurations assuming the 2H:1V slope inclination. All PET bale zone configurations with the exception of the high position resulted in decreased FS values (ratios less than 1.0) in comparison to the control. The stacked configuration was the least favorable option. Figure 6.8 displays the same information and trends for the 3H:1V slope inclination.
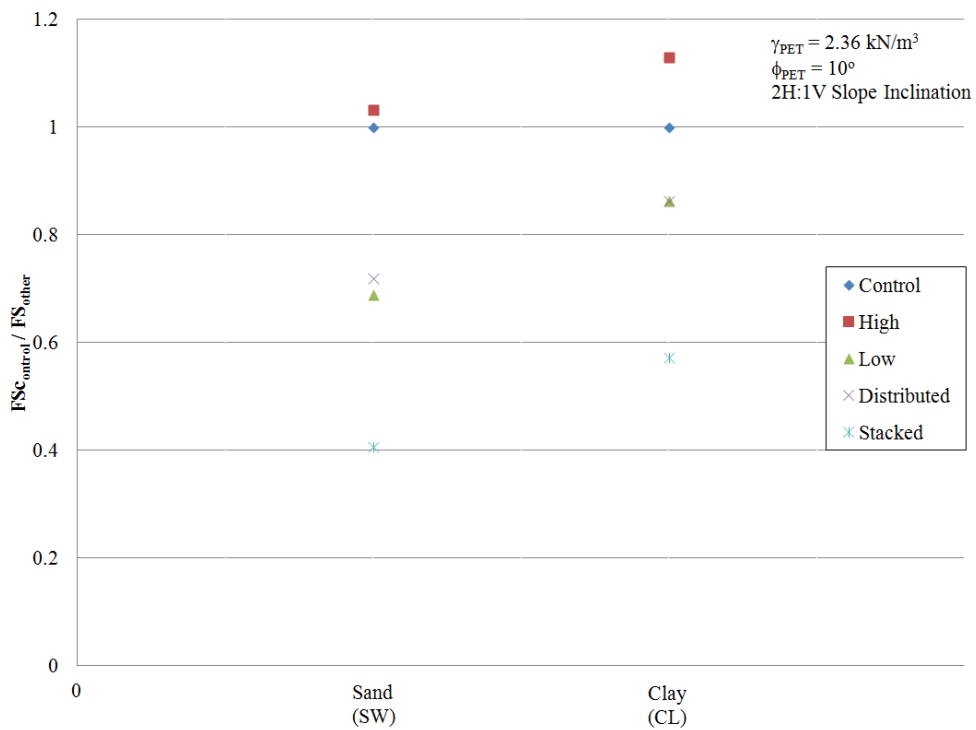
Figure 6.7: Normalized fixed failure surface FS ratios for the 2H:1V slope
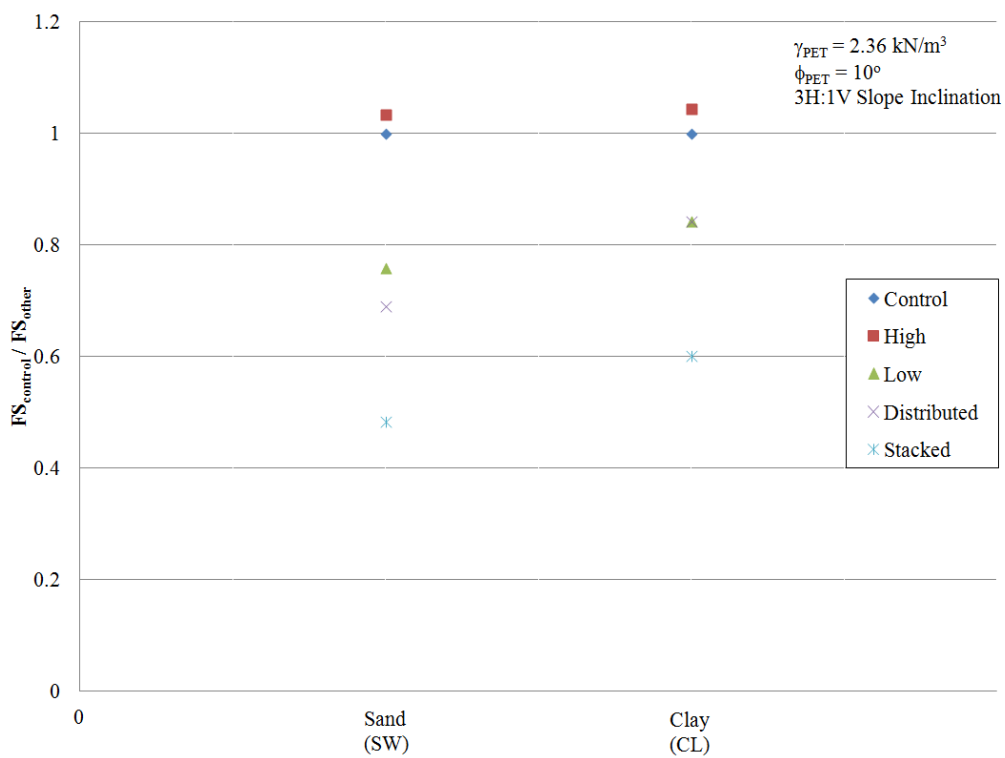
Figure 6.8: Normalized fixed failure surface FS ratios for the 3H:1V slope

The fixed failure surface FS values for the PET bales reported in Table 6.6 for the 3H:1V slope inclination were compared to results acquired assuming the same bale zone configurations (previously shown in Figures 6.3 and 6.4) had the properties of both EPS Geofoam and tire bales. In other words, the material properties originally assigned to the PET bales were replaced with the EPS Geofoam and tire bales material properties acquired from the literature.

Table 6.9 summarizes the material parameters and the fixed failure surface FS values for the EPS Geofoam, tire bales, and PET bales side by side. The FS values for the PET bales were slightly lower for all configurations in comparison to both EPS Geofoam and tire bales, but because the FS are relatively close in magnitude and EPS Geofoam is already used as lightweight material in embankment, there is reason for further analysis to better determine the feasibility of using this material in slope stability applications. Recall that this study only analyzes the FS of a fixed failure surface and does not complete the analysis of all cases to determine the minimum FS. Figure 6.9 displays the same fixed failure surface FS values visually. With the exception of the EPS Geofoam values, which are slightly higher, all other calculated FS values for this fixed failure surface were similar in magnitude.

Table 6.9: Comparison of the PET bale fixed failure surface FS results to the results for EPS Geofoam and tire bales for the 3H:1V slope inclination

Inclusion Material	Configuration	Soil Type (USCS)	Soil Parameters			PET Bale/Geofoam Parameters			Computed OMS FS
			$\gamma_t{}^1$ (kN/m³)	ϕ' (°)	c' (kPa)	$\gamma_t{}^1$ (kN/m³)	ϕ' (°)	c' (kPa)	
EPS Geofoam	Control	Sand (SW)	18	35	0	0.2	35	0	2.9
	High								3.2
	Low								2.9
	Distributed								3.1
	3 rows stacked								3.1
Tire Bale	Control					5.5	25	2.4	2.9
	High								3.1
	Low								2.7
	Distributed								2.9
	3 rows stacked								2.7
PET Bale	Control					2.36	10	0	2.9
	High								3.0
	Low								2.2
	Distributed								2.0
	3 rows stacked								1.4
EPS Geofoam	Control	Clay (CL)	19	20	60	0.2	35	0	15.8
	High								17.1
	Low								14.1
	Distributed								15.1
	3 rows stacked								11.7
Tire Bale	Control					5.5	25	2.4	15.8
	High								16.0
	Low								13.5
	Distributed								13.3
	3 rows stacked								9.9
PET Bale	Control					2.36	10	0	15.8
	High								16.5
	Low								13.3
	Distributed								13.4
	3 rows stacked								9.4
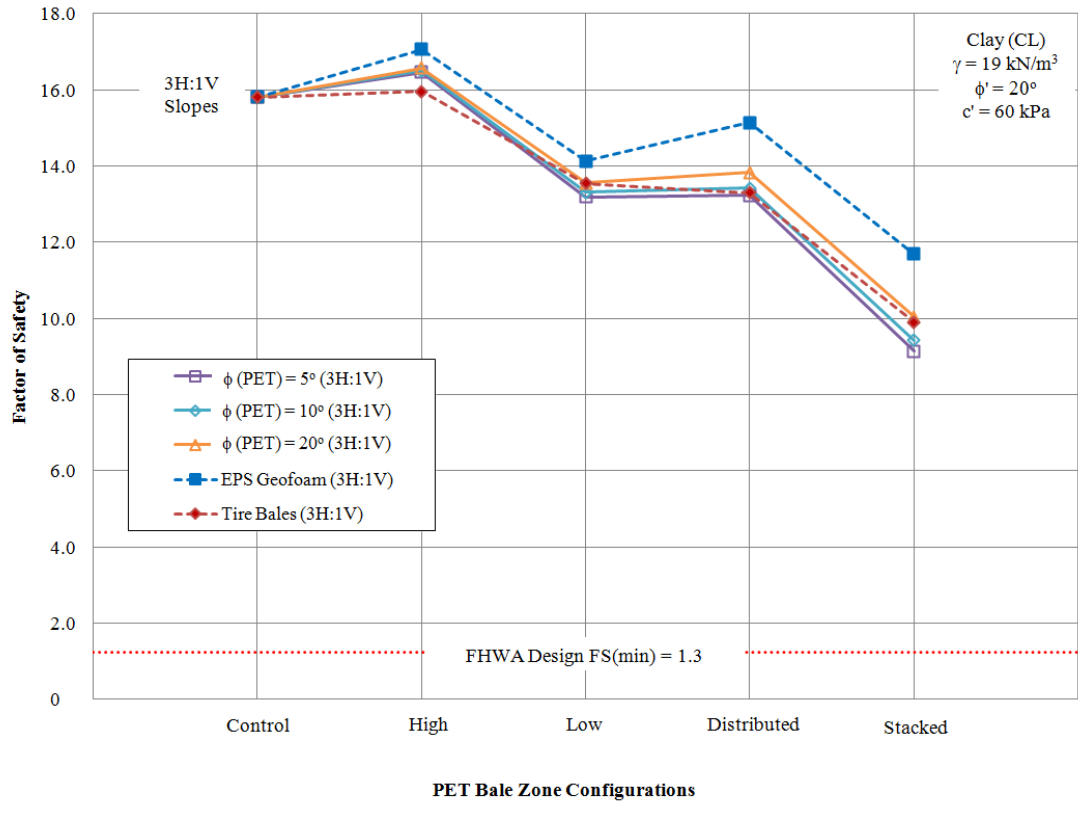
Figure 6.9: Comparison of the PET bale FS results to EPS Geofoam and tire bale FS results for the 3H:1V slope inclination

6.3.2 Local 'Per Slice' Evaluation

To better understand the influence that the recycled PET bale material inclusions on the FS values calculated in the previous section, local normal, resisting, and driving forces were calculated for each individual slice for select cases. Calculation of these forces locally (for each of the 100 individual slices generated) was conducted to better understand and identify the interplay of forces (resisting, driving, and normal) acting along the fixed failure plane arc length with and without the inclusion of the PET bale material.

Figures 6.10 and 6.11 are identical to Figures 6.3 and 6.4 except that they focus on the arc length over which the PET bales intersect the defined failure plane. Each fixed failure plane has arc length identifiers referenced back to the toe of the slope that will be utilized in the following discussion. Figures 6.10(a), 6.10(b), and 6.10(c) display the arc length identifiers for the control, low position, and high position, respectively. Figures 6.11(a) and 6.11(b) display the arc length identifiers for the distributed and stacked configurations, respectively.

Configuration: Control (3:1)
Center of Circle is 30 m above toe
Radius = 30 m

(a)

Configuration: Low (3:1)
Center of Circle is 30 m above toe
Radius = 30 m

(b)

Configuration: High (3:1)
Center of Circle is 30 m above toe
Radius = 30 m

(c)
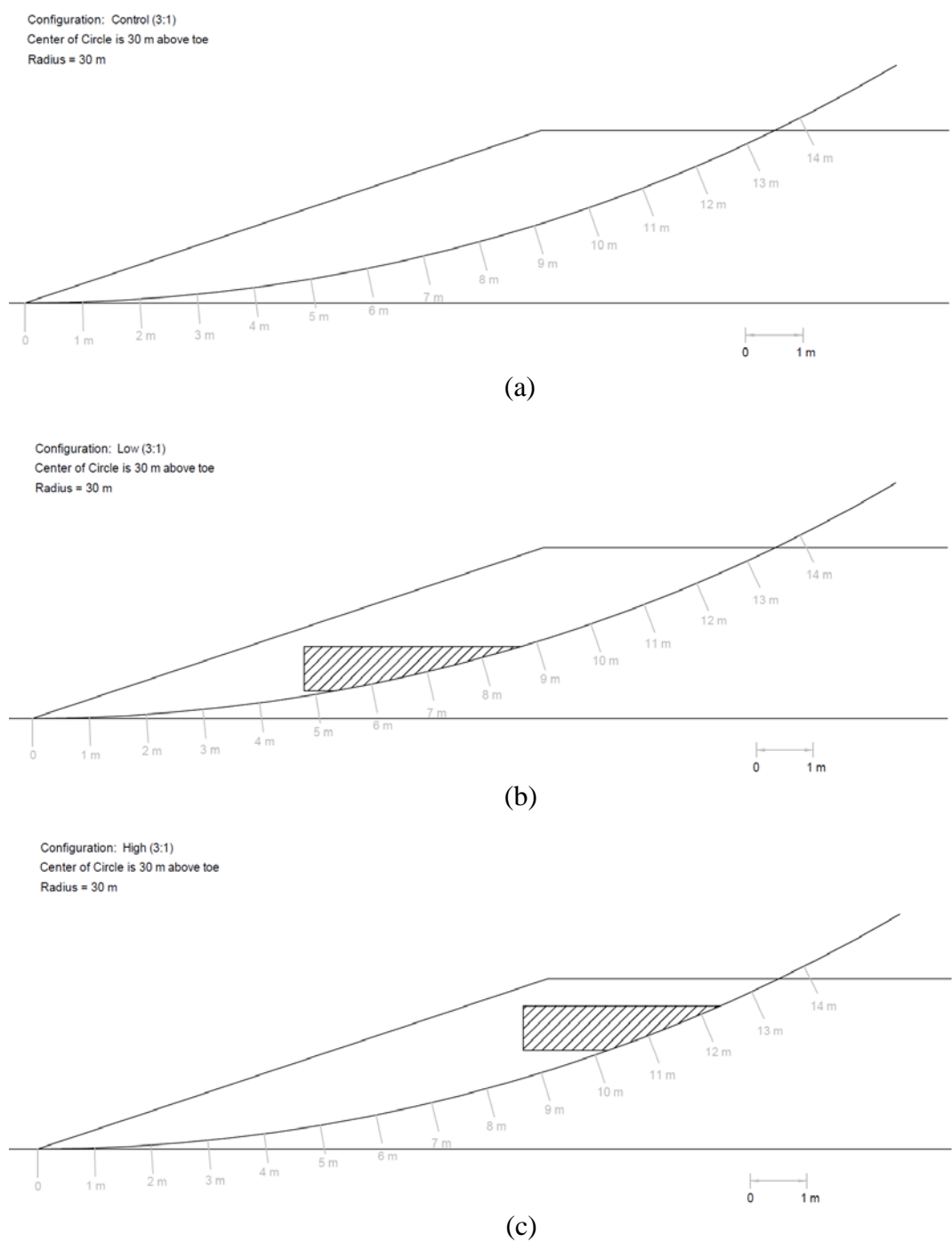
Figure 6.10: Fixed failure plane arc length identifiers for the control and single row PET bale configurations using the 3:1 slope inclination: (a) control (no inclusions); (b) row positioned low; and (c) row positioned high
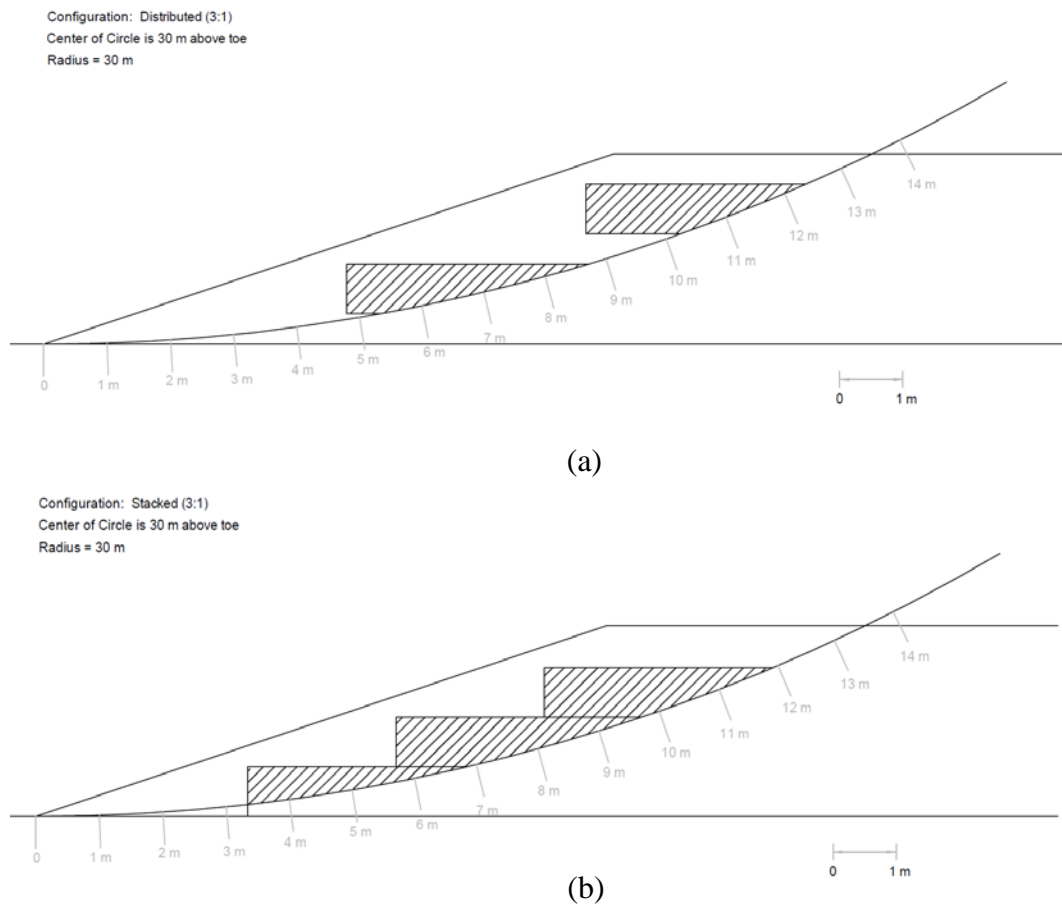
Figure 6.11: Fixed failure plane arc length identifiers for the control and multiple row PET bale configurations using the 3:1 slope inclination: (a) distributed; and (b) stacked

All five PET bale configurations were examined on a 'per slice' basis for the 3H:1V slope inclination assuming a clay (CL) embankment and a 5° PET friction angle. Figure 6.12 displays the 3H:1V clay slope with 100 slices defined as part of the Ordinary Method of Slices (OMS) analysis conducted during this study.

Configuration: Control (3:1)
Center of Circle is 30 m above toe
Radius = 30 m
100 slices
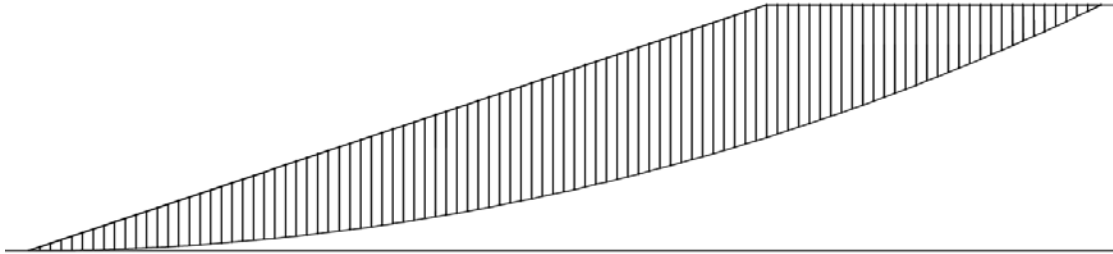
Figure 6.12: OMS 100 slice configuration for the localized FS computations using the 3H:1V slope inclination without PET bale inclusions

The area of the soil, area of the recycled PET material, angle of inclination (α_i), and arc length (l_i) values were determined inside AutoCAD. The weight of each slice (W_i) was calculated using the calculated areas and the unit weights of each corresponding material type assuming a unit length of 1 m. The unit weights of the soil and recycled PET bale material were 19 kN/m^3 and 2.36 kN/m^3, respectively. Using the weight (W_i), angle of inclination (α_i), length along failure plane (l_i), and the material properties (see Table 6.4), the local forces for each slice were calculated. Additionally, the ratio of the weight of recycled PET material to the weight of soil was calculated for each slice to quantify the influence that the recycled PET had on each slice respectively.

Figures 6.13 and 6.14 display the cumulative summation of the driving and resisting forces, respectively, along the arc length of the failure curve (relative to the toe of the slope) for the control configuration assuming a 3H:1V slope inclination. The total summation of driving forces is equal to 56.9 kN and the total summation of resisting forces is equal to 870.72 kN as displayed on these figures. If the cumulative resisting force is divided by the cumulative driving force, the FS for the control configuration is 15.8, which matches the value reported on Table 6.6 for the control configuration assuming the CL embankment. Likewise, Figures 6.15 and 6.16 display the cumulative summation of the driving and resisting forces, respectively, along the arc length of the fixed failure curve (relative to the toe of the slope) for the low position configuration assuming a 3H:1V slope inclination. The cumulative driving and resisting forces labeled on these figures are utilized to calculate the FS for this fixed failure surface, equal to 13.2, which matches the value reported in Table 6.6 for the low position configuration assuming a CL embankment.
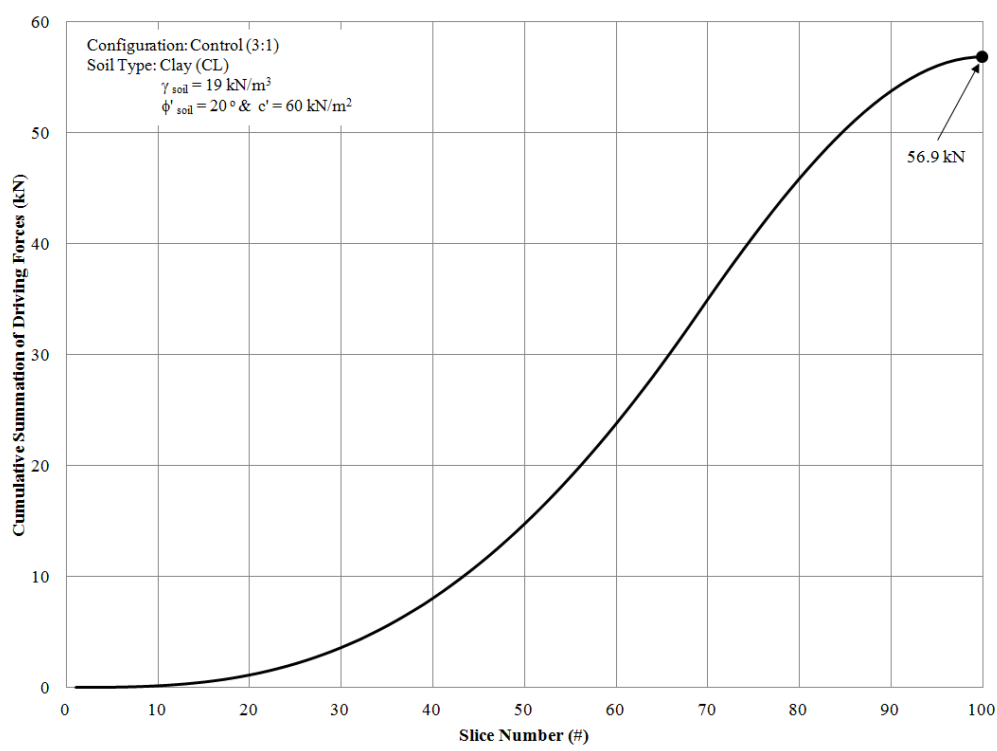
Figure 6.13: Cumulative summation of the driving forces along the length of the failure curve for the control configuration using a 3H:1V slope inclination
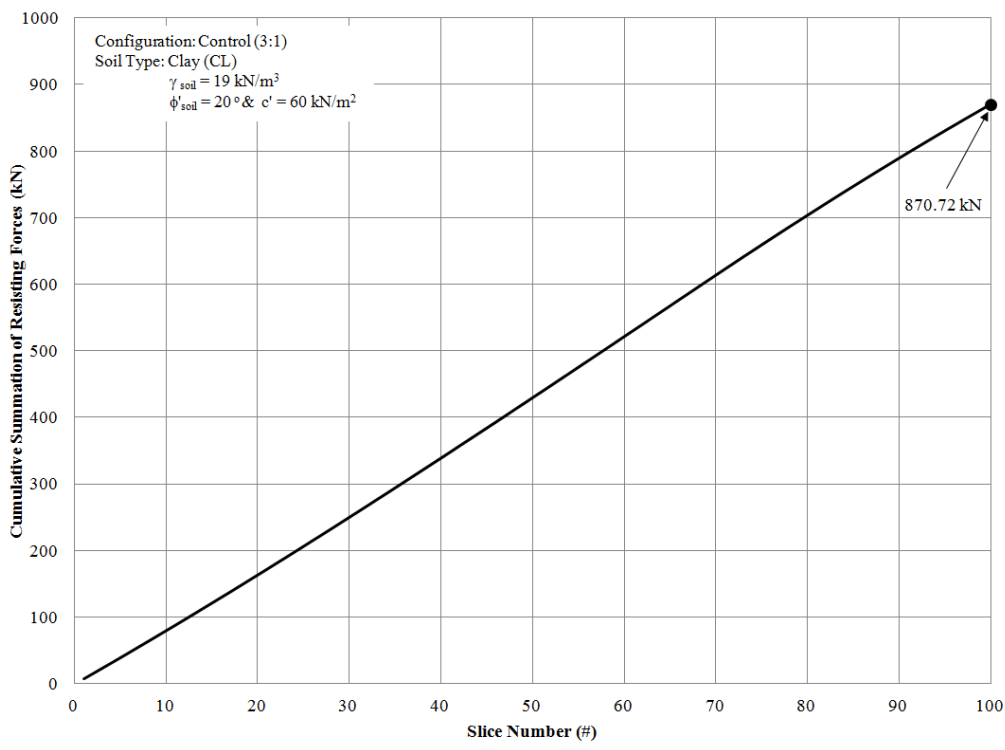
Figure 6.14: Cumulative summation of the resisting forces along the length of the failure curve for the control configuration using a 3H:1V slope inclination
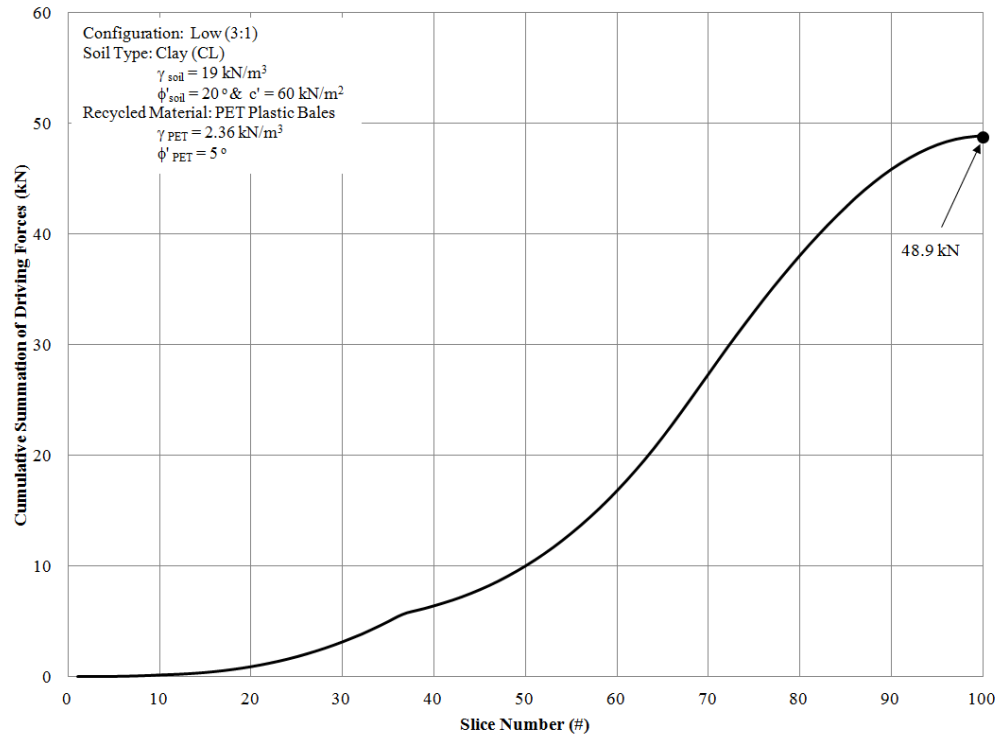
Figure 6.15: Cumulative summation of the driving forces along the length of the failure curve for the low position configuration using a 3H:1V slope inclination
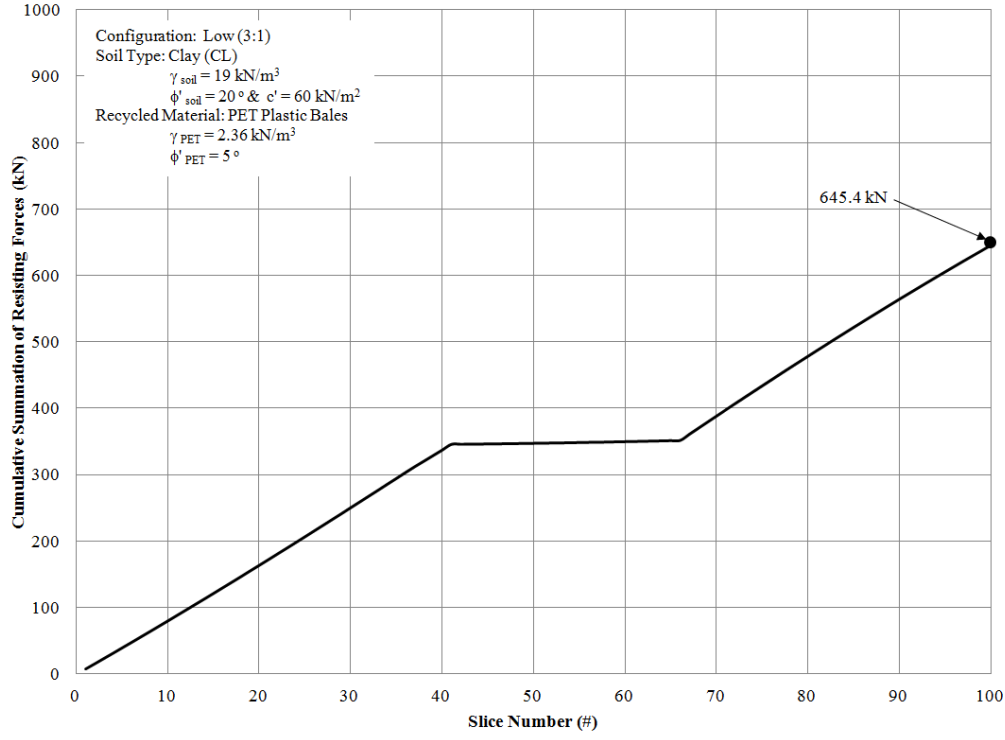
Figure 6.16: Cumulative summation of the resisting forces along the length of the failure curve for the low position configuration using a 3H:1V slope inclination

Figure 6.17(a) displays the normal, resisting, and driving forces for each slice of the control slope configuration (no inclusions). The forces are displayed as a function of the arc length along the fixed failure plane as defined in Figures 6.10 and 6.11. Similarly, Figure 6.17(b) displays the corresponding weight ratio of recycled PET material to soil as a function of arc length. It is clear that the local resisting forces in the control slope are significantly higher in comparison to the local driving forces so the local FS values are well above the acceptable design FS = 1.3. Because the recycled PET material is not incorporated into the control PET bale configuration, the recycled PET to soil ratio remains zero. Figure 6.17 serves as a baseline for the remaining four PET bale configurations.
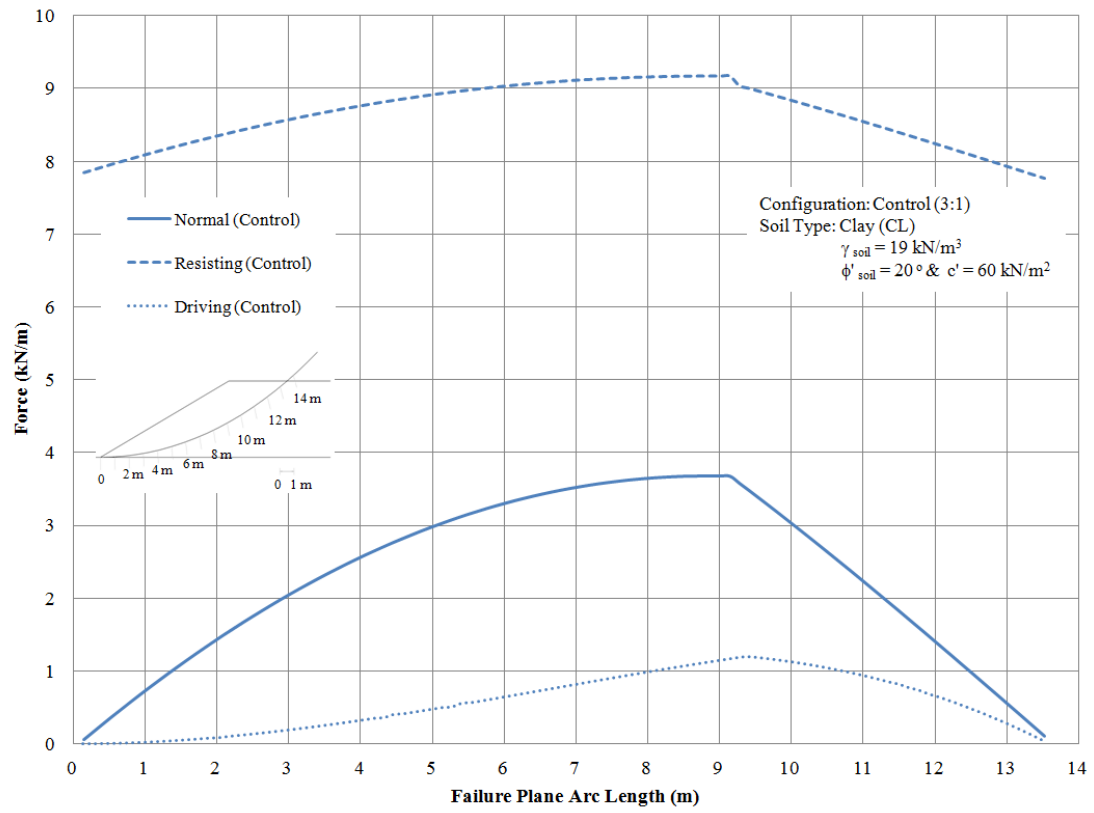
(a)
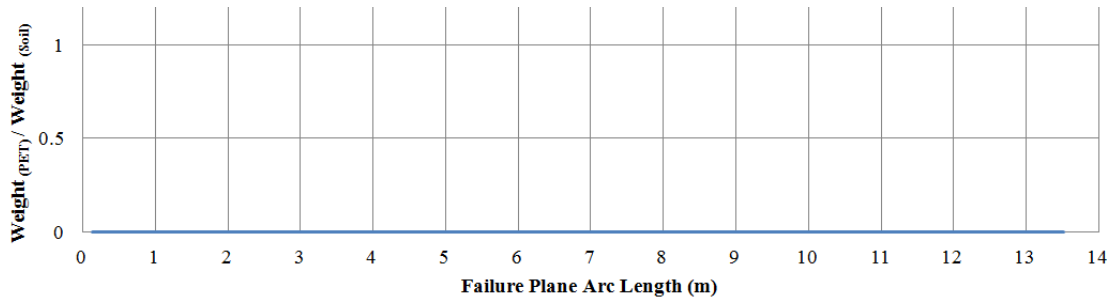
(b)

Figure 6.17: Local 'per slice' forces and weight ratios displayed as a function of arc length for the control configuration using a 3H:1V slope inclination, assuming a CL embankment: (a) normal, resisting, and driving forces as a function of arc length; and (b) weight ratio of PET bale to soil material as a function of arc length

Similar to Figure 6.17, Figure 6.18 displays the normal forces, Figure 6.19 displays the resisting forces, and Figure 6.20 displays the driving forces for the low position PET bale configuration. The ratio of the weight of the PET versus the weight of the soil as a function of arc length are also displayed in part (b) of each figure. All three forces are displayed next to their corresponding force from the control configuration for comparison. The shaded area in each figure highlights the arc length distance along the fixed failure plane that is impacted by recycled PET material. In other words, the shaded area corresponds to the recycled PET bale to soil weight ratios greater than 0 in part (b) of each figure.

For the low position PET bale configuration, there is a decrease in the normal force with arc length due to the integration of the lightweight fill (Figure 6.18), there is a decrease in the resisting force where the PET bale material intersects the fixed failure plane due to the decrease in the shear strength of the PET bale material (Figure 6.19), and there is a slight decrease in the driving force due to the lowered weight of the material (Figure 6.20). Changes in these forces for these figures and the following figures are proportional to the amount of PET material above the point and/or the arc length that is intersected by the PET material in all cases. For example, the largest drop in the normal force for the low position PET bale configuration occurs at the 4.7 m point along the arc length, which corresponds to the thickest point of PET material (Figure 6.18).

Figure 6.18: Local 'per slice' forces and weight ratios displayed as a function of arc length for the low position PET bale configuration using a 3H:1V slope inclination, assuming a CL embankment: (a) normal force as a function of arc length; and (b) weight ratio of PET bale to soil material as a function of arc length

Figure 6.19: Local 'per slice' forces and weight ratios displayed as a function of arc length for the low position PET bale configuration using a 3H:1V slope inclination, assuming a CL embankment: (a) resisting force as a function of arc length; and (b) weight ratio of PET bale to soil material as a function of arc length

Figure 6.20: Local 'per slice' forces and weight ratios displayed as a function of arc length for the low position PET bale configuration using a 3H:1V slope inclination, assuming a CL embankment: (a) driving force as a function of arc length; and (b) weight ratio of PET bale to soil material as a function of arc length

Figure 6.21 displays the normal forces, Figure 6.22 displays the resisting forces, and Figure 6.23 displays the driving forces for the high position PET bale configuration. The ratio of the weight of the PET versus the weight of the soil as a function of arc length are also displayed in part (b) of each figure. All three forces are displayed next to their corresponding force from the control configuration for comparison. The shaded area in each figure highlights the arc length distance along the fixed failure plane that is impacted by recycled PET material. Similar to the previous figures, there is a decrease in the normal force with arc length due to the integration of the lightweight fill (Figure 6.21), there is a decrease in the resisting force where the PET bale material intersects the failure plane due to the decrease in the shear strength of the PET bale material (Figure 6.22), and there is a slight decrease in the driving force due to the lowered weight of the material (Figure 6.23). Changes in these forces for these figures and the following figures are proportional to the amount of PET material above the point and/or the arc length that is intersected by the PET material in all cases.

Figure 6.21: Local 'per slice' forces and weight ratios displayed as a function of arc length for the high position PET bale configuration using a 3H:1V slope inclination, assuming a CL embankment: (a) normal force as a function of arc length; and (b) weight ratio of PET bale to soil material as a function of arc length

(a)

(b)

Figure 6.22: Local 'per slice' forces and weight ratios displayed as a function of arc length for the high position PET bale configuration using a 3H:1V slope inclination, assuming a CL embankment: (a) resisting forces as a function of arc length; and (b) weight ratio of PET bale to soil material as a function of arc length

(a)

(b)
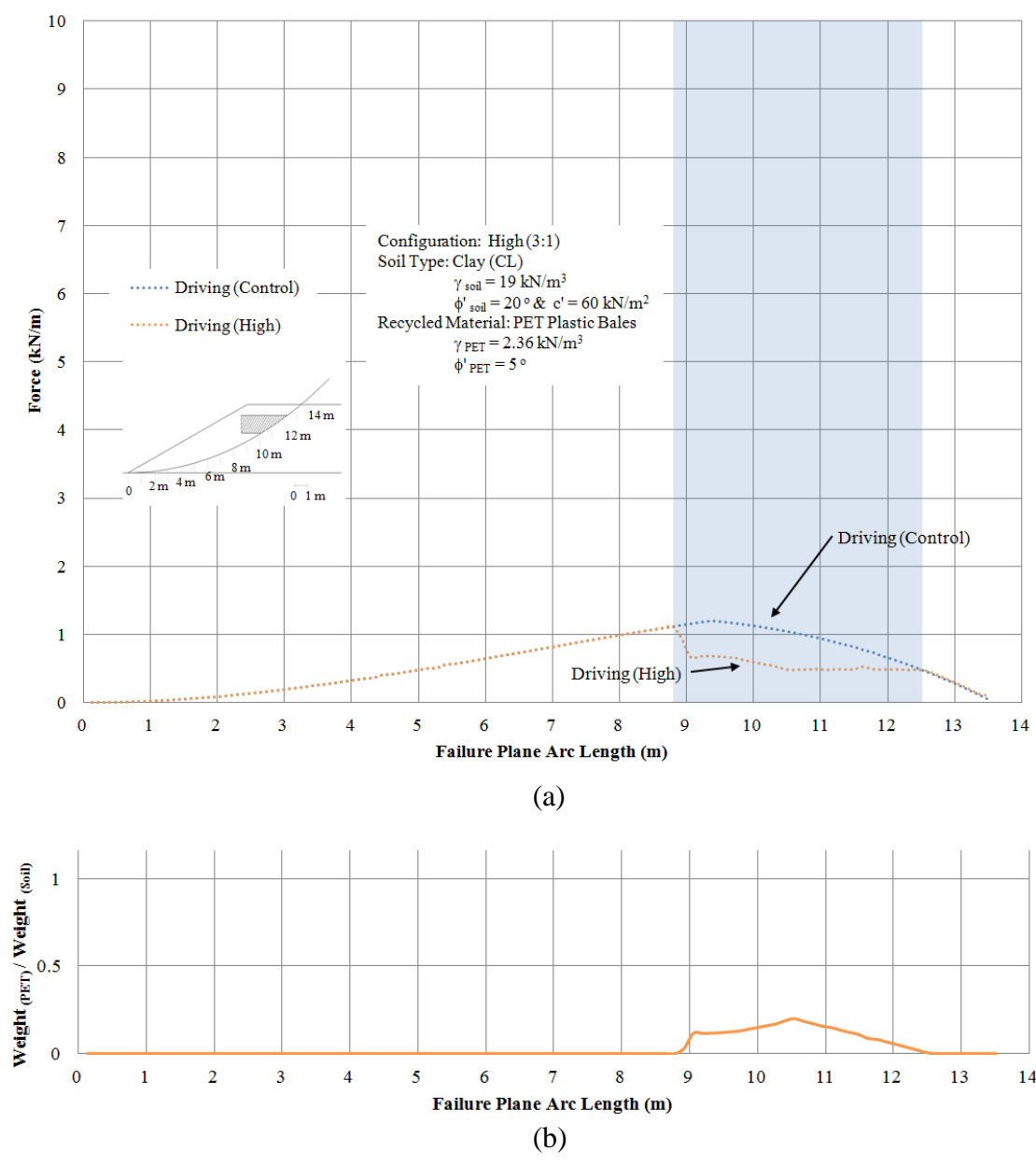
Figure 6.23: Local 'per slice' forces and weight ratios displayed as a function of arc length for the high position PET bale configuration using a 3H:1V slope inclination, assuming a CL embankment: (a) resisting force as a function of arc length; and (b) weight ratio of PET bale to soil material as a function of arc length

Figure 6.24 displays the normal forces, Figure 6.25 displays the resisting forces, and Figure 6.26 displays the driving forces for the distributed PET bale configuration. The ratio of the weight of the PET versus the weight of the soil as a function of arc length are also displayed in part (b) of each figure. All three forces are displayed next to their corresponding force from the control configuration for comparison. The shaded area in each figure highlights the arc length distance along the fixed failure plane that is impacted by recycled PET material. The same trends are exhibited in these figures except the decreases in the forces are accentuated two times across the arc length because of the distributed PET bale configuration (two rows of bales).
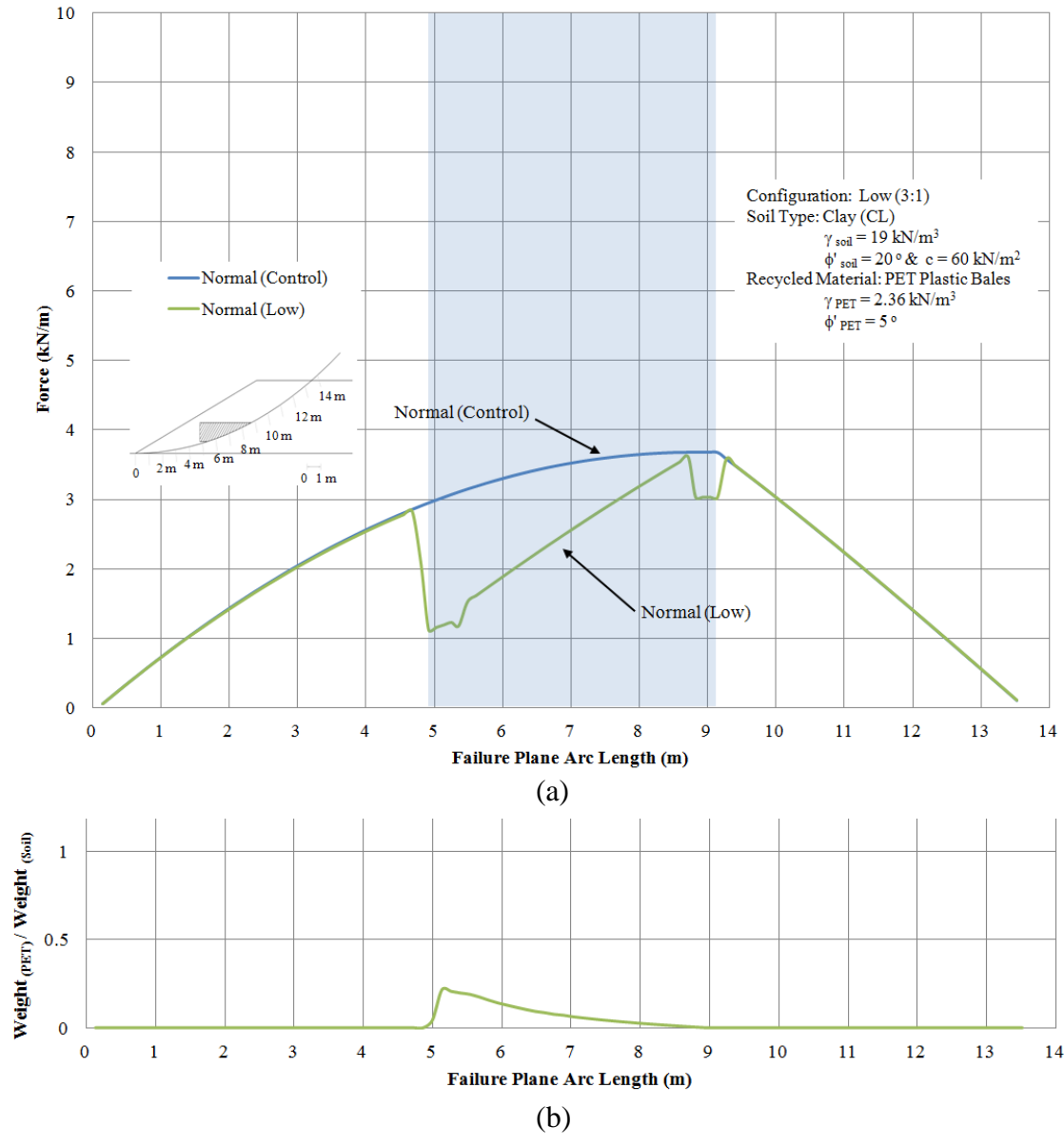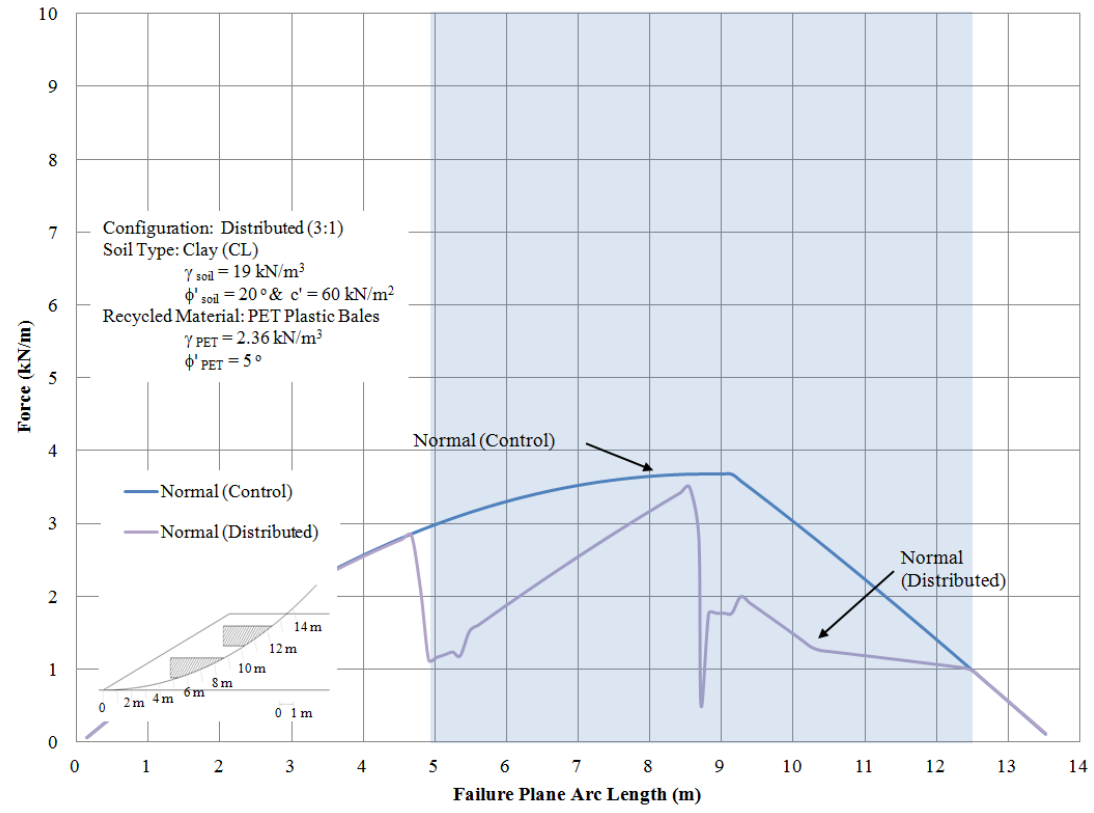
(a)
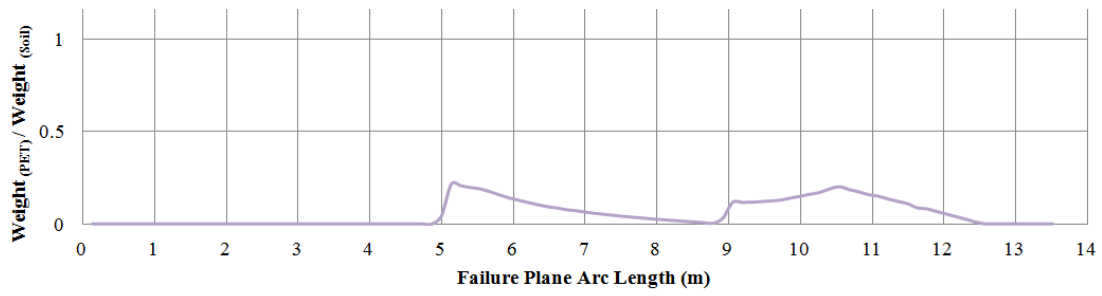
(b)

Figure 6.24: Local 'per slice' forces and weight ratios displayed as a function of arc length for the distributed PET bale configuration using a 3H:1V slope inclination, assuming a CL embankment: (a) normal force as a function of arc length; and (b) weight ratio of PET bale to soil material as a function of arc length
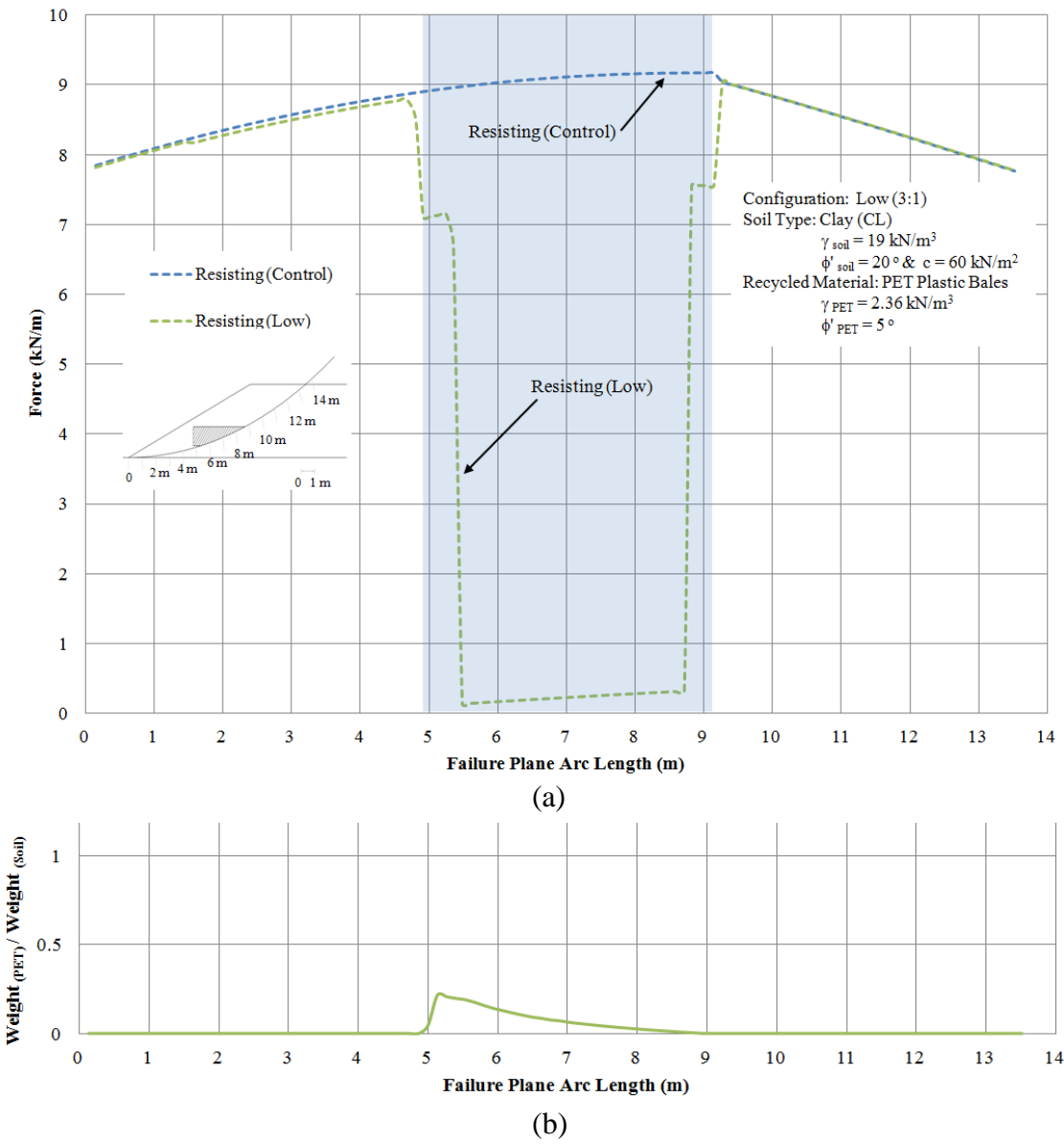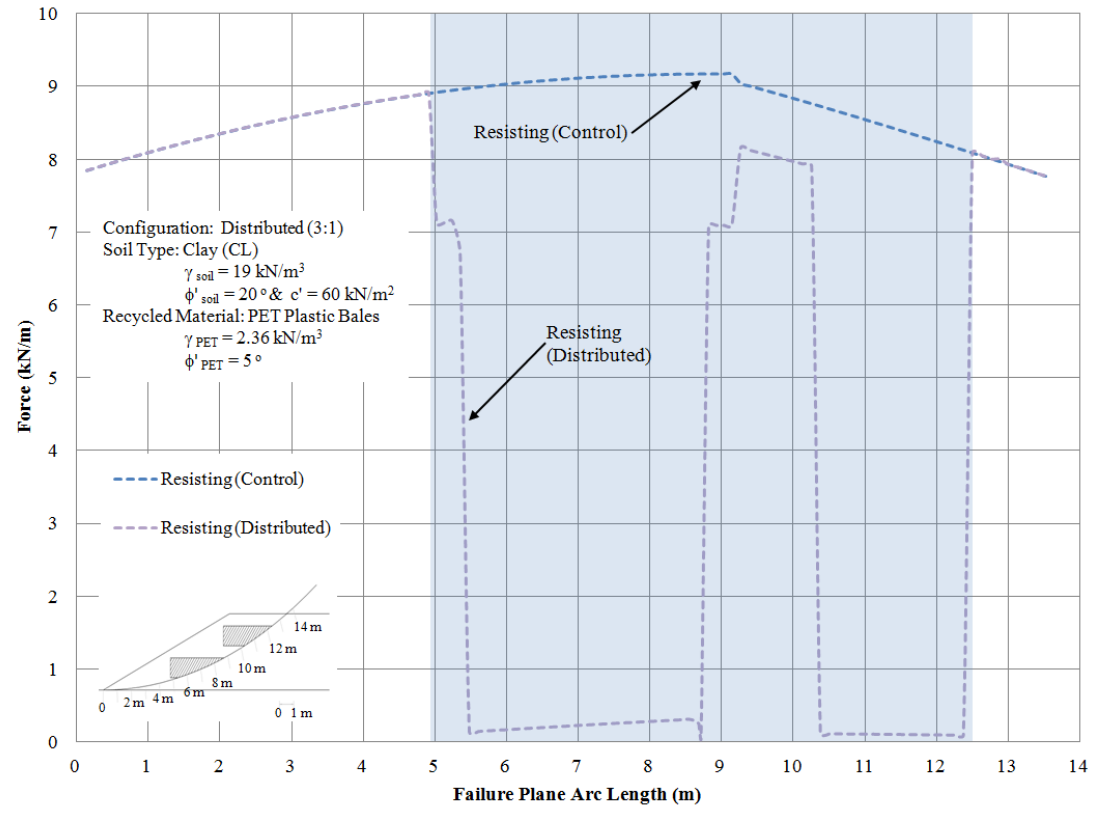
(a)
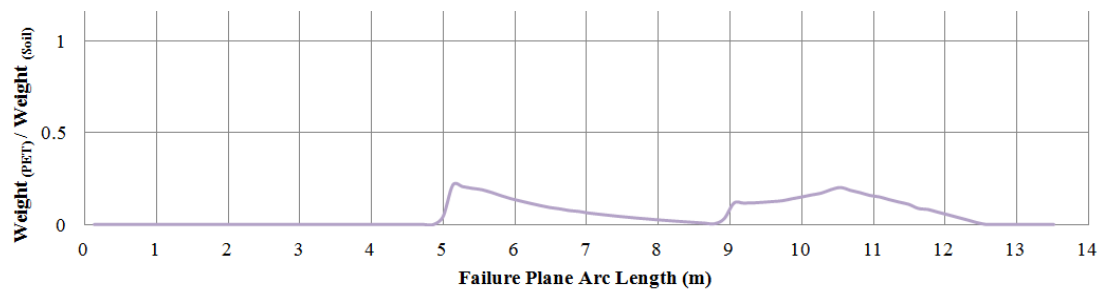
(b)

Figure 6.25: Local 'per slice' forces and weight ratios displayed as a function of arc length for the distributed PET bale configuration using a 3H:1V slope inclination, assuming a CL embankment: (a) resisting force as a function of arc length; and (b) weight ratio of PET bale to soil material as a function of arc length
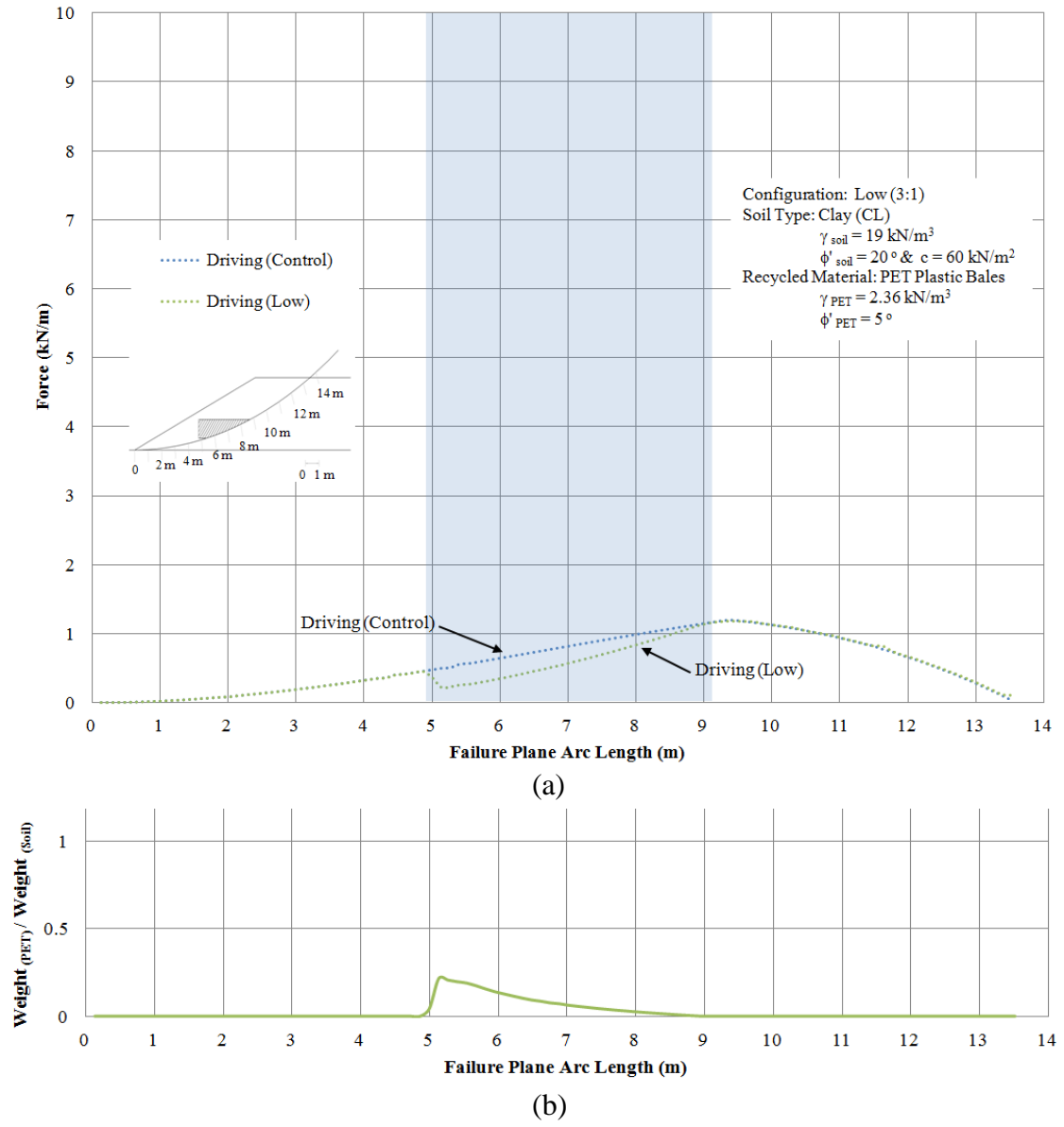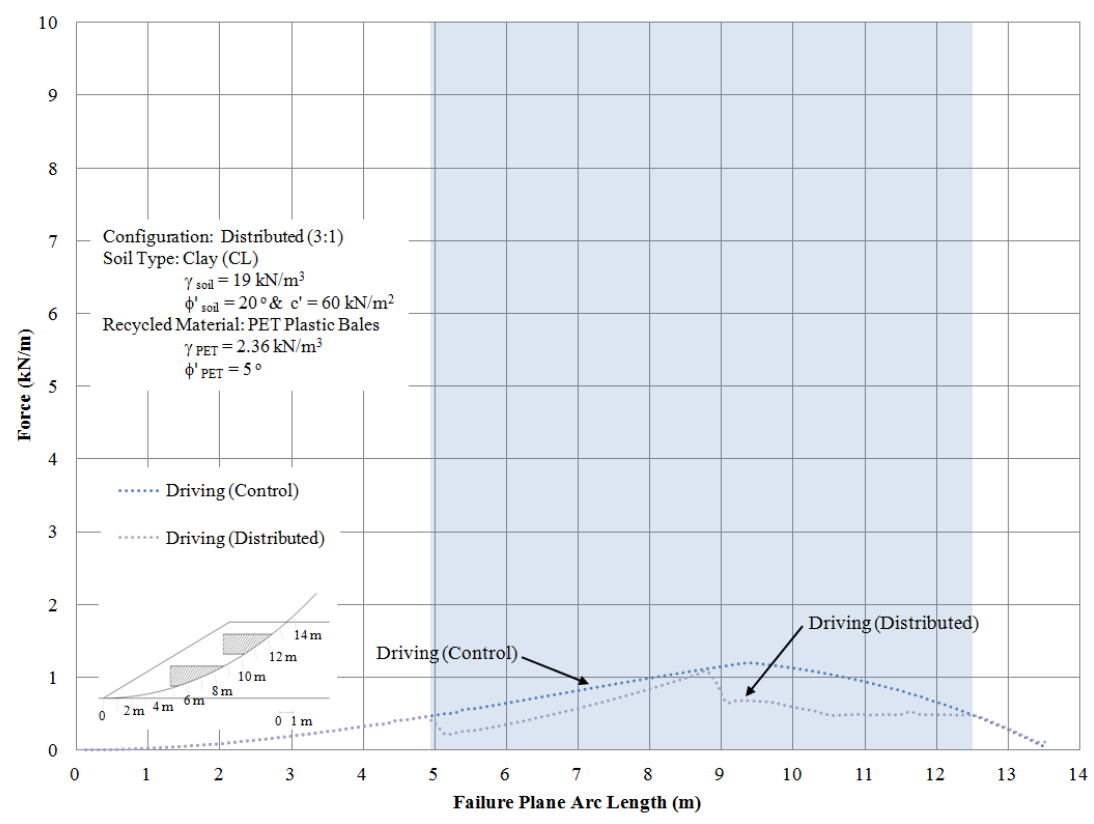
(a)
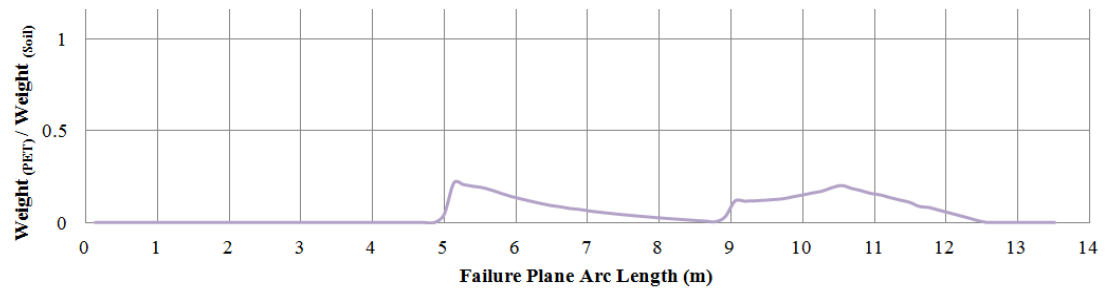
(b)

Figure 6.26: Local 'per slice' forces and weight ratios displayed as a function of arc length for the distributed PET bale configuration using a 3H:1V slope inclination, assuming a CL embankment: (a) driving force as a function of arc length; and (b) weight ratio of PET bale to soil material as a function of arc length

Figure 6.27 displays the normal forces, Figure 6.28 displays the resisting forces, and Figure 6.29 displays the driving forces for the stacked PET bale configuration. The ratio of the weight of the PET versus the weight of the soil as a function of arc length are also displayed in part (b) of each figure. All three forces are displayed next to their corresponding force from the control configuration for comparison. The shaded area in each figure highlights the arc length distance along the fixed failure plane that is impacted by recycled PET material. The same trends are exhibited in these figures except there are three distinct changes in the normal and driving forces since there are three consecutive rows of PET bales on top of each other. Additionally, the decrease in resisting force occurs over a longer arc length since the PET bale material, which has a lower shear strength, intersects the fixed failure surface over a longer arc length.
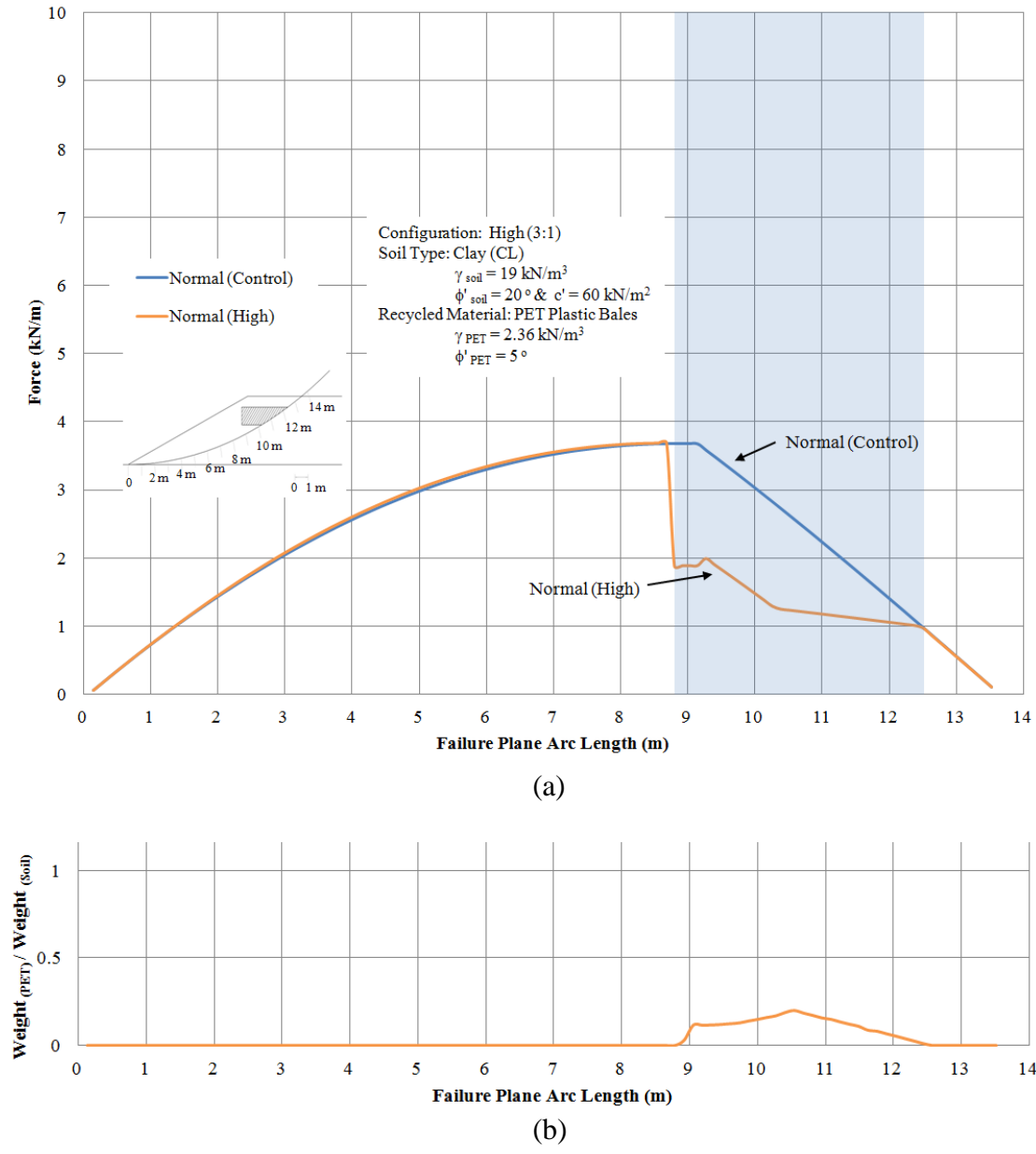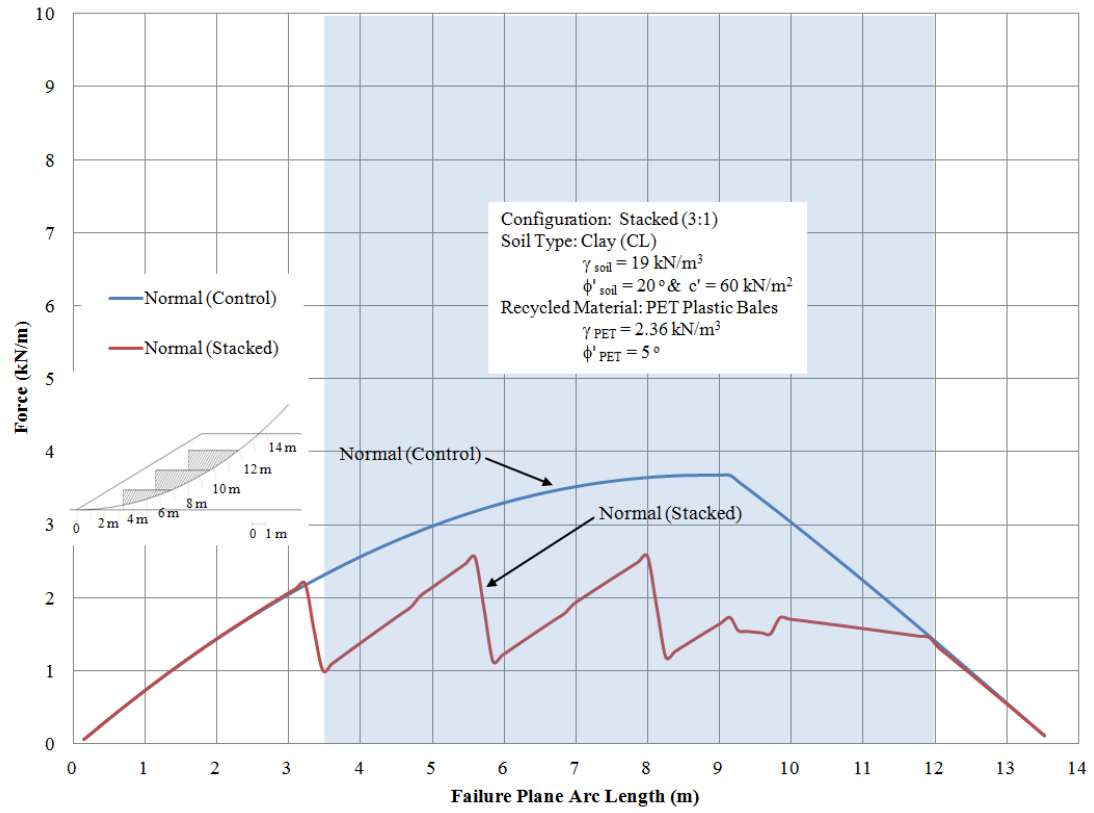
(a)
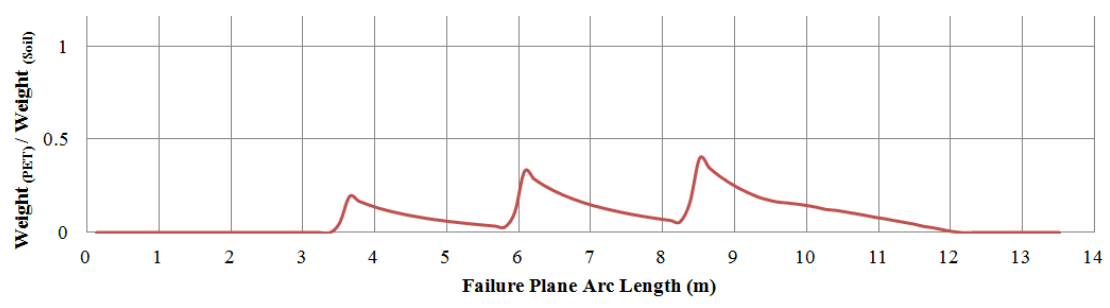
(b)

Figure 6.27: Local 'per slice' forces and weight ratios displayed as a function of arc length for the stacked PET bale configuration using a 3H:1V slope inclination, assuming a CL embankment: (a) normal force as a function of arc length; and (b) weight ratio of PET bale to soil material as a function of arc length
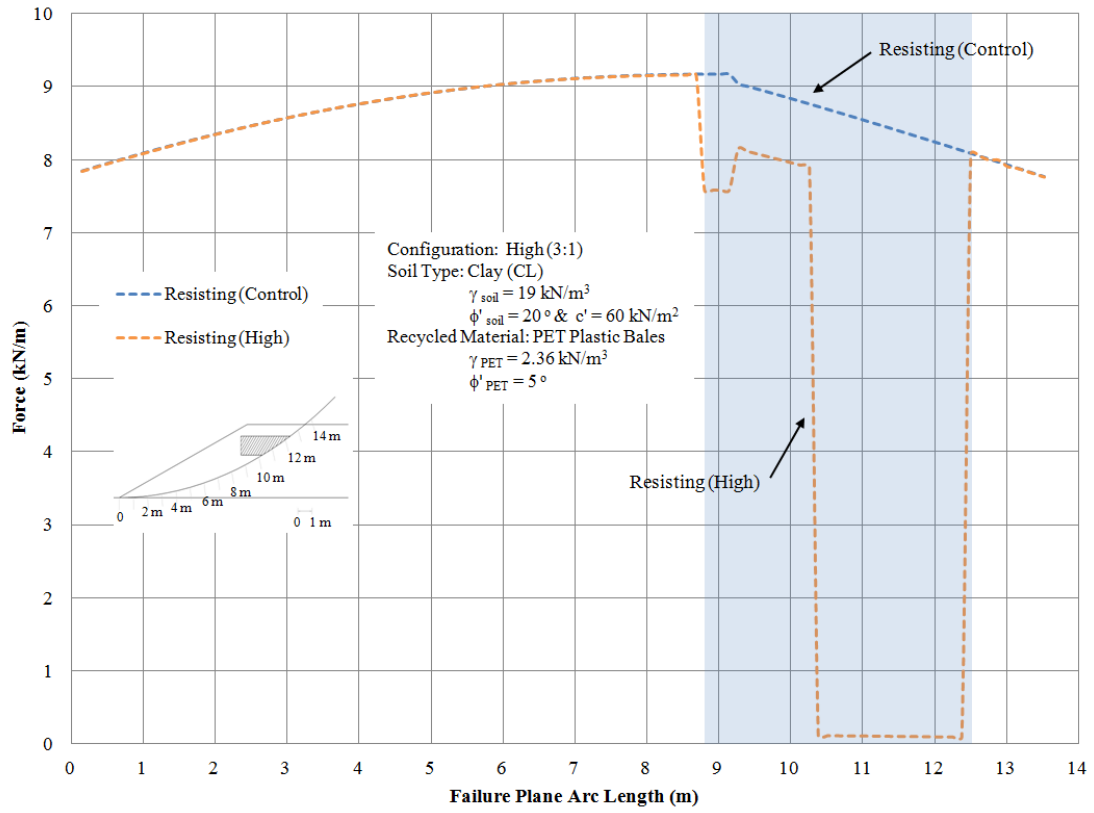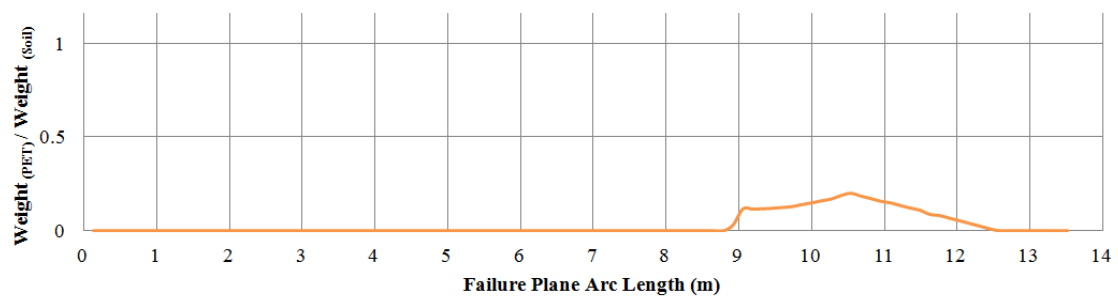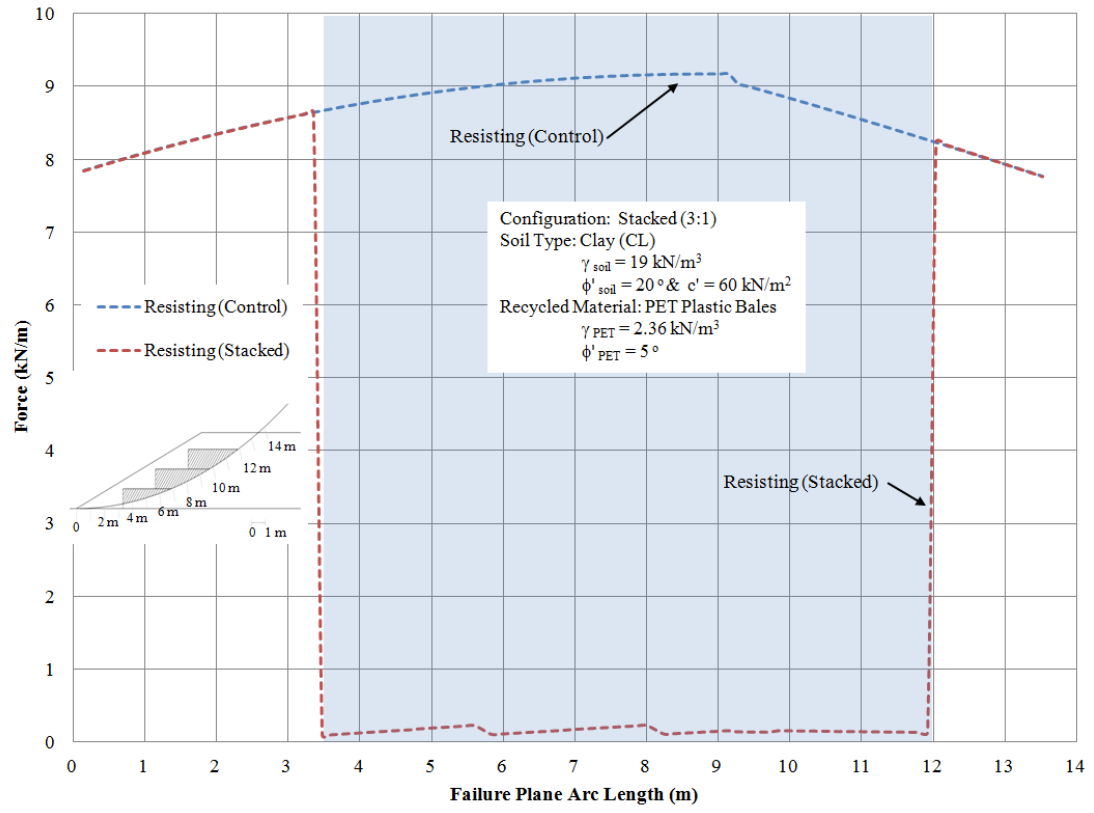
(a)
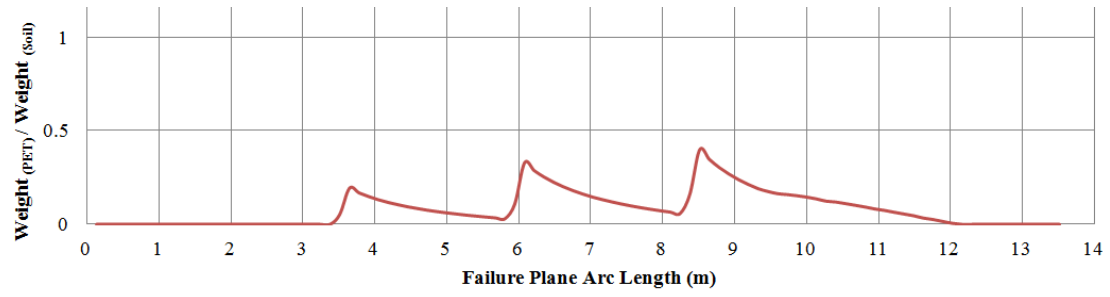
(b)

Figure 6.28: Local 'per slice' forces and weight ratios displayed as a function of arc length for the stacked PET bale configuration using a 3H:1V slope inclination, assuming a CL embankment: (a) resisting force as a function of arc length; and (b) weight ratio of PET bale to soil material as a function of arc length
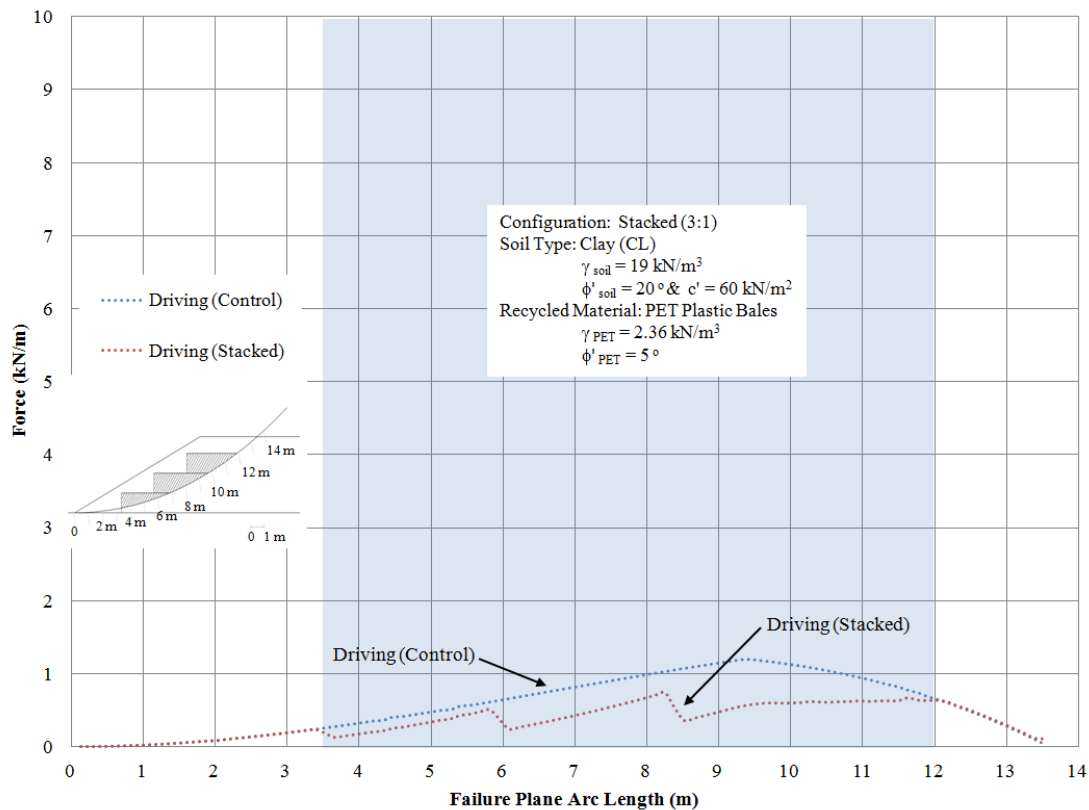
(a)
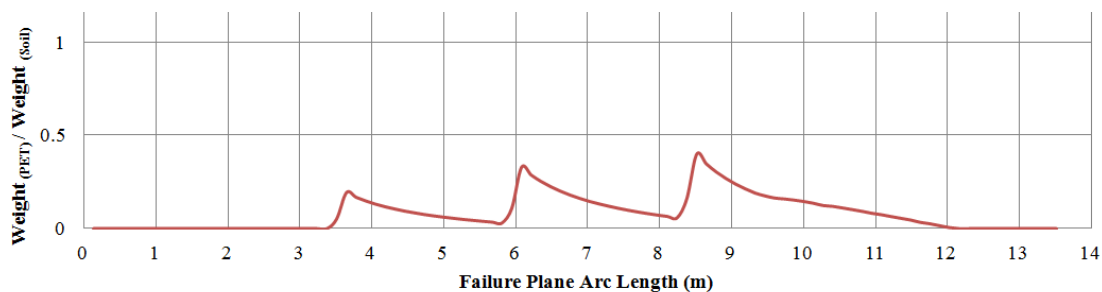
(b)

Figure 6.29: Local 'per slice' forces and weight ratios displayed as a function of arc length for the stacked PET bale configuration using a 3H:1V slope inclination, assuming a CL embankment: (a) driving force as a function of arc length; and (b) weight ratio of PET bale to soil material as a function of arc length

6.4 Discussion of Results: Lightweight Fill Positioned Inside the Fixed Failure Surface

Section 6.3 presents the results from all analyses that configure the PET bale zones to intersect the fixed failure surface. Because the shear strength of the PET bale material was significantly less than the shear strength of the subsurface soil, the fixed surface FS values generally decreased due to the decrease in the resulting resisting force along the fixed failure surface. To better understand the effect of the lightweight fill without being impacted by a decrease in shear strength reduction along the fixed failure surface, a separate analysis was conducted assuming the PET bale material was only inside the fixed failure surface defined as part of this study.

The unit weight of the material mass inside the fixed circular failure surface was adjusted to model the different materials including soil, the low end unit weight of the PET bale material (2.36 kN/m^3), the high end unit weight of the PET bale material (3.93 kN/m^3), the tire bales, and the EPS Geofoam. In all cases, the resisting force developed as a result of the shear strength parameters associated with the soil under the fixed failure surface. The results of the of each slope stability analysis are displayed in Figure 6.30. Figure 6.30 displays the fixed failure surface FS as a function of the unit weight for each material type. The PET bale material is more comparable to the lightweight fill characteristics of the tire bales.
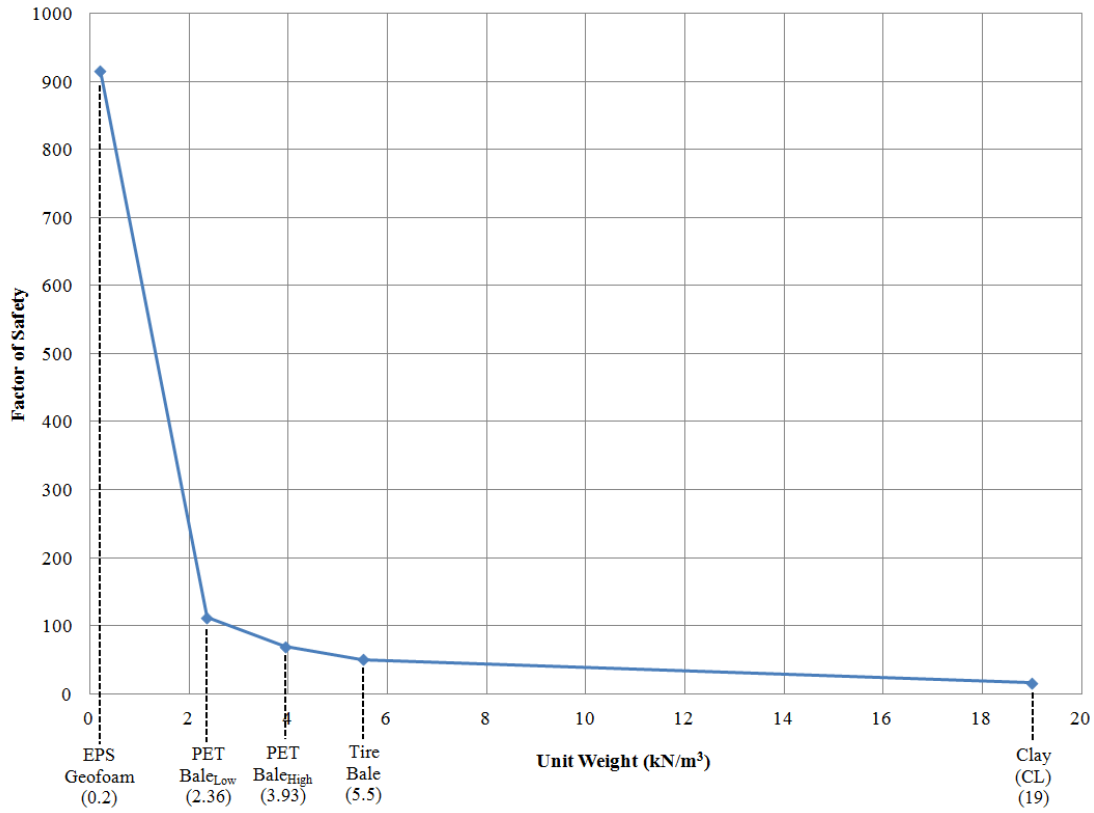
Figure 6.30: FS as a function of unit weight when the material inside the fixed failure surface is represented by material properties associated with soil, tire bales, PET bales, and EPS Geofoam configurations using a 3H:1V slope inclination, assuming a clay (CL) embankment

6.5 Summary: Limit Equilibrium Analysis

A series of slope stability limit equilibrium analyses were conducted using five different PET bale configurations, two different slope inclinations, and two soil types to further assess the feasibility of utilizing PET bales as lightweight material in embankments. It is important to note that the analysis uses a pre-defined fixed failure surface for a more controlled comparison of the FS output so the FS results reported herein do not represent minimum FS values from an extensive limit equilibrium analysis on each embankment. The friction angles determined from the triaxial compression tests (discussed in a previous chapter) were used as conservative shear strength material inputs for the slope stability limit equilibrium analyses.

First, the embankments were analyzed assuming the PET bale zones intersected the failure surface (see Figures 6.1 – 6.4), but the FS values for both slope inclinations generally decreased in comparison to the control condition in all cases (Figures 6.5 and 6.6). For the low, distributed, and stacked PET bale zone configurations, the benefits associated with the lightweight unit weight of the PET bales were not enough to compensate for the decrease in the overall resisting moment associated with the low shear strength of PET zones along the fixed failure surface.

Subsequently, the same analyses were performed using the material properties for EPS Geofoam and tire bales. With the exception of the EPS Geofoam values, which are slightly higher, all other calculated FS values for this fixed failure surface were similar in magnitude (Figure 6.9). If compressibility were not an issue with PET bale material, the use of the PET bales for lightweight fill would likely be feasible.

Additionally, the normal, resisting, and driving forces associated with each 'slice' evaluated during the OMS evaluation of the slope were calculated along the arc length of the fixed failure surface to determine the effect of the intersecting PET bale material with arc length, relative to the toe of the slope. In general, there was a decrease in the normal force with arc length due to the integration of the lightweight fill (PET bale material), there was a decrease in the resisting force where the PET bale material intersects the fixed failure plane due to the decrease in the shear strength of the PET bale material, and there was a slight decrease in the driving force due to the lowered weight of the material. Changes in these forces were proportional to the amount of PET material above the point of measurement and/or the arc length that is intersected by the PET material in all cases as expected.

A separate analysis was conducted assuming the PET bale material was only inside the fixed failure surface and the unit weight of the material mass inside the fixed circular failure surface was also adjusted to model the different materials including soil, tire bales, and EPS Geofoam. In all cases, the resisting force developed as a result of the shear strength parameters associated with the soil under the fixed failure surface. Figure 6.30 displays the fixed failure surface FS as a function of the unit weight for each material type. The PET bale material is more comparable to the lightweight fill characteristics of the tire bales.

CHAPTER 7: SUMMARY AND CONCLUSIONS

7.1 Research Summary

The overall goal of this research was to examine the engineering properties of a typical PET bale from a local MRF and determine the feasibility of using it as a lightweight construction fill in embankment applications. Specifically, an extensive suite of geotechnical tests were selected and modified as needed to evaluate the compressive and shear strength behaviors of the proposed lightweight fill.

Embankments and slopes are typically constructed using in-situ soil and aggregate and/or reinforced with steel or geosynthetic inclusions. Embankments with EPS Geofoam blocks and recycled tire bales have also been evaluated as alternative lightweight fill materials in recent studies (Horvath (1994); Jutkofsky et al, (2000); Mann and Stark (2007); Arellano et al., (2010); Winter et al. (2009); Zornberg et al. (2004), and LaRocque et al., (2005)). The use of the proposed recycled PET plastic bales in embankments would specifically address issues related to 1) waste generation rates that are increasing with decreasing finite spatial resources, 2) a growing population proportional to increasing infrastructure demands, and 3) natural resource availability, which is decreasing due to increasing anthropogenic impacts. This

research project was developed with the concept that there is a need to successfully implement innovative infrastructure components and new ideas for a sustainable future.

At the completion of the testing program described herein, the engineering properties of the PET bales were compared to the available properties reported for the alternative materials mentioned previously. The extensive literature review presented in Chapter 2 indicates that there is some data available regarding the engineering behavior and characteristics of EPS Geofoam and tire bales. In contrast, there is little to no information regarding the engineering behavior of recycled PET bales for use in embankments. As a result, it is worthwhile to determine whether this material is feasible for the proposed application.

The testing program conducted herein is extensive and was summarized in tabular format in Chapter 1. For clarity, the same table has been included on the following page as Table 7.1. In accordance with the information presented in the first column of Table 7.1, the following tests were completed as part of this study:

- 200 - tensile strength tests were performed on Type 1, 2, and 3 individual PET plastic constituents;

- 42 - 1D confined compression tests were conducted on Type 1 PET plastic specimens constructed using both full-bottle and chopped constituents inside two different sized cells using two different unit weights to simulate the low end and high end of the unit weight range generated at the MRF;

- 9 - interface direct shear tests were performed on select PET plastic materials to represent different textures and alignments due to the variability in the constituents of each bale;

- 24 - triaxial compression tests were performed on Type 1 plastic specimens constructed using chopped constituents under varying test conditions;

- 1 – full-scale, unconfined compression test was conducted on PET plastic bale to determine short term and long term compressive behaviors; and

- a series of limit equilibrium analyses were conducted using SLIDE to determine the effects of including PET bale zones in various configurations as lightweight fill.

A summary of the test details are also included in Table 7.1. The results from each test are presented in Chapters 3, 4, 5, and 6 of this dissertation, and the major findings from this study are presented in the following section.

Table 7.1: Summary of key components of experimental research apart of this study

Test Report Sections (No. Tests)	Test Specimen Description	Test Configuration	Test Variables
Tensile Strength Sections 3.3-3.4 (200)	• Individual Recycled PET Constituents (Groups 1/2/3)	• UTS Tensile Machine • Curtis Hydraulic grips	• Displacement Rate = 1.27 mm/min, 12.7 mm/min
1D Confined Compression Section 4.2 (42)	• Full-Bottle Constituents • Chopped Constituents (Group 1 Only)	• Displacement Rate = 3.81 cm/min • 127 cm String Potentiometer (1) • 445 kN Load Cell • Hydraulic Piston • Steel Cylinders	• Loading Scheme = M1, M2 • γ_{PET} = 2.36 kN/m³, 3.93 kN/m³ • Test Specimen Diameter = 22.86 cm, 45.72 cm
Interface Direct Shear Section 4.3 (9)	• Select Recycled PET plastic (Group 1 Only)	• Geotac Direct Shear Apparatus • Displacement Rate = 0.01 cm/min • Normal Stress = 50 kPa, 100 kPa, and 200 kPa	• Texture: Flat, Ribbed-Orthogonal, and Ribbed-Aligned
Triaxial Compression Section 4.4 (24)	• Chopped Constituents (Group 1 Only)	• ELE Load Frame • 4.45 kN Load Cell • Axial Strain Transducer • 15.24 cm Diameter Triaxial Cell • Confining Pressure (17.24 kPa, 34.47 kPa, 51.71 kPa, 68.95 kPa)	• Disp. Rate: 0.02 - 10 mm/min • γ_{PET} = 0.79 kN/m³ -2.36 kN/m³ • Saturation: Dry and Saturated
Unconfined Compression Sections 5.2-5.4 (1)	• Full-Scale Recycled PET Bale (Groups 1/2/3)	• 127 cm String Potentiometers (4) • Short Term (1.5 hours) Applied Stress = 42.4 kPa • Long Term (15,330 hours) Creep Stress = 23.5 kPa	
Limit Equilibrium Analysis Sections 6.1-6.6 (80)	• Simulated Lightweight Zones within the Subsurface	• SLIDE (Version 6.035 – Rocscience) • Fixed Circular Failure Surface (Center Located 30 m Above Toe) • γ_{PET} = 2.36 kN/m³, 3.93 kN/m³ $\gamma_{Geofoam}$ = 0.20 kN/m³ $\gamma_{Tire\,bale}$ = 5.50 kN/m³ γ_{Clay} = 19 kN/m³ γ_{Sand} = 18 kN/m³	• Material Type: SW Soil, CL Soil, EPS Geofoam, and Tire Bales • Bale Configuration • PET Friction Angle: 5°, 10°, 15° • Slope Inclination: 3H:1V, 2H:1V

7.2 Research Conclusions

The following conclusions were drawn from the work conducted as part of this research:

1. Table 4.5 displays typical constrained moduli for soils, EPS Geofoam, and ranges that have been reported for tire derived aggregate for comparison with the constrained moduli calculated from the PET bale test specimens as part of this study. PET bale test specimen constrained moduli ranged from 495 kPa to 1222 kPa depending upon the test parameters, which were slightly higher than tire derived aggregate (130 kPa – 485 kPa), but significantly lower than the constrained moduli reported for EPS Geofoam (4000 kPa) and typical fill materials (10,000 kPa – 100,000 kPa).

2. The effects of loading scheme, test specimen diameter, and test specimen size/shape (full-bottle versus chopped) were evaluated from the short-term, 1D compression test results. While there was a wider variance in the results presented for the larger diameter test specimens (compared to the smaller diameter) and the full-bottle test specimens (compared to the chopped), it was concluded that the wider variance was a direct result of the variance in the constituents of the PET bale (sizes, shapes, and textures of the various packaging). In other words, the increase in volume of the randomly selected, full-bottle constituents increased the variability of the results in the larger test specimens, and the variability of the full-bottle test specimens increased the variability of the results in comparison to test specimens that were generated using only Type 1 PET recycled plastic that was systematically cut into same size and shape particles (chopped). The variability of

the PET bale constituents played a significant role in the results of all testing conducted herein.

3. Data from the short-term, 1D confined compression tests indicate that the larger unit weight test specimens (γ = 3.93 kN/m^3) produced results that exhibited a stiffer response in comparison to the lower unit weight test specimens (γ = 2.36 kN/m^3) as displayed in Figure 4.13.

The angles of internal friction for the flat, ribbed-orthogonal, and ribbed-aligned test specimen configurations were 12.0°, 12.9°, and 17.3°, respectively (Table 4.8 and Figure 4.28). The ribbed-aligned texture displayed in Figure 4.24 had the largest effect on the friction angle due to the rib-to-rib interlocking. Additionally, the measured PET bale test specimen values were compared to a value reported by Shooter and Tabor (1952) for virgin polyethylene (14°), which within the range measured during this study.

4. Friction angles ranged from 5° - 13° at the 5% strain level, 8° - 16° at the 10% strain level, and from 9° - 20° at the 15% strain level during the triaxial tests, depending on displacement rate and saturation (Table 4.11). The saturated specimens produced significantly lower results than the dry specimens. Based on the data presented by Dotmar (2015) in Table 4.12, the measured values are within the ranges presented for other plastics, including virgin PET.

5. The bulk moduli calculated from the triaxial test data ranged from 260 kPa - 285 kPa, and the stress-strain curves displayed a bi-linear trend, similar to the interface direct shear results. The initial modulus of elasticity (E_t) was steeper than the secondary modulus (E_2), and the transition point between the two moduli

occurred between 0.25% and 0.5% axial strain. However, the bi-linear shape was more pronounced for the test specimens tested using higher displacement rates.

6. It is important to note that the initial modulus of elasticity (E_t) was not dependent upon confining stress of the triaxial tests. These results differ from conventional soil behaviors. However, there was a proportional relationship between the second moduli (E_2) and the target unit weight and confining pressure for the dry and saturated test specimens displayed in Figures 4.47, 4.49, 4.51 and 4.55. Both E_t and E_2 were at least three times less when compared to Young's modulus for soil.

7. An average Young's modulus for a full-scale PET bale equal to 333 kPa was measured during the first 90 minutes of the full-scale, unconfined compression test. According to Table 5.3, the modulus reported for EPS Geofoam was 580,000 kPa and the values reported for various types of clay ranged from 475 kPa – 100,000 kPa.

8. The long-term unconfined compression test results confirmed that the PET bale exhibits creep behaviors under a long-term sustained load. For this reason, the proposed lightweight fill may not be a feasible material for the proposed application. However, the unconfined creep behavior was not representative of field conditions. Additional full-scale, confined compression testing is needed to fully assess the compressibility of PET bales for the proposed application.

9. The compression index calculated from the unconfined compression test equal to 0.02 was approximately one order of magnitude lower than the values reported in the literature for soft and hard clay (0.34 and 0.44, respectively). This suggests

that the use of the proposed material as a lightweight fill should be reserved for non-load bearing applications.

10. There was a high degree of consistency between the friction angle values measured in this study and the values reported in the literature. Because the variability associated with size, shape, and texture of the full-bottle constituents was removed when they were chopped for the triaxial test specimens, the friction angles measured during the triaxial tests served as conservative numbers for use in the limit equilibrium analysis. It is hypothesized that the inconsistencies associated with the full-bottle constituents would likely provide a higher level of shear strength.

11. A series of limit equilibrium analyses were performed using a variety of proposed configurations. For the PET bale configurations/rows that intersected the failure surface, the FS decreased in almost all cases excluding the high row configuration. While the PET bales provide a lightweight fill solution, which decreases the driving force associated with each failure surface, the decrease in shear strength of the plastic material (relative to the shear strength of a soil fill) also decreases the resisting force, which governs the FS calculation in almost all cases.

12. To better understand the effect of the proposed lightweight fill without incorporating the reduction in shear strength when the PET material intersects the failure curve, an additional limit equilibrium analysis was conducted to vary the unit weight of the material inside the fixed failure curve. PET bale results were compared to soil, EPS Geofoam, and tire bale material as well (Figure 6.9 and Table 6.9). With the exception of the EPS Geofoam values, which are slightly

higher, all other calculated FS values for this fixed failure surface were similar in magnitude for the fixed failure surface evaluated as part of this study, but more extensive limit equilibrium analyses are needed.

13. PET bales may be a feasible alternative for a lightweight material but should only be considered for non-load bearing applications due to the high compressibility and low shear strength of the material. Further research is needed to confirm the compressibility behavior of a full-scale PET bale under confined conditions.

7.3 Recommendations for Future Research

This interdisciplinary research demonstrated some potential for the application of recycled PET bales for use as lightweight fill material, but there are important limitations that have been highlighted in the conclusions outlined in the previous section. Further areas in need of investigation include: 1) large scale, recycled PET bale-to-bale direct shear testing to better assess the shear strength parameters of this material for use in a full-scale field condition; 2) permeability testing of PET bales to confirm drainage capabilities of a compacted bale that has randomly oriented plastic constituents; 3) long-term performance testing of the metal strapping to identify strap failure conditions; 4) environmental impact testing to identify and compare the negative implications of petrochemical materials have been shown to have impacts on the natural environment and global ecosystems; 5) internal and ambient temperature monitoring of a large scale PET bale to determine the effects it has on its compressive strength associated with the temporal changes of seasonal weather fluctuations; 6) large scale, compressibility testing under confined stresses to better assess the compressibility of the PET bale under in-situ field conditions; 7) additional interface direct shear and triaxial compression testing to

evaluate the bi-linear behaviors observed during this study; and 8) an in-depth limit equilibrium slope stability analysis to further assess the feasibility of using this material for the propsed application.

REFERENCES

1. AFM Technologies. (2015). "Physical Properties Requirments for EPS Geofoam." <http://www.geofoam.org> (Febuary 3, 2015).

2. Ahmed. A., Ugai, K., and Kamei, T. (2010). "Application of Gypsum Waste Plasterboard and Waste Plastic Trays to Enhance the Performance of Sandy Soil." *Ground Improvement and Geosynthetics.* 1(17). 165-173.

3. ASTM (American Society for Testing Materials). (2008). "D6817 - Standard Practice for Coding Plastic Manufactured Articles for Resin Identification." ASTM International.

4. ASTM (American Society for Testing Materials). (2015). "D570 - Standard Test Method for Water Absorption of Plastic." ASTM International.

5. ASTM (American Society for Testing Materials). (2015). "D638 - Standard test Method for Tensile Properties of Plastic." ASTM International.

6. ASTM (American Society for Testing Materials). (2015). "D648 - Standard Test Method for Deflection Temperature of Plastics Under Flexural Load in the Edgewise Position." ASTM International.

7. ASTM (American Society for Testing Materials). (2015). "D696 - Standard Test Method for Coefficient of Linear Thermal Expansion of Plastics Between -30° C and 30° C with a Vitreous Silica Dilatometer." ASTM International.

8. ASTM (American Society for Testing Materials). (2015). "D785 - Standard Test Method for Rockwell Hardness of Plastics and Electrical Insulating Materials." ASTM International.

9. ASTM (American Society for Testing Materials). (2015). "D790 - Standard Test Method for Flexural Properties of Unreinforced and Reinforced Plastics and Electrical Insulating Materials." ASTM International.

10. ASTM (American Society for Testing Materials). (2015). "D792 - Standard Test Method for Density and Specific Gravity of Plastics by Displacement." ASTM International.

11. ASTM (American Society for Testing Materials). (2015). "D1894 - Standard Test Method for Static and Kinetic Coefficients of Friction of Plastic Film and Sheeting." ASTM International.

12. ASTM (American Society for Testing Materials). (2015). "D5321 - Standard Test Method for Determining the Shear Strength of Soil-Geosynthetic and Geosynthetic-Geosynthetic Interfaces by Direct Shear." ASTM International.

13. ASTM (American Society for Testing Materials). (2015). "D7181 - Standard Test Method for Consolidated Drained Triaxial Compression Test for Soils." ASTM International.

14. Amoozegar, A. and Robarge, W. P. (2006). "Evaluation of Tire Chips as a Substitute for Gravel in the Trenches of Septic Systems." *Report to Division of Pollution Prevention and Environmental Assistance Dept. of Environment and Natural Resources.* Report# 569, 79 p.

15. Arellano, D. and Stark, T.D. (2009). "Load bearing analysis of EPS-block geofoam embankments." *Proc., 8th International Conf.on the Bearing Capacity of Roads, Railways, and Airfields.* 2(1). 981-990.

16. Arellano, D., Tatum, J.B., Stark, T.D., Horvath, J.S., and Leshchinsky, D. (2010). "Framework for Design Guideline for Expanded Polystyrene Block Geofoam in Slope Stabilization and Repair." *Transportation Research Record: Journal of the Transportation Research Board.* 3(12). 100-108.

17. Babu, G. and Chouksey, S. K. (2011). "Stress–strain Response of Plastic Waste Mixed Soil." *Waste Management.* 2(9). 481-488.

18. Babu, G. L. S. and Chouksey, S. K. (2011). "Analytical Model for Stress-Strain Response of Plastic Waste Mixed Soil." *Geo-Frontiers 2011: Advances in Geotechnical Engineering - Proc. of the Geo-Fronteries 2011 Conf.* 1(3). 1091-1100.

19. Balazs, G.H. (1985). "Impact of Ocean Debris on Marine Turtles: Entanglement and Ingestion." *Proc. of the Workshop on the Fate and Impact of Marine Debris*, 1(4). 387-429.

20. Benson, C. H. and Khire, M. V. (1994). "Reinforcing Sand with Strips of Reclaimed High-Density Polyethylene." *Journal of Geotechnical Engineering.* 120(5). 838-855.

21. Bernal, A., Lovell, C. and Salgado, R. (1996). "Laboratory Study on the Use of tire Shreds and Rubber-Sand in Backfilled and Reinforced Soil Applications." *Joint Transportation Research Program.* 45(6). 136-145.

22. Bishop, A.W. (1955). "The Use of Slip Circles in the Stability Analysis of Earth Slopes," *Geotechnique*, 5(1), 7-17.

23. Bjorndal, K.A., Bolton, A.B., and Lagueux, C.J. (1993). "Marine Debris Contamination of Beaches in St. Lucia and Dominica." *Marine Pollution Bulleti.* 6(1). 325-328.

24. Bowders, J. J., Loehr, J.E., Salim, H. and Chen, C. W. (2003). "Engineering Properties of Recycled Plastic Pins for Slope Stabilization." *Transportation Research Record: Journal of the Transportation Research Board.* 1849(1): 39-46.

25. CalRecycle (2015). "Tire-Derived Aggregate Uses." <http://www.calrecycle.ca.gov/tires/TDA/Uses/> (January, 6, 2015).

26. Consoli, N. C., Montardo, J. P., Prietto, P. D. M. and Pasa, G. S. (2002). "Engineering Behavior of a Sand Reinforced with Plastic Waste." *Journal of Geotechnical and Geoenvironmental Engineering.* 128(1). 462-472.

27. Day, R.H. (1980). "The Occurrence and Characteristics of Plastic Pollution in Alaska's Marine Birds." *M.S. Thesis.* University of Alaska. Fairbanks, AK, 111.

28. Day, R.H. (1986). "Report on the Cruise of the Pusan 851 to the North Pacific Ocean.", *Final Report to US Department of Commerce, National Marine Fisheries Service, Auke Bay Laboratory.* Auke Bay, AK, 73.

29. Day, R.H. and Shaw, D.G. (1987). "Patterns in the Abundance of Pelagic Plastic and Tar in the North Pacific Ocean." *Marine Pollution Bulletin.* 45(3). 311-316.

30. Dodds, J., Domenico, . P., Evans, D. R., Fish, L. ., Lusahn, P. L., and Toth, . J. (1983). "Scrap Tires: A Resource and Technology Evaluation of Tire Pyrolysis and Other Selected Alternative Technologies." *Report for U.S. Dept. of Energy.* Idaho Falls, Idaho, 47(6). 1-51.

31. Domone, P. and Illston, J. (2001). *Construciton Materials: Their Nature and Behavious.* Third Edition. Spon Press. London. New York.

32. Dotmar Engineering Plastics (2014). "Coefficients of Friction of Plastics." <http://www.dotmar.com.au/co-efficient-of-friction.html> (March 15, 2014).

33. Dutta, R. and Rao, G. V. (2007). "Regression Models for Predicting the Behavior of Sand Reinforced with Waste Plastic." *Turkish Journal of Engineering & Environmental Sciences.* 31(2). 119-126.

34. Elragi, A., Negussey, D. and Kyanka, G. (2000). "Sample Size Effects on the Behavior of EPS geofoam." *Geotechnical Special Publication.* 36(3). 280-291.

35. EPA (Environmental Protection Agency). (2012). "Wastes - Resource Conservation - Common Wastes & Materials - Plastics." <http://www.epa.gov/osw/conserve/materials/plastics.htm> (January, 6, 2013).

36. Fellenius, W. (1936). "Calculation of the Stability of Earth Dams", *Transactions of the 2nd Congress on Large Dam & International Commission on Large Dams of the World Power Conference.* 4(1). 445-462.

37. FHWA (Federal Highway Administration). (2000). "Mechanically Stabilized Earth Walls and Reinforced Soil Slopes: Design and Construction Guideline*." Report FHWA-NHI-00-04, Federal Highway Administration.* U.S. Department of Transportation, Washington D.C.

38. Finney, B., Chandler, Z. Bruce, J. and Apple, B. (2013). "Properties of Tire-Derived Aggregate for Civil Engineering Application." *California Department of Resources Recycling and Recovery*. 121(5). 1-169.

39. Fowler, C.W. (1987). "Marine Debris and Northern Fur Seals: A Case Study". *Marine Pollution Bulletin.* 66(9). 339-343.

40. Frydenlund, T. E. and Aaboe, R. (1988). "Expanded Polystyrene - A Superlight Fill Material." Proc. of the International Symposium of Theory and Practive of Earth Reinforcement. Fukuoka, Japan 5-7 Oct. 1988." 383-388.

41. Geofoam Research Center (2000). "Slope Stabilization Applications." <http://geofoam.syr.edu/> (March 3, 2015).

42. Geotechnicalinfo.com. (2012). "Yougn's Modulus of Soils." <http://www.geotechnicalinfo.com/youngs_modulus.html> (September 2015).

43. Ghiassian, H., Poorebrahim, G. and Gray, D.H. (2004). "Soil Reinforcement with Recycled Carpet Wastes." *Waste Management & Research.* 22(2). 108-114.

44. Gray, D. H. and Al-Refeai, T. (1986). "Behavior of Fabric-Versus Fiber-Reinforced Sand." *Journal of Geotechnical Engineering.* 112(8). 804-820.

45. Gray, D. H. and Ohashi, H. (1983). "Mechanics of Fiber Reinforcement in Sand." *Journal of Geotechnical Engineering.* 109(3). 335-353.

46. Grubb, D. G., Davis, A. F. , Sands, S. C. , Carnivale III, M., Wartman, J., and Gallagher, P. M. (2006). "Field Evaluation of Crushed Glass–Dredged Material Blends." *Journal of geotechnical and geoenvironmental engineering*. 132(5). 577-590.

47. Grubb, D. G., Liu, W. Cadden, A. W., and Humphrey, D. N. (2007). "Bulkhead Design Using Recycled Materials as Backfill", *Proc. of the 11th Triennial International Conference*. 45(5). 1997-2007.

48. Hoare, D. (1979). "Laboratory Study of Granular Soils Reinforced with Randomly Oriented Discrete Fibers." *Proc., Int. Conf. on Soil Reinforcement Paris.* France, Association Amicale des Engenieurs Anciens Eleves de L'Ecole Nationale de Ponts et Chausees. 51(4). 319-333.

49. Horvath, J. (1994). "Expanded polystyrene (EPS) Geofoam: An Introduction to Material Behavior." *Geotextiles and Geomembranes*. 13(4). 263-280.

50. Horvath, J. (2010). "Emerging Trends in Failures Involving EPS-block Geofoam Fills." *Journal of performance of constructed facilities.* 24(4). 365-372.

51. Humphrey, D. N. (2003). "Civil Engineering Applications Using Tire-Derived Aggregate (TDA)." University of Maine, 16(9). 1-142.

52. Humphrey, D. N., Whetten, N., Weaver, J., Recker, K., and Cosgrove, T. A. (1998). "Tire Shreds as Lightweight Fill for Embankments and Retaining Walls." *Recycled Materials in Geotechnical Applications & Session Proc. ASCE Annual Convention*. Boston, MA. 17(2). 51-65.

53. Janbu, N., Bjerrum, L., and Kjaernsli, B. (1956). "Veiledning ved Losning av Fundamenteringsoppgaver." *Soil Mechanics Applied ot Some Engineering Problems.* Publication 16. Norwegian Geotechnical Institute. 1-16.

54. Jutkofsky, W. S., Sung, J. T., and Negussey, D. (2000). "Stabilization of Embankment Slope with Geofoam." *Transportation Research Record: Journal of the Transportation Research Board.* 1736(1). 94-102.

55. Keeler, M. and Burke, B. (2009) *Fundaments of Integrated Desing for Sustainable Buildings*. John Wiley & Sons, Inc. Hoboken, New Jersey.

56. Khoury, N., Khoury, C. and Abousleiman, Y. (2008). "Soil Fused with Recycled Plastic Bottles for Various Geo-Engineering Application." *GeoCongress 2008.* 111(2). 336-343.

57. Laist, D.W. (1997). "Impacts of Marine Debris: Entanglement of Marine Life in Marine Debris Including a Comprehensive List of Species with Entanglement and Ingestion Recrods."*Marine Debris: Sources, Impacts, and Solutions.* 1152 (6). 99-140.

58. LaRocque, C. J., Zornberg, J. G. and Williammee, R. (2005). "Direct Shear Testing of Tire Bales for Soil Reinforcement Applications." *ASCE Geo-Frontiers 2005*. 29(5). 4021-4025.

59. Lawton, E. C., Khire, M. V., and Fox, N. S. (1993). "Reinforcement of Soils by Multioriented Geosynthetic Inclusions." J*ournal of Geotechnical Engineering*. 119(1). 257-275.

60. Loehr, J., Bowders, J., Owen, J., Sommers, L., and Liew, L. (2000). "Stabilization of Slopes Using Recycled Plastic Pins." *Journal of the Transportation Research Board.* 126(2). 1-8.

61. Loehr, J. E., Ang, E. C., Parra, J. R., and Bowders, J. J. (2004). "Design Methodology for Stabilizing Slopes Using Recycled Plastic Reinforcement." *Geotechnical Engineering for Transportation Projects: Proc. of Geo-Trans 2004*. 41(5). 2200-2228.

62. Loehr, J. E., Bowders, J. and Fennessey, T. (2001). "Mechanical Stabilization of Earth Slopes Using Recycled Materials." *Proc. of Beneficial Use of Recycled Materials in Transportation Applications*. Washington, D.C. 1-4.

63. Maher, M. H. and Gray, D. H. (1990). "Static Response of Sands Reinforced with Randomly Distributed Fibers." *Journal of Geotechnical engineering*. 116(11). 1661-1677.

64. Mann, G. and Stark, T. D. (2007). "Slope Stabilization Using Geofoam.", *Proc. of Sessions of Geo-Denver 2007 Congress: Embankments, Dams, and Slopes*. 108(9). 224-238.

65. Mato, Y., Isobe, T., Takada, H., Kanehiro, H., Ohtake, C. and Kaminuma, T. (2001). "Plastic Resin Pellets as a Transport Medium for Toxic Chemicals in the Marine Environment." *Environmental Science Technology.* 35(1). 318-324.

66. Matweb. (2013). "Overview of materials for Low Density Polyethylene (LDPE), Molded." <http:// http://www.matweb.com/search/datasheettext.aspx?matguid= 8e92b9e66e214e1b8fc8222dbff6d480> (Feb. 1, 2013).

67. Moore, C.J., Moore, S.L., Leecaster, M.K., and Weisberg, S.B. (2001). "A Comparisono of Plastic and Plankton in the North Pacific Central Gyre." *Marine Polution Bulletin.* 42(1). 1297-1300.

68. Negussey, D. (2007). "Design parameters for EPS geofoam." *Soils and Foundations.* 47(1). 161-170.

69. Negussey, D. and Jahanandish, M. (1993). "Comparison of Some Engineeringn Properties of Polystyrene with Those of Soils." *Transportation Research Record*. 101(6). 1418-1428.

70. Newman, M. P., Bartlett, S., and Lawton, E. (2010). "Numerical Modeling of Geofoam Embankments." *Journal of Geotechnical and Geoenvironmental Engineering*. 136(1). 290-299.

71. Oh, S. W., Lee, J., Kwon, Y. C. and Lee, B. J. (2002). "Bearing Capacity of Light Weight Soil Using Recycled Styrofoam Beads." *International Offshore and Polar Engineering Conference.* Kitakyushu, Japan. The International Society of Offshore and Polar Engineers. 2(8). 670-674.

72. Okoro, C. C., Vogtman, J., Yousif, A., Agnaou M., and Khoury, N. (2011). "Consolidation Characteristics of Soils Stabilized with Lime, Coal Combustion Product and Plastic Waste." *Proc. of the Geo-Frontiers 2011 Conference*. 56(8). 123-132.

73. Ooi, P. S. K., Li, M. M. W., Sagario, M. L. Q. and Song, Y. (2008). "Shear Strength Characteristics of Recycled Glass." *Transportation Research Record: Journal of the Transportation Research Board*. 2059(1): 52-62.

74. Parra, J. R., Loehr, J. E., Hagemeyer, D. J., and Bowders, J. J. (2003). "Field Performance of Embankments Stabilized with Recycled Plastic Reinforcement." *Transportation Research Record: Journal of the Transportation Research Board*. 1849(1). 31-38.

75. Plastic Products, Inc. (2014). "Physical, Mechanical and Thermal Properties of PET plastic." < http://www.plastic-products.com/part12.htm> (May 6, 2014).

76. Reddy, K. R. (1999). "Use of Glass Cullet as Backfill Material for Retaining Structures." *International Conference on Solid Waste Technology and Management.* Philadelphia, PA. 1278(1). 1-8.

77. Robards, M.D. (1993) "Plastic Ingestion by North Pacific Seabirds." *U.S. Department of Commerce.* NOAA-43ABNF203014. Washington, DC.

78. Ryan, P.G. (1987). "The Effects of Ingested Plastic on Seabirds: Correlations Between Plastic Food and Body Condition." *Environmental Pollution.* 46(1). 119-125.

79. Ryan, P.G. (1990). "The effects of ingested plastic and other marine debris on seabirds." *Proceeding of the Second Conference on Marine Debris.* 119(23). 623-634.

80. Scardaci, A., Cheng, D., and Van Atta, D. (2012). "Tire-Derived Aggregate Gradation Analysis for Humboldt State University TDA Project." *TDA Technology Center.* California State University, Chico, CA. 1161(8). 1-9.

81. Shaw, D.G. and Mapes, G.A. (1979). "Surface Circulation and the Distribution of Pelagic Tar and Plastics." *Marine Pollution Bulletin.* 10(1). 160-162.

82. Shooter, K.V. and Tabor, D. (1952). "The Frictional Properties of Plastics. *Research Laboratory for the Physics and Chemistry of Surfaces.* Department of Physical Chemistry, Cambridge. 458(5). 660-671.

83. Sobhan, K. and M. Mashnad (2003). "Mechanical Stabilization of Cemented Soil–Fly Ash Mixtures with Recycled Plastic Strips." *Journal of Environmental Engineering.* 129(1). 943-947.

84. Soleimanbeigi, A., Edil, T.B. and Benson, C. H. (2011). "Recycled Asphalt Shingles Mixed with Granular Byproducts as Structural Fills." *Journal of ASTM International.* 9(1). 1-19.

85. Spencer, E. (1967). "A Method of Analysis of the Stability of Embankments Assuming Parallel Inter-slice Forces." *Geotechnique.* 17(1). 11-26.

86. Strenk, P.M., Wartman, J., Grubb, D.G., Humphrey, D.N., and Natale, M. F. (2007). "Variability and Scale-Dependency of Tire-Derived Aggregate." *Journal of Materials in Civil Engineering.* 19(3). 233-241.

87. Tatlisoz, N., Benson, C.H., and Edil, T.B. (1997). "Effect of Fines on Mechanical Properties of Soil-Tire Chip Mixtures." *Testing Soil Mixed with Waste or Recycled Materials.* 55(8). 93-108.

88. Viratjandr, C. (2006). "Fiber-Reinforcement of Soils and Stability Analysis of Reinforced Foundation Soils." *Thesis.* University of Michigan.

89. Wallace, N. (1985). "Debris Entanglement in the Marine Environment: A Review." *Proc. of the Workshop on the Fate and Impact of Marine Debris.* 36(5). 259-277.

90. Wang, Y. (2006). "Utilization of Recycled Carpet Waste Fibers for Reinforcement of Concrete and Soil." *Recycling in Textiles.* 238(7). 213-224.

91. Warner, J. D. and Edil, T. B. (2012). "An Evaluation of Reclaimed Asphalt Shingles for Beneficial Reuse in Roadway Construction." *Journal of ASTM International.* 9(1). 1 - 16.

92. Wartman, J., Grubb, D. G., and Strenk, P. (2004). "<u>Engineering Properties of Crushed Glass-Soil Blends</u>." Geotechnical Engineering for Transportation Projects: Proceedings of Geo-Trans 2004. 267(6). 732-739.

93. Whinfield, J.R. and Dickson, J.T. (1941). "Improvements Relating to the Manufacture of Highly Polymeric Substance." *UK Patent 578,079, Polymeric Linear Terephthalic Esters, US Patent 2,465,319*. Issued 1941

94. Winter, M., Williammee, R., and Prikryl, W. (2009). "Application of Tyre Bales to Slope Failure Repair." *Engineering Sustainability: Proc. of the Ice.* 162(1). 1-8.

95. Wyeth, N.C. (1973). "Biaxially Oriented Polyethylene Terephthalate Botte." *US Patent 3,733,309.* Issued 1973.

96. Zornberg, J. (2002). "Discrete Framework for Limit Equilibrium Analysis of Fibre-Reinforced Soil." *Géotechnique.* 52(8). 593-604.

97. Zornberg, J. G., Costa, Y. D., and Vollenweider, B. (2004). "Performance of Prototype Embankment Built with Tire Shreds and Nongranular Soil." *Transportation Research Record: Journal of the Transportation Research Board.* 1874(1). 70-77.

APPENDIX A: EQUIPMENT SPECIFICATIONS

A.1 Equipment Specifications

Table A.1 summarizes the UTS tensile machine specifications and Table A.2 presents the specifications for the hydraulic grips manufactured by Curtis "Sure-Grip" Incorporated. These pieces of equipment were discussed in Chapter 3 associated with the tensile strength examination.

Table A.1: UTS tensile machine specifications

Category	Value	Units
Capacity	100	KN
Full & Return Speeds	508	mm/min
Min. Speed	0.0017	mm/min
Max. Force at Full Speed	100	kN
Max. Speed at Full Speed	508	mm/min
Total Crosshead Travel	1067	Mm
Total Vertical Test Space	1041	mm
Clearance between columns	560	mm
Frame Stiffness	140	kN/mm
Approx. Height	1625	mm
Approx. Width	889	mm
Approx. Depth	660	mm
Weight	364	kg

Table A.2: Hydraulic grips specifications

Category	Value	Units
Capacity	44.48	kN
Weight	11.79	kg
Adapter Threads	19.05	mm
Approx. Width	25.4 - 203.2	mm
Approx. Thickness	0 - 38.1	mm

Tables A.3 and A.4 summarize the specifications for the load cell and string potentiometer, respectively. These pieces of equipment were discussed in Chapter 4 associated with the 1D short term confined compression examination.

Table A.3: Pacific compression canister load cell specifications (Pacific, 2015)

Category	Value
Full Capacity Range	0 - 445 kN
Rated Output	4.00 mV/V +/- 0.25%
Combined Error	+/- 0.02%
Nonlinearity	+/- 0.03%
Hysteresis	+/- 0.05%
Material	Tool Steel
Sealing	IP67
Weight	9.07 kg
Excitation Voltage	10 VDC (20VDC Max)
Compensated Temperature Range	-10° to 40°C
Operating Temperature Range	-40° to 65°C

Table A.4: Measurement Specialties string potentiometer specifications (Measurement Specialties, 2015)

Category	Value
Full Stroke Range	0 - 1270 mm
Output Signal	Voltage divider (potentiometer)
Accuracy	+/- 0.25%
Repeatability	+/- 0.05% full stroke
Resolution	Essentially infinite
Enclosure Material	Polycarbonate
Sensor	Plastic-hybrid precision potentiometer
Weight	141 grams
Input Resistance	10K ohms, +/-10%
Power Rating, Watts	2.0 at 21°C
Operating Temperature Range	-18° to 71°C

Table A.5 summarizes the specifications for the GeoTac direct shear machine. This equipment was discussed in Chapter 4 associated with the direct shear examination.

Table A.5: GeoTac direct shear machine specifications

Category	Value
Excitation	10 V DC
Vertical Load Capacity	5-pin DIN
Horizontal Load Capacity	0.45
Speed	7.8 e^{-7} to 0.079 cm/min
Horizontal Travel	+/- 1.27 cm

The Interface transducer specifications are outlined in Table A.6. The ELE transducer specifications are outlined in Table A.7. These pieces of equipment were discussed in Chapter 4 associated with the triaxial shear strength examination.

Table A.6: Interface force transducer specifications

Category	Value
Accuracy - (Max Error)	
Nonlinearity - % FS	+/- 0.05
Hysteresis - % FS	+/- 0.03
Non-repeatability - % RO	+/- 0.02
Creep in 20 min - %	+/- 0.025
Temperature	
Compensated Range - ^{o}C	-15 to 65
Operating Range - ^{o}C	-55 to 90
Effect on Output - %/^{o}C - Max	+/- 0.0015
Effect on Zero - %/^{o}C - Max	+/- 0.0027
Electrical	
Rated Output - mV/V (Nominal)	3
Zero Balance - % RO	+/- 1
Bridge Resistance - Ohm (Nominal)	350
Excitation Voltage - Max	15 VDC
Insulation Resistance - Megaohm	>5000

Table A.7: ELE axial strain transducer specifications

Category	Value
Excitation	10 V DC
Connector	5-pin DIN
Weight (kg)	0.45
Range (mm)	0 to 76.2

Table A.8 summarizes the specifications of the Danfuss MCX120 string potentiometers. These pieces of equipment were discussed in Chapter 5.

Table A.8: Danfuss MXC120 string potentiometer specifications (Danfuss, 2014)

Category	Value
Input Voltage	9 to 36 VDC
Operating Temperature Range	-40º to 85ºC
Range	545 mm
Resolution	0.1 mm
Current Draw	50 mA maximum
EMI/RFI Rating	100 V/m
Weight	0.34 kg

A.2 Equipment Calibration Factors

Table A.9 summarizes the calibration factors utilized for each experimental phases for load and displacement. The values from Table A.8 were calculated using the information displayed in the corresponding Figures A.1 - A.12, respectively.

Table A.9: Summary of calibration factors for all experimental research

Experimental Phase	Equipment Type	Calibration Factor	R^2
Compression	Load Cell	11,031 kN/V	1
Compression	Displacement	-2.0866 cm/V	1
Direct Shear	Vertical Load Cell	0.2591 kN/V	1
Direct Shear	Horizontal Load Cell	0.2753 kN/V	1
Direct Shear	Vertical Displacement	-0.0812 cm/V	1
Direct Shear	Horizontal Displacement	0.083 cm/V	1
Triaxial	Load Cell	-0.2730 kN/V	1
Triaxial	Displacement	-0.0847 cm/V	1
Creep	Displacement - 1	-1.0858 cm/V	1
Creep	Displacement - 2	1.312 cm/V	1
Creep	Displacement - 3	1.3045 cm/V	1
Creep	Displacement - 4	1.2836 cm/V	1
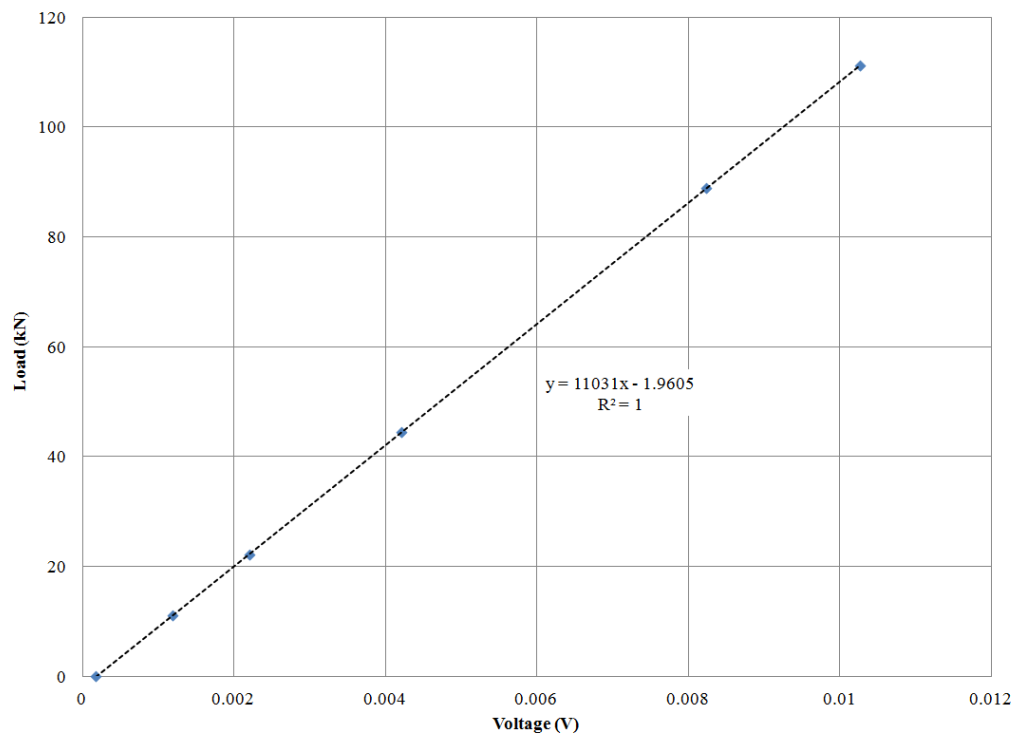
Figure A.1: Compression load cell voltage as a function of load
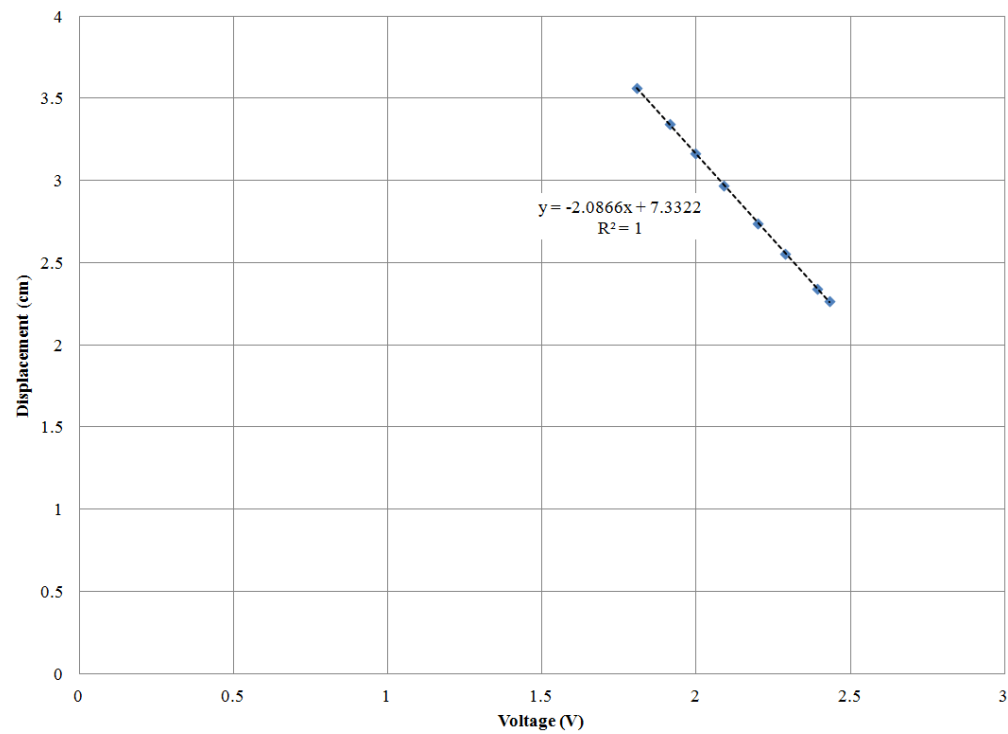
Figure A.2: Compression LVDT voltage as a function of displacement
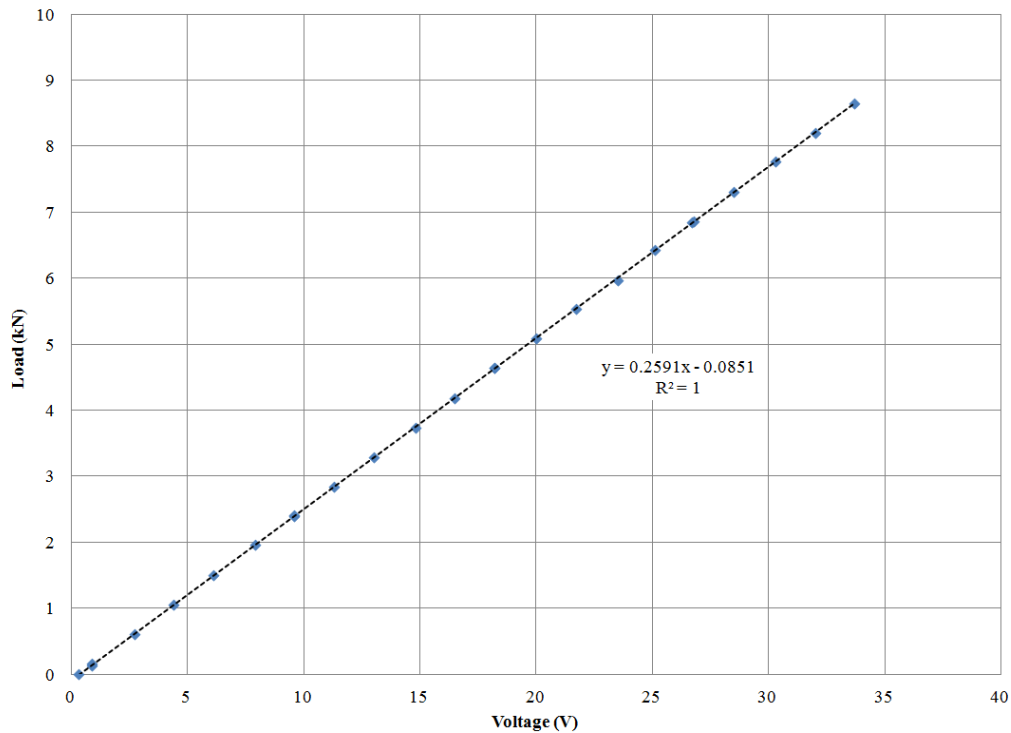
Figure A.3: Direct shear vertical load cell voltage as a function of load
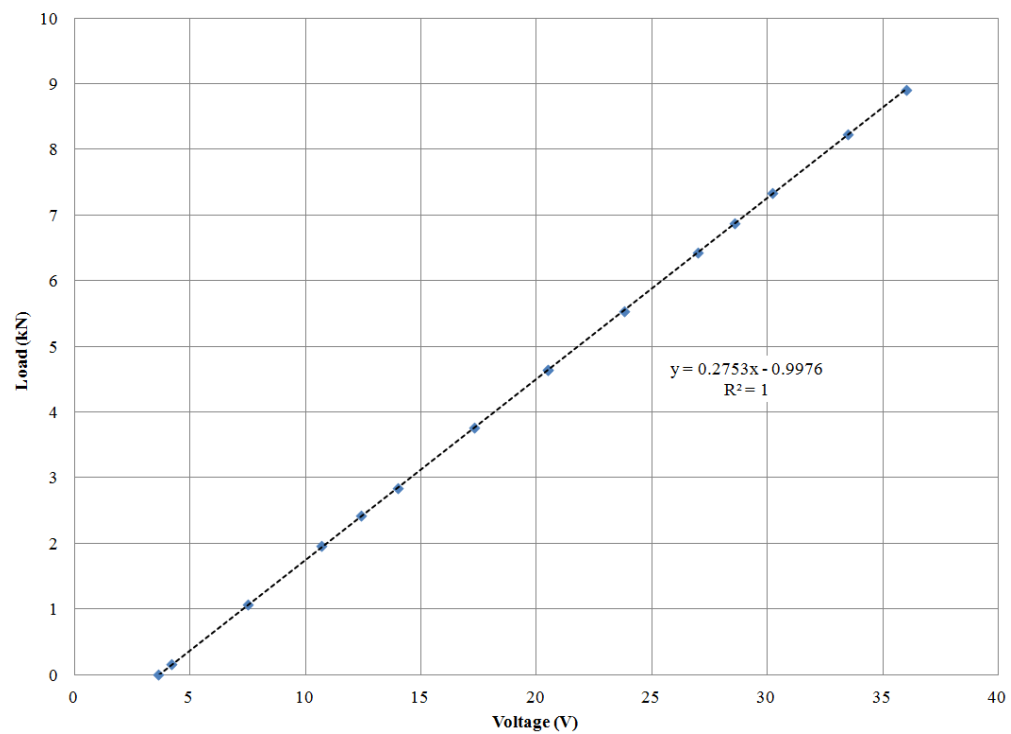

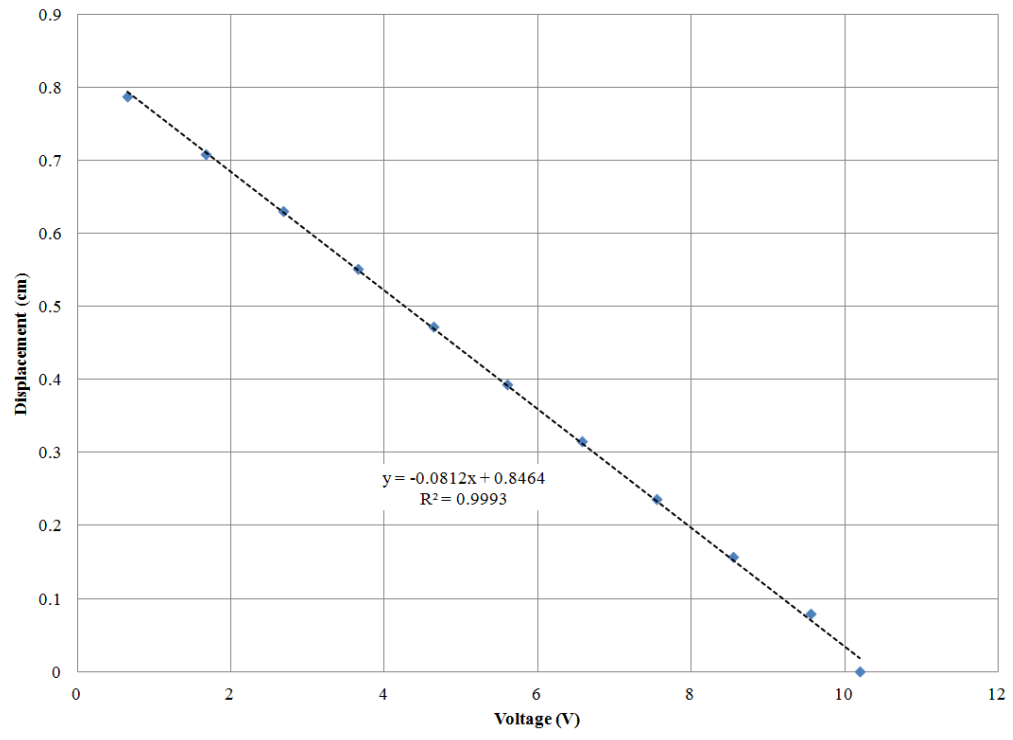Figure A.4: Direct shear horizontal load cell voltage as a function of load

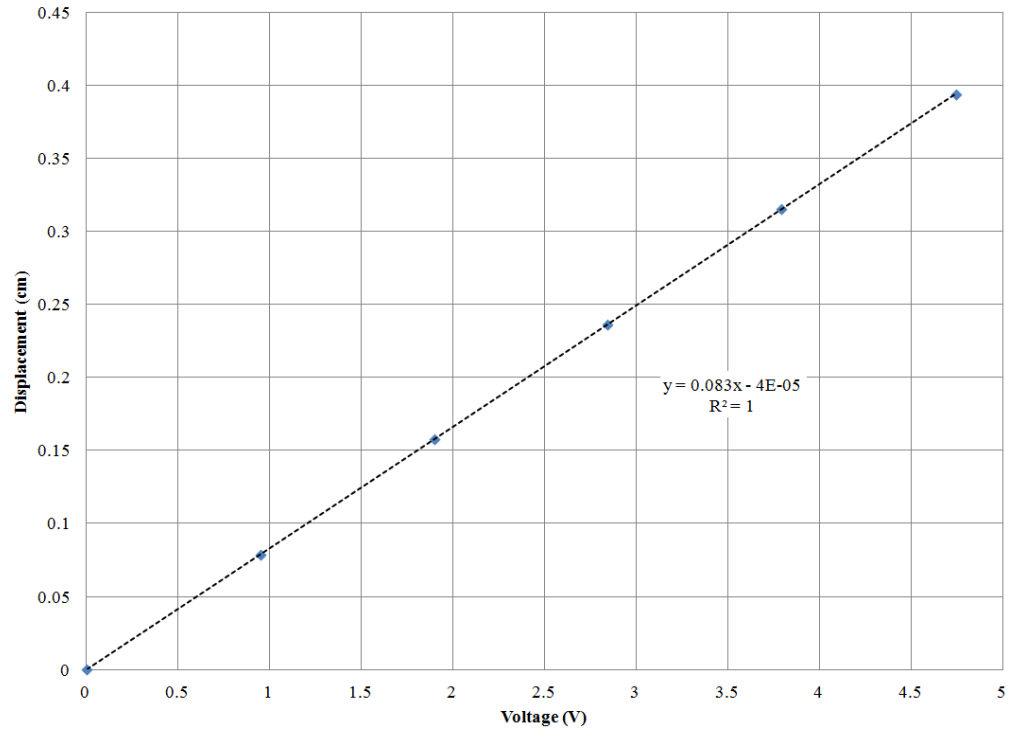Figure A.5: Direct shear vertical LVDT voltage as a function of displacement

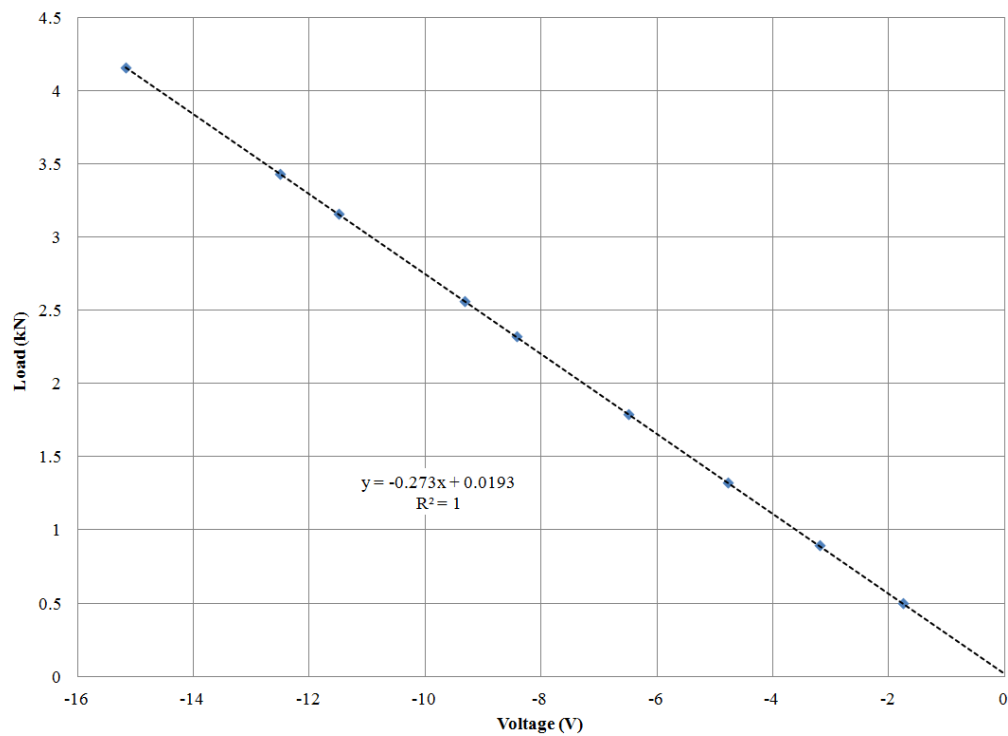Figure A.6: Direct shear horizontal LVDT voltage as a function of displacement
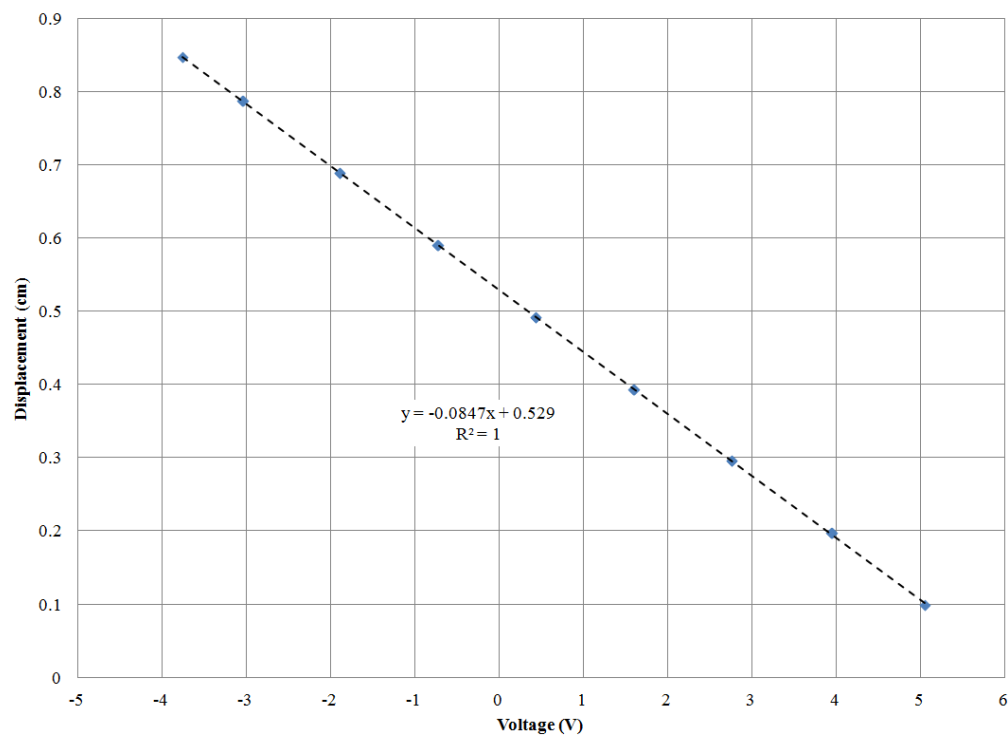
Figure A.7: Triaxial load cell voltage as a function of load

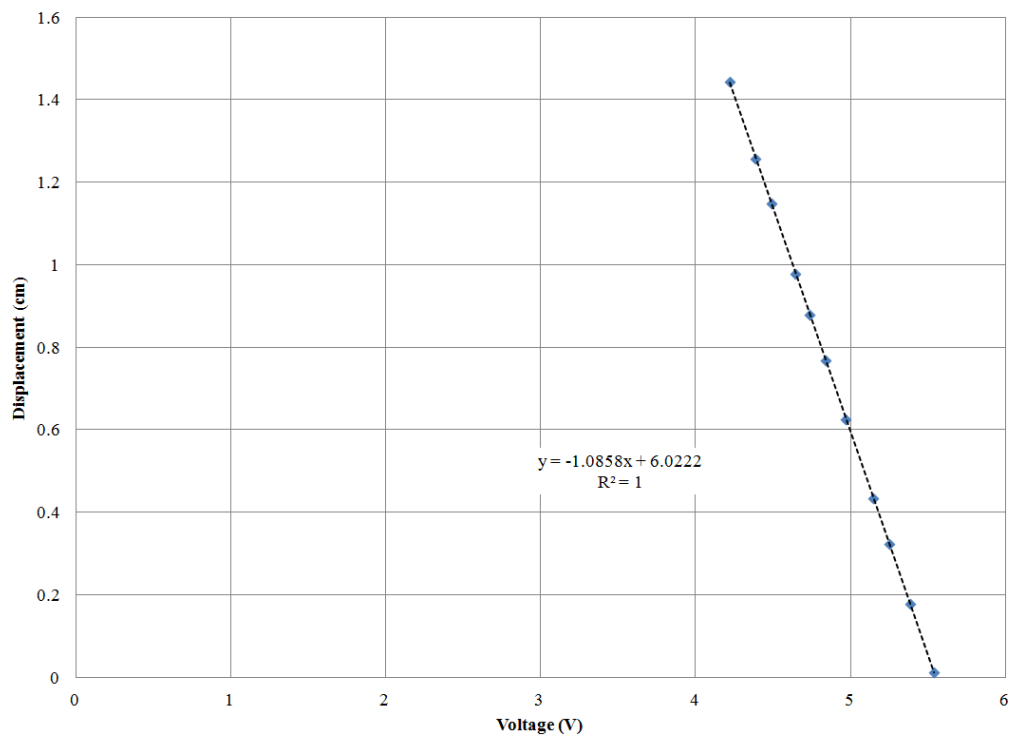Figure A.8: Triaxial LVDT voltage as a function of displacement

Figure A.9: Creep LVDT 1 voltage as a function of displacement
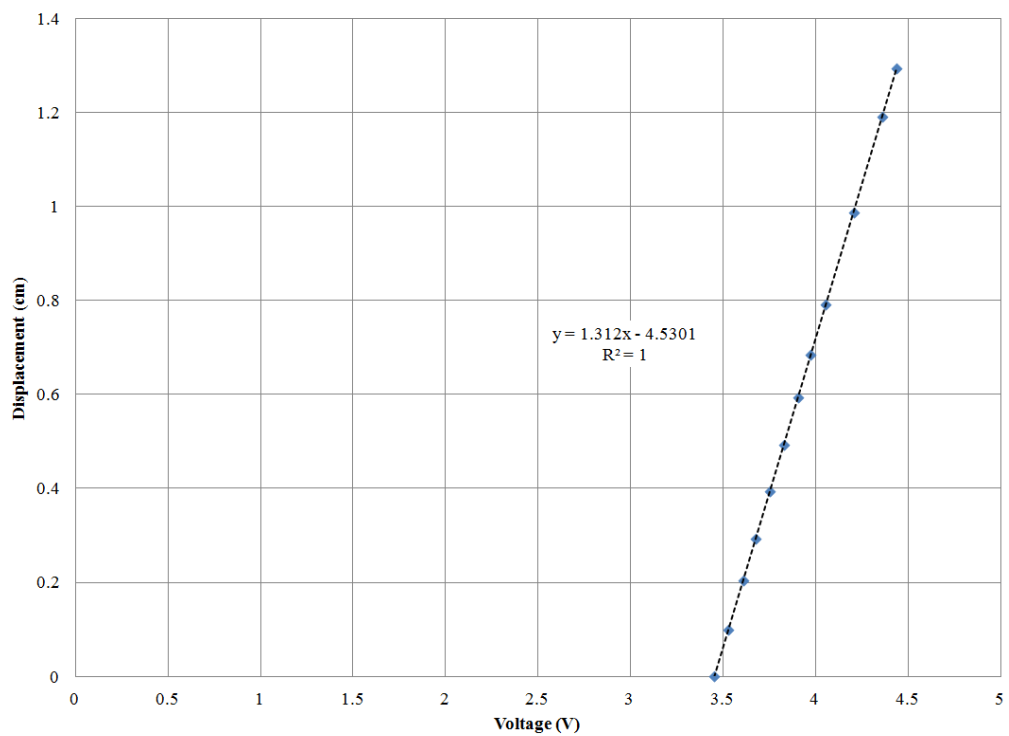

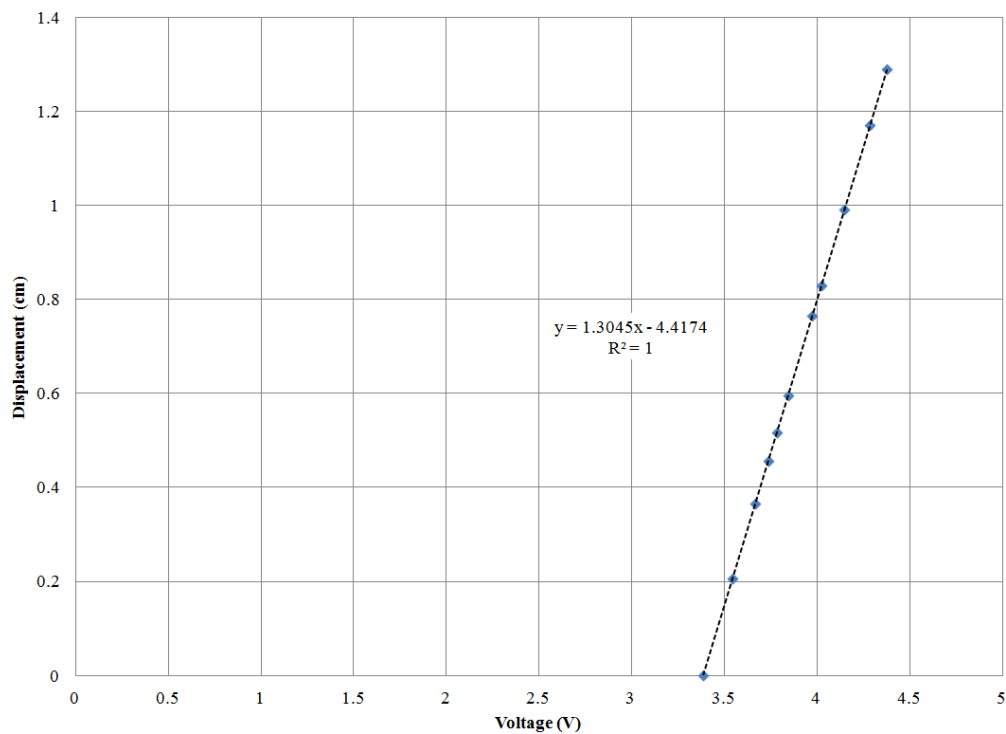Figure A.10: Creep LVDT 2 voltage as a function of displacement

Figure A.11: Creep LVDT 3 voltage as a function of displacement
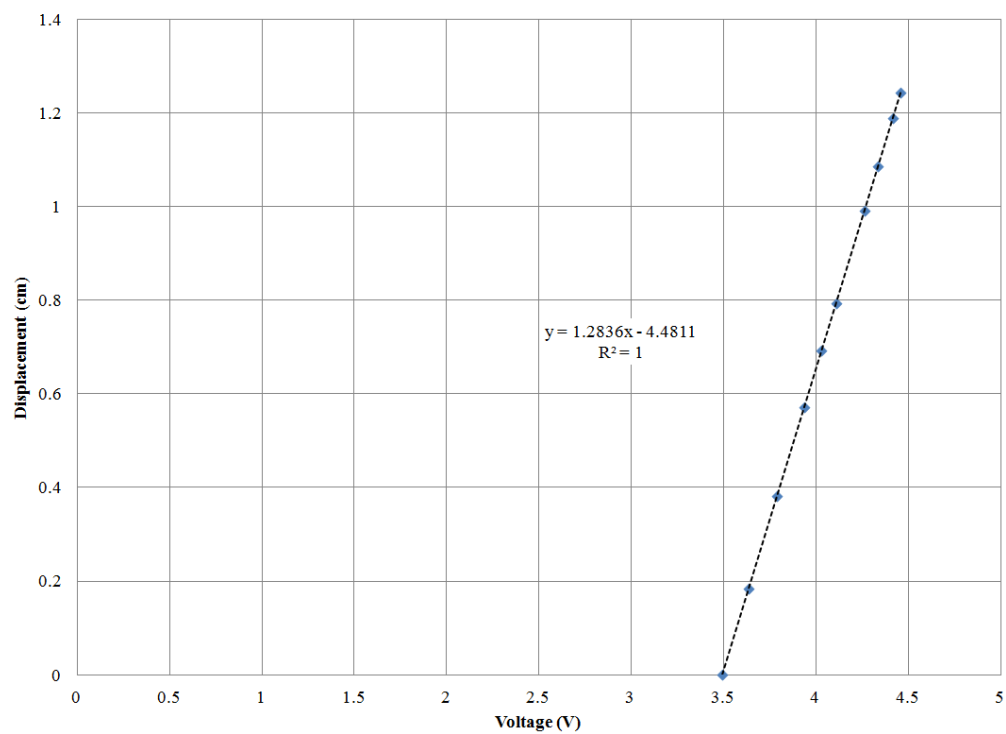
$$y = 1.3045x - 4.4174$$
$$R^2 = 1$$

Figure A.12: Creep LVDT 4 voltage as a function of displacement

$$y = 1.2836x - 4.4811$$
$$R^2 = 1$$